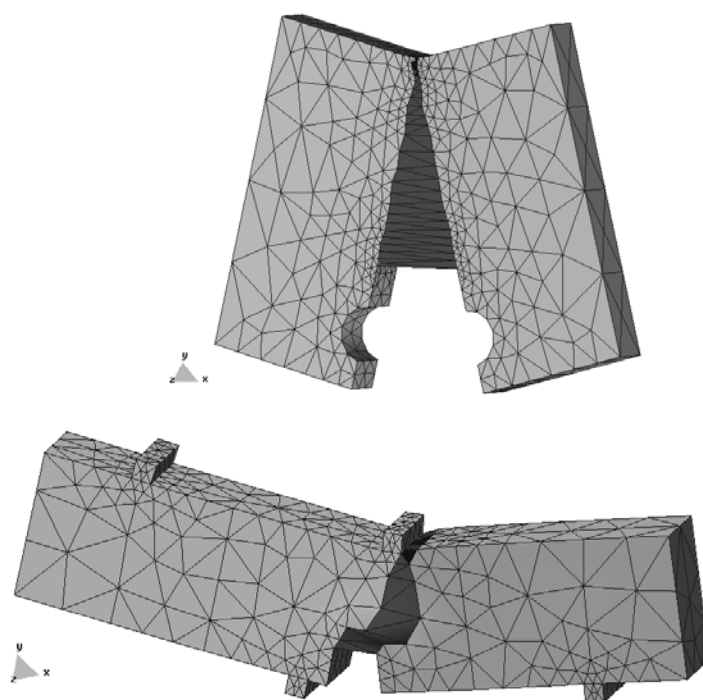# A Three Dimensional Setting for Strong Discontinuities Modelling in Failure Mechanics

E. W.V. Chaves
X. Oliver

A Three Dimensional Setting for Strong Discontinuities Modelling in Failure Mechanics

E. W.V. Chaves
X. Oliver

**A Three Dimensional Setting for Strong
Discontinuities Modelling in Failure Mechanics**

Contents

Nomenclature

$\mathbf{a}_e$	Nodal displacements;
$\mathcal{B}$	Body;
$\mathcal{B}_0$	Configuration of the body in $t = 0$;
$\partial\mathcal{B}$	Boundary of $\mathcal{B}$;
$\mathbf{B}$	Strain interpolation matrix;
$\mathbf{b}(\mathbf{x},t)$	Body forces;
$\mathbb{C}^e$	Matrix with the elastic properties;
$\boldsymbol{\mathcal{C}}$	Elastic matrix (Voigt notation);
$\mathbb{C}^{in}$	Inelastic constitutive tensor;
$\mathbb{C}^d$, $\mathbb{C}^{ep}$	Damage and Elastoplastic constitutive tensor, respectively;
c	Cohesion;
d	Damage parameter;
d	Differentiate;
$\mathcal{D}$	Dissipation;
$e(\mathbf{x},t)$	Specific internal energy;
E	Young's modulus;
$\hat{\mathbf{e}}_i$	Cartesian basis;
$\mathcal{F}$	Yield function;
$\mathbf{F}_{ext}$	Global nodal external forces;
$\mathcal{F}_{int}$	Vector of nodal internal forces;
$\mathcal{G}_f = G_I$	Fracture energy correspondent to mode I;
G_{II}	Fracture energy correspondent to mode II;
G_{III}	Fracture energy correspondent to mode III;
$\mathcal{G}$	Plastic potential;
G	Shear modulus;
g_f	Energy per unit volume;
$\mathcal{H}^p$	Plastic hardening/softening modulus;
$\mathcal{H}^d$	Damage hardening/softening modulus;
$\overline{\mathcal{H}}^d$	Discrete (or intrinsic) hardening/softening parameter;
$\mathcal{H}_{crit}$	Critical hardening/softening parameter;
$H_{\mathcal{B}_h}(\mathbf{x})$	Ramp function;
$H_{\mathcal{S}}$	Heaviside function, step function, unit jump function;
$h(\eta)$	Bandwidth;
$\mathbb{I}, \mathbb{I}_{ijkl}$	Components of the 4$^{\text{th}}$ order identity tensor and components, respectively;
I_1, I_2, I_3	First, third and fourth invariants, respectively;
$[\mathbf{J}]$	Jacobian matrix;
$\mathbb{K}$	Global stiffness matrix;

k	Yield stress in pure shear;
k	Bandwidth value in the strong discontinuity regime, $k \ll 1$;
ℓ^*	Characteristic length;
$\mathcal{L}$	Discontinuity line;
$\mathbf{M}$	Polarization direction;
$\mathbf{m}$	Unity vector normal to the plastic potential;
$\mathbf{n}$	Unity vector normal to yield surface;
$\mathbf{N}$	Propagation direction ;
$\mathbf{N}_{crit}$	Critical direction of propagation;
$\mathbb{N}$	Displacement interpolation functions;
p	Spherical or hydrostatic stress tensor;
$\mathcal{P}$	Material point;
$\mathbf{q}$	Heat flux vector;
$\mathbf{Q}^e(\mathbf{N})$	Elastic acoustic tensor;
$\mathbf{Q}(\mathbf{N})$	Localization tensor;
$q(r)$	Stress-like hardening/softening variable;
r_0	Initial threshold value;
$r(\mathbf{x},t)$	Volumetric density of the internal heat production;
$\mathbf{s}$	Deviatoric stress tensor;
$\mathbf{s}_1, \mathbf{s}_2, \mathbf{s}_3$	Principal deviatoric stress ;
$\Delta \mathbf{R}$	Residual vector;
$s(\mathbf{x},t)$	Specific entropy per unit mass;
$\mathcal{S}$	Discontinuity surface;
$\mathcal{T}$	Traction vector;
$T(\mathbf{x},t)$	Temperature;
t	Pseudo-time;
$\mathbf{t}(\mathbf{x})$	Tractions;
$\mathbf{t}^*(\mathbf{x})$	Prescribed surface traction;
U	Elastic energy;
$\mathbf{u}$	Displacement filed;
$\mathbf{u}^*$	Prescribed displacement;
$[\![\mathbf{u}]\!]$	Jump in displacement;
$\boldsymbol{\upsilon}$	Outward unit normal to the boundary $\partial\mathcal{B}$;
$\mathcal{W}_{int}$	Work of the internal forces or internal virtual work or strain energy stored;
$\mathcal{W}_{ext}$	External virtual work;
W_f	Work of extenal force;
$\boldsymbol{\alpha}_e$	Jump displacement(global coordinates) ;
$\mathcal{T}_\varepsilon$	Norm of the strain;
$\mathcal{T}_\sigma$	Norm of the stress;
$\delta_\mathcal{S}$	Dirac delta distribution;
$\delta_\mathcal{S}^k$	Regularized Dirac's delta;
$\delta_\mathcal{S}^h$	Regularized Dirac's delta by means of a bandwidth parameter h;
δ_{ij}	Components of the 2nd order identity tensor (Kronecker Delta) ;

$\boldsymbol{\varepsilon}(\mathbf{x},t)$, ε_{ij}	Strain tensor and components, respectively;
$\{\boldsymbol{\varepsilon}\}$	Strain vector (Voigt notation) ;
$\varepsilon_1, \varepsilon_2, \varepsilon_3$	Principal strain;
$\boldsymbol{\varepsilon}^{eff}$	Effective strain;
$\bar{\boldsymbol{\varepsilon}}$	Regular part of the strain tensor;
$\tilde{\boldsymbol{\varepsilon}}$	Enhanced part of the strain tensor;
Φ_{ref}	Reference temperature;
ϕ	Angle of internal friction;
κ	Bulk (compression) modulus;
λ, μ	Lamé's elastic constants ;
$\hat{\lambda}$	Lagrange multipliers;
ν	Poisson's ratio;
θ_{crit}	Critical angle of propagation;
ρ	Material density;
$\boldsymbol{\sigma}(\mathbf{x},t)$, σ_{ij}	Cauchy stress tensor and components, respectively;
$\{\boldsymbol{\sigma}\}$	Stress vector (Voigt notation) ;
$\sigma_1, \sigma_2, \sigma_3$	Principal stress;
$\bar{\sigma}$	Effective stress;
σ_y	Peak stress (or elastic strength) ;
σ_t	Tensile yield stress;
τ_{oct}	Octahedral shear stress;
τ_{max}	Maximum shearing stress;
ψ	Helmholtz free energy;
ψ	Dilatant angle;
Π_{HW}	Hu-Washizu functional;
Π	Potential;
Γ_∞	Infinity boundary;
Ω_∞	Infinity domain;

Abbreviations

SDA	Strong Discontinuity Approach
BVP	Boundary Value Problem
IBVP	Initial Boundary Value Problem
FEM	Finite Element Method
BEM	Boundary Element Method
FDM	Finite Difference Method
CST	Constant Strain Triangle
EAS	Enhanced Assumed Strains
PVW	Principle of Virtual Work
VBM	Variable Bandwidth Model
SOS	Statically Optimal Symmetric
KOS	Kinematically Optimal Symmetric
SKON	Statically and Kinematically Optimal Nonsymmetric
CMSD	Crack Mouth Sliding Displacement

Latin

i.e.	*id est*	that is
et al.	*et alii*	and the others
e.g.	*exempli gratia*	for example
etc.	*et cetera*	and so on
v., vs.	*versus*	versus
viz.	*vidilicet*	namely

Journals

Comput. Mech.	*Computational Mechanics*
Comput. Method Appl. Mech. Eng.	*Computer Methods in Applied Mechanics and Engineering*
Comput. & Struct.	*Computers & Structures*
Eng. Computation	*Engineering Computations*
Eng. Fracture Mech.	*Engineering Fracture Mechanics*
Finite Elem. Anal. Des.	*Finite Elements in Analysis and Design*
Int. J. Fracture	*International Journal of Fracture*
Int. J. Numer. Anal. Meth. Geomech.	*International Journal for Numerical and Analytical Methods in Geomechanics*

Int. J. Numer. Meth. Eng.   *International Journal for Numerical Methods in Engineering*

Int. J. Plasticity   *International Journal of Plasticity*

Int. J. Rock Mech. Min.   *International Journal of Rock Mechanics and Mining Sciences*

Int. J. Solids Struct.   *International Journal of Solids and Structures*

J. Appl. Mech.   *Journal of Applied Mechanical*

J. Eng. Mater. Tech.   *Journal of Engineering Materials and Technology*

J. Eng. Mech.-ASCE   *Journal of Engineering Mechanics*

J. Mech. Phys. Solids   *Journal of the Mechanics and Physics of Solids*

J. Struct. Eng.-ASCE   *Journal of Structural Engineering - ASCE*

Mater. Struct.   *Materials and Structures*

Mech. Cohes.-Frict. Mater.   *Mechanics of Cohesive-Frictional Materials*

Mech. Mater.   *Mechanics of Materials*

Nucl. Eng. Des.   *Nuclear Engineering and Design*

Operators

$$\langle \bullet \rangle = \frac{|\bullet| + \bullet}{2}$$ MacAuley brakets

$\|\bullet\|$ Euclidian norm of $\bullet$

$\text{Tr}(\bullet)$ trace of $(\bullet)$

A   Standard finite-element assembly operator

$(\bullet)^T$ transpose of $(\bullet)$

$(\bullet)^{-1}$ inverse of $(\bullet)$

$(\bullet)^{sym}$ symmetric part of $(\bullet)$

$[\![\bullet]\!]$ jump of $\bullet$

$\det(\bullet) = |\bullet|$ Determinant of $(\bullet)$

$:$ Inner-product – Scalar product of tensors

∇^2 Scalar differential operator

$\otimes$ Open product

$\overset{def}{=}$ by definition is equal to

Abstract

CHAVES, E.W.V. (2003). *A three dimensional setting for strong discontinuities modelling in failure mechanics*. Barcelona. Ph.D. – Technical University of Catalonia (UPC) – Spain.

This work deals with the simulation of strain localization phenomena through the Strong Discontinuity Approach (SDA) for three dimensional (3D) problems. The main assumptions of this work are the isothermal quasi-static regime, small deformations and rotations, and a material described as homogeneous and isotropic.

The theory is developed in the ambit of Continuum Mechanics using an Isotropic Continuum Damage model and its variations, which serves to simulate materials like concrete, ceramics, rocks and ice, for example. The basic ingredients of a 3D finite element formulation with an embedded discontinuity are presented. Also the ingredients for the transition from a weak discontinuity to a strong discontinuity (a bandwidth variable model) are presented.

An extensive analysis of material bifurcation is performed. It gives us the information necessary for the propagation of a discontinuity surface. Two proposals to track this discontinuity surface are presented.

In order to illustrate the effectiveness of the method, several numerical simulations are presented. The agreement with experimental data is also shown. In this work new possibilities are open by giving the necessary tools for the extension of the method to the study of more complex examples which require more complex constitutive models.

Keywords: Strong Discontinuity Approach, localization, bifurcation, finite element.

<div align="right">

1

Introduction

</div>

1.1 Why failure mechanics?

Nowadays modeling fracture and failure processes in structures remains as a challenging problem in Mechanics. It plays an important role in the development of new materials for industry as well as in the understanding of their durability and resistance. Some examples that have stimulated this challenge are presented in the remaining of this section.

Ship failure

In the beginning of the 1900's, interest increased in the behavior of steel (the most used material of that time) after fatigue and fracture mechanisms were detected in various types of structures including in ships; as examples one can mention: the Titanic(1912), the Olympic(1911) and several ships during World War One (1914-1918) and World War II (see Figure 1.1).

Figure 1.1: Ship failure – Callister (1997).

Dam collapse

Most concrete dams develop cracks, giving a heterogeneous character to the material which can affect its integrity. Depending on the stress states, microcracks can develop into a macrocrack formation, which can result in inefficient operation or even in a complete collapse.

In 1928 the St. Francis Dam near Los Angeles, California, collapsed killing hundreds of people. Figure 1.2 shows the dam before and after collapse. In 1959, the Malpasset Dam (France) failed and the resulting flood killed about 450 people. In October 1963 about 2500 people died as a consequence of the Vajont dam collapsing (Longarone - Italy).
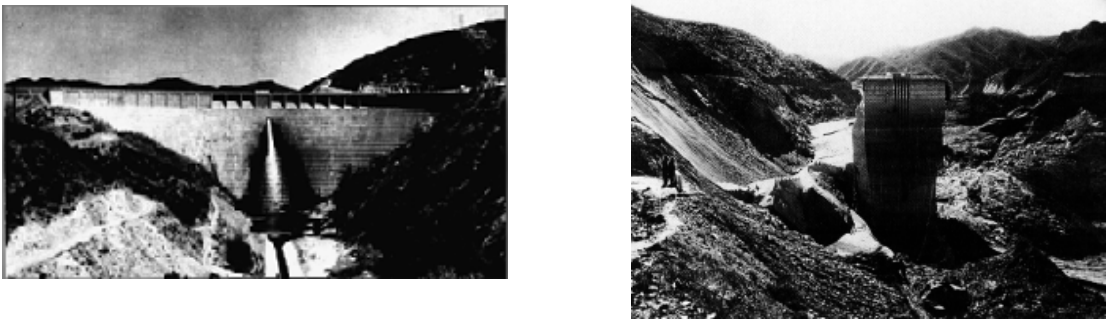
Figure 1.2: The St. Francis Dam, before and after collapse.

While monitoring displacements in the *El Atazar* dam in Spain, (a double curvature concrete arch buttress dam) it was noticed that the left side was moving more than the right side and in 1977 a crack appeared in the left of center part of the dam (see Figure 1.3). Water began to leak out through the crack into drains in the dam at a rate of 1.5 m^3/min. Fortunately, the dam did not collapse.
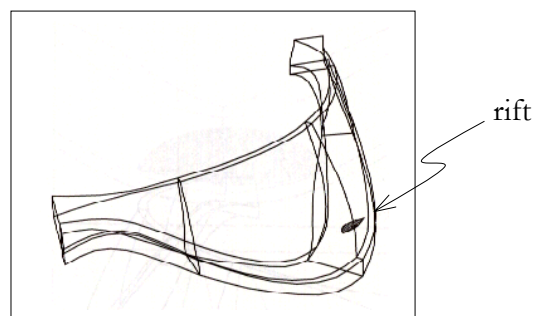
Figure 1.3: Atazar Dam-rift position.

Many other dams not mentioned herein have had some types of problems or collapsed, killing people and devastating large areas.

Oil/gas pipeline rupture

Thousands of kilometers of gas and oil transmission pipelines are currently in operation around the world. A rupture of a pipeline can release diesel fuel, gas, etcetera, which can kill or injure people or, sometimes, lead to an ecological disaster. Since 1986 in the United States alone there have been 3140 incidents, 1407 injuries, and 322 deaths from ruptures of natural gas pipelines.
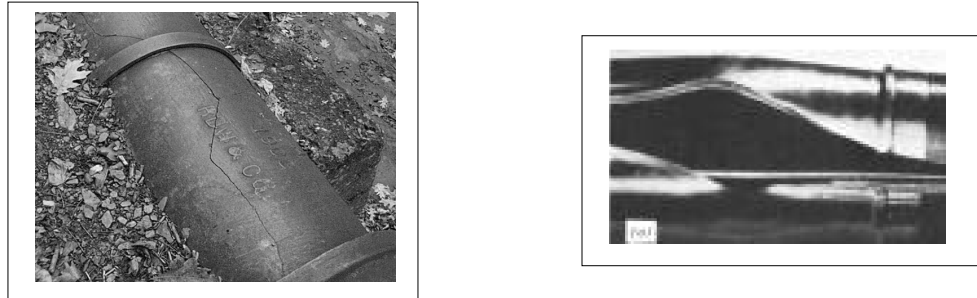
Figure 1.4: Pipeline rupture.

Fracture in the biomedical engineering field

In the field of biomedical engineering we can quote as a typical problem the disease called osteoporosis, a condition involving decreased bone mass which strongly increases the risk of bone fracture (as age progresses). Not only can these fractures strongly influence the quality of everyday live, they may also result in death. To prevent such fractures it is necessary to evaluate with a high degree of accuracy the strength of the bone and the propensity to fracture must be reliably estimated.
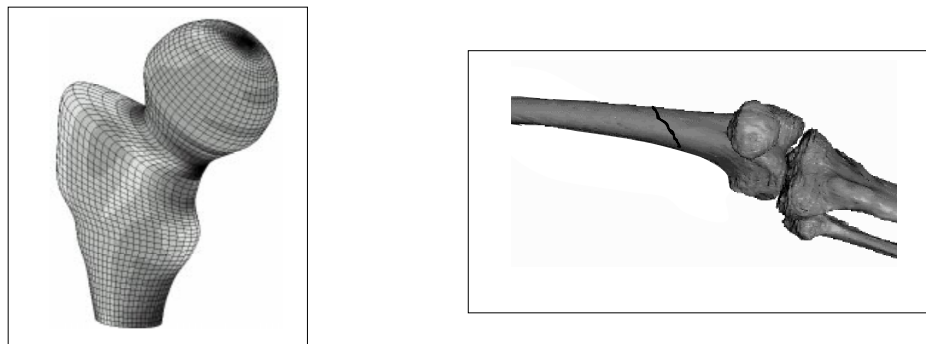
Figure 1.5: Biomedical engineering.

For the above reasons and many others that are not mentioned in this chapter, material behavior, especially material fracture problems have been of great interest to researchers. In the last decades there has been an increasing amount of interest in the study of the experimental and theoretical behavior of the response of materials under extreme load conditions.

1.2 How to face the problem

According to Willam(2000) *Material Science* has been studied on different scales. From the point of view of characterization and design, engineering materials are divided into several sub-ranges (see Figure 1.6) as follows:

- **Meter level**

   The most common problem in civil, mechanical and aerospace engineering structures.

- **Millimeter level**

   The laboratory specimen, which serves to yield material properties.

- **Micrometer level**

   Micro-structural features, such as micro-defects and the hydration products in cement-based materials, are observed in this scale.

- **Nanometer level**

   In this level, molecular and atomic processes take place.

$1 \times 10^{0} \, m$ — Structural Mechanics

$1 \times 10^{-3} \, m$ — Macro Mechanics

$1 \times 10^{-6} \, m$ — Meso Mechanics

— Micro Mechanics

$1 \times 10^{-9} \, m$ — Nano Mechanics
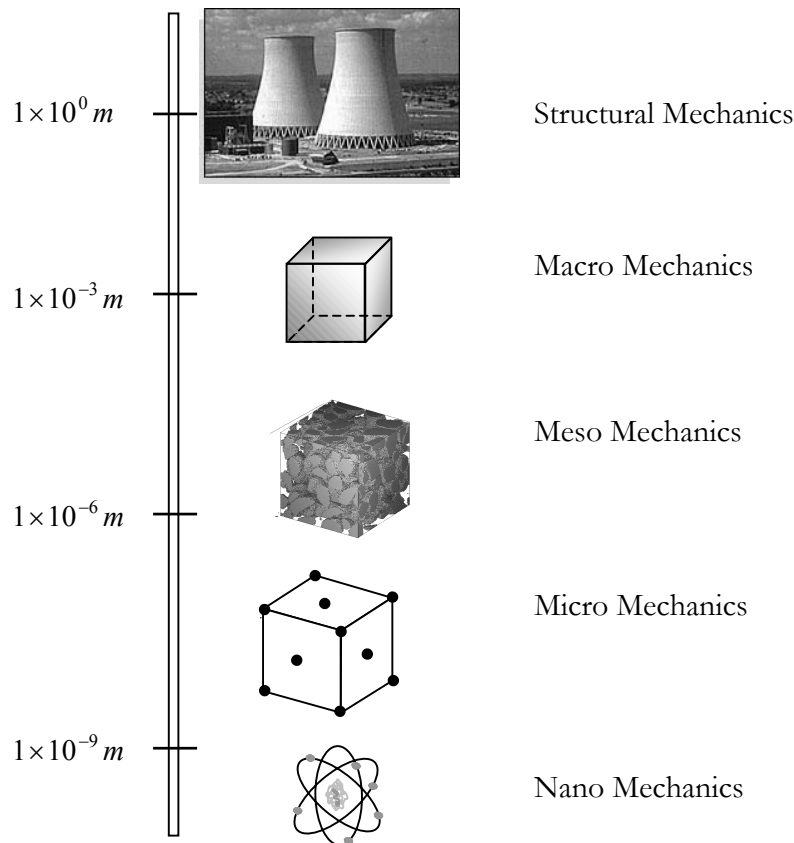
Figure 1.6: Multiscale material mechanics, Willam(2000).

Several theories have been formulated at different levels to simulate the problem of crack initiation/propagation. This work will concentrate on the material behavior at a

macroscopic point of view (material failure mechanics), such macro-mechanical model is well established in simulating the fracture process.

1.3 Material behavior (meter-millimeter level)

In 1911 von Karmán showed that rocks, when compressed under high hydrostatic pressure, undergo a transition of plastic deformation characterized by the appearance of crossed net shear bands at approximately 45°. Later, the same effect was observed in other materials like soil, sand, ceramics, composites, ice, and so on. The morphology of bands in rocks is very similar to the one observed in metals (known as *Lüders bands*) (see Figure 1.7).
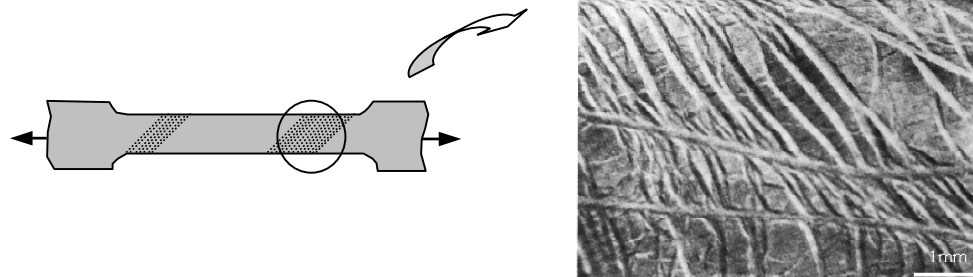
Figure 1.7: Lüders bands.

In soils, when a set of forces provokes instability, a zone with a concentration of deformations is observed. It is called the slip line (see Figure 1.8). The zone where there is a concentration of strain is called the zone of localization.
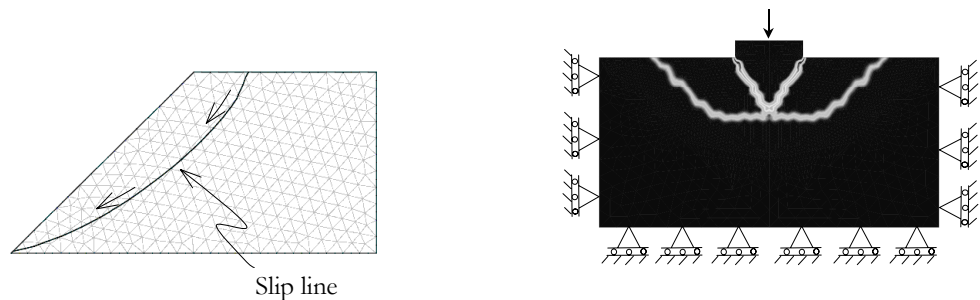
Slip line

Figure 1.8: Soil collapse.

Although localization is a phenomenon that has its origins at a microscopic level, caused by the presence of voids, microcracks, and other phenomena, cracks in concrete or rocks, slip lines in soils and shear bands in metals are observed at the macroscopic level.

The zone of localization is characterized by the concentration of inelastic strains in a narrow band while the surrounding material undergoes unloading. Figure 1.9 shows strain localization as a precursor to faulting and macroscopic fracture of the material.
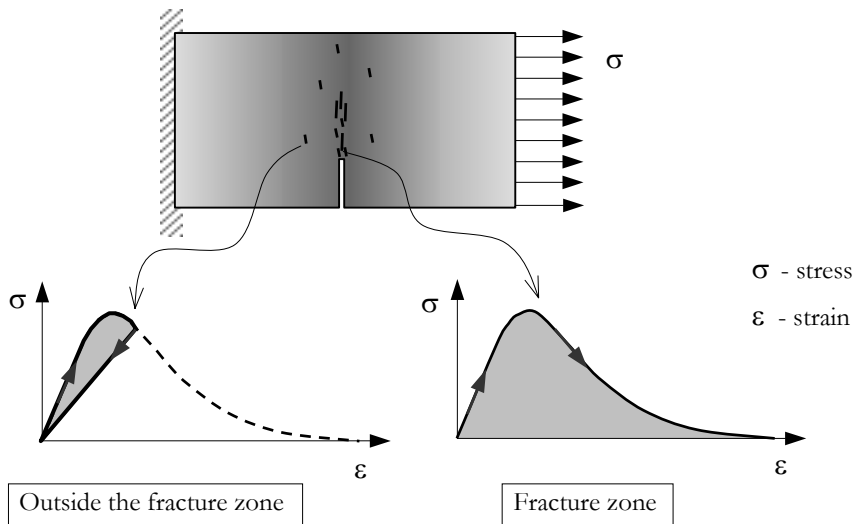
Figure 1.9: Localization behavior.

From the numerical point of view, the initiation of localization (when the material is within the softening regime) produce problems of instability. Rudnicki&Rice(1975) analyzed localization as instability in macroscopic constitutive descriptions of inelastic deformation of the material. These aspects will also be discussed in Chapter 3.

Brittle *vs.* ductile materials

Material classifications traditionally fall into two categories: brittle and ductile. The terms brittle and ductile relate to the relative values of the elastic limit and failure threshold. If the failure threshold nearly coincides with the elastic limit, then the material will experience only negligible plastic deformation before fracture. The term brittle refers to such a material. In contrast, for a ductile material the failure threshold is significantly larger than the elastic limit so that as the material deforms it experiences an elastic regime, followed by a plastic regime, and then finally it fractures. Materials fail in different ways depending on the temperature and pressure (see Figure 1.10). The following are the most relevant features of these two types of materials:

- Brittle Materials: small deformations, no warning before failure (abrupt). Example: concrete, ceramic, glass, ice, rocks, etc.

- Ductile Materials: large deformations, warning before failure (Not abrupt). Example: steel, aluminum, etc.

Remark 1.1: Some kinds of steel have brittle behavior, depending on the process of manufacture – *e.g.:* casting; hot-working; cold-working; heat treatment – and depending on the amount of carbon –more carbon implies more strength and more brittleness– . □
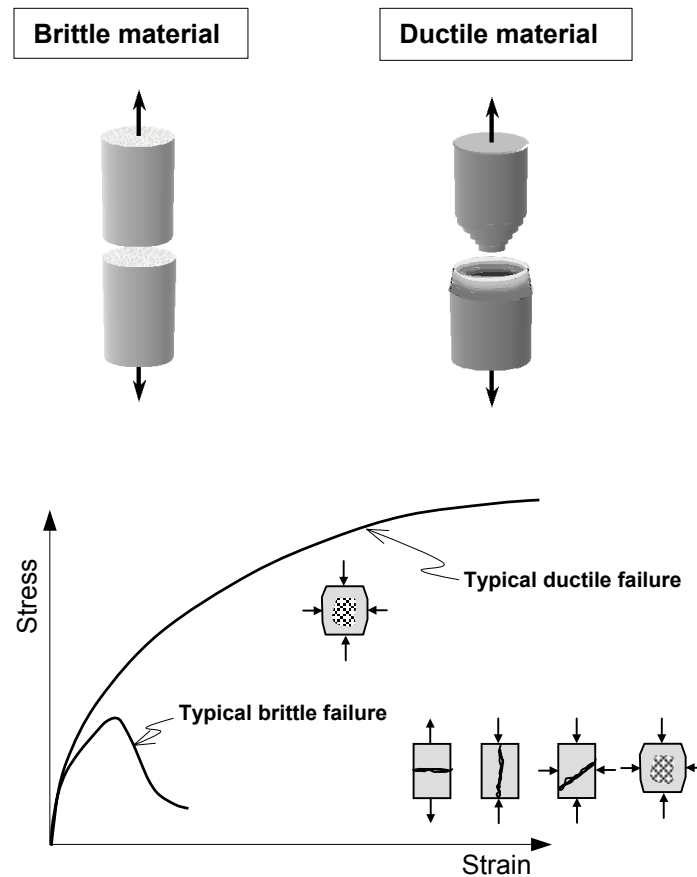
Figure 1.10: Brittle *vs.* Ductile materials.

1.4 Some approaches to the modeling of failure

To simulate the material failure mechanisms at a macroscopic level, the most accepted frameworks are: Fracture Mechanics and Continuum Mechanics. Basically, the main difference between these two general approaches is that in Fracture Mechanics after failure initiation a traction-separation relationship ($\mathbf{t}^{*} - w$) is invoked, whereas continuum mechanics assumes a stress-strain relationship ($\sigma - \varepsilon$) after strain localization, which is a precursor to failure and macroscopic fracture of the material (as the stress vanishes) based on this very general classification, here we present a more specific account of the most important to failure modeling.

1.4.1 Linear Elastic Fracture Mechanics – LEFM

Fracture mechanics was stimulated by Inglis (1913). Using elasticity fundamentals he studied the stress concentration in a large plate of elastic material with an elliptical hole. Later, Griffith (1921) used Inglis' stress analysis of an elliptical flaw in a linear elastic material to predict the critical stress under which a crack irreversibly grows, causing the material to fracture. He proposed an energy criterion of failure after considering that the stress value cannot be used as a failure criterion since the stress at the tip of a sharp crack

in an elastic continuum is infinite. These concepts served as the basis of classical linear elastic fracture mechanics (LEFM).

To study the propagation of fissures Irwin (1957), introduced the so-called Fracture Modes (see Figure 1.11) whose combinations give rise to the mixed-mode cracks.

Another very important concept in Fracture Mechanics is the strain energy release rate (G), which is defined as the amount of energy required to open a unit of crack area. Irwin expressed this energy in terms of the *stress intensity factor*. Other possible modes of deformation at a crack tip are sliding mode II and tearing mode III (see Figure 1.11).

Mode I Pure opening mode	Mode II In-plane shear mode	Mode III Antiplane shear mode
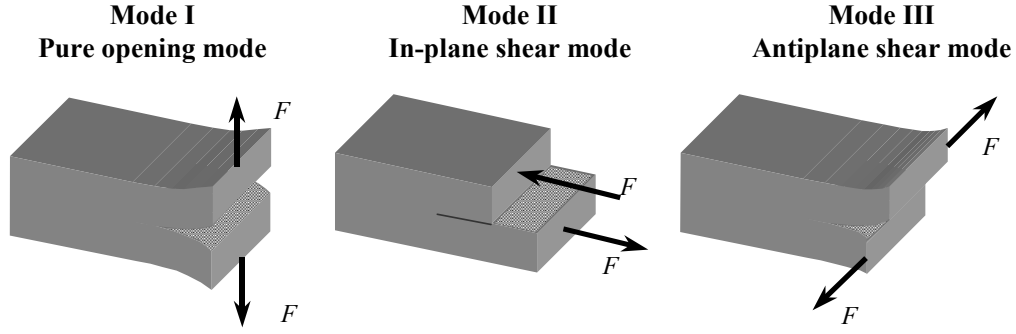
Figure 1.11: Fracture Modes.

The concept of specific fracture energy, $\mathcal{G}_f = G_I$ or simply *fracture energy* (correspondent to the case of Mode-I crack opening) was formulated having as point of departure the inter atomic energy. Nowadays, this concept is very widespread in the field of continuum mechanics and is used to simulate the process of failure. When the work, W_f, necessary to develop a fracture surface, A_f, is known in a cylindrical piece, the fracture energy is obtained as
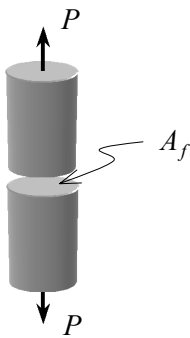
$$W_f = \mathcal{G}_f A_f \qquad (1.1)$$

Figure 1.12: Fracture area normal to load P.

With respect to the Fracture Energy correspondent to Mode II, is G_{II} a representative fracture energy? Nowadays this discussion is still open in the ambit of Continuum Media.

In 1993, Carpinteri and co authors, in a paper entitled: *"Is mode II fracture energy a real material property?"* concluded that Mode II fracture energy does not seem to be a material property.

In fracture mechanics the procedure used to determine the crack propagation is indicated as follows:

- Step 1: Determine the stress intensity factor;

- Step 2: Verify the crack stability based on a criterion which is a function of the stress intensity factor, and determine the crack increase and its orientation;

- Step 3: The crack tip is established in a new point. The whole process is repeated until the crack stability is ensured.

1.4.2 Discrete crack approach

Hillerborg *et al.* (1976) introduced the *fictitious crack model*, based in a Cohesive Crack Model where the fictitious crack can transfer stress from one side to another (Figure 1.13). This material can be characterized by two couples of constitutive laws: a stress-strain relationship ($\sigma - \varepsilon$) in a non damaged zone and a stress-crack opening displacement relationship ($\sigma - w$). In the latter, it is possible to distinguish another two zones: a real crack where there is no more stress transfer and a damaged zone, extended in the fracture process zone, in which stresses are still transferred. The $\mathcal{G}_f$ coefficient is also equal to the area defined by the softening law (descending branch of the ($\sigma - w$)).
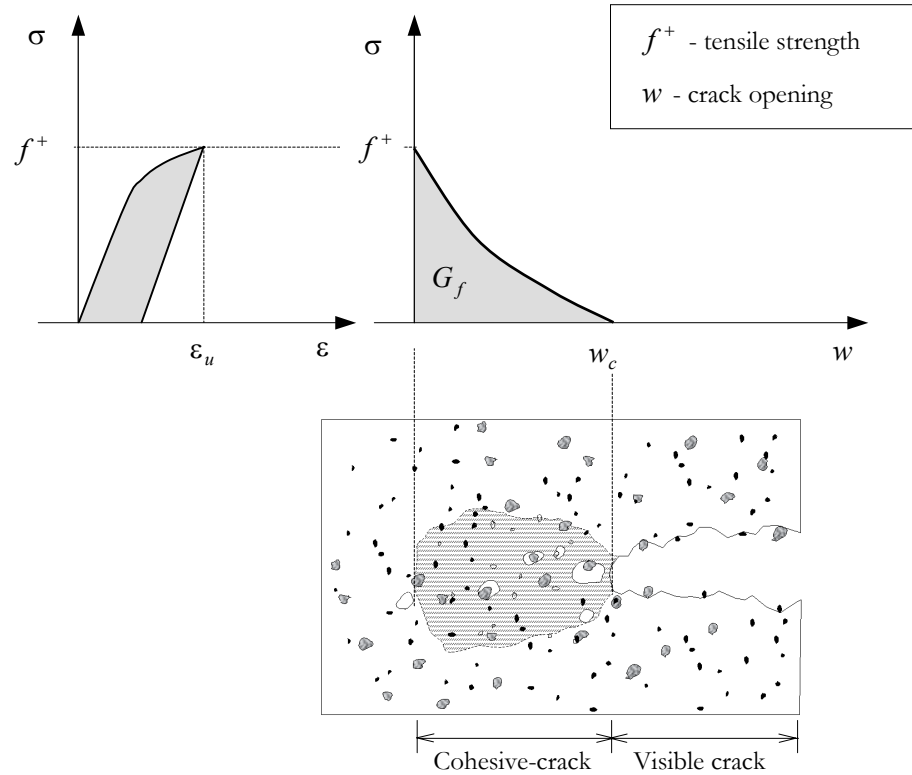
Figure 1.13: Hillerborg's cohesive crack model; the Fictitious Crack Model.

At the first glance, the discrete crack approach –introduced by Ngo & Scordelis(1967)– is well matched with the nature of the physical crack (Ingraffea(1977), Blaauwendraad & Grootenboer(1981), Hillerborg(1985), Ingraffea & Saouma(1985)). However, in these methods there is an *interelement* discontinuity, for this reason an interface element or special boundary conditions between adjacent solid elements are required to simulate the crack propagation. This avoids the spurious stress across the discontinuities. The crack region must be pre-defined or remeshed, Ingrafea&Saouma(1985). Accurate results for a fixed mesh can only be obtained if the crack pattern is known in advance and if elements have been oriented in the crack direction.
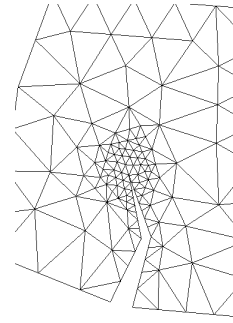
Figure 1.14: Discrete crack model.

1.4.3   Smeared crack model

In 1958, Kachanov introduced the concept of "effective stress" to describe the behavior of a degraded material (isotropic damage) in the context of a continuum medium. This paper, Kachanov(1958), starts a new tendency to face up to the problem of fracture in materials, following this idea and concepts several researches began to conceive several approaches to attack the localization problem.

In the approach (*Smeared crack approach*) proposed by Rashid (1968), infinitely many parallel cracks of infinitely small opening are imagined to be continuously distributed (smeared) over the finite element (see Figure 1.15). This finite element exhibits a complete loss of stiffness at the onset of failure. This methodology was very well welcomed because the Finite Element Method was getting powerful with the advance of computer development, and principally because this new approach treated the two behaviors, continuum and fracture, in the same framework of the continuum. This new methodology had been followed by several researchers like: Červenka(1970), Bažant&Cedolin(1979), Rots *et al.* (1985).
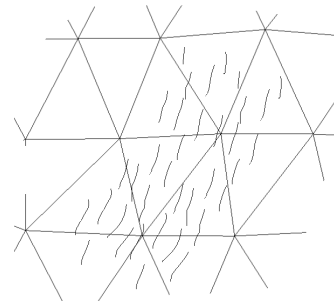
Figure 1.15: Smeared crack model.

To simulate material behavior up to full fracture implies strain-softening (after the load reaches the peak, the postpeak is characterized by stress declining with an increasing of strain). With this, some problems appear like mesh dependency and localization instability. Such problems were unknown by the researchers, causing certain theoretical difficulties. This instability will be tackled in more details in Chapter 3 – Material Bifurcation.

Currently there are two types of models for the post-cracking of concrete that are based on the smeared crack model: the **fixed-crack model** and the **rotating-crack model**. In the fixed crack model a crack forms perpendicular to the principal tensile stress direction when the principal stress exceeds the concrete tensile strength and the crack orientation does not change anymore. The rotating-crack model –proposed by Cope *et al.* (1980)– allows the crack to rotate with the principal strain directions during loading, unlike the fixed crack model.

At later stages, the standard rotating crack model leads to stress locking. Some researchers have used the combination of the rotating crack model with a scalar damage model to reduce spurious stress transfer, Jirásek&Zimmermann(1998).

The smeared crack shows the presence of the so-called localization instability when the material is in *softening*, and is non-objective. In order to overcome such difficulties the Band Smeared Crack Model was developed by Bažant&Oh(1983), Rots *et al.*(1985). Such ideas appeared according to experiments, since the dimensions of the failure regions are independent of the structural size and they are assumed as fictitious planes. In the case of tensile cracks, this approach is known as "Crack Band Model" Bažant & Oh(1983), which they adapted from concept of the Fictitious Crack Model (Discrete Model). In this model the fracture energy was smeared out over the width of the area of the crack domain .
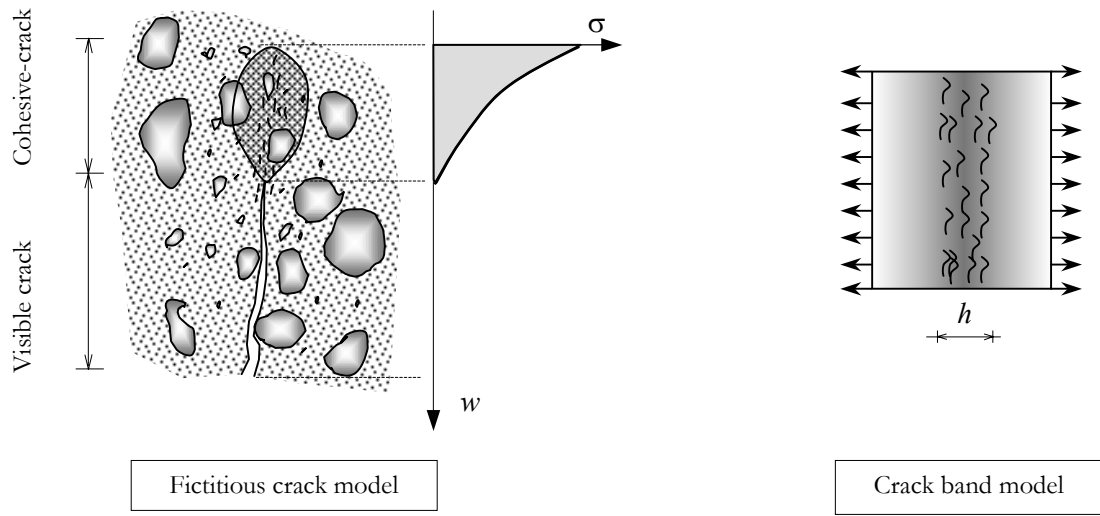
Figure 1.16: Fictitious *vs.* crack band model

The concept of constant fracture energy in tension is widely used to regularize mesh-sensitive smeared cracks, Bažant&Oh(1983). The fracture energy $\mathcal{G}_f$ is defined as the amount of energy required to produce one unit of area of a continuous crack and is considered a material property. This definition results in the following expression for the fracture energy $\mathcal{G}_f$

$$\mathcal{G}_f = \int \sigma_{nn} \, \mathrm{d}w \qquad (1.2)$$

where w is the sum of the opening displacements of all microcracks within the fracture zone.

In the Band Smeared Crack Model w is represented by a crack opening strain ε_{nn}^{cr}, which is equal to the strain normal to the crack direction in the cracked state and which acts over a certain width within the finite element, h^*. Thus:

$$w = \int \varepsilon_{nn}^{cr} \, d\ell \tag{1.3}$$

Assuming that the microcracks are uniformly distributed across the crack bandwidth h^*, equation (1.3) reduces to:

$$w = h^* \varepsilon_{nn}^{cr} \Rightarrow \mathcal{G}_f = h^* \int \sigma_{nn} \, d\varepsilon_{nn}^{cr} \tag{1.4}$$

the area g_f, energy per unit volume, under the curve in Figure 1.17 can be expressed as:

$$g_f = \int \sigma_{nn} \, d\varepsilon_{nn}^{cr} \quad \Rightarrow \quad g_f = \frac{\mathcal{G}_f}{h^*} \tag{1.5}$$

Bažant & Oh (1983) introduced the crack band theory for the analysis of plain concrete panels.

$$\varepsilon_o = \frac{2\mathcal{G}_f}{f_t \, h^*} \tag{1.6}$$
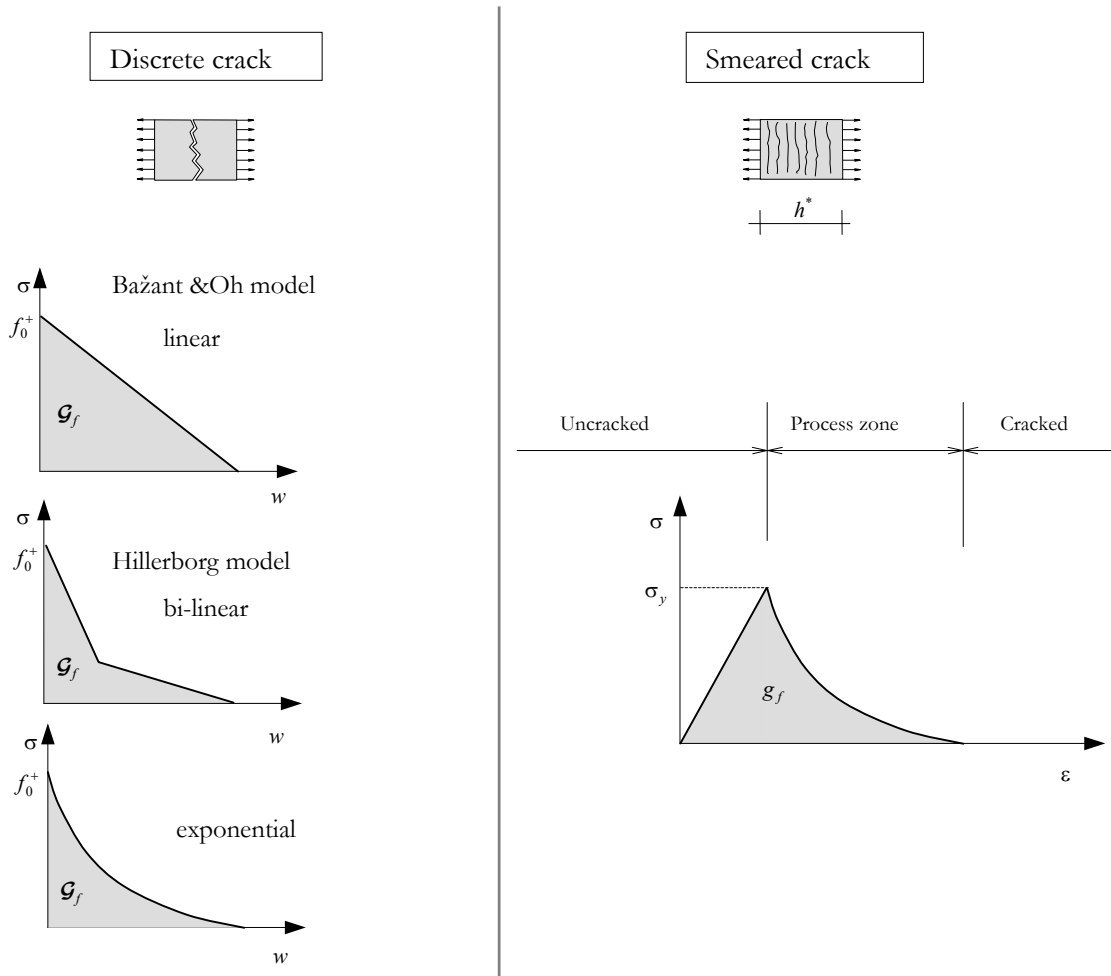
Figure 1.17: Discrete crack *vs.* Smeared model.

The smeared crack approach can however overestimate the shear stiffness of the structure, known as stress locking. This method cannot capture the displacement jump. The lack of displacement jump in the kinematics can lead to a spurious stress transfer across a wide open crack. As a consequence the structure will support more in reality than it can, and the force displacement curve has an appearance as shown in Figure 1.18.
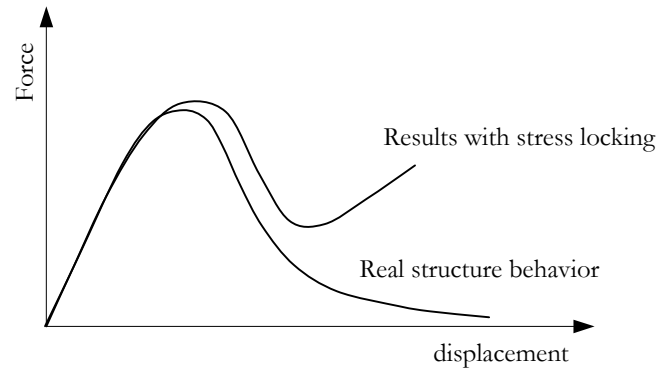
Figure 1.18: Locking consequence.

Usually when the smeared crack model is applied, very fine meshes are needed to capture the zones of high displacement gradient. When a code includes some automatic mechanism for altering the element size (h) in response to the characteristics of a specific problem, it is said to be h-adaptive. The act of increasing the number of elements (reducing the characteristic size) is called refinement (see Figure 1.19). This technique can be computationally expensive and difficult to implement.
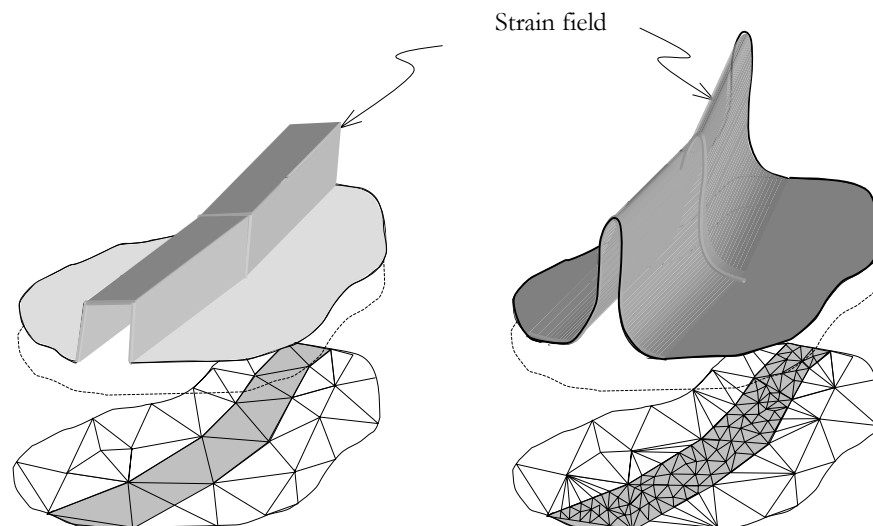
Figure 1.19: Mesh adaptivity techniques.

1.4.4   Intraelement crack

In this approach, the crack propagates throughout the element (see Figure 1.20). It is like the Band Crack Model, which is concentrated in a band within the finite element. In this case a lot of hypothesis have been adopted and among them one can quote: Enhanced Strain (*e.g.* Weak discontinuity approach) and Enhanced Displacement (*e.g.* the *Strong Discontinuity Approach* – Simo *et al.*(1993)). All these ramifications have one thing in common, which is that after localization a softening relation between traction and relative displacement can be reproduced by the stress-strain constitutive relation. Belytschko *et al.* (1988) have developed a method by which the localized zone can be embedded using a four-node quadrilateral element. The jumps in strain in localized zone are obtained by imposing traction continuity.
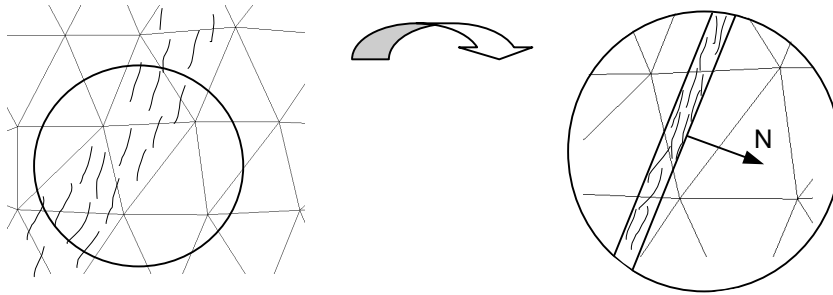
Figure 1.20: Intraelement crack model.

1.4.5 Enhanced continuum approaches

As it is mentioned above, when models equipped with strain softening are used in a framework of classical continuum, the corresponding Boundary Value Problem (BVP) becomes ill-posed. The governing equations can be regularized to remain elliptic by resorting to higher order continuum theories. To make this possible some enhanced continua have been proposed.

This kind of enrichment imposes a minimal width of the zone of localized strain, and hence they are called *localization limiters.*

Cosserat continua

The Cosserat continuum was originally developed by the Cosserat brothers in 1909. The Cosserat theory of elasticity incorporates a local rotation of material points as an independent parameter in addition to the translation assumed in the classical continuum. As consequence a nonsymmetrical stress tensor is derived. The elastic Cosserat continuum theory has been extended to elastic-plasticity and applied in the analysis of strain localization describing the microstructure of the material (micropolar method) with a parameter (internal length), Mühlhaus & Vadoulakis(1987); de Borst (1991); Steinmann & Willam(1991), Iordache(1996).

Non-local models

In non-local models, the stress at a point depends on the state at this point and on the deformation in its neighborhood. The model has become non-local once the constitutive model no longer satisfies the principle of local action. This method is proposed to achieve a shear band independent of the computational grid size, Bažant *et al.* (1984), Pijaudier-Cabot&Bažant(1987), Tvergaard&Needleman(1995).

Gradient-enhanced models

This model may be derived as an approximation of the nonlocal damage models. A characteristic of one class of gradient-enhanced model is the explicit dependence of the yield function on the Laplacian of the effective plastic strain where a material parameter (material length) is introduced, Aifantis(1984), Pamin(1994), Peerling (1999). de Borst & Mühlhaus(1992).

In gradient elastoplasticity models the displacement field and effective plastic strains are discretized using C^1 –continuous shape functions.

1.5 Weak/strong discontinuity approach

Strain localization can also be treated as a discontinuity in the strain field by maintaining continuity in the displacement field (weak discontinuity) or as a discontinuity in the displacements field (strong discontinuity). This is the essential difference between the two approaches.

Ortiz *et al.* (1987) considered a continuous displacement field (weak discontinuity), where the strain localization in narrow bands appears as a possible tool to model the discontinuities in the displacement field [Belytschko *et al.*, (1988)].

According to Simo&Rifai(1990), the classical method of incompatible modes –originally introduced by Bazely *et al.* (1965) in the context of a plate bending problem and Wilson *et al.*(1973) in the context of plate elasticity–, consists of low order elements with enhanced performance in a coarse mesh. Simo&Rifai(1990), using the three-field variational formulation of elasticity, proposed a class of mixed assumed strain method whose central idea was that the strain field is compounded of two parts:

$$\boldsymbol{\varepsilon} = \nabla^{sym}\mathbf{u} + \widetilde{\boldsymbol{\varepsilon}} \tag{1.7}$$

where $\nabla^{sym}\mathbf{u}$ is the symmetric gradient of the displacement field and $\widetilde{\boldsymbol{\varepsilon}}$ is the enhanced part of the strain field. They showed that $\widetilde{\boldsymbol{\varepsilon}}$ is not subjected to any interelement continuity requirement.

From the class of *assumed enhanced strain* methods (AES), mentioned before, emerges the *strong discontinuity approach* (SDA) in Simo *et al.* (1993), Simo&Oliver(1994). The SDA refers to the capture of jumps in the displacement field across a surface with zero bandwidth measure by using standard solid mechanics models with continuum constitutive equations. It has been shown that the discrete theoretical model can be interpreted as the limit case of the continuum when the localization band goes to zero (discontinuity surface). In this case the strain has the sense of a Dirac delta distributions. The interesting point is that the whole analysis is done in the Continuum Mechanics framework. The SDA leads to mesh-

independent finite element discretization without introducing a material length scale (non-physical property).

This new proposal has lately been followed by several researchers because it presents certain attractive characteristics like:

- The implementation in a finite element code is very easy;

- It is mesh-independent with respect to size and orientation; and, as consequence, no remeshing is needed to capture the high strain gradients;

- There is no need to introduce any material length scale.

In Oliver(1995a,b) a discontinuous shape function (to capture the displacement field) into a triangular element has been used allowing a precise representation of the crack opening (see Figure 1.21).
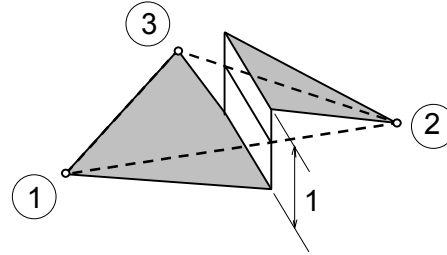
Figure 1.21: Discontinuous shape function.

A transition between Weak Discontinuity and Strong discontinuity –a **variable bandwidth model**– was introduced in Oliver *et al.*(1997) and Manzoli (1998). The material behavior will be in a strong discontinuity regime when the so called *strong discontinuity conditions*, Oliver (2000), are fulfilled. In the next Chapter we will tackle this transition in more detail.

This methodology has been used with many constitutive models (damage, Drucker-Prager, Rankine), Oliver (1995b), (1996a),(1996b), (1998); Armero&Garikipati(1996); Larsson *et al.* (1996); Oliver *et al.* (1997-1999); Armero(1997). Garikipati(1996) has extended the problem to finite deformations in the framework of the Assumed Enhanced Strain Finite Element Method. Steinmann (1998), has used SDA, by using a finite element discretization where interface element is endowed with these kinematics and, based on these developments, a model adaptive strategy was proposed. Extensions to localization analyses of saturated soils has been addressed by Armero&Callari(1999) and Steinmann(1999). Oliver *et al.* (2000) using strong discontinuity approach showed the links with cohesive models.

1.6 Failure simulation in three dimensions

In some cases, only a three-dimensional analysis can provide certain information of interest to the designer that 2D analysis cannot provide, thus three-dimensional models become necessary to obtain quantitative insight of these mechanical behaviors. In a 3D framework, however, the complexity increases significantly even for growth limited to Mode I conditions.

With the increasing progress of computing process velocity and with a good pre processor mesh generator it has provided an important tool in the extrapolating to three dimensions for all the methods described above.

1.7 Adopted approach and aim of this work

This work deals with the extension of the two-dimensional Strong Discontinuity Approach to the general 3D non-linear problem that presents crack formation in a macro level, mainly in Brittle Materials (like concrete, rocks, ice, glass, etc.).

Numerically these problems will be modeled using the Finite Element method. We will extend into 3D the special finite element developed by Oliver (1995a,b), which considers that the jump in displacement which is the base of the *Strong Discontinuity Approach* concepts. The type of finite elements used will be the tetrahedral and hexahedral finite elements to simulate numerical examples.

The main assumptions made in this work are the *isothermal quasi-static regime* and *small deformation and rotations*, assuming a material described as homogeneous and isotropic.

In this work the material's behavior associated to the development of a crack in a loading process is described as (see Figure 1.22):

- **Diffuse failure zone:** The strain and displacement fields are continuous, but there is a concentration of the strains in the zone where material begins to soften.

- **Weak discontinuity zone:** The strain field becomes discontinuous, but the displacement field remains continuous, across the limits of a narrow band (strain localization band).

- **Strong discontinuity zone:** The strain localization band collapses into a surface (the discontinuity interface). The displacement field becomes discontinuous across that surface and the strain field becomes unbounded.
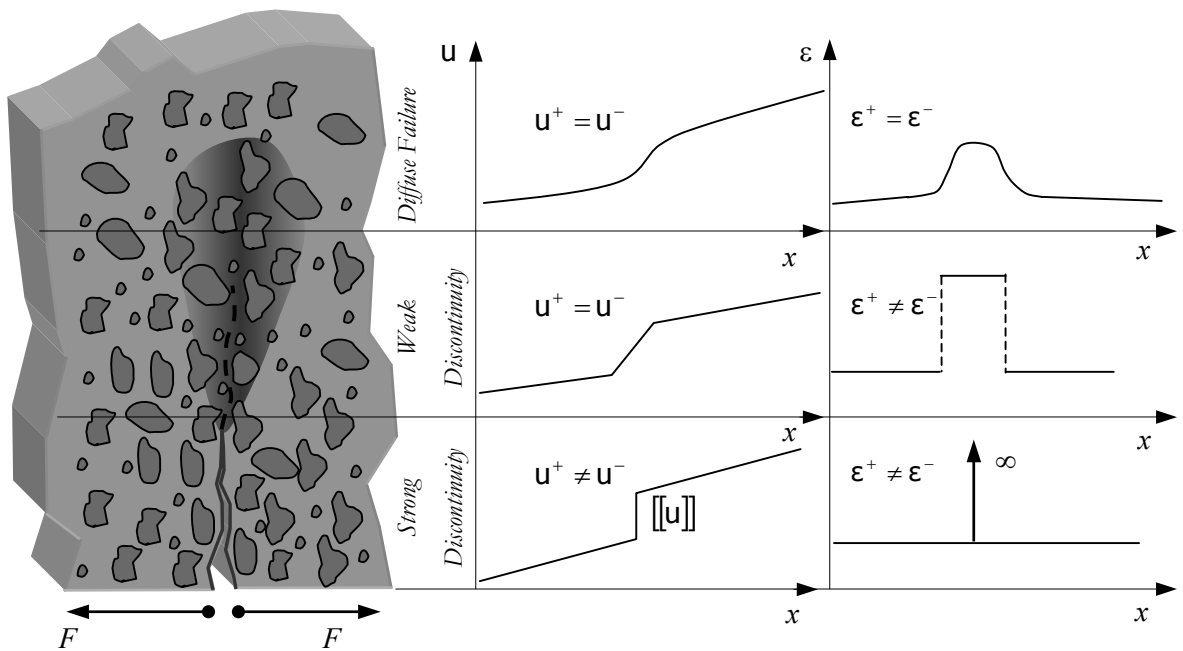
Figure 1.22: Fracture evolution.

1.7.1   Contents of this work

The remaining of this work consists of the following chapters:

- Chapter 2: The Boundary Value Problem of quasi-static equilibrium for an isothermal solid with a discontinuity is presented. Isotropic damage is presented as well as the regularization of the model and the strong discontinuity conditions.

- Chapter 3: Once the Elliptic Boundary Value Problem has been posed, in this chapter we will tackle the loss of ellipticity, that is, material instability.

- Chapter 4: After all variables are presented, we will describe the numerical approach used to solve the BVP laid out in chapter 3.

- Chapter 5: This chapter is devoted to presenting the results of classic examples and the discussion of them.

- Chapter 6: The summary, future lines of research and conclusions will be presented.

2

Strong Discontinuities in Solid Mechanics

"Philosophy is written in this grand book - the universe - which stands continuously open to our gaze. But the book cannot be understood unless one first learns to comprehend the language and interpret the characters in which it is written. It is written in the language of mathematics, and its characters are triangles, circles, and other geometrical figures, without which it is humanly impossible to understand a single word of it; without these one is wandering about in a dark labyrinth."

Galileo Galilei (1623)
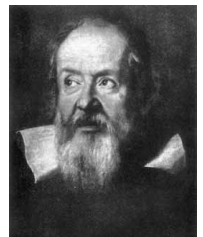
2.1 Introduction

This chapter is devoted to studying the theoretical concepts related with the presence of discontinuities in a continuum, more specifically, the appearance of discontinuities in the displacement field. As a point of departure, we state the Boundary Value Problem (BVP) for a continuous medium. Then a representative continuum damage model is described in detail. Next, we present the two basic types of discontinuity kinematics: weak and strong discontinuity kinematics. The so-called Strong Discontinuity Approach (SDA) already used by several researchers (*e.g.*, Simo *et al.* (1993), Oliver&Simo(1994), Simo&Oliver(1994), Oliver(1995), Manzoli(1998), Regueiro&Borja(1999), Armero&Garikipati(1996), Larsson *et al.* (1995)) is adopted as the theoretical framework for this work.

Basically, this chapter lays out all the ingredients that constitute the theoretical basis of the numerical analysis of strain localization in structures composed by materials that can be described by continuum damage models (*e.g.*, quasi-brittle materials like concrete, ceramics, ice, rocks).

2.2 Governing equations

We start by stating the standard Boundary Value Problem (BVP) of solid mechanics. Let us consider a three dimensional body, that takes up an open bounded domain $\mathcal{B} \in \mathbb{R}^3$ with density ρ (see Figure 2.1). Let $\partial\mathcal{B}$ be the boundary of $\mathcal{B}$ and υ the unit outward normal to $\partial\mathcal{B}$. The body is assumed to be in static equilibrium under the action of body forces density, $\mathbf{b}(\mathbf{x})$, and surface tractions, $\mathbf{t}^*(\mathbf{x})$. The boundary $\partial\mathcal{B}$ consists of a portion $\partial_{\mathbf{u}}\mathcal{B}$ with prescribed displacements, $\mathbf{u}^*(\mathbf{x})$, and a part $\partial_{\boldsymbol{\sigma}}\mathcal{B}$, with prescribed traction, $\mathbf{t}^*(\mathbf{x})$, such that $\partial_{\mathbf{u}}\mathcal{B} \cap \partial_{\boldsymbol{\sigma}}\mathcal{B} = \varnothing$ and $\overline{\partial_{\mathbf{u}}\mathcal{B} \cup \partial_{\boldsymbol{\sigma}}\mathcal{B}} = \partial\mathcal{B}$. In addition let $\boldsymbol{\sigma}(\mathbf{x})$ denote the *Cauchy stress* tensor and $\boldsymbol{\varepsilon}(\mathbf{x})$ the infinitesimal strain tensor. The governing equations of the Boundary Value Problem (BVP) for this quasi-static problem are summarized in (2.1) - (2.3):

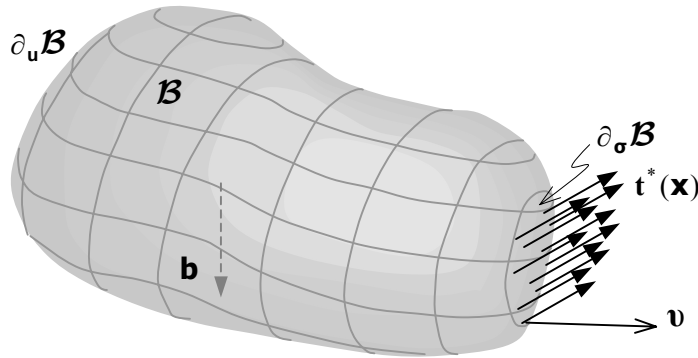| BOUNDARY VALUE PROBLEM - BVP			
Partial differential equations *(equilibrium equation)*	$\nabla \cdot \boldsymbol{\sigma}(\mathbf{x}) + \mathbf{b}(\mathbf{x}) = \mathbf{0}$	$\forall\, \mathbf{x} \in \mathcal{B}$	(2.1)
Essential boundary conditions *(Dirichlet's boundary conditions)*	$\mathbf{u} = \mathbf{u}^*(\mathbf{x})$	$\forall\, \mathbf{x} \in \partial_{\mathbf{u}}\mathcal{B}$	(2.2)
Natural boundary conditions *(Neumann's boundary conditions)*	$\mathbf{t} = \mathbf{t}^*(\mathbf{x}) = \upsilon \cdot \boldsymbol{\sigma}$	$\forall\, \mathbf{x} \in \partial_{\boldsymbol{\sigma}}\mathcal{B}$	(2.3)

Figure 2.1: Three dimensional body.

Now consider the body $\mathcal{B} \in \mathbb{R}^3$ experiencing a displacement discontinuity across a discontinuity surface $\mathcal{S}$ with normal $\mathbf{N}$ (see Figure 2.2).

Let us consider the virtual work principle which states:

$$\underbrace{\int_{\mathcal{B}} \boldsymbol{\sigma} : \nabla^{sym} \boldsymbol{\eta} \mathrm{d}V}_{\mathcal{W}_{int}} = \underbrace{\int_{\mathcal{B}} \mathbf{b} \cdot \boldsymbol{\eta} \mathrm{d}V + \int_{\partial_\sigma \mathcal{B}} \mathbf{t}^* \cdot \boldsymbol{\eta} \mathrm{d}A}_{\mathcal{W}_{ext}} \tag{2.4}$$

under the assumption of infinitesimal deformation $\boldsymbol{\gamma} = \nabla^{sym} \boldsymbol{\eta}$, for all admissible virtual displacement $\boldsymbol{\eta} \in \hat{\mathcal{V}}$, where $\hat{\mathcal{V}}$ is the space of the kinematically admissible variations defined by:

$$\hat{\mathcal{V}} := \left\{ \boldsymbol{\eta} \in \mathcal{C}^0 \qquad \boldsymbol{\eta}|_{\partial_u \mathcal{B}} = \mathbf{0} \right\} \tag{2.5}$$

$\mathcal{W}_{int}$ and $\mathcal{W}_{ext}$ represent the internal and the external virtual work, respectively. After integrating by parts the first integral of equation (2.4), we obtain:

$$\int_{\mathcal{B}} \boldsymbol{\sigma} : \boldsymbol{\gamma} \mathrm{d}V = - \int_{\mathcal{B} \backslash \mathcal{S}} \nabla \cdot \boldsymbol{\sigma} \cdot \boldsymbol{\eta} \mathrm{d}V + \int_{\partial_\sigma \mathcal{B}} \mathbf{U} \cdot \boldsymbol{\sigma} \cdot \boldsymbol{\eta} \mathrm{d}A - \int_{\mathcal{S}} \mathbf{N} \cdot \left(\boldsymbol{\sigma}^+ - \boldsymbol{\sigma}^- \right) \cdot \boldsymbol{\eta} \mathrm{d}A \tag{2.6}$$

where $\boldsymbol{\sigma}^+$ and $\boldsymbol{\sigma}^-$ stand for the stress fields in $\mathcal{B}^+$ and $\mathcal{B}^-$, respectively. Substituting the above equation into equation (2.4) we finally obtain:

$$- \int_{\mathcal{B} \backslash \mathcal{S}} \left(\nabla \cdot \boldsymbol{\sigma} + \mathbf{b} \right) \cdot \boldsymbol{\eta} \mathrm{d}V + \int_{\partial_\sigma \mathcal{B}} \left(\mathbf{U} \cdot \boldsymbol{\sigma} - \mathbf{t}^* \right) \cdot \boldsymbol{\eta} \mathrm{d}A - \int_{\mathcal{S}} \mathbf{N} \cdot \left(\boldsymbol{\sigma}^+ - \boldsymbol{\sigma}^- \right) \cdot \boldsymbol{\eta} \mathrm{d}A = 0 \tag{2.7}$$

so the strong form of equation (2.7) is schematically shown below:

BOUNDARY VALUE PROBLEM – BVP – With discontinuity			
Equilibrium equation	$\nabla \cdot \boldsymbol{\sigma}(\mathbf{x}) + \mathbf{b}(\mathbf{x}) = \mathbf{0}$	$\forall \, \mathbf{x} \in \mathcal{B} \backslash \mathcal{S}$	(2.8)
Constitutive equation	$\boldsymbol{\sigma} = \Sigma(\boldsymbol{\varepsilon}(\mathbf{x}))$	$\forall \, \mathbf{x} \in \mathcal{B}$	(2.9)
Kinematics equation	$\boldsymbol{\varepsilon} = \nabla^{sym} \mathbf{u} = \dfrac{1}{2} \left(\nabla \otimes \mathbf{u} + \mathbf{u} \otimes \nabla \right)$	$\forall \, \mathbf{x} \in \mathcal{B}$	(2.10)
Outer traction continuity	$\mathcal{T}^- = \mathcal{T}^+ \Leftrightarrow \mathbf{N} \cdot \boldsymbol{\sigma}^- = \mathbf{N} \cdot \boldsymbol{\sigma}^+$	$\forall \, \mathbf{x} \in \mathcal{S}$	(2.11)
Essential boundary conditions	$\mathbf{u} = \mathbf{u}^*(\mathbf{x})$	$\forall \, \mathbf{x} \in \partial_u \mathcal{B}$	(2.12)
Natural boundary conditions	$\mathbf{t} = \mathbf{t}^*(\mathbf{x}) = \boldsymbol{\upsilon} \cdot \boldsymbol{\sigma}$	$\forall \, \mathbf{x} \in \partial_\sigma \mathcal{B}$	(2.13)

Additionally, we postulate the so-called inner traction continuity condition, characteristic of problems involving strong discontinuities[1]:

Inner traction continuity	$\mathcal{T}^{+} = \mathcal{T}_{\mathcal{S}} \Leftrightarrow \mathbf{N} \cdot \boldsymbol{\sigma}^{+} = \mathbf{N} \cdot \boldsymbol{\sigma}_{\mathcal{S}}$	$\forall \, \mathbf{x} \in \mathcal{S}$	(2.14)

In equation (2.9), $\boldsymbol{\Sigma}(\boldsymbol{\varepsilon})$ stands for the nonlinear constitutive equation returning the stresses in terms of the strains.
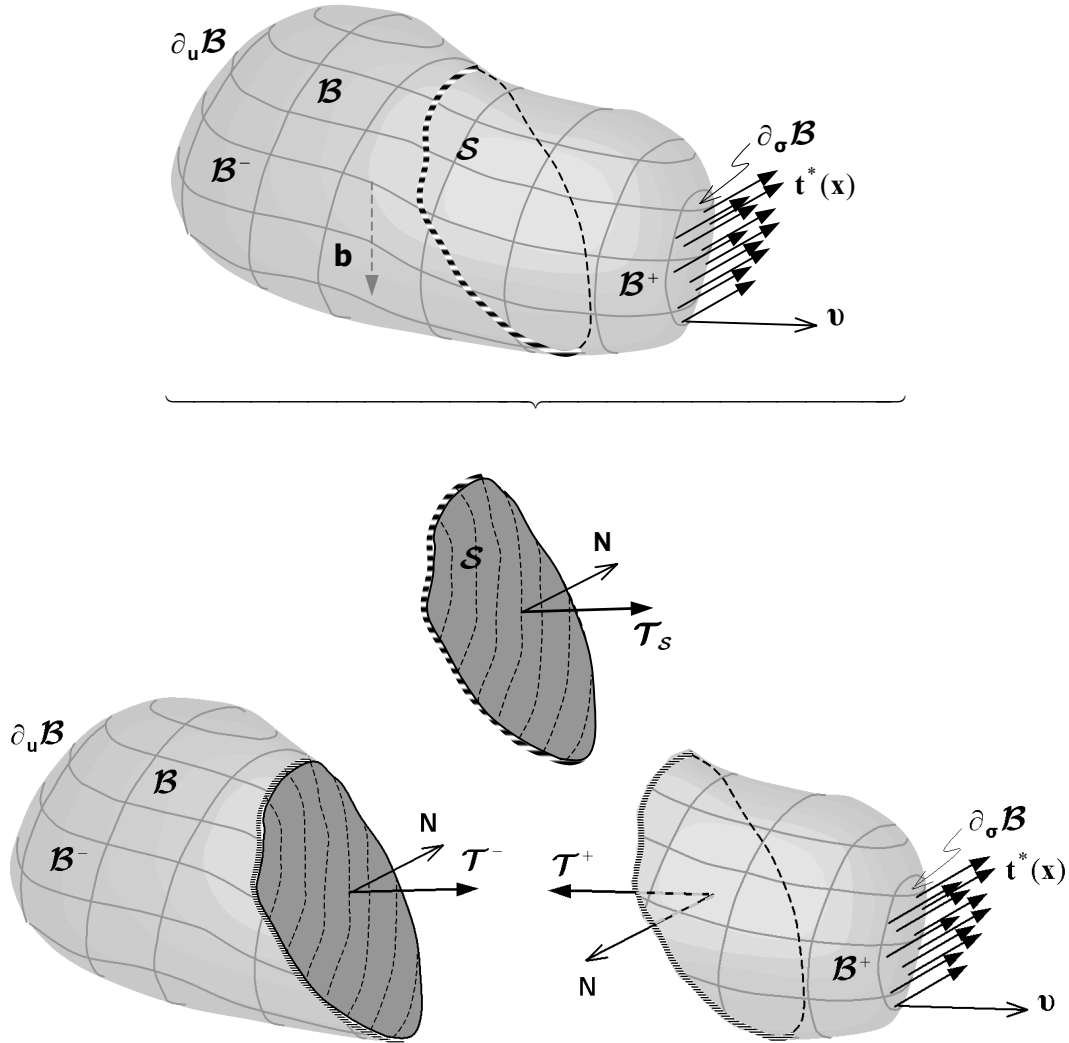

Figure 2.2: Three dimensional body and discontinuous interface.

---

[1] Although here we postulate this condition, it can be derived from the principle of virtual work if the so-called kinematics of strong discontinuities are assumed. This result was obtained in Simo&Oliver(1994).

2.3 Representative continuum damage model

The term Damage Mechanics has been used to refer to models that are characterized by a loss of stiffness, that is to say, a reduction of the secant constitutive modulus. In Kachanov(1958)'s pioneering work, the concept of effective stress was defined. In that work, Kachanov treated the damage variable as a scalar (isotropic damage), whose value ranged from 0 to 1. Later, several researchers extended this theory by treating the damage variable as a tensor (anisotropic damage). Another important work is the one by Rabotnov(1969) intended to include the loss of rigidity of the material as a consequence of the appearance of fissures, further called *Continuum Damage Mechanics*. This became a very powerful and consistent theory based on the thermodynamics of irreversible processes. This thermodynamical formalism was developed by Lemaitre & Chaboche(1985). The damage models were used not only to simulate fragile materials, but also to simulate creep, plasticity, viscoplaticity and fatigue phenomena.

Other important works can also be mentioned. For instance, Mazars(1986) considered distinct damage variables for compression (d^-) and tension (d^+). Later, Faria and Oliver developed this idea in Faria&Oliver(1993). Mazars&Pijaudier-Cabot(1996) have found a correlation between Fracture Mechanics and Damage models. On the other hand, Chaboche(1979) has used a damage variable with tensorial character. Carol *et al.* (1998) have proposed a general unifying framework for degradation and damage using a terminology and notation analogous to the well-known theory of elasto-plasticity. Additionally, key developments in continuum damage fundamentals and numerical applications can be found in Simo&Ju(1987a,b), Oliver *et al.* (1990), among others.

2.3.1 Isotropic damage model

The so-called Continuum Damage Models have been used thoroughly to simulate the behavior of materials that present degradation of the mechanical properties due to small fissures that appear during the loading process. To characterize this, the concept of effective stress, $\overline{\sigma}$, is introduced (see Figure 2.3).
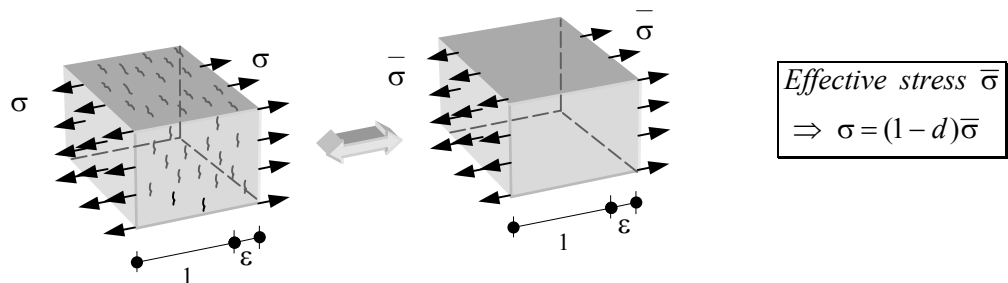
Figure 2.3: Effective stress concept.

In one dimension (see Figure 2.4) we can write:

$$\sigma = (1-d)\overline{\sigma} \tag{2.15}$$

where $\overline{\sigma}$ is the effective stress and d is the damage parameter which ranges from 0 to 1, *i.e.*, $0 \le d \le 1$.

The effective stress $\overline{\sigma}$ and the strain are related by the Hooke's law:

$$\overline{\sigma} = E\varepsilon \tag{2.16}$$

where E is the elastic modulus of the material or Young's modulus. Thus, substituting (2.16) into (2.15) yields

$$\sigma = (1-d)E\varepsilon \qquad 0 \le d \le 1 \tag{2.17}$$
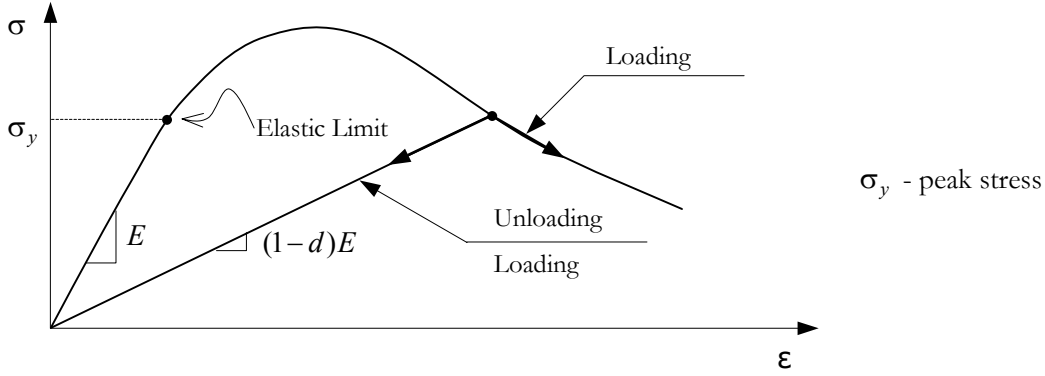
Figure 2.4: Stress-strain curve.

2.3.1.1 Constitutive equation

Here, the generalization of the damage model sketched in the previous section to 3D cases is made. Only the case of isotropic damage is considered. The Helmholtz density of free energy ψ function can be written as follows:

$$\psi = (1-d)\psi^e = (1-d)\frac{1}{2}\boldsymbol{\varepsilon} : \mathbb{C}^e : \boldsymbol{\varepsilon} \tag{2.18}$$

In the case of a completely isotropic elastic response, the standard fourth-order isotropic elastic modulus tensor $\mathbb{C}^e$ as a function of Lamé's parameters λ, μ, is defined as:

$$\mathbb{C}^e = 2\mu\mathbb{I} + \lambda(\mathbf{1} \otimes \mathbf{1}) \tag{2.19}$$

where $\mathbf{1}$ is the second order unit tensor and $\mathbb{I}$ is the fourth order unit tensor, defined in components as $\mathbb{I}_{ijkl} = \frac{1}{2}(\delta_{ik}\delta_{jl} + \delta_{il}\delta_{jk})$. The Lamé's parameters, the Young's modulus, E, and the Poisson's ratio, ν are related by:

$$\lambda = \frac{\nu E}{(1+\nu)(1-2\nu)} \quad ; \quad \mu = \frac{E}{2(1+\nu)} \tag{2.20}$$

From equation (2.18) we obtain the following stress-strain relationship (the constitutive equation):

$$\boldsymbol{\sigma} = \frac{\partial \mathcal{V}(\boldsymbol{\varepsilon}, d)}{\partial \boldsymbol{\varepsilon}} = (1-d)\,\overline{\boldsymbol{\sigma}} \tag{2.21}$$

where $\overline{\boldsymbol{\sigma}}$ is the effective stress tensor defined as:

$$\overline{\boldsymbol{\sigma}} = \mathbb{C}^e : \boldsymbol{\varepsilon} \tag{2.22}$$

The reduced dissipation $\mathcal{D}$ becomes:

$$\mathcal{D} = -\dot{\mathcal{V}} + \boldsymbol{\sigma} : \dot{\boldsymbol{\varepsilon}} = \dot{d}\,\mathcal{V}^e \geq 0 \tag{2.23}$$

which characterizes an irreversible process (for further details in thermodynamics aspects see Lemaitre(1996)). Since $\mathcal{V}^e \geq 0$ by definition, $\dot{d} \geq 0$ must hold to satisfy the thermodynamic requirement (2.23).

The following norms in the stress space and in the strain space are defined, respectively, as:

$$\underbrace{\mathcal{T}_\sigma = \| \boldsymbol{\sigma} \|_{\mathbb{C}^{e-1}} = \sqrt{\boldsymbol{\sigma} : \mathbb{C}^{e-1} : \boldsymbol{\sigma}} \quad ; \quad \mathcal{T}_\varepsilon = \| \boldsymbol{\varepsilon} \|_{\mathbb{C}^e} = \sqrt{\boldsymbol{\varepsilon} : \mathbb{C}^e : \boldsymbol{\varepsilon}} = \sqrt{2\mathcal{V}^e}}$$
$$\Downarrow$$
$$\mathcal{T}_\sigma = (1-d)\mathcal{T}_\varepsilon \tag{2.24}$$

With these concepts in hand, we can define the elastic region (see Figure 2.5(b)) in the strain space as:

$$\mathbb{E}_\varepsilon := \left\{ \boldsymbol{\varepsilon} \;\middle|\; \mathcal{G}(\mathcal{T}_\varepsilon, r) < 0 \right\} \tag{2.25}$$

and in the stress space (see Figure 2.5(a)) as:

$$\mathbb{E}_\sigma := \left\{ \boldsymbol{\sigma} \;\middle|\; \mathcal{F}(\mathcal{T}_\sigma, q) < 0 \right\} \tag{2.26}$$

where r is the internal variable whose value defines the elastic limit. Thus we can define the damage criterion which defines the elastic limits and reads

$$\underbrace{\mathcal{F}(\mathcal{T}_\sigma, q) = \mathcal{T}_\sigma - q(r) \leq 0}_{stress \; space} \quad \text{or} \quad \underbrace{\mathcal{G}(\mathcal{T}_\varepsilon, r) = \mathcal{T}_\varepsilon - r \leq 0}_{strain \; space} \tag{2.27}$$

From equation (2.24) and Figure 2.4, for the uniaxial case, we can obtain:

$$\mathcal{T}_\varepsilon = \sqrt{\boldsymbol{\varepsilon} : \mathbb{C}^e : \boldsymbol{\varepsilon}} \quad \Rightarrow \quad r_0 = \frac{\sigma_y}{\sqrt{E}} \tag{2.28}$$

where r_0 is an initial threshold value and σ_y is the elastic strength. On the other hand, q is the stress-like hardening/softening variable defined as:

$$q(r) = (1-d)r \tag{2.29}$$

where $q(r)$ defines the hardening/softening rule in terms of r. The relationship between q and r (linear and exponential softening law) is given in Figure 2.6 and Figure 2.7. Using equation (2.29) and equation (2.21) we can obtain the following expression:

$$\boldsymbol{\sigma} = \frac{q(r)}{r}\overline{\boldsymbol{\sigma}}$$
(2.30)

From the damage function $\mathscr{F}(\mathcal{T}_\sigma, q)$ and equation (2.29) we obtain:

$$\mathscr{F}(\mathcal{T}_\sigma, q) = 0 \Leftrightarrow \mathcal{T}_\sigma - q = (1-d)\mathcal{T}_\varepsilon - (1-d)r = 0 \Leftrightarrow \mathscr{G}(\mathcal{T}_\varepsilon, r) \equiv 0 \Leftrightarrow \mathcal{T}_\varepsilon - r = 0$$
(2.31)

a) Stress space   b) Strain space
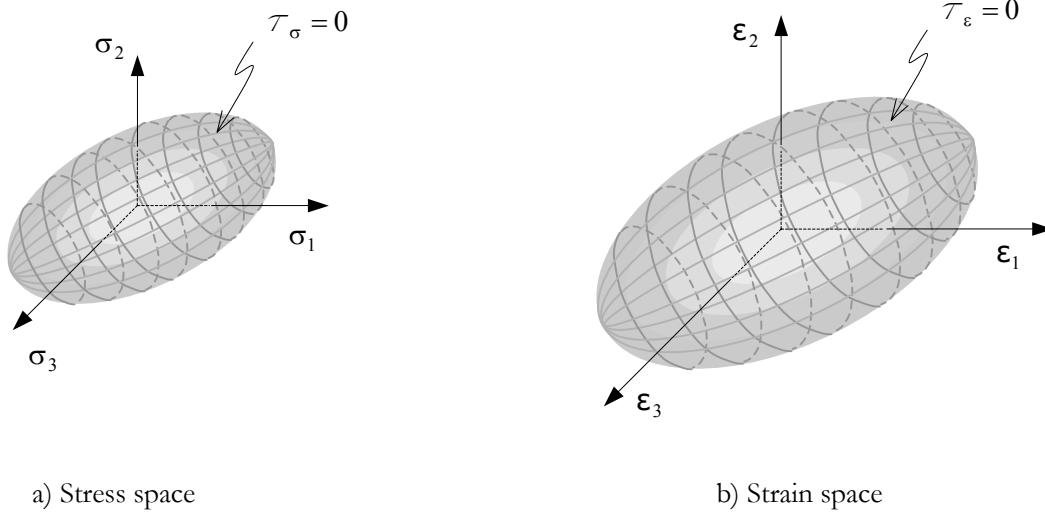
Figure 2.5: Norm surface - Elastic limit.

2.3.2 Hardening rule

The hardening rule is characterized by:

$$\dot{q} = \mathcal{H}^d(r)\dot{r} \;\; ; \qquad \mathcal{H}^d(r) = q'(r) \le 0 \;\; ; \qquad q \in \left[0, \sigma_y\right] ; \qquad q_0 = r_0 = \frac{\sigma_y}{\sqrt{E}}$$
(2.32)

where $\mathcal{H}^d$ is the continuum hardening/softening parameter.

2.3.2.1 Linear hardening law

$$q(r) = \begin{cases} r_0 & r \le r_0 \\ \\ r_0 + \mathcal{H}^d(r - r_0) \nless 0 & r > r_0 \end{cases}$$
(2.33)

thus based on the previous step the damage variable becomes:

$$d = 1 - \frac{q}{r} = \begin{cases} 0 & r \leq r_0 \\[2ex] 1 - \frac{r_0}{r} - \mathcal{H}^d \left(1 - \frac{r_0}{r}\right) \not> 1 & r > r_0 \end{cases} \tag{2.34}$$
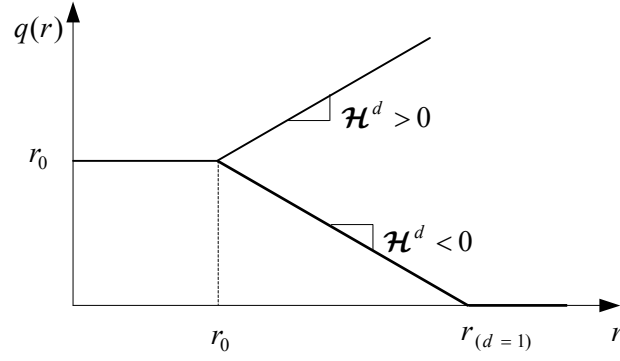
Figure 2.6: Linear hardening/softening law.

2.3.2.2 Exponential hardening law

As described in Figure 2.7.
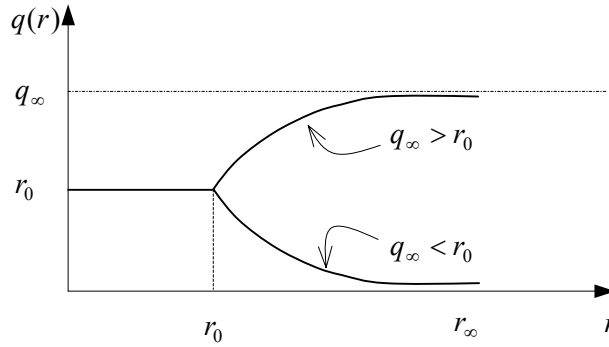
Figure 2.7: Exponential hardening/softening law.

The evolution laws for the damage threshold and the damage variable are:

$$\dot{r} = \gamma$$

$$\dot{d} = \gamma \frac{\partial \mathcal{F}(\tau_\sigma, q(r))}{\partial r} \tag{2.35}$$

where γ is a damage consistency parameter used to define loading/unloading conditions (Kuhn-Tucker conditions):

$$\gamma \geq 0 \quad ; \quad \mathscr{F}(\tau_\sigma, q) \leq 0 \quad ; \quad \gamma \, \mathscr{F}(\tau_\sigma, q) = 0 \tag{2.36}$$

and the persistency condition

$$\gamma \, \dot{\mathscr{F}}(\tau_\sigma, q) = 0 \tag{2.37}$$

We can summarize the load/unloading process schematically as:

$$
\begin{cases}
\mathscr{F} < 0 & \Rightarrow \quad \gamma = 0 \quad \Rightarrow \quad \dot{d} = 0 \quad \Rightarrow \quad \text{(Elastic)} \\[2mm]
\mathscr{F} = 0
\begin{cases}
\dot{\mathscr{F}} < 0 & \Rightarrow \quad \gamma = 0 \quad \Rightarrow \quad \dot{d} = 0 \quad \Rightarrow \quad \text{(Unloading)} \\[2mm]
\dot{\mathscr{F}} = 0 \Rightarrow
\begin{cases}
\gamma = 0 & \Rightarrow \quad \dot{d} = 0 \quad \Rightarrow \quad \text{(Neutral loading)} \\[2mm]
\gamma > 0 & \Rightarrow \quad \dot{d} > 0 \quad \Rightarrow \quad \text{(Loading)}
\end{cases}
\end{cases}
\end{cases}
\tag{2.38}
$$

2.3.3 Time integration of the evolution laws, Tangent moduli

The incremental constitutive equation in terms of the stress and strain rates reads:

$$\dot{\boldsymbol{\sigma}} = \mathbb{C}^d : \dot{\boldsymbol{\varepsilon}} \tag{2.39}$$

Consider the constitutive equation:

$$\boldsymbol{\sigma} = (1-d)\mathbb{C}^e : \boldsymbol{\varepsilon} \quad \xrightarrow[\text{with respect to time}]{\textit{differentiating}} \quad \dot{\boldsymbol{\sigma}} = (1-d)\mathbb{C}^e : \dot{\boldsymbol{\varepsilon}} - \dot{d}\, \mathbb{C}^e : \boldsymbol{\varepsilon} \tag{2.40}$$

When the material point considered is not in loading, then $\dot{d} = 0$, and thus:

$$\dot{\boldsymbol{\sigma}} = (1-d)\mathbb{C}^e : \dot{\boldsymbol{\varepsilon}} \quad \Rightarrow \quad \mathbb{C}^d = (1-d)\mathbb{C}^e \tag{2.41}$$

The value of the internal variable d is given by the corresponding damage condition and evolution laws. After some particularizations, the damage variable evolution can be integrated in closed form at time t (see Figure 2.8) giving:

$$
\left.
\begin{aligned}
& \dot{r} = \gamma \\
& r > 0 \Rightarrow \mathscr{F}(\boldsymbol{\sigma}, q) = 0 \Leftrightarrow \mathscr{G}(\boldsymbol{\varepsilon}, q) = 0 \Leftrightarrow r = \tau_\varepsilon \\
& r \, \big|_{t=0} = r_0
\end{aligned}
\right\}
\Rightarrow \quad r_t = \max_{s \in (-\infty, t)} \left\{ r_0, \tau_\varepsilon(s) \right\}
\tag{2.42}
$$
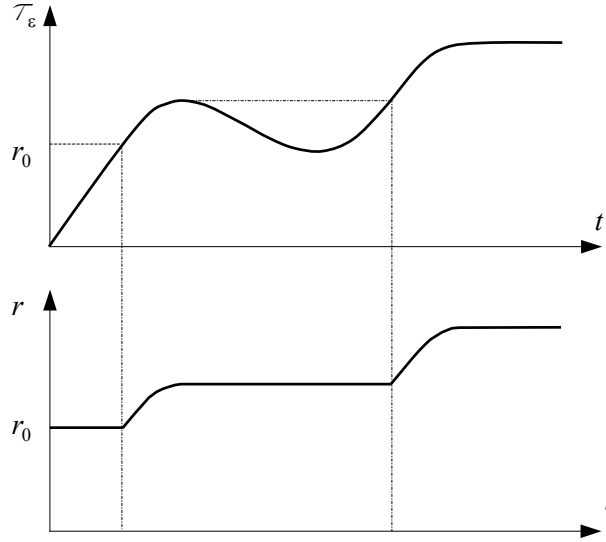
Figure 2.8: Variation of τ_ε and r in the time t.

Differentiating τ_ε with respect to time yields:

$$\tau_\varepsilon = \sqrt{\boldsymbol{\varepsilon} : \mathbb{C}^e : \boldsymbol{\varepsilon}} \quad \longrightarrow \quad \dot{\tau}_\varepsilon = \dot{r} = \frac{1}{\tau_\varepsilon}\overline{\boldsymbol{\sigma}} : \dot{\boldsymbol{\varepsilon}} \tag{2.43}$$

and considering equation (2.29), we can obtain:

$$\dot{d} = \left(\frac{q(r) - q'(r)r}{r^2}\right)\dot{r} \quad \therefore \quad \dot{d} = \left(\frac{q(r) - \mathcal{H}^d r}{r^2}\right)\dot{r} \tag{2.44}$$

thus we can obtain $\mathbb{C}^d$ substituting (2.44) into (2.40):

$$\mathbb{C}^d = (1-d)\,\mathbb{C}^e - \left(\frac{q(r) - q'(r)r}{r^3}\right)\left(\underbrace{\mathbb{C}^e : \boldsymbol{\varepsilon}}_{\boldsymbol{\sigma}} \otimes \underbrace{\boldsymbol{\varepsilon} : \mathbb{C}^e}_{\boldsymbol{\sigma}}\right) \tag{2.45}$$

A general expression of the tangential material stiffness $\mathbb{C}^d$ is the following:

$$\mathbb{C}^d = \begin{cases} \mathbb{C}^e & elastic & \text{(a)} \\ \xi\,\mathbb{C}^e - \mathcal{K}\left(\mathbb{C}^e : \mathbf{m} \otimes \mathbf{n} : \mathbb{C}^e\right) & loading \Big/ \underbrace{unloading}_{\dot{r}=0 \to \mathcal{K}=0} & \text{(b)} \end{cases} \tag{2.46}$$

where $\mathbf{n}$ is the flow plastic normal to the Yield Function ($\mathcal{F}$), defined as: $\mathbf{n} = \dfrac{\partial \mathcal{F}}{\partial \boldsymbol{\sigma}}$ and $\mathbf{m}$ is the flow of the plastic potential which is normal to the Plastic Potential ($\mathcal{G}$), defined as : $\mathbf{m} = \dfrac{\partial \mathcal{G}}{\partial \boldsymbol{\sigma}}$.

In the case of equation (2.45) we have $\mathbf{n} = \boldsymbol{\varepsilon}$, $\mathbf{m} = \boldsymbol{\varepsilon}$ and $\mathcal{K} = \dfrac{q(r) - \mathcal{H}^d r}{r^3}$ and $\xi = (1-d)$

Table 2.1: Isotropic damage model summary.

ISOTROPIC DAMAGE MODEL		
Helmholtz free energy	$\psi(\boldsymbol{\varepsilon}, r) = [1 - d(r)]\psi^e$ with $\psi^e = \frac{1}{2}(\boldsymbol{\varepsilon} : \mathbb{C}^e : \boldsymbol{\varepsilon})$	(2.47)
Damage variable	$d(r) = 1 - \dfrac{q}{r}$; $q \in [r_0, 0]$; $d \in [0,1]$	(2.48)
Constitutive equation	$\boldsymbol{\sigma} = \dfrac{\partial \psi}{\partial \boldsymbol{\varepsilon}} = (1 - d)\mathbb{C}^e : \boldsymbol{\varepsilon}$	(2.49)
Evolution law	$\dot{r} = \gamma$ $\begin{cases} r \in [r_0, \infty) \\ r_0 = r\big|_{t=0} = \dfrac{\sigma_y}{\sqrt{E}} \end{cases}$	(2.50)
Damage criterion	$\mathscr{F}(\boldsymbol{\sigma}, q) \equiv \mathcal{T}_\sigma - q = \sqrt{\boldsymbol{\sigma} : \mathbb{C}^{e^{-1}} : \boldsymbol{\sigma}} - q$; $\begin{cases} q \in [0, r_0] \\ q\big|_{t=0} = r_0 \end{cases}$	(2.51)
Hardening rule	$\dot{q} = \mathcal{H}^d(r)\dot{r}$; $\left(\mathcal{H}^d = q'(r) \leq 0\right)$	(2.52)
Loading-unloading condition	$\mathscr{F} < 0$; $\gamma \geq 0$; $\gamma\mathscr{F} = 0$	(2.53)
Consistency condition	$\gamma \dot{\mathscr{F}} = 0$ if $\mathscr{F} = 0$	(2.54)

2.3.4 Tension-only damage model

This model is based on the isotropic damage model presented in the preceding section. The evolution of r $(\dot{r} > 0)$ is only activated upon tension in the principal stresses. This is achieved by defining the positive stress counterpart of the stress tensor:

$$\boldsymbol{\sigma}^+ = \sum_{i=1}^{i=3} \langle \sigma_i \rangle \mathbf{p}_i \otimes \mathbf{p}_i \tag{2.55}$$

where $\langle \bullet \rangle \overset{def}{=} \dfrac{|\bullet| + \bullet}{2}$ is the Macaulay bracket and $\mathbf{p}_i$ stands for the elements of the principal directions base.

The tangential stiffness is given by:

$$\mathbb{C}^d = \begin{cases} \mathbb{C}^e & elastic & (a) \\ \xi\,\mathbb{C}^e - \mathcal{K}\left(\overline{\boldsymbol{\sigma}}^+ \otimes \overline{\boldsymbol{\sigma}}\right) & \underset{\dot{r}=0 \to \mathcal{K}=0}{loading\,/\,unloading} & (b) \end{cases} \tag{2.56}$$

where $\boldsymbol{\sigma} = (1-d)\bar{\boldsymbol{\sigma}}$ is the relation between stress and effective stress, and the damage criterion is given by:

$$\mathscr{F}^+\left(\boldsymbol{\sigma}^+, q\right) = \sqrt{\boldsymbol{\sigma}^+ : \mathbb{C}^{e^{-1}} : \boldsymbol{\sigma}} - q \qquad (2.57)$$
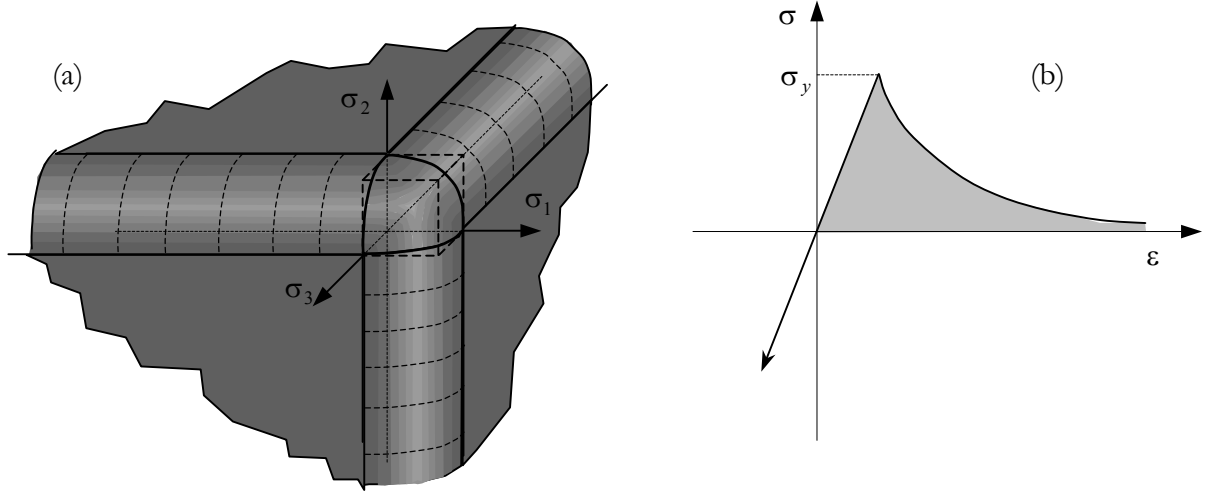
Figure 2.9: Tension-only model: (a) elastic domain in the principal stress space; (b) Stress strain relationship in 1D.

Box 1 shows the very simple algorithm that has been used to evaluate stresses with the proposed model (Oliver *et al.*(1990)).

Box 1:

INITIAL DATA FOR TIME $t+1$

Material properties: σ_y, E, ν, $G_f \Rightarrow r_0$

Current values: ε^{t+1}, d^t, r^t

1) If $t = 0$ then initialize $r = r_0$
2) Evaluate effective stresses
$$\bar{\boldsymbol{\sigma}}^{t+1} = \mathbb{C}^e : \boldsymbol{\varepsilon}^{t+1}$$
3) Evaluate τ_ε^{t+1}
4) Update internal variables
$$r^{t+1} = \max\left\{r^t, \tau_\varepsilon^{t+1}\right\}$$
$$d^{t+1}(r^{t+1})$$
5) Update stresses
$$\boldsymbol{\sigma}^{t+1} = (1 - d^{t+1})\bar{\boldsymbol{\sigma}}^{t+1}$$

2.4 Discontinuity kinematics

For a better understanding of the kinematics we will resort to 2D visualization (see Figure 2.10) where we consider an orthogonal system of curvilinear coordinates ξ and η such that $\mathcal{L}$ corresponds to the coordinate line $\xi = 0$ $\left(\mathcal{L} := \{ \mathbf{x}(\xi, \eta) \in \mathcal{B} \, ; \, \xi = 0 \} \right)$. Let us denote by $\{ \hat{\mathbf{e}}_\xi \, ; \, \hat{\mathbf{e}}_\eta \}$ the physical (orthonormal) base associated to this system of coordinates and let $r_\xi(\xi, \eta)$ and $r_\eta(\xi, \eta)$ be the corresponding scale factors such that $ds_\xi = r_\xi d\xi$ and $ds_\eta = r_\eta d\eta$, where ds_ξ and ds_η are, respectively, differential arc lengths along the coordinate lines ξ and η. We shall also consider the lines $\mathcal{L}^+$ and $\mathcal{L}^-$ which coincide with the coordinate lines $\xi = \xi^+$ and $\xi = \xi^-$, respectively, enclosing a discontinuity band,

$$\mathcal{B}_h := \left\{ \mathbf{x}(\xi, \eta); \ \xi \in \left[\xi^-, \xi^+ \right] \right\} \tag{2.58}$$

whose representative width $h(\eta)$, from now on named the *bandwidth*, is taken as $h(\eta) = r_\xi(0, \eta)(\xi^+ - \xi^-)$. Let us finally define $\mathcal{B} = \mathcal{B}^- \cup \mathcal{B}^+ \cup \mathcal{B}_h$.
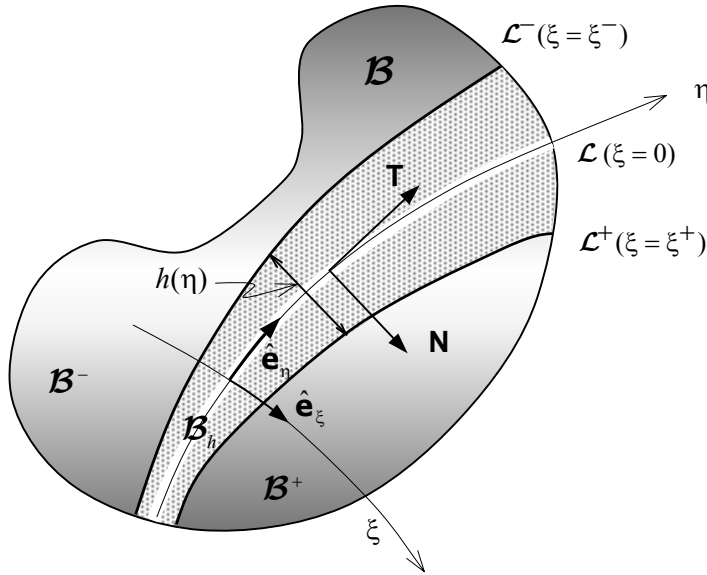

Figure 2.10: Domain with discontinuity-2D.

According to the value of the bandwidth h, one can distinguish the following types of discontinuity kinematics:

- Weak discontinuities $(h \neq 0)$;

- Strong discontinuities $(h = 0)$.

2.4.1 Weak discontinuity kinematics

The weak discontinuity is characterized by the presence of a discontinuous strain field while the displacement field remains continuous. The displacement field rate can be expressed as:

$$\dot{\mathbf{u}}(\mathbf{x},t) = \dot{\bar{\mathbf{u}}}(\mathbf{x},t) + H_{\mathcal{B}_h}(\mathbf{x})[\![\dot{\mathbf{u}}]\!](\mathbf{x},t) \tag{2.59}$$

where $\dot{\bar{\mathbf{u}}}$ is the regular part of the displacement field. And the strain field defined as:

$$\dot{\boldsymbol{\varepsilon}}(\mathbf{x},t) = \nabla^{sym}\dot{\mathbf{u}} = \nabla^{sym}\dot{\bar{\mathbf{u}}}(\mathbf{x},t) + H_{\mathcal{B}_h}(\mathbf{x})\nabla^{sym}[\![\dot{\mathbf{u}}]\!](\mathbf{x},t) + \nabla^{sym}H_{\mathcal{B}_h}(\mathbf{x})[\![\dot{\mathbf{u}}]\!](\mathbf{x},t) \tag{2.60}$$

where $(\bullet)^{sym}$ is the symmetric part of $(\bullet)$ and $H_{\mathcal{B}_h}$, the unit ramp function, is also a continuous function in $\mathcal{B}$ defined by:

$$H_{\mathcal{B}_h} = \begin{cases} 0 & \mathbf{x} \in \mathcal{B}^- \;\; (\xi \leq \xi^-) \\ 1 & \mathbf{x} \in \mathcal{B}^+ \;\; (\xi \geq \xi^+) \\ \dfrac{\xi - \xi^-}{\xi^+ - \xi^-} & \mathbf{x} \in \mathcal{B}_h \;\; (\xi^- < \xi \leq \xi^+) \end{cases} \tag{2.61}$$

Clearly $H_{\mathcal{B}_h}$ exhibits a unit jump, the difference from its values at $\mathcal{L}^+$ and $\mathcal{L}^-$ for the same coordinate line ξ $\left([\![H_{\mathcal{B}_h}]\!] = H_{\mathcal{B}_h}(\xi^+,\eta) - H_{\mathcal{B}_h}(\xi^-,\eta) = 1 \;\; \forall \eta \right)$. From the definition of $H_{\mathcal{B}_h}$ in equation (2.61), the corresponding gradient can be computed as:

$$\nabla H_{\mathcal{B}_h} = \frac{1}{r_\xi}\frac{\partial H_{\mathcal{B}_h}}{\partial \xi}\hat{\mathbf{e}}_\xi + \frac{1}{r_\eta}\frac{\partial H_{\mathcal{B}_h}}{\partial \eta}\hat{\mathbf{e}}_\eta = \chi_{\mathcal{B}_h}\frac{1}{h_\xi}\hat{\mathbf{e}}_\xi$$

$$h_\xi(\xi,\eta) = r_\xi(\xi,\eta)(\xi^+ - \xi^-) \tag{2.62}$$

$$h(0,\eta) = r_\xi(0,\eta)(\xi^+ - \xi^-) = h(\eta)$$

where $\chi_{\mathcal{B}_h}$ is a collocation function defined as

$$\chi_{\mathcal{B}_h} = \begin{cases} 1 & \mathbf{x} \in \mathcal{B}_h \\ 0 & \mathbf{x} \notin \mathcal{B}_h \end{cases} \tag{2.63}$$

Thus

$$\nabla^{sym}H_{\mathcal{B}_h}(\mathbf{x})[\![\dot{\mathbf{u}}]\!](\mathbf{x},t) = \frac{1}{h}\left([\![\dot{\mathbf{u}}]\!] \otimes \mathbf{N} \right)^{sym} \tag{2.64}$$
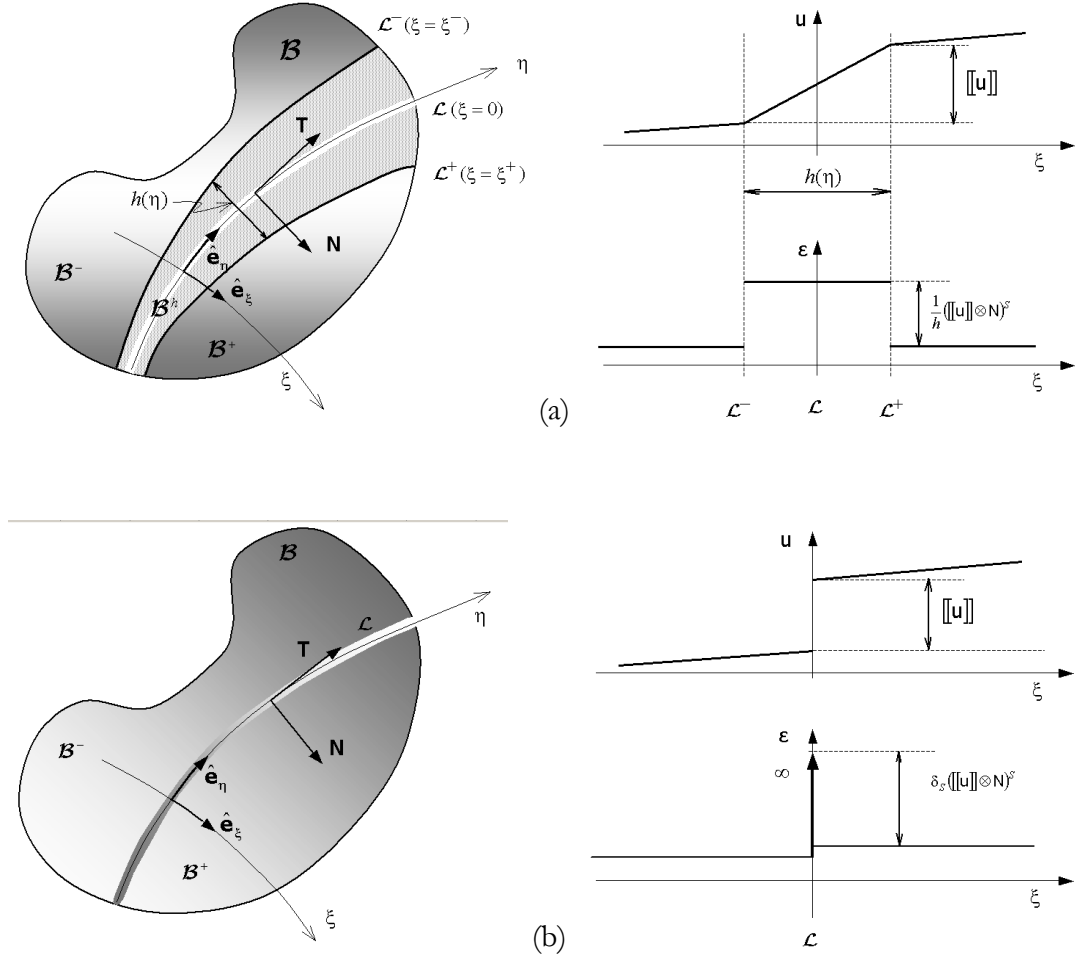
Figure 2.11: Kinematics (a) kinematic state of weak discontinuity; (b) kinematic state of strong discontinuity.

In the case where the jump is constant along $\mathcal{L}$ (or along $\mathcal{S}$ in 3D case[2]), equation (2.60) can be rewritten as:

$$\dot{\boldsymbol{\varepsilon}}(\mathbf{x},t) = \underbrace{\nabla^{sym}\dot{\mathbf{u}}}_{\dot{\bar{\boldsymbol{\varepsilon}}}} + \delta_{\mathcal{S}}^{h}(\mathbf{x})([[\dot{\mathbf{u}}]]\otimes\mathbf{N})^{sym} \tag{2.65}$$

where

$$\delta_{\mathcal{S}}^{h}(\mathbf{x}) = \frac{1}{h}\chi_{\mathcal{S}}(\mathbf{x}) \qquad ; \qquad \chi_{\mathcal{S}}(\mathbf{x}) = \begin{cases} 1 & \forall\mathbf{x}\in\mathcal{S} \\ 0 & \forall\mathbf{x}\in\mathcal{B}\setminus\mathcal{S} \end{cases} \tag{2.66}$$

and $\chi_{\mathcal{S}}(\mathbf{x})$ stands again for the collocation function. Function $\delta_{\mathcal{S}}^{h}$ can be interpreted as the impulse function (see Figure 2.12) defined as:

---

[2] All the equation are expressed in a general 3D case.

$$g(\xi) = \begin{cases} \dfrac{1}{h} & \xi^- < \xi < \xi^+ \\[2mm] 0 & \xi^- > \xi \ \text{ or } \ \xi > \xi^+ \end{cases}$$

$$\int_{-\infty}^{+\infty} g(\xi)\,d\xi = 1$$

(2.67)
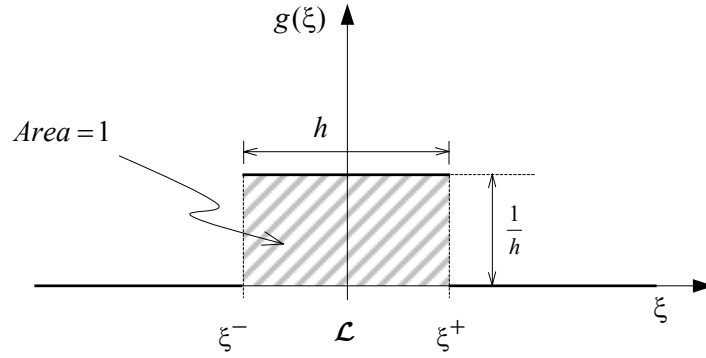
Figure 2.12: Impulse function.

2.4.2 Strong discontinuity kinematics

The strong discontinuity is considered as the limit case of a weak discontinuity, when the band $\mathcal{B}_h$ collapses into the discontinuity line $\mathcal{L}$ (see Figure 2.11). In 3D cases, the band $\mathcal{B}_h$ collapses into the discontinuity surface $\mathcal{S}$. In this limit case the unit ramp function becomes the step function (Heaviside function $\boldsymbol{H_S}$). So, the impulse function (see Figure 2.13) that we obtain as a result of this limiting operation reads:

$$\underbrace{\xi^- \to \ 0 \ \leftarrow \xi^+}$$

$$\lim_{h \to 0} g(\xi) = 0 \quad , \quad \xi \neq 0$$

$$\int_{-\infty}^{+\infty} g(\xi)\,\mathrm{d}\xi = 1$$

(2.68)

Figure 2.13: Limit of the impulse function when the bandwidth tends to zero.

Remark 2.1: We define a *unit impulse function* δ, which imparts an impulse of magnitude one at $\xi = 0$, and an impulse of magnitude zero for all values of ξ other than zero. This "function" is the well known *Dirac delta distribution*, defined to have the following properties:

$$\delta(\xi) = 0 \quad , \quad \xi \neq 0$$

$$\int_{-\infty}^{\infty} \delta(\xi)\, d\xi = 1$$

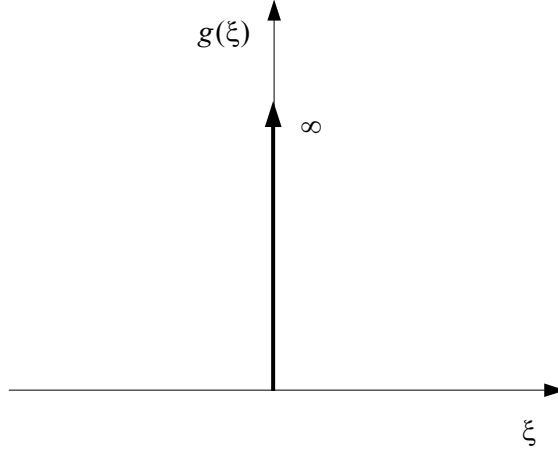$$\int_{-\infty}^{\infty} \delta(\xi, \xi_0)\Psi(\xi)\, d\xi = \Psi(\xi_0) \quad ; \quad \forall \ \Psi(\xi) \in \mathcal{C}_0^{\infty} \qquad \square \tag{2.69}$$

So, the kinematics of a body $\mathcal{B}$ exhibiting a discontinuity of value $[\![\dot{\mathbf{u}}]\!](\mathbf{x}, t)$ in the rate of displacement field (see Figure 2.11) across a material surface denoted by $\mathcal{L}$, whose normal $\mathbf{N}$ points at $\mathcal{B}^+$, can be described as:

Displacement field
$$\dot{\mathbf{u}}(\mathbf{x}, t) = \underbrace{\bar{\dot{\mathbf{u}}}(\mathbf{x}, t)}_{regular} + \underbrace{H_{\mathcal{S}}(\mathbf{x})[\![\dot{\mathbf{u}}]\!](\mathbf{x}, t)}_{discontinuity} \tag{2.70}$$

Strain field
$$\begin{cases} \dot{\boldsymbol{\varepsilon}}(\mathbf{x}, t) = (\nabla \dot{\mathbf{u}})^{sym} = \underbrace{\nabla^{sym}\bar{\dot{\mathbf{u}}} + H_{\mathcal{S}}(\mathbf{x})\nabla^{sym}[\![\dot{\mathbf{u}}]\!]}_{regular} + \underbrace{\delta_{\mathcal{S}}\left([\![\dot{\mathbf{u}}]\!] \otimes \mathbf{N}\right)^{sym}}_{singular} \\ \Rightarrow \dot{\boldsymbol{\varepsilon}}(\mathbf{x}, t) = \bar{\dot{\boldsymbol{\varepsilon}}}(\mathbf{x}, t) + \delta_{\mathcal{S}}\left([\![\dot{\mathbf{u}}]\!] \otimes \mathbf{N}\right)^{sym} \end{cases} \tag{2.71}$$

where $\delta_{\mathcal{S}}$ is the Dirac delta distribution

2.4.3 Representative Weak-Strong discontinuity kinematics

Now consider the kinematics described by the following expressions in the rate of displacement field and strain field:

$$\dot{\mathbf{u}}(\mathbf{x},t) = \dot{\bar{\mathbf{u}}}(\mathbf{x},t) + H_{\mathcal{B}_h}(\mathbf{x})[\![\dot{\mathbf{u}}]\!](\mathbf{x},t) \tag{2.72}$$

$$\dot{\boldsymbol{\varepsilon}}(\mathbf{x},t) = \underbrace{\nabla^{sym}\dot{\bar{\mathbf{u}}}}_{\bar{\boldsymbol{\varepsilon}}} + \underbrace{\delta_{\mathcal{S}}^h(\mathbf{x})\left([\![\dot{\mathbf{u}}]\!]\otimes\mathbf{N}\right)^{sym}}_{\tilde{\boldsymbol{\varepsilon}}} \tag{2.73}$$

Equation (2.73) is a regularized version of the kinematics in equation (2.71) which is obtained by introducing a regularized Dirac delta distribution by means of a bandwidth parameter h and a collocation function $\chi_{\mathcal{S}}(\mathbf{x})$:

$$\delta_{\mathcal{S}}^h(\mathbf{x}) = \frac{1}{h}\chi_{\mathcal{S}}(\mathbf{x}) \qquad \text{with} \qquad \chi_{\mathcal{S}}(\mathbf{x}) = \begin{cases} 1 & \forall \mathbf{x}\in\mathcal{B}_h \\ 0 & \forall \mathbf{x}\in\mathcal{B}\setminus\mathcal{B}_h \end{cases} \tag{2.74}$$

This allows for the transition from the weak discontinuity to the strong discontinuity. Figure 2.14 illustrates the transition of $\delta_{\mathcal{S}}^h$ from an impulse function to the Dirac delta distribution $\delta_{\mathcal{S}}$.
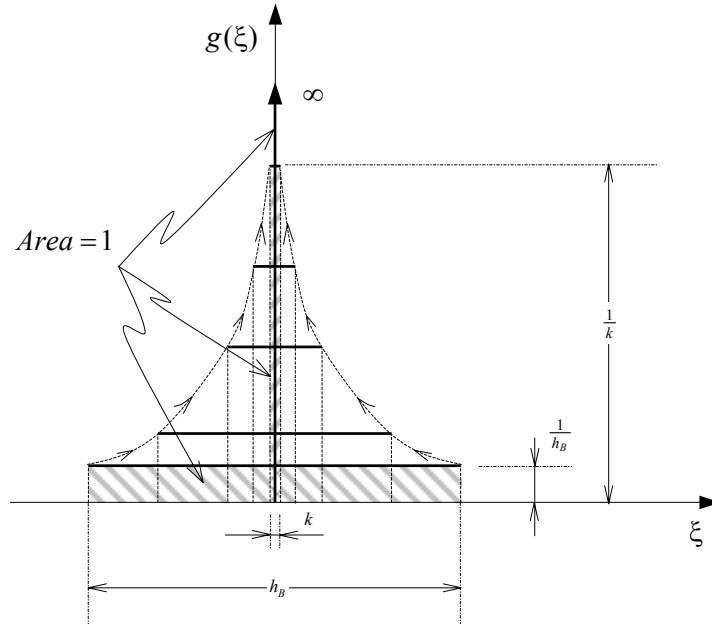

Figure 2.14: Dirac delta distribution as the limit of the impulse function.
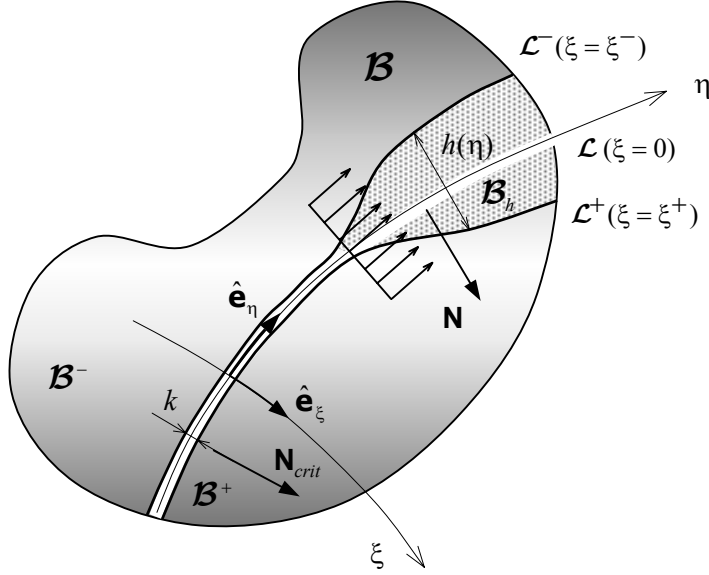
Figure 2.15: Domain with a discontinuity-2D.

2.4.3.1 Regularized Dirac's delta

For the subsequent mathematical treatment, lets us approximate the Dirac delta distribution $\delta_{\mathcal{S}}$ by a $k-$regularized sequence $(k \ll 1)$, $\delta_{\mathcal{S}}^{k}$, defined as follows: instead of considering the discontinuity surface $\mathcal{S}$, we shall consider a discontinuity band of bandwidth k (where k is very small regularization parameter $k \ll 1$) which gives:

$$\delta_{\mathcal{S}}^{k}(\mathbf{x}) = \frac{1}{k}\chi_{\mathcal{S}}(\mathbf{x}) \qquad \text{with} \qquad \chi_{\mathcal{S}}(\mathbf{x}) = \begin{cases} 1 & \mathbf{x} \in \mathcal{S} \\ 0 & \mathbf{x} \notin \mathcal{S} \end{cases} \qquad (2.75)$$

so that, k, which converges to a delta-distribution when k tends to zero *i.e.:*

$$\lim_{k \to 0} \delta_{\mathcal{S}}^{k} = \delta_{\mathcal{S}} \qquad (2.76)$$

For numerical purposes k can be as small as permitted by the machine precision.

2.4.4 Phases of the stress-strain curve

We consider in this work the typical stages of a loading process for a given material point graphically represented in Figure 2.16 and described as follows:

I. **Elastic phase:** it is limited by the point **Y**. In this phase the material obeys the Hooke's generalized law:

$$\boldsymbol{\sigma} = \mathbb{C}^{e} : \boldsymbol{\varepsilon} \qquad (2.77)$$

II. **Inelastic phase**: Point **Y** (yielding) in Figure 2.16 corresponds to the initiation of the non-linear behavior. The elastic limit is surpassed and the loading process is in the range between **Y** and **B**, where **B** stands for the bifurcation point.

III. **Weak discontinuity phase**: The weak discontinuity regime begins as soon as the bifurcation condition $\det[\mathbf{Q(N)}] = 0$ ($\mathbf{Q(N)}$-localization tensor) is satisfied (bifurcation point **B**). This phase is characterized by a discontinuity in the strain field while the displacement field remains continuous.

$$[[\dot{\mathbf{u}}]] = \dot{\mathbf{u}}^+ - \dot{\mathbf{u}}^- = \mathbf{0}$$

$$\widetilde{\boldsymbol{\varepsilon}} = [[\nabla\dot{\mathbf{u}}]] = \nabla\dot{\mathbf{u}}^+ - \nabla\dot{\mathbf{u}}^- \neq \mathbf{0}$$

(2.78)

In this stage the variable bandwidth model starts working, which serves as a transition between weak and strong discontinuity through a bandwidth law.

IV. **Strong discontinuity phase**: When the strong discontinuity condition is satisfied, phase IV begins. It is characterized by the appearance of the second order singularity in the displacement field, *i.e.:*

$$[[\dot{\mathbf{u}}]] = \dot{\mathbf{u}}^+ - \dot{\mathbf{u}}^- \neq \mathbf{0}$$

$$\widetilde{\boldsymbol{\varepsilon}} = [[\nabla\dot{\mathbf{u}}]] = \nabla\dot{\mathbf{u}}^+ - \nabla\dot{\mathbf{u}}^- \neq \mathbf{0}$$

(2.79)
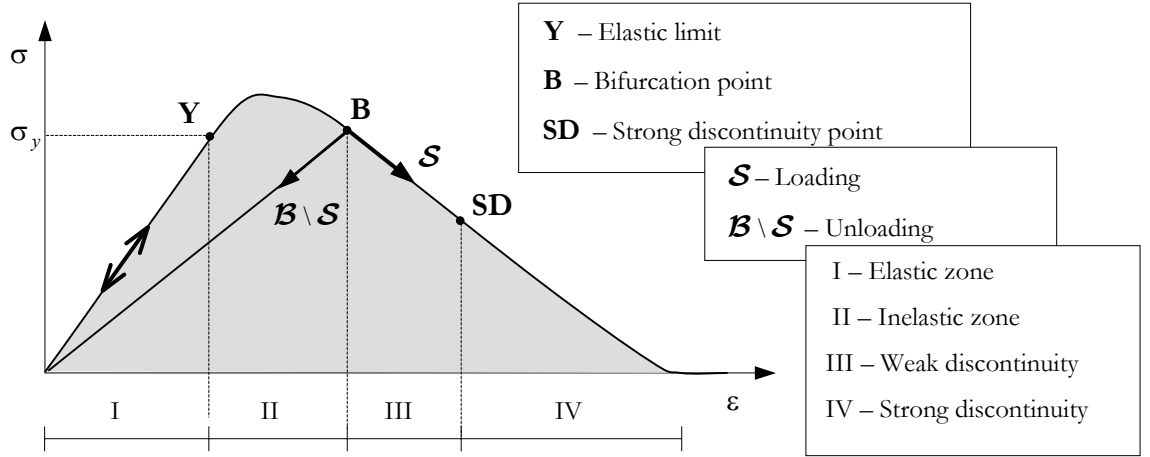
Figure 2.16: Characteristic points during the loading process.

The time at which each point analyzed above ($\mathbf{Y}$, $\mathbf{B}$ and $\mathbf{SD}$) is reached depends on the material (*i.e.*, on the constitutive model) as well as on the evolution of the stress state. For some circumstances, phases II, III, and IV are coincident, see Figure 2.17(a) and (b).
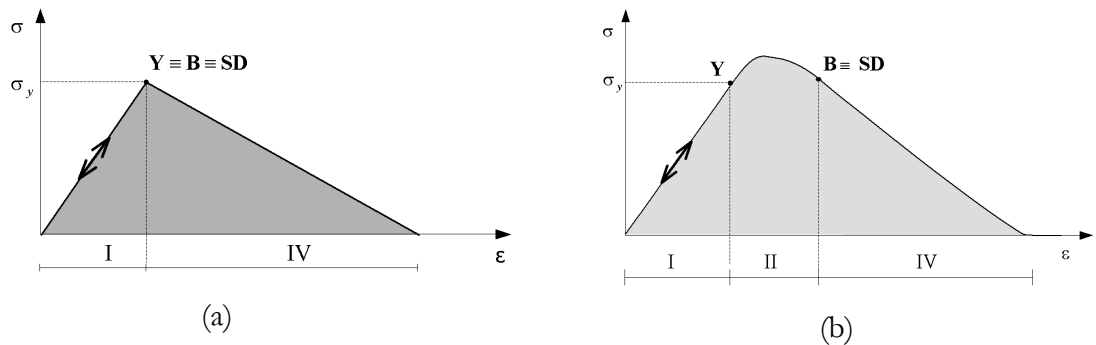
Figure 2.17: Characteristic points during the loading process.

In this context, the formation process of a strong discontinuity at a material point $\mathcal{P}$ of the solid can be modeled as a weak discontinuity that collapses into a strong discontinuity at a certain time in the deformation process (see Figure 2.18). At time t_B, the bifurcation time, the stress-strain field bifurcates resulting in a localization band of bandwidth h_B (see Figure 2.18(a)) which characterizes the onset of a weak discontinuity. At subsequent times the bandwidth decreases ruled by a certain (material property) bandwidth evolution law (see Figure 2.18(d)) until reaching a null value (for computational purposes, a very small parameter k) at time t_{SD}, the strong discontinuity time, which characterizes the onset of the strong discontinuity, Oliver *et al.*(2002).
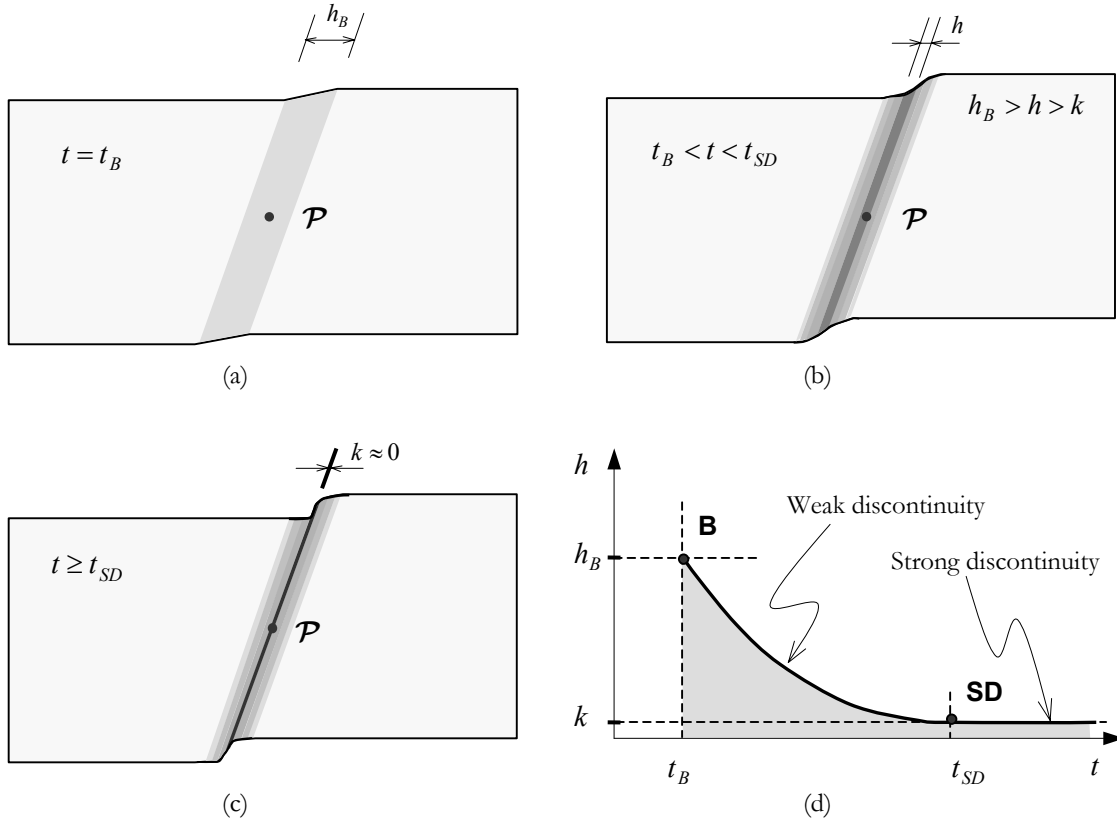
Figure 2.18: Idealized model from weak discontinuity to strong discontinuity: a) weak discontinuity at the time of bifurcation; b) → c) evolution of the bandwidth; d) Bandwidth law, Manzoli (1998).

2.4.5 Bifurcation time

We will now focus on the problem of the bifurcation of the stress-strain fields in the neighborhood of a given material point $\mathcal{P}$ in $\mathcal{S}$ (see Figure 2.19), constrained by the rate form of the traction vector continuity condition. In the very moment of bifurcation we will consider the following scenario: loading in $\mathcal{S}$ and neutral loading in $\mathcal{B} \setminus \mathcal{S}$, see Figure 2.16.
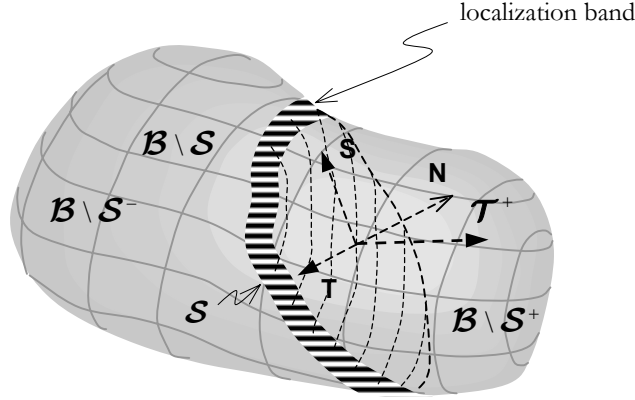

Figure 2.19: Localization band $\mathcal{S}$.

Consider a material point with its stress state in point **B** (the bifurcation point) as shown in the Figure 2.16. In this point we have the following stress state outside and inside of the localized band, respectively:

$$\begin{cases} \dot{\boldsymbol{\sigma}}_{\mathcal{B}\setminus\mathcal{S}} = \mathbb{C}_{\mathcal{B}\setminus\mathcal{S}}^{in} : \dot{\boldsymbol{\varepsilon}}_{\mathcal{B}\setminus\mathcal{S}} & in \quad \mathcal{B}\setminus\mathcal{S} \qquad (2.80) \\[2ex] \dot{\boldsymbol{\sigma}}_{\mathcal{S}} = \mathbb{C}_{\mathcal{S}}^{in} : \dot{\boldsymbol{\varepsilon}}_{\mathcal{S}} & in \quad \mathcal{S} \qquad (2.81) \end{cases}$$

where $\boldsymbol{\sigma}_{\mathcal{S}}$ and $\boldsymbol{\sigma}_{\mathcal{B}\setminus\mathcal{S}}$ stand for the stresses at the interface $\mathcal{S}$ and the neighborhood of $\mathcal{P}$, respectively and $\mathbb{C}^{in}$ the inelastic constitutive tensor[3]. The strain field reads:

$$\begin{cases} \dot{\boldsymbol{\varepsilon}}_{\mathcal{B}\setminus\mathcal{S}} = \dot{\bar{\boldsymbol{\varepsilon}}} & in \quad \mathcal{B}\setminus\mathcal{S} \\[3ex] \dot{\boldsymbol{\varepsilon}}_{\mathcal{S}} = \dot{\bar{\boldsymbol{\varepsilon}}} + \dfrac{1}{h}\left([[\dot{\mathbf{u}}]]\otimes\mathbf{N}\right)^{sym} & in \quad \mathcal{S} \end{cases} \qquad (2.82)$$

The inner traction vector continuity yields:

$$\underbrace{\dot{\mathcal{T}}_{\mathcal{B}\setminus\mathcal{S}} = \dot{\mathcal{T}}_{\mathcal{S}}}$$

$$\dot{\boldsymbol{\sigma}}_{\mathcal{B}\setminus\mathcal{S}} \cdot \mathbf{N} = \dot{\boldsymbol{\sigma}}_{\mathcal{S}} \cdot \mathbf{N} \qquad (2.83)$$

---

[3] We denote by $\mathbb{C}^{in}$ the inelastic constitutive tensor and by $\mathbb{C}^{d}$ in damage case and $\mathbb{C}^{ep}$ in the elastoplasticity case.

Substituting equations (2.80), (2.81) and (2.82) into equation (2.83) after some mathematical manipulations we can obtain:

$$\underbrace{\left(\mathbf{N}\cdot\mathbb{C}_{\mathcal{S}}^{in}\cdot\mathbf{N}\right)}_{\mathbf{Q(N)}}\cdot\frac{[\![\dot{\mathbf{u}}]\!]}{h}=\left[\left(\mathbb{C}_{\mathcal{B}\backslash\mathcal{S}}^{in}-\mathbb{C}_{\mathcal{S}}^{in}\right):\dot{\bar{\boldsymbol{\varepsilon}}}_{\mathcal{S}}\right]\cdot\mathbf{N} \tag{2.84}$$

where $\mathbf{Q(N)}$ is the localization tensor.

At the instant of the bifurcation we will consider that $\mathbb{C}^{in}$ inside and outside of the localization band is the same, *i.e.:*

$$\mathbb{C}_{\mathcal{B}\backslash\mathcal{S}}^{in}=\mathbb{C}_{\mathcal{S}}^{in} \tag{2.85}$$

The bifurcation condition is satisfied when the solution of the equation (2.84) is different from the trivial solution $[\![\dot{\mathbf{u}}]\!]=\mathbf{0}$, resulting the condition:

$$\det[\mathbf{Q(N)}]=0 \tag{2.86}$$

The material bifurcation analysis is presented in the Chapter 3. From the bifurcation we get $\mathcal{H}_{crit}^{d}$ and $\mathbf{N}_{crit}$ which are the critical values of $\mathcal{H}^{d}$ and $\mathbf{N}$, respectively.

2.4.6 Strong discontinuity analysis of the isotropic damage model

The strong discontinuity analysis has the aim of obtaining the conditions that have to be imposed in a standard continuum constitutive equation (stress-strain) to be compatible with the kinematics of strong discontinuities. The analysis developed here is based on the fact that, adopting the inner traction continuity condition as a point of departure, it can be shown that the stress as well as its time derivative must be bounded, even when the strain is not. This result was obtained in Oliver *et al.*(2002).

Now, from the constitutive equation (2.49), one can obtain:

$$\boldsymbol{\sigma}=(1-d)\,\mathbb{C}^{e}:\boldsymbol{\varepsilon}\quad\Rightarrow\quad\boldsymbol{\varepsilon}=\frac{r}{q}\,\mathbb{C}^{e^{-1}}:\boldsymbol{\sigma} \tag{2.87}$$

and differentiating with respect to time:

$$\dot{\boldsymbol{\varepsilon}}=\frac{\partial}{\partial t}\left(\frac{r}{q}\,\mathbb{C}^{e^{-1}}:\boldsymbol{\sigma}\right) \tag{2.88}$$

Considering now the expression of strain (in rate) given by equation (2.71), we can obtain:

$$\dot{\boldsymbol{\varepsilon}}(\mathbf{x})\,\big|_{\mathbf{x}\in\mathcal{S}}\overset{def}{=}\dot{\boldsymbol{\varepsilon}}_{\mathcal{S}}=\underbrace{\dot{\bar{\boldsymbol{\varepsilon}}}}_{bounded}+\frac{1}{k}\left([\![\dot{\mathbf{u}}]\!]\otimes\mathbf{N}\right)^{sym}=\frac{\partial}{\partial t}\left(\frac{r}{q}\,\mathbb{C}^{e^{-1}}:\boldsymbol{\sigma}\right) \tag{2.89}$$

Now, multiplying the above equation by k, we can obtain, for the strong discontinuity regime ($[\![\dot{\mathbf{u}}]\!] \neq 0$ and $k \to 0$)[4]:

$$\lim_{k \to 0} \left[k\, \dot{\overline{\boldsymbol{\varepsilon}}} + \left([\![\dot{\mathbf{u}}]\!] \otimes \mathbf{N} \right)^{sym} \right] = \left([\![\dot{\mathbf{u}}]\!] \otimes \mathbf{N} \right)^{sym} = \lim_{k \to 0} \frac{\partial}{\partial t} \left(\frac{kr}{q} \mathbb{C}^{e-1} : \boldsymbol{\sigma} \right) \tag{2.90}$$

since $\boldsymbol{\sigma}$ and q are bounded, for the condition $[\![\dot{\mathbf{u}}]\!] \neq 0$ to hold, the following expression must be satisfied:

$$\lim_{k \to 0} \; kr \neq 0 \tag{2.91}$$

Now defining the rate of the discrete internal variable $\overline{\alpha}$ as:

$$\underbrace{\dot{\overline{\alpha}}}_{bounded} \overset{def}{=} \begin{cases} \dot{\overline{\alpha}} = k\,\dot{r} \\ \\ \overline{\alpha} \in [0, \infty\} \end{cases} \Rightarrow r = r_{SD} + \int_0^{\overline{\alpha}} \frac{1}{k(m)}\, \mathrm{d}m \tag{2.92}$$

Since for the strong discontinuity regime $k = ctte$, we obtain:

$$\begin{cases} r = r_{SD} + \frac{1}{k}\overline{\alpha} \\ \\ \overline{\alpha} = k(r - r_{SD}) \end{cases} \tag{2.93}$$

where $(\bullet)_{SD}$ denotes the value of $(\bullet)$ at the inception of the strong discontinuity regime. Substituting equation (2.93) into equation (2.90) yields:

$$\left([\![\dot{\mathbf{u}}]\!] \otimes \mathbf{N} \right)^{sym} = \frac{\partial}{\partial t} \left(\frac{\overline{\alpha}}{q} \mathbb{C}^{e-1} : \boldsymbol{\sigma} \right) \tag{2.94}$$

The above equation is known as *strong discontinuity equation*. Substituting equation (2.92) into (2.52) results in:

$$\dot{q} = \mathcal{H}^d \dot{r} = \frac{1}{k} \mathcal{H}^d \, \dot{\overline{\alpha}} \tag{2.95}$$

Since q is bounded ($q \in [0, r_0]$) as well as $\overline{\alpha}$ and $\dot{\overline{\alpha}}$ the mathematical consistency of (2.95) requires that:

$$\mathcal{H}^d = k\,\overline{\mathcal{H}}^d \tag{2.96}$$

thus, for the case of a linear hardening/softening law,

$$\dot{q} = \overline{\mathcal{H}}^d \, \dot{\overline{\alpha}} \quad \Rightarrow \quad q = q_{SD} + \overline{\mathcal{H}}^d \overline{\alpha} \tag{2.97}$$

---

[4] The final bandwidth value is set to $h\,\big|_{t=t_{SD}} = k$.

where the parameter $\overline{\mathcal{H}}^d$ is termed the *discrete (or intrinsic) hardening/softening parameter* and shall be considered as a material property.

The parameter $\overline{\alpha}$ from equation (2.92) can be reinterpreted as follows: Considering loading regime ($\dot{r} \neq 0$), equation (2.31) entails that:

$$r = \mathcal{T}_\varepsilon = \sqrt{\boldsymbol{\varepsilon} : \mathbb{C}^e : \boldsymbol{\varepsilon}} \quad \Rightarrow \quad \dot{r} = \frac{1}{r} \underbrace{\boldsymbol{\varepsilon} : \mathbb{C}^e}_{\frac{\boldsymbol{\sigma}}{1-d}} : \dot{\boldsymbol{\varepsilon}} = \frac{1}{r(1-d)} \boldsymbol{\sigma} : \dot{\boldsymbol{\varepsilon}} = \frac{1}{q} \boldsymbol{\sigma} : \dot{\boldsymbol{\varepsilon}} \tag{2.98}$$

Substituting the kinematics (2.73) and taking the limit when $k \to 0$:

$$\dot{\overline{\alpha}} = \lim_{k \to 0} k\dot{r} = \lim_{k \to 0} k \frac{1}{q} \boldsymbol{\sigma} : \left[\dot{\bar{\boldsymbol{\varepsilon}}} + \frac{1}{k} \left([\![\dot{\mathbf{u}}]\!] \otimes \mathbf{N} \right)^{sym} \right] = \frac{1}{q} \boldsymbol{\sigma} : \left([\![\dot{\mathbf{u}}]\!] \otimes \mathbf{N} \right)^{sym} =$$

$$= \frac{1}{q} [\![\dot{\mathbf{u}}]\!] \cdot (\boldsymbol{\sigma} \cdot \mathbf{N}) = \frac{1}{q} [\![\dot{\mathbf{u}}]\!] \cdot \mathcal{T} \tag{2.99}$$

where $\mathcal{T} = \boldsymbol{\sigma} \cdot \mathbf{N}$ is the traction vector in the normal direction to the discontinuity surface $\mathcal{S}$.

2.4.6.1 Discrete constitutive equation

Equation (2.94) can manipulated as follows: multiplying the both sides by the tensor $\mathbb{C}^e$, we obtain:

$$\mathbb{C}^e : \left([\![\dot{\mathbf{u}}]\!] \otimes \mathbf{N} \right)^{sym} = \left(\mathbb{C}^e \cdot \mathbf{N} \right) \cdot [\![\dot{\mathbf{u}}]\!] = \frac{\partial}{\partial t} \left(\frac{\overline{\alpha}}{q} \boldsymbol{\sigma} \right) \tag{2.100}$$

once again multiplying both sides by $\mathbf{N}$ results in:

$$\underbrace{\left(\mathbf{N} \cdot \mathbb{C}^e \cdot \mathbf{N} \right)}_{\mathbf{Q}^e} \cdot [\![\dot{\mathbf{u}}]\!] = \mathbf{Q}^e \cdot [\![\dot{\mathbf{u}}]\!] = \frac{\partial}{\partial t} \left(\frac{\overline{\alpha}}{q} \mathbf{N} \cdot \boldsymbol{\sigma} \right) = \frac{\partial}{\partial t} \left(\frac{\overline{\alpha}}{q} \mathcal{T} \right)$$

$$\Rightarrow [\![\dot{\mathbf{u}}]\!] = \frac{\partial}{\partial t} \left(\frac{\overline{\alpha}}{q} \mathbf{Q}^{e-1} \cdot \mathcal{T} \right) \tag{2.101}$$

where we have introduced the elastic acoustic tensor ($\mathbf{Q}^e = \mathbf{N} \cdot \mathbb{C}^e \cdot \mathbf{N}$), Willam&Sobh(1987), which is a positive definite tensor, see Appendix A.5.2. Finally, equation (2.101) can lead to:

$$[\![\mathbf{u}]\!] = \frac{\overline{\alpha}}{q} \mathbf{Q}^{e-1} \cdot \mathcal{T} \quad \Rightarrow \quad \mathcal{T} = \frac{q}{\overline{\alpha}} \mathbf{Q}^e \cdot [\![\mathbf{u}]\!] \tag{2.102}$$

Observe that the equation (2.102) is a discrete constitutive equation which relates the traction over the discontinuity surface with the jump in the displacement field: $\mathcal{T} = \mathcal{T}([\![\mathbf{u}]\!])$. Now substituting the equation (2.102) into (2.99) yields:

$$\dot{\alpha} = \frac{1}{q}[\![\dot{\mathbf{u}}]\!]\cdot\boldsymbol{\mathcal{T}} = \frac{1}{\alpha}[\![\dot{\mathbf{u}}]\!]\cdot\mathbf{Q}^e\cdot[\![\mathbf{u}]\!] \tag{2.103}$$

and defining:

$$\mathcal{T}_{[\![\mathbf{u}]\!]} \overset{def}{=} \|\,[\![\mathbf{u}]\!]\,\|_{\mathbf{Q}^e} = \sqrt{[\![\mathbf{u}]\!]\cdot\mathbf{Q}^e\cdot[\![\mathbf{u}]\!]} \Rightarrow \dot{\mathcal{T}}_{[\![\mathbf{u}]\!]} = \frac{1}{\mathcal{T}_{[\![\mathbf{u}]\!]}}[\![\dot{\mathbf{u}}]\!]\cdot\mathbf{Q}^e\cdot[\![\mathbf{u}]\!] \tag{2.104}$$

and substituting (2.104) into the equation (2.103) we can obtain, for loading ($\dot{\alpha} \neq 0$):

$$\begin{cases} \dot{\overline{\alpha}}\overline{\alpha} = \mathcal{T}_{[\![\mathbf{u}]\!]}\,\dot{\mathcal{T}}_{[\![\mathbf{u}]\!]} \\ \overline{\alpha}_{SD} = \mathcal{T}_{[\![\mathbf{u}]\!]} = 0 \end{cases} \Rightarrow \overline{\alpha} = \mathcal{T}_{[\![\mathbf{u}]\!]} \Rightarrow \mathcal{F}\big([\![\mathbf{u}]\!],\overline{\alpha}\big) \equiv \mathcal{T}_{[\![\mathbf{u}]\!]} - \overline{\alpha} = 0 \tag{2.105}$$

Being now possible to define the traction vector norm:

$$\mathcal{T}_{\boldsymbol{\mathcal{T}}} = \frac{q}{\alpha}\mathcal{T}_{[\![\mathbf{u}]\!]} = \sqrt{\frac{q}{\alpha}[\![\mathbf{u}]\!]\cdot\mathbf{Q}^e\cdot[\![\mathbf{u}]\!]\frac{q}{\alpha}} = \sqrt{\boldsymbol{\mathcal{T}}\cdot\mathbf{Q}^{e^{-1}}\cdot\boldsymbol{\mathcal{T}}} = \|\boldsymbol{\mathcal{T}}\|_{\mathbf{Q}^{e^{-1}}} \tag{2.106}$$

where Equation (2.102) has been considered. From equation (2.102) and (2.105) is trivial to show (in loading regime, $\dot{\overline{\alpha}} \neq 0$) that:

$$G\big([\![\mathbf{u}]\!],\overline{\alpha}\big) = \frac{\overline{\alpha}}{q}\mathcal{T}_{\boldsymbol{\mathcal{T}}} - \overline{\alpha} = 0 \iff \mathcal{F}\big(\boldsymbol{\mathcal{T}},q\big) \equiv \mathcal{T}_{\boldsymbol{\mathcal{T}}} - q = 0 \tag{2.107}$$

Taking into account equations (2.102) to (2.107), we can conclude that the continuum constitutive model described in Table 2.1 induce a discrete constitutive damage model by means of the strong discontinuity regime in the presence of an unbounded strain field. Notice that the initial stiffness of the model is infinite ($(1-\omega)\big|_{t=t_{SD}} = \infty$) and that, consequently, the resulting discrete model is a *rigid damage model* (see Figure 2.20).
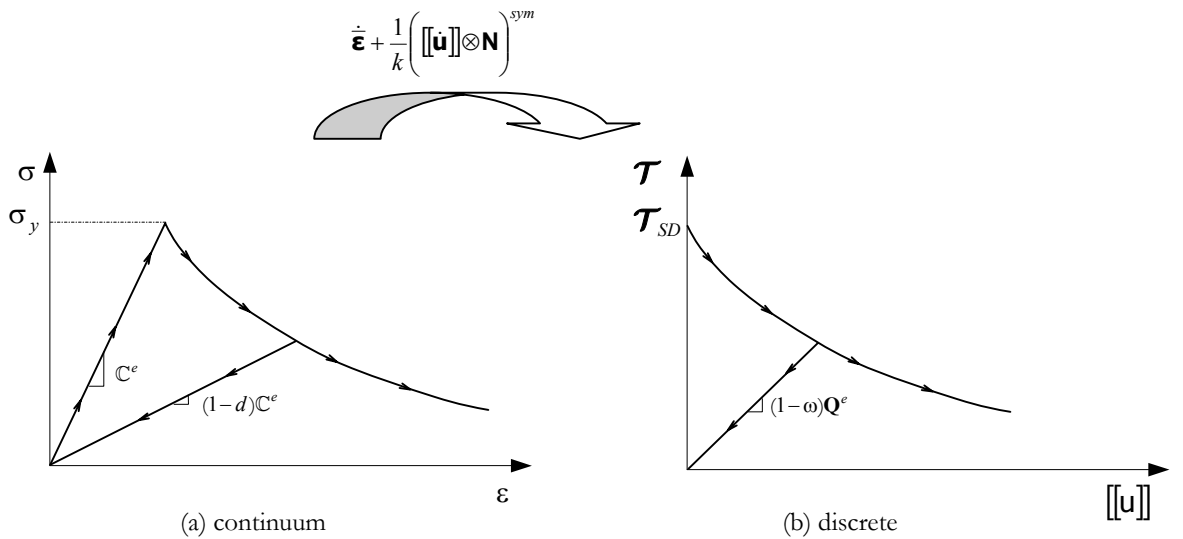

Figure 2.20: Damage constitutive equation: continuum *vs.* discrete.

We can conclude that the introduction of the strong discontinuity kinematics $\dot{\boldsymbol{\varepsilon}} + \dfrac{1}{k}\Big([[\dot{\mathbf{u}}]] \otimes \mathbf{N}\Big)^{sym}$ into a continuum constitutive model induces a discrete constitutive model in the interface of discontinuity, with the only requirement of the regularization of the continuum hardening parameter ($\mathcal{H}^d = k\,\overline{\mathcal{H}}^d$).

2.4.6.2 Strong discontinuity conditions

Let us consider a material point $\mathcal{P}$ in the discontinuity surface $\mathcal{S}$ and a local system constituted by the three versors $(\hat{\mathbf{e}}_1, \hat{\mathbf{e}}_2, \hat{\mathbf{e}}_3)$ such that $\mathbf{N} \equiv \hat{\mathbf{e}}_1$. Consider also the displacement jump $[[\dot{\mathbf{u}}]]$, the unit normal vector $\mathbf{N}$ as well as the stress tensor $\boldsymbol{\sigma}_{\mathcal{S}}$ and the strain tensor $\boldsymbol{\varepsilon}_{\mathcal{S}}$ expressed in that base:

$$
[[\dot{\mathbf{u}}]]_i = \underbrace{\left\{\begin{array}{c} [[\dot{\mathbf{u}}]]_1 \\ [[\dot{\mathbf{u}}]]_2 \\ [[\dot{\mathbf{u}}]]_3 \end{array}\right\} \quad ; \quad N_i = \left\{\begin{array}{c} 1 \\ 0 \\ 0 \end{array}\right\}}
$$

$$
\Downarrow
$$

$$
\left([[\dot{\mathbf{u}}]]_i \;\; N_j\right)^{sym} = \begin{bmatrix} [[\dot{\mathbf{u}}]]_1 & \frac{1}{2}[[\dot{\mathbf{u}}]]_2 & \frac{1}{2}[[\dot{\mathbf{u}}]]_3 \\[2mm] \frac{1}{2}[[\dot{\mathbf{u}}]]_2 & 0 & 0 \\[2mm] \frac{1}{2}[[\dot{\mathbf{u}}]]_3 & 0 & 0 \end{bmatrix} \tag{2.108}
$$

$$
\sigma_{ij} = \begin{bmatrix} \sigma_{11} & \sigma_{12} & \sigma_{13} \\ \sigma_{21} & \sigma_{22} & \sigma_{23} \\ \sigma_{31} & \sigma_{32} & \sigma_{33} \end{bmatrix}_{\mathcal{S}} \quad ; \quad \varepsilon_{ij} = \begin{bmatrix} \varepsilon_{11} & \varepsilon_{12} & \varepsilon_{13} \\ \varepsilon_{21} & \varepsilon_{22} & \varepsilon_{23} \\ \varepsilon_{31} & \varepsilon_{32} & \varepsilon_{33} \end{bmatrix}_{\mathcal{S}} \tag{2.109}
$$

Equation (2.94) can be rewritten as:

$$
\begin{bmatrix} [[\dot{\mathbf{u}}]]_1 & \frac{1}{2}[[\dot{\mathbf{u}}]]_2 & \frac{1}{2}[[\dot{\mathbf{u}}]]_3 \\[2mm] \frac{1}{2}[[\dot{\mathbf{u}}]]_2 & 0 & 0 \\[2mm] \frac{1}{2}[[\dot{\mathbf{u}}]]_3 & 0 & 0 \end{bmatrix} = \frac{\partial}{\partial t}\left(\frac{\overline{\alpha}}{q}\begin{bmatrix} \varepsilon_{11}^{eff} & \varepsilon_{12}^{eff} & \varepsilon_{13}^{eff} \\ \varepsilon_{21}^{eff} & \varepsilon_{22}^{eff} & \varepsilon_{23}^{eff} \\ \varepsilon_{31}^{eff} & \varepsilon_{32}^{eff} & \varepsilon_{33}^{eff} \end{bmatrix}_{\mathcal{S}}\right) \tag{2.110}
$$

where we have considered the components of the effective strain tensor (ε_{ij}^{eff}):

$$\boldsymbol{\varepsilon}^{\mathit{eff}} = \mathbb{C}^{e^{-1}} : \boldsymbol{\sigma} = (1-d)\,\boldsymbol{\varepsilon} \tag{2.111}$$

The components $(\bullet)_{11}$, $(\bullet)_{12}$ and $(\bullet)_{13}$ from equation (2.110) have been used to obtain the discrete constitutive equation (2.102). The other components in that equation give us conditions which must be satisfied in the inception of the strong discontinuity regime. In particular components $(\bullet)_{22}$, $(\bullet)_{23}$ and $(\bullet)_{33}$ have to fulfill the following conditions:

$$\frac{\partial}{\partial t}\left[\frac{\bar{\alpha}}{q}\,\boldsymbol{\varepsilon}_{22}^{\mathit{eff}}\right]=0 \quad \Rightarrow \quad \frac{\bar{\alpha}}{q}\,\boldsymbol{\varepsilon}_{22}^{\mathit{eff}}=C_1 \qquad \forall\, t \geq t_{SD}$$

$$\frac{\partial}{\partial t}\left[\frac{\bar{\alpha}}{q}\,\boldsymbol{\varepsilon}_{23}^{\mathit{eff}}\right]=0 \quad \Rightarrow \quad \frac{\bar{\alpha}}{q}\,\boldsymbol{\varepsilon}_{23}^{\mathit{eff}}=C_2 \qquad \forall\, t \geq t_{SD} \tag{2.112}$$

$$\frac{\partial}{\partial t}\left[\frac{\bar{\alpha}}{q}\,\boldsymbol{\varepsilon}_{33}^{\mathit{eff}}\right]=0 \quad \Rightarrow \quad \frac{\bar{\alpha}}{q}\,\boldsymbol{\varepsilon}_{33}^{\mathit{eff}}=C_3 \qquad \forall\, t \geq t_{SD}$$

The constants of integration C_1, C_2 and C_3 are obtained in the particular instant t_{SD} where $\alpha_{SD}=0$, thus $C_1=C_2=C_3=0$, resulting:

Strong discontinuity condition
$$\begin{cases} \boldsymbol{\varepsilon}_{22\ \mathcal{S}}^{\mathit{eff}}=\left[\mathbb{C}^{e^{-1}}:\boldsymbol{\sigma}_{\mathcal{S}}\right]_{22}=0 \\[2mm] \boldsymbol{\varepsilon}_{23\ \mathcal{S}}^{\mathit{eff}}=\left[\mathbb{C}^{e^{-1}}:\boldsymbol{\sigma}_{\mathcal{S}}\right]_{23}=0 \qquad \forall\ t \geq t_{SD} \\[2mm] \boldsymbol{\varepsilon}_{33\ \mathcal{S}}^{\mathit{eff}}=\left[\mathbb{C}^{e^{-1}}:\boldsymbol{\sigma}_{\mathcal{S}}\right]_{33}=0 \end{cases} \tag{2.113}$$

It is easy to prove that invoking the strong discontinuity conditions (2.113) into the expression of the $\mathcal{H}_{crit}^{d}$ yields $\mathcal{H}_{crit}^{d}=0$. This result can be justified as follows:

- equation (2.84) holds at any stage of the problem since it comes from equations (2.80) - (2.83) which hold for all the stages of the analysis;

- the strong discontinuity regime is characterized by the limit case $k \to 0$ which implies that, for $[\![\dot{\mathbf{u}}]\!] \neq \mathbf{0}$ in equation (2.84) and loading cases $\mathbb{C}_{\mathcal{B}\backslash\mathcal{S}}^{in}=\mathbb{C}_{\mathcal{S}}^{in}$, then $\det\!\left(\mathbf{N}\cdot\mathbb{C}_{\mathcal{S}}^{in}\cdot\mathbf{N}\right)=\det\!\left[\mathbf{Q}(\mathbf{N})\right]=0$.

Remark 2.2: Since $\mathcal{H}_{crit}^{d}=0$ is a necessary condition to induce a strong discontinuity, if that condition occurs at the bifurcation stage the bifurcation could take place under the form of a strong discontinuity. In the general case ($\mathcal{H}_{crit}^{d} \neq 0$) bifurcation will take place under the form of a weak discontinuity and the strong discontinuity conditions (2.113) must be induced in subsequent stage. □

2.4.7 Variable Bandwidth Model - VBM

2.4.7.1 VBM by pre-established law

Beyond the bifurcation point a variable bandwidth model governs the transition between the Weak Discontinuity and the Strong Discontinuity regimes, Oliver *et al.*(1998).

For the damage model the state law for parameter d is:

$$d = 1 - \frac{q(r)}{r} \qquad (2.114)$$

Consider that the $q(r)$ law is given by Figure 2.21, thus we can establish the following equation:

$$q(r) = r_0 + \mathcal{H}_y^d (r - r_0) \qquad (2.115)$$

and

$$\dot{q} = \overline{\mathcal{H}}^d \dot{r} \qquad (2.116)$$

with

$$\overline{\mathcal{H}}^d = \begin{cases} \mathcal{H}_y^d & \text{if} \quad r_0 \leq r \leq r_B \\ \mathcal{H}^d h(q) & \text{if} \quad r_B \leq r \leq r_{SD} \\ \mathcal{H}^d k & \text{if} \quad r_{SD} \leq r \end{cases} \qquad (2.117)$$
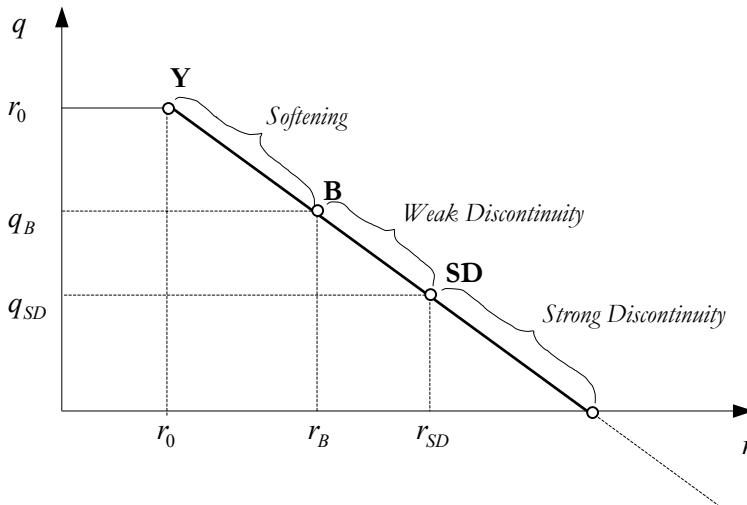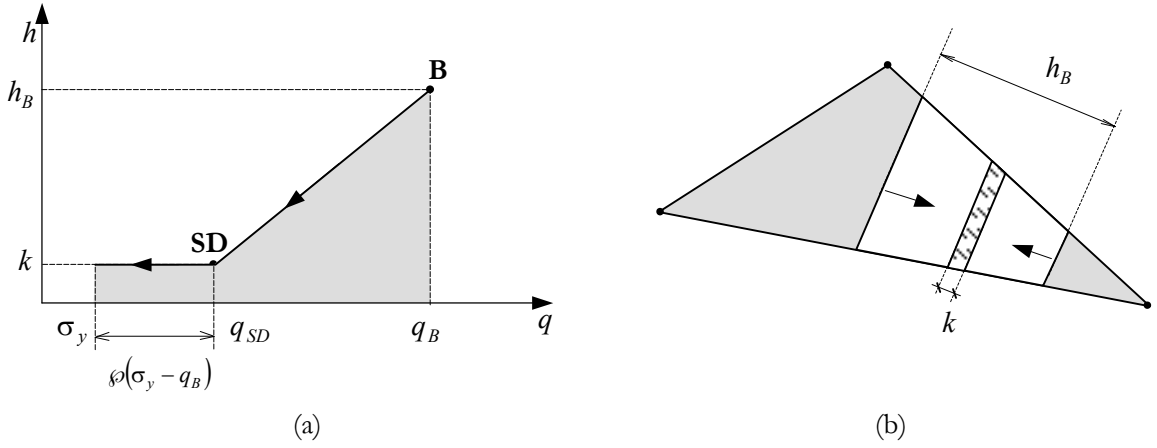

Figure 2.21: Bandwidth law - q *vs.* r.

Figure 2.22: Bandwidth law - h *vs.* q.

Now consider a bandwidth variation (h) in which the evolution criterion is a function of $q(r)$ as shown in Figure 2.22. Thus we can say:

$$h(q) = \begin{cases} k + \dfrac{h_B - k}{q_B - q_{SD}}(q - q_{SD}) & \textit{iff} \quad q_{SD} < q \le q_B \quad \textit{transition} \\ k & \textit{iff} \quad q \le q_{SD} \quad\quad \textit{strong discontinuity} \end{cases} \tag{2.118}$$

Differentiating q:

$$\frac{\partial q}{\partial r} = \overline{\mathcal{H}}_y^d = h(q)\overline{\mathcal{H}}^d \qquad \therefore \qquad \frac{\partial q}{\partial r} = \overline{\mathcal{H}}^d k + \overline{\mathcal{H}}^d R(q - q_{SD}) \tag{2.119}$$

where

$$R = \frac{h_B - k}{q_B - q_{SD}} \tag{2.120}$$

Solving the differential equation (2.119), we can obtain:

$$q = q_{SD} - \frac{k}{R} + \left(q_B + \frac{k}{R} - q_{SD} \right) \exp^{\overline{\mathcal{H}}^d R(r - r_0)} \tag{2.121}$$

Using equation (2.121) when $r \to r_{SD} \Leftrightarrow q \to q_{SD}$, we can obtain the value of the r_{SD}, that is:

$$r_{SD} = r_B + \frac{q_B - q_{SD}}{\overline{\mathcal{H}}^d (h_B - k)} \ell n\left(\frac{k}{h_B} \right) \tag{2.122}$$

In the strong discontinuity regime $\mathcal{H}^d \to \overline{\mathcal{H}}^d k$, thus:

$$\dot{q} = \overline{\mathcal{H}}^d k \dot{r} \tag{2.123}$$

thus

$$q_i = q_{i-1} + \overline{\mathcal{H}}^d k \left(r_i - r_{i-1} \right) \tag{2.124}$$

Figure 2.23 shows the evolution of $\mathcal{H}^d_{crit}$ along the analysis. For a given material point in yielding begins at point **Y** of Figure 2.23, in which the hardening/softening parameter takes the value $\mathcal{H}^d_y$. While $\mathcal{H}^d_{crit} < \mathcal{H}^d_y$ bifurcation is precluded and the behavior is continuous. As soon as $\mathcal{H}^d_{crit} = \mathcal{H}^d_y$ the bifurcation point **B** is detected. At this point $h_B = \mathcal{H}^d_{crit} / \overline{\mathcal{H}}^d$, which determines the initial value of the bandwidth law shown in Figure 2.22(a). Beyond point **B** the bandwidth decreases from h_B to k, according to the bandwidth evolution law of Figure 2.22(a) in terms of $q - q_B$. At point **SD,** when $q = q_{SD}$, the bandwidth, h, equals k. Beyond point **SD** a kinematic state of strong discontinuity is induced, the bandwidth is kept constant and equal to the regularization parameter k and the corresponding softening reads $\mathcal{H}^d = \overline{\mathcal{H}}^d k \approx 0$.
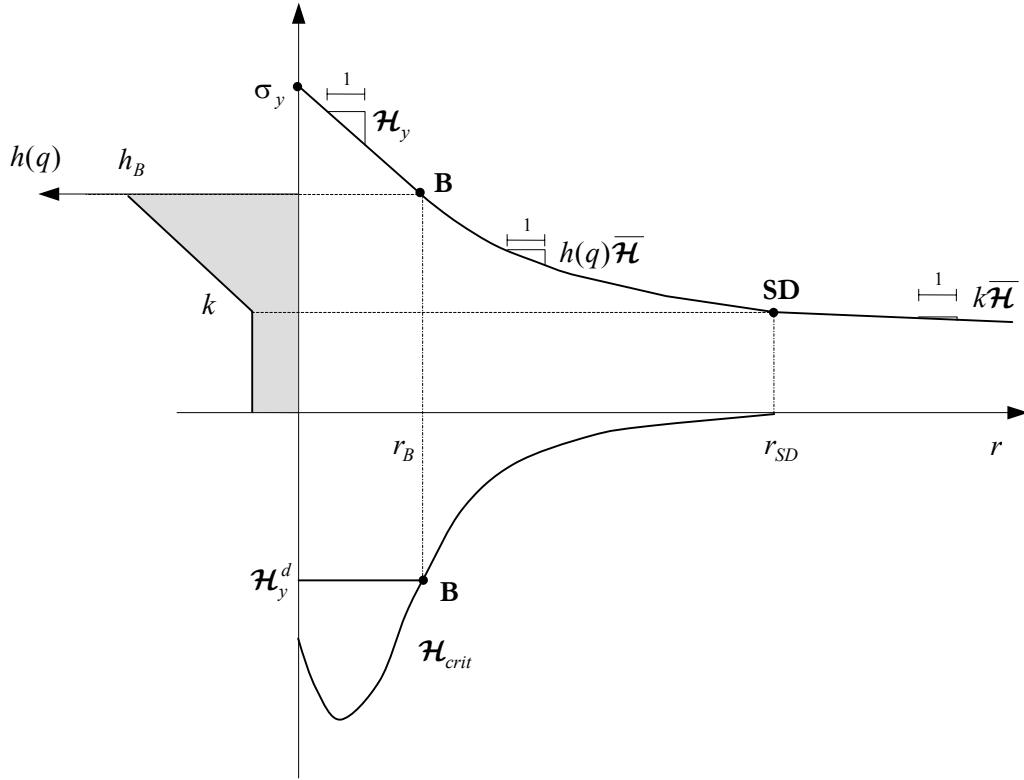

Figure 2.23: Bandwidth law, Oliver *et al.* (1999).

Remark 2.3: The drawback of this variable bandwidth model (VBM) is that when a pre-established law is used, we must establish a priori a variable $\wp$ described in Figure 2.22. This variable indicates the length of the transition between the Bifurcation point and the strong discontinuity point. $\wp$ varies from material to material and for different stress states, and sometimes, when this variable has a too small value, reloading can be observed. □

2.4.7.2 Automatic VBM

Here, an alternative model is proposed, where the bandwidth h is obtained automatically without assuming any law, avoiding the necessity of variable $\wp$. Once the bifurcation point is detected an initial bandwidth h_B is obtained:

$$h_B = \frac{\mathcal{H}^d_{crit}}{\mathcal{H}^d_y} \tag{2.125}$$

Normal $\mathbf{N}_{crit}$ will be kept fixed from time t_B onward. On the other hand, we obtain $\widetilde{\mathcal{H}}^d_{crit}$ as function of $\mathbf{N}_{crit}$ (frozen at time $t = t_B$) and the current stress states; thus, we can define a new bandwidth as:

$$h = \frac{\widetilde{\mathcal{H}}^d_{crit}}{\mathcal{H}^d_y} \tag{2.126}$$

this process is used in the successive load steps until $\widetilde{\mathcal{H}}^d_{crit} \approx 0$ which is the necessary condition to induce a strong discontinuity according to Remark 2.2. At this point the strong discontinuity regime begins, *i.e.,* the point **SD** of Figure 2.23, thus $h \to k \ll 1$.

2.4.8 Fracture Energy

It is illustrative to compute the energy release for the formation of the discontinuity during the time interval $t \in (0, t_\infty]$, where t_∞ stands for the time at which complete decohesion of the crack is achieved $(\sigma \big|_{t=t_\infty} = 0)$, for a one-dimensional bar. In virtue of the theorem of the expended power, and neglecting the kinetic energy (as corresponds to the quasistatic case), the external power input in the bar equals the stress power:

$$d\mathcal{W}(t) = \int_\mathcal{B} \sigma \, \dot{\varepsilon} \, dV = \int_\mathcal{B} \sigma \left(\dot{\bar{\varepsilon}} + \delta_\mathcal{S} \, [\![\dot{u}]\!] \right) dV \tag{2.127}$$

Now consider the Dirac's delta property:

$$d\mathcal{W}(t) = \int_{\mathcal{B} \setminus \mathcal{S}} \sigma \, \dot{\bar{\varepsilon}} \, dV + \int_\mathcal{S} \sigma \, [\![\dot{u}]\!] \, dA = A \int_0^l \frac{d}{dt} \left(\frac{\sigma^2}{2E} \right) dx + \sigma \, [\![\dot{u}]\!] A \tag{2.128}$$

Now, by integration along time, the total mechanical work $\mathcal{W}(t)$ can be computed as:

$$\mathcal{W} = \int_0^{t_\infty} d\mathcal{W}(t) \, dt = \int_0^{t_\infty} \left(A \int_0^l \frac{d}{dt} \left(\frac{\sigma^2}{2E} \right) dx + \sigma \, [\![\dot{u}]\!] A \right) dt = A \underbrace{\int_0^{t_\infty} \sigma \, [\![\dot{u}]\!] \, dt}_{G_f} = A\mathcal{G}_f \tag{2.129}$$

which identifies the area under the discrete $\sigma_\mathcal{S} - [\![u]\!]$ constitutive law of Figure 2.24 as the energy release per unit surface to produce the discontinuity.
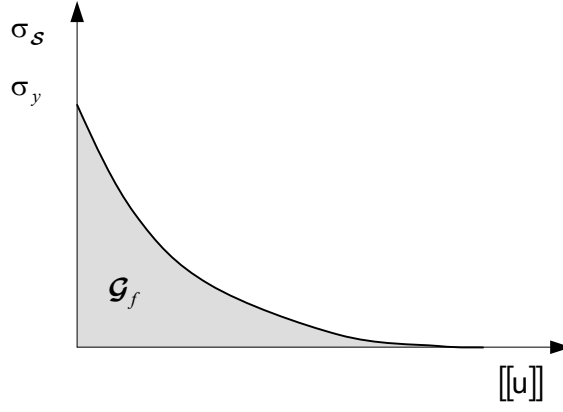
Figure 2.24: Discrete $\sigma_{\mathcal{S}} - [\![u]\!]$ constitutive model.

Now we focus on the continuum constitutive model and the discontinuity interface $\mathcal{S}$. For the loading conditions occurring there, it can be readily shown that both couples $(\sigma, \dot{\varepsilon})$ and $(q, (1/E)\dot{r})$ are conjugate variables for the stress power so that we can write:

$$\sigma \dot{\varepsilon}_S = \sigma_S \dot{\varepsilon}_S = q_s \frac{1}{E} \dot{r}_s \tag{2.130}$$

Now, substituting the k-regularized strong discontinuity kinematics $\left(\varepsilon = \overline{\varepsilon} + \frac{1}{k}[\![u]\!] \right)$ and the regularized hardening softening law from (2.95) $\dot{q}_s = \overline{\mathcal{H}}^d \dot{\overline{\alpha}}$ into equation (2.130) yields:

$$\sigma \dot{\varepsilon}_S = \sigma\left(\dot{\overline{\varepsilon}} + \frac{1}{k}[\![\dot{u}]\!]\right) = q_s \frac{1}{E}\dot{r}_s = \frac{1}{kE\overline{\mathcal{H}}^d} \dot{q}_s q_s = \frac{1}{kE\overline{\mathcal{H}}^d} \frac{\mathrm{d}}{\mathrm{d}t}\left(\frac{1}{2}q_s^2\right)$$

$$\tag{2.131}$$

$$\Rightarrow \lim_{k \to 0} k\sigma \dot{\varepsilon}_{\mathcal{S}} = \sigma[\![\dot{u}]\!] = \frac{1}{E\overline{\mathcal{H}}^d} \frac{\mathrm{d}}{\mathrm{d}t}\left(\frac{1}{2}q_s^2\right)$$

therefore the fracture energy in equation (2.129) can be computed as:

$$\mathcal{G}_f = \int_0^{t_\infty} \sigma[\![\dot{u}]\!]\,\mathrm{d}t = \int_0^{t_\infty} \frac{1}{E\overline{\mathcal{H}}^d}\frac{\mathrm{d}}{\mathrm{d}t}\left(\frac{1}{2}q^2\right)\mathrm{d}t = \frac{1}{E\overline{\mathcal{H}}^d}\left[\frac{1}{2}q^2\right]_{q=q_0=\sigma_y}^{q=q_\infty=0} = -\frac{1}{2}\frac{\sigma_y^2}{E\overline{\mathcal{H}}^d}$$

$$\tag{2.132}$$

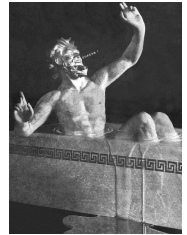$$\Rightarrow \overline{\mathcal{H}}^d = -\frac{1}{2}\frac{\sigma_y^2}{E\mathcal{G}_f}$$

where, for the sake of simplicity, a constant value for $\overline{\mathcal{H}}^d$ has been considered (linear softening). The above equation states the material property character of the discrete softening parameter $\overline{\mathcal{H}}^d$ which can be characterized in terms of the fracture mechanics properties: σ_y, E and $\mathcal{G}_f$.

3
Material Bifurcation

3.1 Introduction

In the field of structural engineering, bifurcation theory has been extensively applied to geometrical non-linearity problems, *e.g.,* stability problems involving buckling, as well as constitutive non-linearity, *i.e.,* material instability phenomena (material bifurcation).

In this chapter we will tackle the problem of localization as an instability in materials in the spirit of Rudnicki&Rice(1975): " *…Localization can be understood as an instability in the macroscopic constitutive description of inelastic deformation of the material…*". The main aim here is to obtain general explicit expressions for the critical failure direction and the critical hardening modulus (Willam(2000)) corresponding to the best-known classical continuum constitutive models (namely, continuum damage and plasticity models). Then, specific expressions for some constitutive models will be obtained as particular cases of the above mentioned general expressions. To reach this aim, the ellipticity condition of the constitutive tangent operator will play a determinant role.

3.2 Historical aspects on localization

The basic principle of localization was first proposed by Hadamard(1903) using classical material stability concepts. In 1952 Drucker proposed that a material is stable if the second-order work density is positive, resulting in a sufficient condition for the uniqueness of the solution:

$$\mathrm{d}^2 \mathscr{W} = \frac{1}{2}\dot{\boldsymbol{\varepsilon}} : \dot{\boldsymbol{\sigma}} = \frac{1}{2}\dot{\boldsymbol{\varepsilon}} : \mathbb{C} : \dot{\boldsymbol{\varepsilon}} > 0 \qquad (3.1)$$

for any arbitrary value of $\dot{\boldsymbol{\varepsilon}} \neq 0$. This criterion was further developed by Hill(1958) and Drucker(1959), Maier&Hueckel(1979), Runesson&Mroz(1989), Bigoni&Hueckel(1991), and others. Hill(1958) showed that $\dot{\boldsymbol{\varepsilon}} : \dot{\boldsymbol{\sigma}} = 0$ is a necessary condition for any type of bifurcation and loss of uniqueness.

For the associated plasticity case, where $\mathbb{C}$ is symmetric, the nullity of equation (3.1) only takes place when $\mathbb{C}$ is singular, and the result is that for associated models localization cannot occur in hardening regime.

Following Hadamard(1903), Thomas(1961) applied this theory to elastoplastic solids using wave propagation analyses to associate localization with stationary waves. Mandel(1966) was inclined to study the tangent material operator $\mathbb{C}$ to establish a localization criterion. Mandel(1964) determined the critical value of the hardening modulus for a Mohr material assuming the general three-dimensional nonassociated plasticity theory.

Rudnicki&Rice(1975) used Lagrange multipliers to obtain an explicit expression for the critical conditions of the hardening modulus for localization in pressure-sensitive dilatant materials in the setting of infinitesimal theory and showed that the inclusion of a nonassociated flow rule and a vertex-like yield surface into a Drucker-Prager model strongly influences its prediction of localization.

A critical hardening modulus as well as the direction of the shear planes using plane stress and plane strain for a Mohr-Coulomb material was obtained by Runesson *et al.*(1991). In Ottosen&Runesson(1991a) a spectral analysis of the acceleration wave problem in general elasto-plastic materials was carried out, and an explicit expression for the eigenvalues and eigenvectors of the localization tensor was obtained (see also Bigoni&Hueckel(1991), and Runesson *et al.* (1991)).

3.3 Continuous and discontinuous bifurcation

In the work by Rice&Rudnick(1980), conditions for strain localization in a planar band were derived (see Figure 3.1). They started by considering a homogeneous solid sustaining a uniform stress $\boldsymbol{\sigma}_\mathcal{B}$.

Restricting the analysis to small deformation settings, the development of a localized band, see Figure 3.1, entails the following kinematical condition:

$$\dot{\boldsymbol{\varepsilon}}_{\mathcal{S}} = \dot{\boldsymbol{\varepsilon}}_{\mathcal{B}\backslash\mathcal{S}} + \left(\mathbf{M} \otimes \mathbf{N}\right)^{sym} \tag{3.2}$$

where $\dot{\boldsymbol{\varepsilon}}_{\mathcal{S}}$ and $\dot{\boldsymbol{\varepsilon}}_{\mathcal{B}\backslash\mathcal{S}}$ are the symmetric strain rates inside and outside the band, respectively, $\mathbf{N}$ is the unit vector normal to the localized band, and $\mathbf{M}$, which is a function of bandwidth h, stands for the vector defining the direction of the velocity jump.
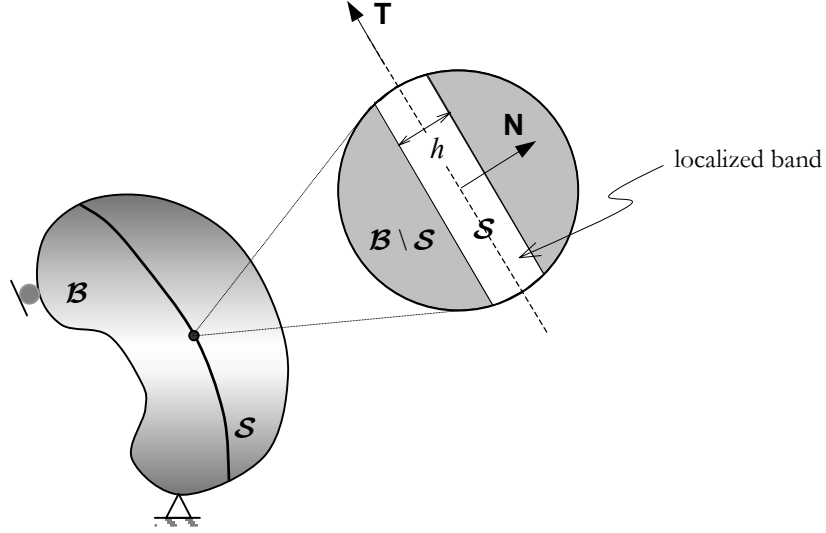
Figure 3.1: Planar localization band.

Applying the traction vector continuity:

$$\mathbf{N} \cdot \left(\dot{\boldsymbol{\sigma}}_{\mathcal{B}\backslash\mathcal{S}} - \dot{\boldsymbol{\sigma}}_{\mathcal{S}}\right) = \mathbf{0} \tag{3.3}$$

we can obtain the following expression:

$$\left(\mathbf{N} \cdot \mathbb{C}_{\mathcal{S}} \cdot \mathbf{N}\right) \cdot \mathbf{M} = \mathbf{N} \cdot \left(\mathbb{C}_{\mathcal{B}\backslash\mathcal{S}} - \mathbb{C}_{\mathcal{S}}\right) : \dot{\boldsymbol{\varepsilon}}_{\mathcal{B}\backslash\mathcal{S}} \tag{3.4}$$

where $\mathbb{C}_{\mathcal{S}}$ and $\mathbb{C}_{\mathcal{B}\backslash\mathcal{S}}$ are the constitutive tensor inside and outside the localization band, respectively.

Rice&Rudnicki(1980) distinguished between continuous bifurcation and discontinuous bifurcation, depending on whether $\mathbb{C}_{\mathcal{S}} = \mathbb{C}_{\mathcal{B}\backslash\mathcal{S}}$ or $\mathbb{C}_{\mathcal{S}} \neq \mathbb{C}_{\mathcal{B}\backslash\mathcal{S}}$, respectively; namely:

- Continuous bifurcation (Plastic-Plastic localization) $\rightarrow \mathbb{C}_{\mathcal{S}} = \mathbb{C}_{\mathcal{B}\backslash\mathcal{S}}$;

- Discontinuous bifurcation (Elastic-Plastic localization) $\rightarrow \mathbb{C}_{\mathcal{S}} \neq \mathbb{C}_{\mathcal{B}\backslash\mathcal{S}}$.

Continuous bifurcation

In the case of continuous bifurcation ($\mathbb{C}_{\mathcal{S}} = \mathbb{C}_{\mathcal{B} \setminus \mathcal{S}}$), *i.e.*, the material inside and outside of the localization band remain in loading, equation (3.4) becomes:

$$(\mathbf{N} \cdot \mathbb{C}_{\mathcal{S}} \cdot \mathbf{N}) \cdot \mathbf{M} = \mathbf{0} \tag{3.5}$$

The localization condition is satisfied when the solution of the above equation is different from the trivial solution $\mathbf{M} = \mathbf{0}$, which entails:

$$\det(\mathbf{N} \cdot \mathbb{C}_{\mathcal{S}} \cdot \mathbf{N}) = 0 \tag{3.6}$$

For the case of elastoplasticity, the tangential constitutive operator for the plastic loading case is given by:

$$\mathbb{C}_{\mathcal{S}} = \mathbb{C}^e - \frac{\mathbb{C}^e : \mathbf{m} \otimes \mathbf{n} : \mathbb{C}^e}{\mathcal{H}_{cont.}^p + \mathbf{n} : \mathbb{C}^e : \mathbf{m}} \tag{3.7}$$

where $\mathbb{C}^e$ is the elastic tensor, $\mathcal{H}_{cont.}^p$ is the plastic modulus, and $\mathbf{n}$ and $\mathbf{m}$ are the normal to the yield surface and to the plastic potential surface, respectively. Rice(1976) obtained the hardening modulus $\mathcal{H}_{cont.}^p$ corresponding to condition (3.6):

$$\frac{\mathcal{H}_{cont.}^p}{2G} = 2\mathbf{N} \cdot \mathbf{m} \cdot \mathbf{n} \cdot \mathbf{N} - (\mathbf{N} \cdot \mathbf{m} \cdot \mathbf{N})(\mathbf{N} \cdot \mathbf{n} \cdot \mathbf{N}) - \mathbf{m} : \mathbf{n} - \frac{\nu}{1-\nu}(\mathbf{N} \cdot \mathbf{m} \cdot \mathbf{N} - \mathrm{Tr}(\mathbf{m}))(\mathbf{N} \cdot \mathbf{n} \cdot \mathbf{N} - \mathrm{Tr}(\mathbf{n})) \tag{3.8}$$

where ν denotes the Poisson's ratio; G is the elastic shear modulus and $\mathrm{Tr}(\bullet)$ stands for the trace of $(\bullet)$.

Discontinuous bifurcation

A common observation in experiments is that the constitutive response at localization is not continuous; that is, the material outside the localized zone apparently does not continue loading, but rather unloads elastically. In the case of discontinuous bifurcations ($\mathbb{C}_{\mathcal{S}} \neq \mathbb{C}_{\mathcal{B} \setminus \mathcal{S}}$), provided that $(\mathbf{N} \cdot \mathbb{C}_{\mathcal{S}} \cdot \mathbf{N})$ can be inverted, the non trivial solutions will be:

$$\mathbf{M}_D = (\mathbf{N} \cdot \mathbb{C}_{\mathcal{S}} \cdot \mathbf{N})^{-1} \cdot \left[\mathbf{N} \cdot (\mathbb{C}_{\mathcal{B} \setminus \mathcal{S}} - \mathbb{C}_{\mathcal{S}}) : \dot{\boldsymbol{\varepsilon}}_{\mathcal{B} \setminus \mathcal{S}} \right] \tag{3.9}$$

Rice&Rudnicki(1980) searched the conditions for which the solution of (3.9) corresponds to continued plastic loading in the localized band when there is elastic unloading outside this zone. The condition obtained (*i.e.*, the condition for discontinuous bifurcation) was the following:

$$\frac{\mathcal{H}^p + \mathbf{n} : \mathbb{C}^e : \mathbf{m}}{\mathcal{H}^p - \mathcal{H}_{cont.}^p} < 0 \tag{3.10}$$

They concluded that localization with elastic unloading outside the localized zone of non-uniform deformation is only possible when $\mathcal{H}^p < \mathcal{H}_{cont.}^p$. Also, due to the fact that $\mathcal{H}^p$ decreases in value as the plastic deformations increase, the above inequality means that localization with elastic unloading outside the band takes place when the condition for

continuous bifurcation ($\mathcal{H}^p = \mathcal{H}^p_{cont.}$) is fulfilled for the first time. Consequently, continuous bifurcation sets the lower limit to the range of discontinuous bifurcation.

Based on the above analysis, the condition for continuous bifurcation, regarded as a lower limit of the discontinuous bifurcation scenario, will be adopted for further developments in this work, *i.e.*, the case when the system of equations:

$$\mathbf{Q(N)} \cdot \mathbf{M} = \mathbf{0} \tag{3.11}$$

has a nontrivial solution $\mathbf{M} \neq \mathbf{0}$, Ottosen&Runesson(1991). Equation (3.11) is the so called strain localization condition, where $\mathbf{Q(N)} = (\mathbf{N} \cdot \mathbb{C}_S \cdot \mathbf{N})$, and $\mathbf{M}$ is known as polarization direction. Thus, we can say that a necessary condition for the appearance of localization is

$$\det[\mathbf{Q(N)}] = \mathbf{0} \tag{3.12}$$

which is known as the Rice's criterion, characterizing the discontinuous failure, *Rizzi et al.* (1995).

Strong ellipticity condition

Here we present the definition of strong ellipticity that will be used throughout this work.

If for all vectors $\mathbf{N}$ and $\mathbf{M}$ with $\mathbf{N} \otimes \mathbf{M} \neq 0$, the inequality

$$(\mathbf{N} \otimes \mathbf{M}) : \mathbb{C} : (\mathbf{N} \otimes \mathbf{M}) > 0 \tag{3.13}$$

holds, then it is said that the tangential operator $\mathbb{C}$ is *strongly elliptic*. Rearranged, this inequality can be written as:

$$\mathbf{M} \cdot \mathbf{Q(N)} \cdot \mathbf{M} > 0 \tag{3.14}$$

where $\mathbf{Q} = \mathbf{N} \cdot \mathbb{C} \cdot \mathbf{N}$ is a second-order tensor known in literature as the Tangent Acoustic Tensor. By analogy with the theory of wave propagation, the eigenvalues of $\mathbf{Q(N)}$ are the wave propagation velocities, $\mathbf{N}$ is the propagation direction and $\mathbf{M}$ is the polarization direction.

The pair $(\mathbf{N}, \mathbf{M})$ indicates the orientation and nature of the discontinuity, *i.e.*, opening when $\mathbf{N}$ is parallel to $\mathbf{M}$, shear when $\mathbf{N}$ is orthogonal to $\mathbf{M}$, or the combination of both (see Figure 3.2).

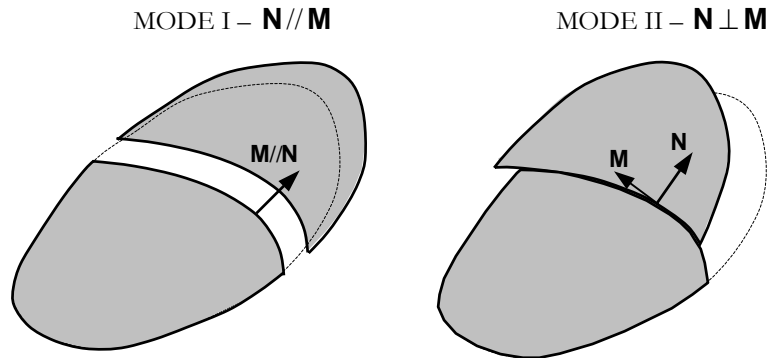MODE I – $\mathbf{N} // \mathbf{M}$ MODE II – $\mathbf{N} \perp \mathbf{M}$

Figure 3.2: Nature of the discontinuity.

An inequality weaker than (3.14) is:

$$\mathbf{M} \cdot \mathbf{Q(N)} \cdot \mathbf{M} \equiv (\mathbf{N} \otimes \mathbf{M}) : \mathbb{C} : (\mathbf{N} \otimes \mathbf{M}) \geq 0 \tag{3.15}$$

known as *Hadamard's conditions* (or *Legendre-Hadamard*), Ogden (1943).

Ellipticity condition

If $\mathbf{Q(N)}$ is symmetric, condition (3.14) will be violated if, for some $\mathbf{N}$, there exists a $\mathbf{M} \neq \mathbf{0}$ such that

$$\mathbf{Q(N)} \cdot \mathbf{M} = 0 \tag{3.16}$$

that is:

$$\mathbf{Q(N)} \cdot \mathbf{M} = 0 \quad \Rightarrow \quad \det[\mathbf{Q(N)}] = 0 \tag{3.17}$$

Condition (3.14) means that tensor $\mathbf{Q(N)}$ is positive definite for all $\mathbf{N} \neq \mathbf{0}$ implying that uniqueness and stability is guaranteed.

When the constitutive tangent operator has major and minor symmetries, the so-called ellipticity condition is satisfied if

$$\det[\mathbf{Q(N)}] \neq 0 \tag{3.18}$$

Correspondingly, condition (3.16) is satisfied. One can note that strong ellipticity implies ellipticity with $\det[\mathbf{Q(N)}] > 0$, but the reciprocity is not generally true, nevertheless for certain constitutive laws ellipticity and strong ellipticity are equivalent. In Table 3.1 there is a summary of the concepts presented.

Remark 3.1: Uniform point-wise stability implies strong ellipticity, but not conversely. In the associated case the strong ellipticity condition reduces to the ellipticity condition $\det[\mathbf{Q(N)}] > 0$; $\forall \mathbf{N} \neq \mathbf{0}$. □

Table 3.1:

Summary of bifurcation criteria	
Criterion	**Condition**
Loss of strong ellipticity	$\mathbf{M} \cdot \mathbf{Q(N)} \cdot \mathbf{M} = 0$
Loss of ellipticity	$\mathbf{Q(N)} \cdot \mathbf{M} = 0$

$$\tag{3.19}$$

3.4 Material bifurcation condition

Let us consider a material whose behavior is described by a constitutive model characterized by

- An inelastic tangent constitutive tensor, $\mathbb{C}^{in}$ (or tangent material operator), whose expression reads:

$$\mathbb{C}^{in} = \xi\mathbb{C}^e - \mathcal{K}\left(\mathbb{C}^e : \mathbf{m} \otimes \mathbf{n} : \mathbb{C}^e\right) \qquad (3.20)$$

where:

MODELS	
DAMAGE	**PLASTICITY**
$\xi = \dfrac{q}{r} = (1-d)$	$\xi = 1$
$\mathcal{K} = \dfrac{q(r) - \mathcal{H}^d r}{r^3}$	$\mathcal{K} = \dfrac{1}{\mathcal{H}^p + \mathbf{n} : \mathbb{C}^e : \mathbf{m}}$

$$(3.21)$$

with:

- $\mathbf{n}$: the flow plastic, normal to the Yield Function ($\mathcal{F}$), defined as $\mathbf{n} = \dfrac{\partial \mathcal{F}}{\partial \boldsymbol{\sigma}}$ (gradient of the Yield Function);

- $\mathbf{m}$: the flow of the plastic potential, which is normal to the Plastic Potential ($\mathcal{G}$), defined as $\mathbf{m} = \dfrac{\partial \mathcal{G}}{\partial \boldsymbol{\sigma}}$ (gradient of the Plastic Potential).

As mentioned above, the following analysis will be performed from a general point of view, and, later, it will be particularized for some specific cases. As point of departure we will analyze the acoustic tensor, $\mathbf{Q(N)}$, in order to obtain the value of $\mathbf{N}$ that minimizes $\det[\mathbf{Q(N)}]$. Using equation (3.20), the acoustic tensor can be written as:

$$\mathbf{Q(N)} = \xi\mathbf{N} \cdot \mathbb{C}^e \cdot \mathbf{N} - \mathcal{K}\,\mathbf{N} \cdot \left(\mathbb{C}^e : \mathbf{m} \otimes \mathbf{n} : \mathbb{C}^e\right) \cdot \mathbf{N} \qquad (3.22)$$

Applying the definition of the standard fourth-order isotropic elastic modulus tensor in function of Lamé's parameters (λ, μ), *i.e.:* $\mathbb{C}^e = 2\mu\mathbb{I} + \lambda(\mathbf{1} \otimes \mathbf{1})$ (see Appendix A.5) equation (3.22) can be rewritten in the following way:

$$\mathbf{Q(N)} = \xi\left\{ \mathbf{Q}^e - \frac{\mathcal{K}}{\xi}\underbrace{\left[\lambda\,\mathbf{N}\,\mathrm{Tr}(\mathbf{m}) + 2\mu\,\mathbf{N} \cdot \mathbf{m}\right]}_{\hat{\mathbf{c}}} \otimes \underbrace{\left[\lambda\,\mathbf{N}\,\mathrm{Tr}(\mathbf{n}) + 2\mu\,\mathbf{N} \cdot \mathbf{n}\right]}_{\hat{\mathbf{b}}} \right\} \qquad (3.23)$$

where $\mathbf{Q}^e$ is the elastic acoustic tensor (see Appendix A.5.2) and $\mathsf{Tr}(\bullet)$ stands for the trace of $(\bullet)$. Thus, $\mathsf{Tr}(\mathbf{m}) = m_{ii} = m_{11} + m_{22} + m_{33}$ and $\mathsf{Tr}(\mathbf{n}) = n_{ii} = n_{11} + n_{22} + n_{33}$.

Making use of a change of variables, we can write equation (3.23) as:

$$\mathbf{Q} = \xi \left\{ \mathbf{Q}^e - \frac{\mathcal{K}}{\xi} \hat{\mathbf{c}} \otimes \hat{\mathbf{b}} \right\} \quad \therefore \quad \mathbf{Q} = \xi \mathbf{Q}^e \left\{ \mathbf{1} - \frac{\mathcal{K}}{\xi} \hat{\mathbf{a}} \otimes \hat{\mathbf{b}} \right\} \tag{3.24}$$

where $\hat{\mathbf{a}} = \hat{\mathbf{c}} \cdot \mathbf{Q}^{e-1}$ and assuming that $\mathbf{Q}^e$ is positive definite we can say that:

$$\det(\mathbf{Q}) = \xi \det(\mathbf{Q}^e) \det \left\{ \mathbf{1} - \frac{\mathcal{K}}{\xi} \hat{\mathbf{a}} \otimes \hat{\mathbf{b}} \right\} \tag{3.25}$$

Using the property:

$$\det\left(\mathbf{1} + \hat{\mathbf{a}} \otimes \hat{\mathbf{b}} \right) = 1 + \hat{\mathbf{a}} \cdot \hat{\mathbf{b}} \tag{3.26}$$

we obtain:

$$\det \left\{ \mathbf{1} - \frac{\mathcal{K}}{\xi} \hat{\mathbf{a}} \otimes \hat{\mathbf{b}} \right\} = 1 - \frac{\mathcal{K}}{\xi} \hat{\mathbf{a}} \cdot \hat{\mathbf{b}} = 1 - \frac{\mathcal{K}}{\xi} \hat{\mathbf{c}} \cdot \mathbf{Q}^{e-1} \cdot \hat{\mathbf{b}} \tag{3.27}$$

Taking into account the fact that $\xi \det(\mathbf{Q}^e) > 0$ and equation (3.27), the bifurcation condition $\det[\mathbf{Q(N)}] = \mathbf{0}$ is reduced to solving the following problem:

$$1 - \frac{\mathcal{K}}{\xi} \hat{\mathbf{c}} \cdot \mathbf{Q}^{e-1} \cdot \hat{\mathbf{b}} = \mathbf{0} \tag{3.28}$$

Using the expressions of $\hat{\mathbf{c}}$ and $\hat{\mathbf{b}}$ laid out in equation (3.23), the above equation can be rewritten as:

$$1 - \frac{\mathcal{K}(\mathcal{H})}{\xi} \underbrace{\left[\lambda \, \mathbf{N} \, \mathsf{Tr}(\mathbf{m}) + 2\mu \, \mathbf{N} \cdot \mathbf{m} \right] \mathbf{Q}^{e-1} \left[\lambda \, \mathbf{N} \, \mathsf{Tr}(\mathbf{n}) + 2\mu \, \mathbf{N} \cdot \mathbf{n} \right]}_{Z(\mathbf{N})} = 0 \tag{3.29}$$

From equation (3.29) we can say:

$$\frac{\xi}{\mathcal{K}(\mathcal{H})} = Z(\mathbf{N}) \tag{3.30}$$

Expanding the value of $Z(\mathbf{N})$ in equation (3.29), it yields:

$$\begin{aligned} Z(\mathbf{N}) = {}& \lambda^2 \mathsf{Tr}(\mathbf{m})\mathsf{Tr}(\mathbf{n})(a+b) + 2\lambda\mu\mathsf{Tr}(\mathbf{n})(\mathbf{N}\cdot\mathbf{m}\cdot\mathbf{N})(a+b) + \\ & + 2\lambda\mu\mathsf{Tr}(\mathbf{m})(\mathbf{N}\cdot\mathbf{n}\cdot\mathbf{N})(a+b) + 4\mu^2 a(\mathbf{N}\cdot\mathbf{n}\cdot\mathbf{N}\cdot\mathbf{m}) + \\ & + 4\mu^2 b(\mathbf{N}\cdot\mathbf{m}\cdot\mathbf{N})(\mathbf{N}\cdot\mathbf{n}\cdot\mathbf{N}) \end{aligned} \tag{3.31}$$

where:

$$a = \frac{1}{\mu} \quad ; \quad b = -\frac{(\lambda + \mu)}{(\lambda + 2\mu)}\frac{1}{\mu} \tag{3.32}$$

The problem to be solved here is to find the critical normal vector $\mathbf{N}_{crit}$, which can be done by maximizing function (3.31). Once we have obtained the critical values $\mathbf{N}_{crit}$, we can obtain $\mathcal{H}_{crit}$ by replacing $\mathbf{N}_{crit}$ in equation (3.30). The expressions of $\mathcal{H}$ for damage and plasticity models are:

- Damage:

$$\mathcal{H}^d = (1-d)\left[1 - \frac{r^2}{Z(\mathbf{N})}\right] \tag{3.33}$$

- Plasticity:

$$\mathcal{H}^p = Z(\mathbf{N}) - \mathbf{n} : \mathbb{C}^e : \mathbf{m} \tag{3.34}$$

Thus, the problem of finding the critical normal $\mathbf{N}_{crit}$ can be stated as the following minimization problem:

$$\mathbf{N}_{crit} = \underset{\|\mathbf{N}\|=1}{\arg\ \min}\left\{\det[\mathbf{Q}(\mathbf{N})]\right\} \tag{3.35}$$

3.5 Critical values

In this section, we will explain how to obtain the critical values of the normal vector $\mathbf{N}_{crit}$ and the hardening parameter $\mathcal{H}_{crit}$, for the following cases:

- The general case, where the principal directions of $\mathbf{n}$ do not coincide with the principal directions of $\mathbf{m}$, ($\mathbf{n}$ and $\mathbf{m}$ are not colinear);

- The colinear case, where $\mathbf{n}$ and $\mathbf{m}$ are coaxials (the principal directions of $\mathbf{n}$ and $\mathbf{m}$ are coincident);

- The associated case, a particular coaxial case where $\mathbf{n} = \mathbf{m}$.

3.5.1 General case

3.5.1.1 Critical angle

Consider the tensor $\mathbf{n}$ expressed in its principal directions components[1]:

---

[1] For simplicity we use the same notation for the tensor ($\mathbf{n}$) and for its matrix representation.

$$\mathbf{n} = \begin{bmatrix} n_1 & 0 & 0 \\ 0 & n_2 & 0 \\ 0 & 0 & n_3 \end{bmatrix} \tag{3.36}$$

Tensor $\mathbf{m}$ is also expressed in the base formed by the principal directions of $\mathbf{n}$ for the non coaxial case:

$$\mathbf{m} = \begin{bmatrix} m_{11} & m_{12} & m_{13} \\ m_{12} & m_{22} & m_{23} \\ m_{13} & m_{23} & m_{33} \end{bmatrix} \tag{3.37}$$

Developing expression (3.31) and using the restriction $\|\mathbf{N}\| = 1$, we can obtain the following expression for $Z(\mathbf{N})$:

$$
\begin{aligned}
Z(\mathbf{N}) = \ & \overline{A}N_1^4 + \overline{B}N_2^4 + \overline{C}N_3^4 + \overline{D}N_1^3N_2 + \overline{F}N_1^3N_3 + \overline{G}N_2^2N_1^2 + \overline{H}N_1^2N_3^2 + \overline{I}N_3^2N_2^2 + \\
& + \overline{J}N_1^2N_2N_3 + \overline{K}N_2^2N_1N_3 + \overline{L}N_3^2N_2N_1 + \overline{O}N_2^3N_3 + \overline{P}N_2^3N_1 + \overline{Q}N_3^3N_1 + \\
& + \overline{R}N_3^3N_2 + \overline{S}N_1^2 + \overline{T}N_2^2 + \overline{U}N_3^2 + \overline{V}N_1N_2 + \overline{X}N_2N_3 + \overline{Y}N_2N_3 + \overline{W}
\end{aligned} \tag{3.38}
$$

where

$$\overline{A} = \beta(n_1 m_{11}) \; ; \qquad\qquad \overline{B} = \beta n_2 m_{22} \; ; \qquad\qquad \overline{C} = \beta n_3 m_{33} \; ;$$

$$\overline{D} = \beta[2m_{12}n_1] \; ; \qquad\qquad \overline{F} = \beta[2m_{13}n_1] \; ; \qquad\qquad \overline{G} = \beta[m_{22}n_1 + m_{11}n_2] \; ;$$

$$\overline{H} = \beta[m_{11}n_3 + m_{33}n_1] \; ; \quad \overline{I} = \beta[m_{22}n_3 + m_{33}n_2] \; ; \qquad \overline{J} = \beta[2m_{23}n_1] \; ;$$

$$\overline{K} = \beta[2m_{13}n_2] \; ; \qquad\qquad \overline{L} = \beta[2m_{12}n_3] \; ; \qquad\qquad \overline{O} = \beta[2m_{23}n_2] \; ;$$

$$\overline{P} = \beta[2m_{12}n_2] \; ; \qquad\qquad \overline{Q} = \beta[2m_{13}n_3] \; ; \qquad\qquad \overline{R} = \beta[2m_{23}n_3] \; ;$$

$$\overline{S} = \frac{2\lambda\mu}{(\lambda + 2\mu)}[\mathrm{Tr}(\mathbf{n})m_{11} + \mathrm{Tr}(\mathbf{m})n_1] + 4\mu[n_1 m_{11}] \; ;$$

$$\overline{T} = \frac{2\lambda\mu}{(\lambda + 2\mu)}[\mathrm{Tr}(\mathbf{n})m_{22} + \mathrm{Tr}(\mathbf{m})n_2] + 4\mu[n_2 m_{22}] \; ;$$

$$\overline{U} = \frac{2\lambda\mu}{(\lambda + 2\mu)}[\mathrm{Tr}(\mathbf{n})m_{33} + \mathrm{Tr}(\mathbf{m})n_{33}] + 4\mu[n_3 m_{33}] \; ;$$

$$\overline{V} = \frac{2\lambda\mu}{(\lambda + 2\mu)}[\mathrm{Tr}(\mathbf{n})m_{12}] + 4\mu[n_1 m_{12} + n_2 m_{12}] \; ;$$

$$\overline{X} = \frac{2\lambda\mu}{(\lambda + 2\mu)}[\mathrm{Tr}(\mathbf{n})m_{23}] + 4\mu[n_2 m_{23} + n_3 m_{23}] \; ;$$

$$\overline{Y} = \frac{2\lambda\mu}{(\lambda + 2\mu)}[\mathrm{Tr}(\mathbf{n})m_{13}] + 4\mu[n_1 m_{13} + n_3 m_{13}] \; ;$$

$$\overline{W} = \frac{\lambda^2 Tr(\mathbf{m})Tr(\mathbf{n})}{(\lambda + 2\mu)} \quad ; \quad \beta = -\frac{4\mu(\lambda + \mu)}{(\lambda + 2\mu)} \quad ;$$

The maximum and minimum values of $Z(\mathbf{N})$ can be obtained from (3.38) using the *Lagrange multiplier method*. The procedure consists of constructing the following function:

$$\Phi = Z(\mathbf{N}) - \hat{\lambda}(N_i N_i - 1) \tag{3.39}$$

where $\hat{\lambda}$ is the *Lagrange multiplier*. The solution for the critical direction will correspond to finding the values N_1, N_2 and N_3 which maximize $Z(\mathbf{N})$, with the restriction $\|\mathbf{N}\| = 1$. One way to achieve this would be solving the following set of equations:

$$\begin{cases} \dfrac{\partial Z}{\partial N_1} - 2\hat{\lambda}N_1 = 0 \\[2mm] \dfrac{\partial Z}{\partial N_2} - 2\hat{\lambda}N_2 = 0 \\[2mm] \dfrac{\partial Z}{\partial N_3} - 2\hat{\lambda}N_3 = 0 \\[2mm] N_1^2 + N_2^2 + N_3^2 = 1 \end{cases} \tag{3.40}$$

A numerical alternative would be to express $Z(\mathbf{N})$ in terms of α and $\hat{\phi}$ (see Figure 3.3), discretizing then α and $\hat{\phi}$ in order to check when $Z(\mathbf{N})$ reaches a maximum by sweeping the corresponding range of variations of α and $\hat{\phi}$. This has to be subsequently refined using one of the iterative gradient schemes, Ortiz(1987). The methodology has to be repeated at each step during the integration process at each quadrature point.

$$\begin{cases} N_1 = \cos\alpha\cos\hat{\phi} \\ N_2 = \sin\alpha\cos\hat{\phi} \\ N_3 = \sin\hat{\phi} \end{cases}$$

$$\|\mathbf{N}\| = 1$$
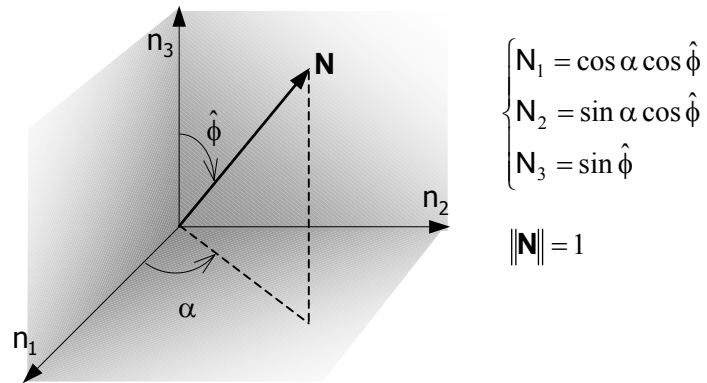
Figure 3.3: Normal $\mathbf{N}$ in the principal direction of $\mathbf{n}$.

3.5.1.2 Calculation of $\mathcal{H}_{crit}$

Once the value of the critical direction ($\mathbf{N}_{crit}$) is obtained, the calculation of the critical value of $\mathcal{H}$ consists of replacing $\mathbf{N}_{crit}$ into equation (3.30), that is:

$$\frac{\xi}{\mathcal{K}(\mathcal{H}_{crit})} = Z(\mathbf{N}_{crit}) \tag{3.41}$$

Resulting in:

Damage

$$\mathcal{H}^d(\mathbf{N}) = \xi\left(1 - \frac{r^2}{\hat{\mathbf{c}} \cdot \mathbf{Q}^{e-1} \cdot \hat{\mathbf{b}}}\right) \qquad \text{(a)}$$

$$\mathbf{N} = \mathbf{N}_{crit}$$

$$\Downarrow \tag{3.42}$$

$$\mathcal{H}^d_{crit} = \xi\left(1 - \frac{r^2}{Z(\mathbf{N}_{crit})}\right) \qquad \text{(b)}$$

Plasticity

$$\mathcal{H}^p(\mathbf{N}) = \hat{\mathbf{c}} \cdot \mathbf{Q}^{e-1} \cdot \hat{\mathbf{b}} - \mathbf{n} : \mathbb{C}^e : \mathbf{m} \qquad \text{(a)}$$

$$\mathbf{N} = \mathbf{N}_{crit}$$

$$\Downarrow \tag{3.43}$$

$$\mathcal{H}^p_{crit} = Z(\mathbf{N}_{crit}) - \mathbf{n} : \mathbb{C}^e : \mathbf{m} \qquad \text{(b)}$$

with

$$\mathbf{n} : \mathbb{C}^e : \mathbf{m} = 2\mu\,\mathbf{n} : \mathbf{m} + \lambda\,\text{Tr}(\mathbf{n})\,\text{Tr}(\mathbf{m}) \tag{3.44}$$

3.5.2 Case of colinearity between **n**, **m**

3.5.2.1 Non-associated case

For the coaxial non-associated case the principal directions of **n** coincide with the principal directions of **m**, but $\mathbf{n} \neq \mathbf{m}$.

3.5.2.1.1 Critical angle

In this case we assume the follwing format for the tensors **n** and **m** :

$$\mathbf{n} = \begin{bmatrix} n_1 & 0 & 0 \\ 0 & n_2 & 0 \\ 0 & 0 & n_3 \end{bmatrix} \quad ; \quad \mathbf{m} = \begin{bmatrix} m_1 & 0 & 0 \\ 0 & m_2 & 0 \\ 0 & 0 & m_3 \end{bmatrix} \tag{3.45}$$

Since entries $m_{12} = m_{13} = m_{23}$ are null, then the expression of $Z(\mathbf{N})$ can be rewritten as:

$$Z(\mathbf{N}) = \overline{A}N_1^4 + \overline{B}N_2^4 + \overline{C}N_3^4 + \overline{G}N_2^2N_1^2 + \overline{H}N_1^2N_3^2 + \overline{I}N_3^2N_2^2 + \overline{S}N_1^2 + \overline{T}N_2^2 + \overline{U}N_3^2 + \overline{W} \tag{3.46}$$

The relative maximums and minimums of function (3.46) are presented in Table 3.2, where the values of the direction $\mathbf{N}(\theta)$ are expressed in terms of the angle θ, which is defined with respect to the principal directions, see Figure 3.4. For instance, row $1-1$, in Table 3.2, indicates that the solution coincides with the first principal direction, *i.e.*, $\theta_1 = 0$, and row $2-3$ means that the solution lies in the plane generated by the second and the third principal directions and the angle with respect to the latter is equal to θ_{32}.

Table 3.2: Relative maximums and minimums of $Z(\mathbf{N})$.

PLANE	N_1	N_2	N_3	ANGLE	$Z(N)$
$1-1$	± 1.0	0.0	0.0	$\tan^2 \theta_1 = 0$	$\overline{A} + \overline{S} + \overline{W}$
$2-2$	0.0	± 1.0	0.0	$\tan^2 \theta_2 = 0$	$\overline{B} + \overline{T} + \overline{W}$
$3-3$	0.0	0.0	± 1.0	$\tan^2 \theta_3 = 0$	$\overline{C} + \overline{U} + \overline{W}$
$2-3$	0.0	$\pm\sqrt{\dfrac{-I}{2F}}$	$\pm\sqrt{1 + \dfrac{I}{2F}}$	$\tan^2 \theta_{32} = -\dfrac{2F+I}{I}$	$Z_{23} = T_3 - \dfrac{I^2}{4F}$
$1-3$	$\pm\sqrt{\dfrac{-\hat{G}}{2A}}$	0.0	$\pm\sqrt{1 + \dfrac{\hat{G}}{2A}}$	$\tan^2 \theta_{31} = -\dfrac{2A+\hat{G}}{\hat{G}}$	$Z_{13} = T_3 - \dfrac{\hat{G}^2}{4A}$
$1-2$	$\pm\sqrt{1 + \dfrac{\hat{H}}{2B}}$	$\pm\sqrt{\dfrac{-\hat{H}}{2B}}$	0.0	$\tan^2 \theta_{12} = -\dfrac{2B+\hat{H}}{\hat{H}}$	$Z_{12} = T_1 - \dfrac{\hat{H}^2}{4B}$

where

$$A = -\frac{4\mu(\lambda + \mu)}{(\lambda + 2\mu)} \left[(n_1 - n_3)(m_1 - m_3) \right]$$

$$B = -\frac{4\mu(\lambda + \mu)}{(\lambda + 2\mu)} \left[(n_1 - n_2)(m_1 - m_2) \right]$$

$$C = -\frac{4\mu(\lambda+\mu)}{(\lambda+2\mu)}[(m_1-m_3)(n_2-n_3)+(m_2-m_3)(n_1-n_3)]$$

$$F = -\frac{4\mu(\lambda+\mu)}{(\lambda+2\mu)}[(n_2-n_3)(m_2-m_3)]$$

$$\hat{G} = \frac{2\lambda\mu}{(\lambda+2\mu)}[\mathrm{Tr}(\mathbf{n})(m_1-m_3)+\mathrm{Tr}(\mathbf{m})(n_1-n_3)]+$$
$$-\frac{4\mu(\lambda+\mu)}{(\lambda+2\mu)}[m_3(n_1-n_3)+n_3(m_1-m_3)]+4\mu[n_1m_1-n_3m_3]$$

$$\hat{H} = \frac{2\lambda\mu}{(\lambda+2\mu)}[\mathrm{Tr}(\mathbf{n})(m_2-m_1)+\mathrm{Tr}(\mathbf{m})(n_2-n_1)]+$$
$$-\frac{4\mu(\lambda+\mu)}{(\lambda+2\mu)}[m_1(n_2-n_1)+n_1(m_2-m_1)]+4\mu[n_2m_2-n_1m_1]$$

$$I = \frac{2\lambda\mu}{(\lambda+2\mu)}[\mathrm{Tr}(\mathbf{n})(m_2-m_3)+\mathrm{Tr}(\mathbf{m})(n_2-n_3)]+$$
$$-\frac{4\mu(\lambda+\mu)}{(\lambda+2\mu)}[m_3(n_2-n_3)+n_3(m_2-m_3)]+4\mu[n_2m_2-n_3m_3]$$

$$T_3 = \frac{1}{(\lambda+2\mu)}[(\lambda\mathrm{Tr}(\mathbf{m})+2\mu m_3)(\lambda\mathrm{Tr}(\mathbf{n})+2\mu n_3)]$$

$$T_1 = \frac{1}{(\lambda+2\mu)}[(\lambda\mathrm{Tr}(\mathbf{m})+2\mu m_1)(\lambda\mathrm{Tr}(\mathbf{n})+2\mu n_1)]$$

Thus we can explicitly express the corresponding angles as:

- Angle on the plane $3-2$:

$$\begin{cases} \tan^2\theta_{32} = -\dfrac{[(4m_3-2m_2)n_3-2m_3n_2]\mu+[(m_3-m_2)n_1+(m_1-2m_2+4m_3)n_3-(2m_3+m_1)n_2]\lambda}{[(4m_2-2m_3)n_2-2m_2n_3]\mu+[(m_2-m_3)n_1+(m_1-2m_3+4m_2)n_2-(m_1+2m_2)n_3]\lambda} \\[12pt] \tan^2\theta_{32} = \dfrac{[(m_3-m_2)n_1+(n_3-n_2)m_1]\nu+(2n_3-n_2)m_3-m_2n_3}{[(m_2-m_3)n_1+(n_2-n_3)m_1]\nu+(2n_2-n_3)m_2-n_2m_3} \end{cases} \qquad (3.47)$$

- Angle on the plane $1-3$:

$$\begin{cases} \tan^2\theta_{13} = -\dfrac{[(4m_3-2m_1)n_3-2m_3n_1]\mu+[(m_3-m_1)n_2+(m_2-2m_1+4m_3)n_3-(2m_3+m_2)n_1]\lambda}{[(2m_3-4m_1)n_1+2m_1n_3]\mu+[(m_3-m_1)n_2+(-m_2+2m_3-4m_1)n_1+(m_2+2m_1)n_3]\lambda} \\[12pt] \tan^2\theta_{13} = \dfrac{[(m_3-m_1)n_2+(n_3-n_1)m_2]\nu+(2n_3-n_1)m_3-m_1n_3}{[(m_1-m_3)n_2+(n_1-n_3)m_2]\nu+(2n_1-n_3)m_1-n_1m_3} \end{cases} \qquad (3.48)$$

- Angle on the plane $1-2$:

$$
\begin{cases}
\tan^2 \theta_{12} = -\dfrac{\left[(4m_1 - 2m_2)n_1 - 2m_1 n_2\right]\mu + \left[(m_1 - m_2)n_3 + (m_3 - 2m_2 + 4m_1)n_1 - (2m_1 + m_3)n_2\right]\lambda}{\left[(2m_1 - 4m_2)n_2 + 2m_2 n_1\right]\mu + \left[(m_1 - m_2)n_3 + (-m_3 + 2m_1 - 4m_2)n_2 + (m_3 + 2m_1)n_1\right]\lambda} \\[4mm]
\tan^2 \theta_{12} = \dfrac{\left[(m_2 - m_1)n_3 + (n_2 - n_1)m_3\right]\nu - (2n_1 - n_2)m_1 - m_2 n_1}{\left[(m_1 - m_2)n_3 + (n_1 - n_2)m_3\right]\nu - (2n_2 - n_1)m_2 - n_2 m_1}
\end{cases}
\tag{3.49}
$$

It is interesting to observe that the critical angle does not depend on the Young's modulus (E).
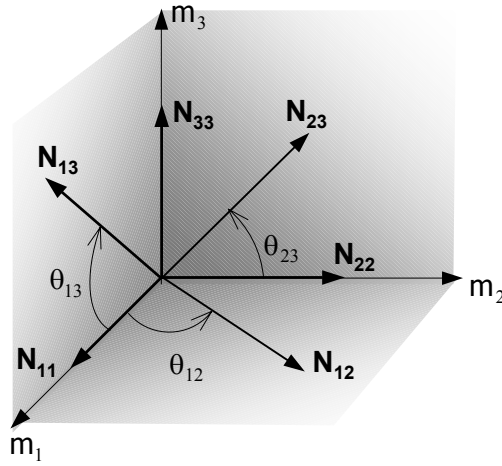
Figure 3.4: Normal **N** in the principal direction of **m**.

The function $Z(\mathbf{N})$ in equation (3.46) is a continuous surface having maximum and minimum relative values. The objective is to obtain the absolute maximum among them. The shape of this surface when $\mathbf{n} \neq \mathbf{m}$ is schematized in Figure 3.5 and Figure 3.6, with its maximum and minimum points. The values of N_1, N_2 and N_3 are expressed in spherical coordinates, that is, in terms of α and $\hat{\phi}$ (see Figure 3.3).
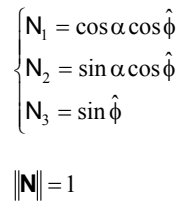
Figure 3.5: Surface $Z(\mathbf{N})$ - Case $\mathbf{n} \neq \mathbf{m}$ (Drucker-Prager non-associated).
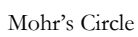
Figure 3.6: Surface $Z(\mathbf{N})$ - Case $\mathbf{n} = \mathbf{m}$ (Isotropic Damage Case).

3.5.2.1.2   Calculation of $\mathcal{H}_{crit}$

Damage

For the isotropic damage case $\mathcal{H}_{crit}^{d}$ is given by:

$$\mathcal{H}_{crit}^{d} = \xi\left(1 - \frac{r^2}{Z_{\max}(\mathbf{N})}\right) \tag{3.50}$$

where $Z_{\max}(\mathbf{N})$ is the maximum value from Table 3.2. Once $Z_{\max}(\mathbf{N})$ is obtained, it is possible to obtain $\mathbf{N}_{crit}$.

Plasticity

The values of $\mathcal{H}^{p}$ corresponding to the values of $Z(\mathbf{N})$ laying on the planes $2-3$, $1-3$, and $1-2$ according to the Table 3.2 are, respectively:

$$\mathcal{H}_{23}^{p} = -\frac{I^2}{4F} + \left(T_3 - \mathbf{n}:\mathbb{C}^e:\mathbf{m}\right) = -\frac{I^2}{4F} + \mathcal{P}_3 \tag{3.51}$$

$$\mathcal{H}_{13}^{p} = -\frac{\hat{G}^2}{4A} + \left(T_3 - \mathbf{n}:\mathbb{C}^e:\mathbf{m}\right) = -\frac{\hat{G}^2}{4A} + \mathcal{P}_3 \tag{3.52}$$

$$\mathcal{H}_{12}^{p} = -\frac{\hat{H}^2}{4B} + \left(T_1 - \mathbf{n}:\mathbb{C}^e:\mathbf{m}\right) = -\frac{\hat{H}^2}{4B} + \mathcal{P}_1 \tag{3.53}$$

where

$$\left\{\begin{array}{l} \mathcal{P}_3 = -\dfrac{2\mu}{(\lambda+\mu)}\left\{2(\lambda+\mu)(m_2 n_2 + m_1 n_1) + \lambda(m_2 n_1 + m_1 n_2)\right\} \hfill (3.54)\\[3ex] \mathcal{P}_3 = -\dfrac{E}{(1-\nu^2)}\left[\ \nu(m_2 n_1 + m_1 n_2) + (m_2 n_2 + m_1 n_1)\ \right] \hfill (3.55) \end{array}\right.$$

$$\mathcal{P}_1 = -\frac{E}{(1-\nu^2)}\left[\ \nu(m_2 n_3 + m_3 n_2) + (m_3 n_3 + m_2 n_2)\ \right] \tag{3.56}$$

$$\frac{I^2}{4F} = \frac{-E}{4(1-\nu^2)}\frac{\left[(m_2 - m_3)(\nu n_1 + n_2) + (n_2 - n_3)(\nu m_1 + m_2)\right]^2}{(m_2 - m_3)(n_2 - n_3)} \tag{3.57}$$

$$\frac{\hat{G}^2}{4A} = \frac{-E}{4(1-\nu^2)}\frac{\left[(m_1 - m_3)(\nu n_2 + n_1) + (n_1 - n_3)(\nu m_2 + m_1)\right]^2}{(m_1 - m_3)(n_1 - n_3)} \tag{3.58}$$

$$\frac{\hat{H}^2}{4B} = \frac{-E}{4(1-v^2)} \frac{\left[(m_1 - m_2)(vn_3 + n_2) + (n_1 - n_2)(vm_3 + m_2)\right]^2}{(m_1 - m_2)(n_1 - n_2)} \tag{3.59}$$

The variables: A, B, F, $\hat{G}$, $\hat{H}$, I, T_1, T_3 are the same as defined in the Table 3.2.

3.5.2.2 Associated case ($\mathbf{n} = \mathbf{m}$)

3.5.2.2.1 Geometrical interpretation – localization ellipse

Using equations (3.31) and (3.30) and after some mathematical manipulations we can obtain the following equation:

$$\boxed{\frac{(\Phi_N + m_0)^2}{\hat{A}^2} + \frac{\Sigma_N^2}{\hat{B}^2} = 1} \tag{3.60}$$

which defines the localization ellipse in the (Φ_N, Σ_N) space, where:

$$\Phi_N = \mathbf{N} \cdot \mathbf{m} \cdot \mathbf{N}; \quad m_0 = \frac{\lambda}{2\mu} \mathrm{Tr}(\mathbf{m}) = \frac{v}{(1-2v)} \mathrm{Tr}(\mathbf{m}) \tag{a}$$

$$\Sigma_N^2 = (\mathbf{N} \cdot \mathbf{m} \cdot \mathbf{N} \cdot \mathbf{m}) - \Phi_N^2 \tag{b}$$

$$\hat{A}^2 = \frac{(\lambda + 2\mu)\xi}{4\mu^2 \mathcal{K}} = \frac{2(1-v)}{(1-2v)} \hat{B}^2 \tag{c} \tag{3.61}$$

$$\hat{B}^2 = \frac{\xi}{4\mu \mathcal{K}} \tag{d}$$

m_0 determines the ellipse center, while $\hat{A}$ and $\hat{B}$ determine the half axes of the ellipse in the normal and tangential directions, respectively, Willam(2000). And ξ and $\mathcal{K}$ are given by expression (3.21). The geometrical properties of the localization ellipse are illustrated in Figure 3.7 together with the three Mohr's circles in the (Φ, Σ) space in terms of the eigenvalues of $\mathbf{m}$, Oliver (2002). Note that the center and the shape of the ellipse are not influenced by the plastic hardening modulus $\mathcal{H}(\mathbf{N})$. The hardening modulus only influences the size of the ellipse, Willam(2000).

As mentioned above, for a given stress state, $\mathcal{H}_{crit}$ corresponds to a maximum value of $\mathcal{H}$, *i.e.*:

$$\mathcal{H}_{crit} = \max[\mathcal{H}(\mathbf{N})] \tag{3.62}$$
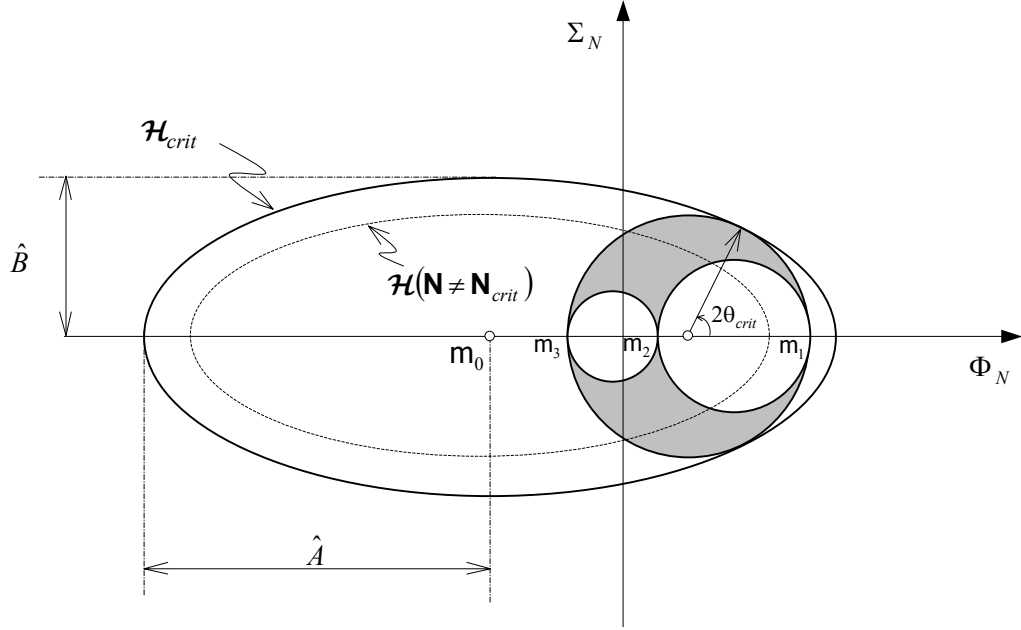
Figure 3.7: Localization ellipse and Mohr's circle.

With this interpretation we can conclude that the solution that furnishes the maximum ellipse will be the solution laying on the plane $1-3$ of the Table 3.2, *i.e.:* when $\mathsf{N}_2 = 0$. Thus the value of $Z(\mathbf{N}_{crit})$ is:

$$Z(\mathbf{N}_{crit}) = \frac{\left\{ \lambda^2 \left(\mathsf{Tr}(\mathbf{m})\right)^2 + \left[(m_2 - m_3)^2 + 2\mathsf{Tr}(\mathbf{m})(m_2 + m_3)\right] \lambda\mu + 2\mu^2\left(m_2^2 + m_3^2\right) \right\}}{(\lambda + \mu)} \qquad (3.63)$$

or, in terms of E and ν:

$$Z(\mathbf{N}_{crit}) = \frac{E}{(1+\nu)(1-2\nu)} \left\{ 2\,\nu m_1 \left[\nu m_1 + (m_2 - m_3)m_1 + m_2 m_3\right] + (1-\nu)\left(m_2^2 + m_3^2\right) \right\} \qquad (3.64)$$

3.5.2.2.2   Critical angle – Associated case ($\mathbf{n} = \mathbf{m}$)

The critical angle (see Figure 3.8) could be obtained by directly using equation (3.48) with $\mathbf{n} = \mathbf{m}$:

$$\tan^2 \theta_{crit} = -\frac{m_3 + \nu m_2}{m_1 + \nu m_2} \qquad (3.65)$$
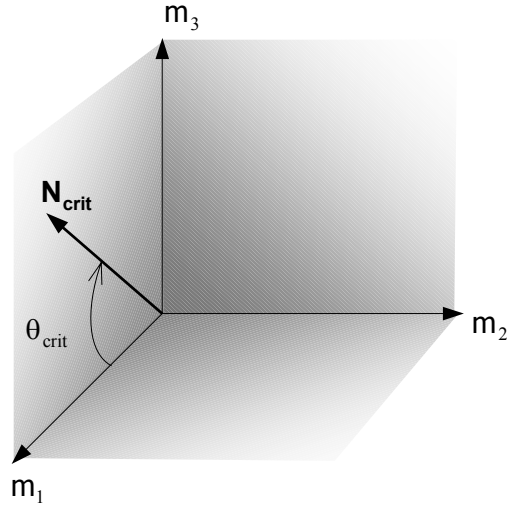
Figure 3.8: Normal **N** in principal direction of **m** - associated case.

3.5.2.2.3   Calculation of the $\mathcal{H}_{crit}$ – Associated case ($\mathbf{n} = \mathbf{m}$)

Damage

$$\mathcal{H}_{crit}^{d} = (1-d)\left[1 - \frac{(\lambda+\mu)r^2}{\left\{\lambda^2(\text{Tr}(\mathbf{m}))^2 + \left[(m_1 - m_3)^2 + 2\text{Tr}(\mathbf{m})(m_1 + m_3)\right]\lambda\mu + 2\mu^2(m_1^2 + m_3^2)\right\}}\right] \tag{3.66}$$

Plasticity

For the associated case $\mathbf{n} = \mathbf{m}$, one can obtain from equations (3.51) to (3.59) that:

$$\mathcal{H}_{23}^{p} = -\frac{I^2}{4F} + \mathcal{P}_3 = -\frac{(3\lambda + 2\mu)\mu}{(\lambda+\mu)}m_1^2 = -E\,m_1^2 \tag{3.67}$$

$$\boxed{\mathcal{H}_{crit}^{p} = \mathcal{H}_{13}^{p} = -\frac{\hat{G}^2}{4A} + \mathcal{P}_3 = -\frac{(3\lambda + 2\mu)\mu}{(\lambda+\mu)}m_2^2 = -E\,m_2^2} \tag{3.68}$$

$$\mathcal{H}_{12}^{p} = -\frac{\hat{H}^2}{4B} + \mathcal{P}_1 = -\frac{(3\lambda + 2\mu)\mu}{(\lambda+\mu)}m_3^2 = -E\,m_3^2 \tag{3.69}$$

Notice that the maximum value among (3.67), (3.68) and (3.69) is given by (3.68).

It can be shown that the solution $2-3$, $1-3$ and $1-2$ from Table 3.2 correspond to the localization ellipse which intercepts the Mohr's circle $\sigma_2 - \sigma_3$, $\sigma_1 - \sigma_3$ and $\sigma_1 - \sigma_3$, respectively.
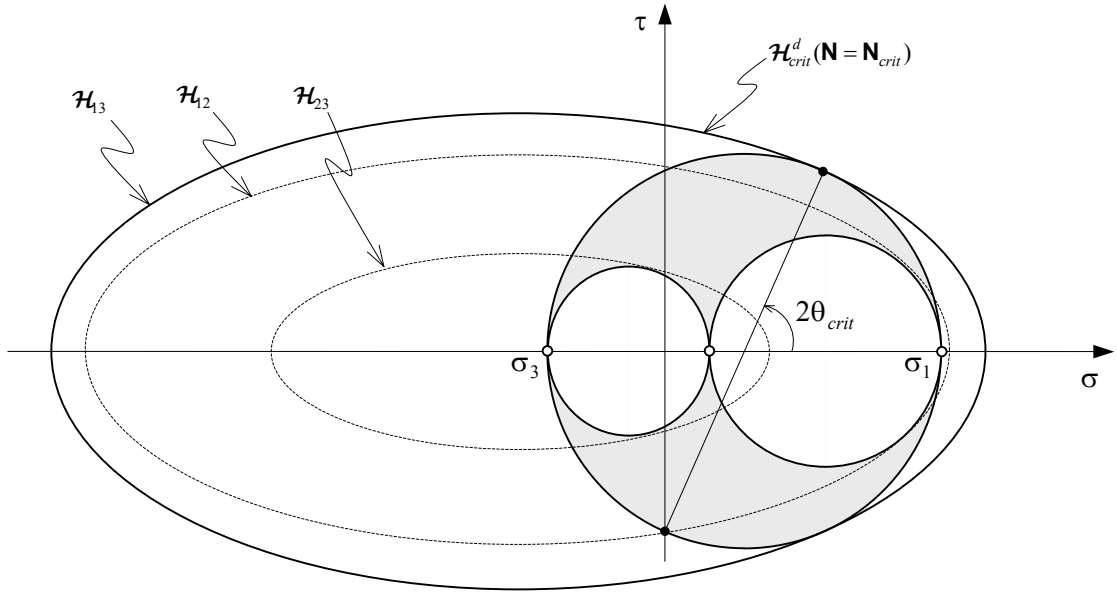
Figure 3.9: Localization ellipse.

3.6 Critical values for several constitutive models

In solid mechanics there are several families of constitutive equations. Some typical examples are elasticity, plasticity, viscoelasticity, continuum damage, and viscoplasticity. In this section, critical values for the localization direction and the hardening modulus for some of these models will be derived. Several classic models of plasticity and damage are employed with this purpose. A detailed study of their features is out of the scope of this work. For further details on the constitutive models presented here, the reader is referred to: Chen&Han(1988), Chen(1982), Potts&Zdravković (1999), Desai&Siriwardane(1984), Oller(2001), Willam(2000).

3.6.1   One-parameter models

3.6.1.1   Rankine criterion

This is a model defined by a *maximum-tensile-stress criterion* (see Figure 3.10) and was formulated by Rankine in 1876. It is characterized by only depending on a parameter. This can be sketched as:

$$\mathcal{F} = \mathcal{G} = \sigma_1 - \sigma_t = 0 \Rightarrow \mathbf{n} = \mathbf{m} = \begin{bmatrix} 1 & 0 & 0 \\ 0 & 0 & 0 \\ 0 & 0 & 0 \end{bmatrix} \tag{3.70}$$

where $\sigma_1 > \sigma_2 > \sigma_3$ (positive stress) are the principal stresses and σ_t is the tensile yield stress satisfying $\sigma_t > 0$.

Using the above yield criterion and substituting it into equation (3.65) and considering (3.68), we readily obtain the critical angle and $\mathcal{H}_{crit}^{p}$:

| Critical values for RANKINE Criterion	
critical angle	$\tan^2 \theta_{crit} = 0 \Rightarrow \begin{cases} \theta_1 = 0 \\ \theta_2 = 0 \end{cases}$
critical hardening modulus	$\mathcal{H}_{crit}^{p} = 0$

$$\tag{3.71}$$
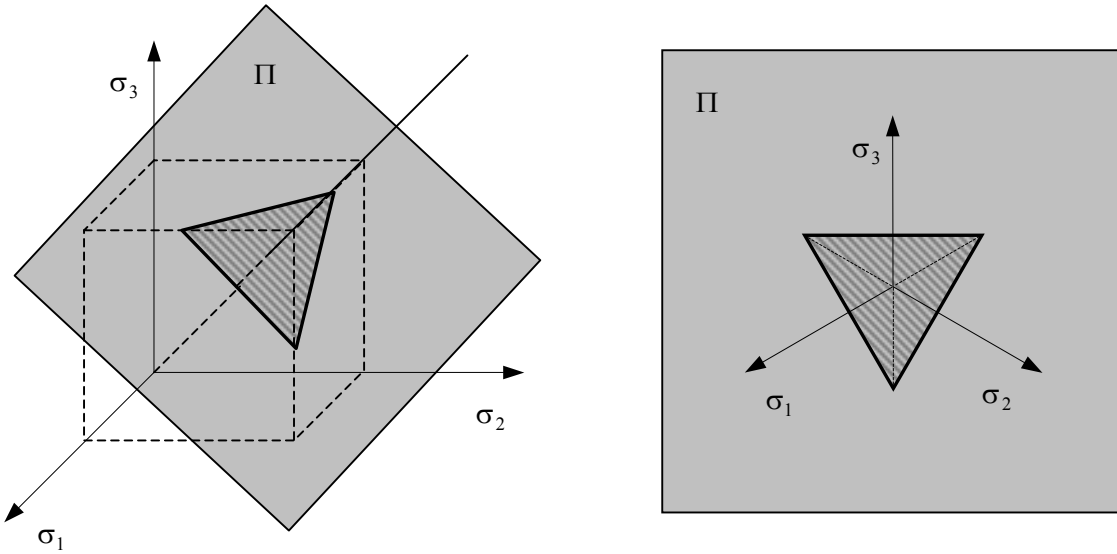
Figure 3.10: Rankine yield surface.

3.6.1.2 *von Mises yield* criterion

In this criterion the elastic limit is reached when the *octahedral shear stress* τ_{oct} reaches a critical value k (yield stress in pure shear), *i.e.:* $\tau_{oct} = \sqrt{\frac{2}{3}J_2} = \sqrt{\frac{2}{3}}k$. We can write the yield criterion as:

$$\mathcal{F}(J_2) = J_2 - k^2 = 0 \tag{3.72}$$

We will consider the J_2 plasticity model, associated von Mises, where:

$$\mathbf{n} = \mathbf{m} = \sqrt{\frac{3}{2}}\frac{\mathbf{s}}{\|\mathbf{s}\|} = \sqrt{\frac{3}{2}}\,\boldsymbol{\eta} \qquad \|\boldsymbol{\eta}\| = \sqrt{\boldsymbol{\eta} : \boldsymbol{\eta}} = 1 \tag{3.73}$$

and $\mathbf{s}$ is the *deviatoric stress tensor*[2], which is given by:

$$\mathbf{s} = \begin{bmatrix} \dfrac{2\sigma_1 - \sigma_2 - \sigma_3}{3} & 0 & 0 \\[2mm] 0 & \dfrac{2\sigma_2 - \sigma_1 - \sigma_3}{3} & 0 \\[2mm] 0 & 0 & \dfrac{2\sigma_3 - \sigma_1 - \sigma_2}{3} \end{bmatrix} \tag{3.74}$$

Its norm reads: $\|\mathbf{s}\| = \sqrt{\left(\sigma_1^2 + \sigma_2^2 + \sigma_3^2\right)}$.
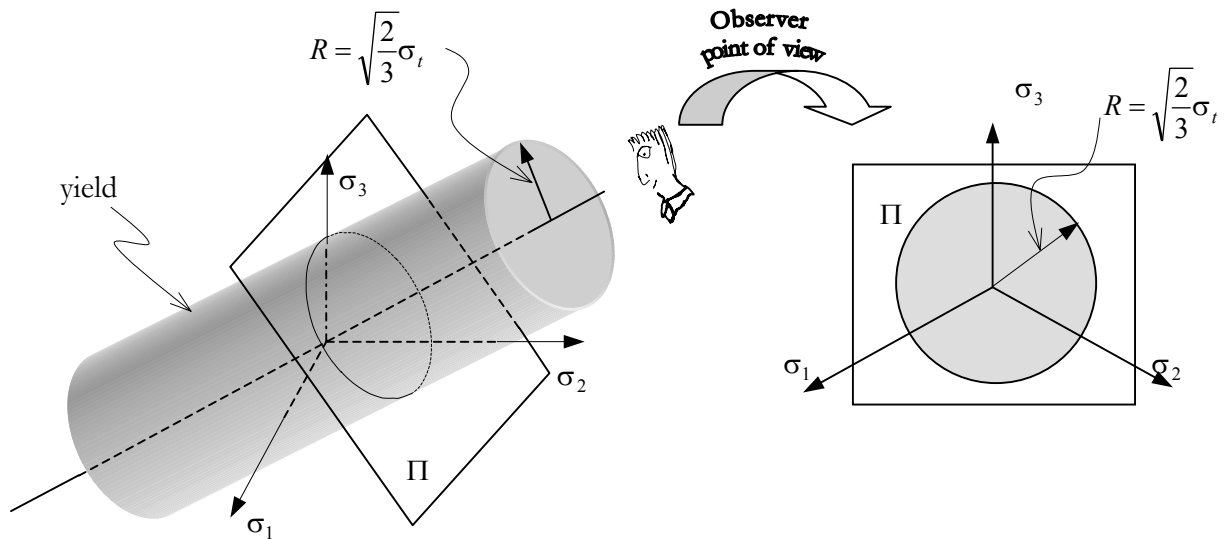
Figure 3.11: von Mises yield surface.

---

[2] $\boldsymbol{\sigma} = \mathbf{s} + p\mathbf{1}$, where $p = \frac{1}{3}\mathrm{Tr}(\boldsymbol{\sigma})$

According to equation (3.65) the critical angle is determined by:

$$\tan^2\theta_{crit} = -\frac{s_3 + \nu s_2}{s_1 + \nu s_2} = \frac{s_1 + (1-\nu)s_2}{s_1 + \nu s_2} = \frac{(-2\sigma_2 + \sigma_1 + \sigma_3)\nu + (\sigma_2 + \sigma_1 - 2\sigma_3)}{(2\sigma_2 - \sigma_1 - \sigma_3)\nu + (-\sigma_2 + 2\sigma_1 - \sigma_3)} \qquad (3.75)$$

To obtain $\mathcal{H}_{crit}^p$, equation (3.68) is used, resulting in:

$$\mathcal{H}_{crit}^p = -\frac{3E\,s_2^2}{2(s_1^2 + s_2^2 + s_3^2)} = -\frac{E(-2\sigma_2 + \sigma_1 + \sigma_3)^2}{4(\sigma_1^2 + \sigma_2^2 + \sigma_3^2 - \sigma_1\sigma_2 - \sigma_1\sigma_3 - \sigma_2\sigma_3)} \qquad (3.76)$$

Using the condition $\sigma_1 > \sigma_2 > \sigma_3$ we can conclude that:

$$\left.\begin{array}{l}(s_1^2 - s_2^2) = \dfrac{1}{3}\left[(\sigma_1 - \sigma_3)^2 - (\sigma_2 - \sigma_3)^2\right] > 0 \\[2mm] (s_3^2 - s_2^2) = \dfrac{1}{3}\left[(\sigma_1 - \sigma_3)^2 - (\sigma_2 - \sigma_1)^2\right] > 0\end{array}\right\} \Rightarrow \begin{array}{l} s_2^2 < s_1^2 \\[1mm] s_2^2 < s_3^2\end{array} \qquad (3.77)$$

It can be shown that the maximum value of $\mathcal{H}^p$ between (3.67), (3.68) and (3.69) is $\mathcal{H}_{13}^p$. Thus, we can summarize the following for the von Mises criterion:

CRITICAL VALUES FOR VON MISES CRITERION	
critical angle	$\tan^2\theta_{crit} = -\dfrac{s_3 + \nu s_2}{s_1 + \nu s_2}$
critical hardening modulus	$\mathcal{H}_{crit}^p = -\dfrac{3E s_2^2}{2(s_1^2 + s_2^2 + s_3^2)}$

$$(3.78)$$

Localization ellipse

Considering, $\mathbf{n} = \mathbf{m} = \alpha_1 \mathbf{s}$, with $\alpha_1 = \sqrt{\dfrac{3}{2}}\dfrac{1}{\|\mathbf{s}\|}$, we can obtain the equation of the localization ellipse:

$$\boxed{\frac{(\sigma_N - \sigma_0)^2}{\hat{A}^2} + \frac{\tau^2}{\hat{B}^2} = 1} \qquad (3.79)$$

with

$$\sigma_0 = p; \qquad \hat{A}^2 = \frac{2(1-\nu)}{(1-2\nu)}\hat{B}^2; \qquad \hat{B}^2 = \frac{\mathcal{H}^p}{4\mu\alpha_1^2} + J_2 \qquad (3.80)$$

where p is the *spherical* or *hydrostatic stress tensor*, and $2J_2 = (s_1^2 + s_2^2 + s_3^2)$.

3.6.1.3 Tresca yield criterion

This model is also known as the *maximum shearing stress* criterion, which has the following yield criterion:

$$\mathcal{F}(\sigma, \tau_{\max}) = \max\left[\frac{1}{2}\left|\sigma_i - \sigma_j\right|\right] - \tau_{\max} = 0 \tag{3.81}$$

from the condition $\sigma_1 > \sigma_2 > \sigma_3$ (positive stress), equation (3.81) results in $\max\left[\frac{1}{2}\left|\sigma_i - \sigma_j\right|\right] = \frac{1}{2}\left|\sigma_1 - \sigma_3\right|$, thus:

$$\mathbf{n} = \mathbf{m} = \begin{bmatrix} \frac{1}{2} & 0 & 0 \\ 0 & 0 & 0 \\ 0 & 0 & -\frac{1}{2} \end{bmatrix} \tag{3.82}$$

The critical angle and the critical hardening modulus are summarized as follows:

CRITICAL VALUES FOR TRESCA CRITERION	
critical angle	$\tan^2 \theta_{crit} = 1 \Rightarrow \begin{cases} \theta_1 = +45° \\ \theta_2 = -45° \end{cases}$
critical hardening modulus	$\mathcal{H}_{crit}^p = 0$

(3.83)
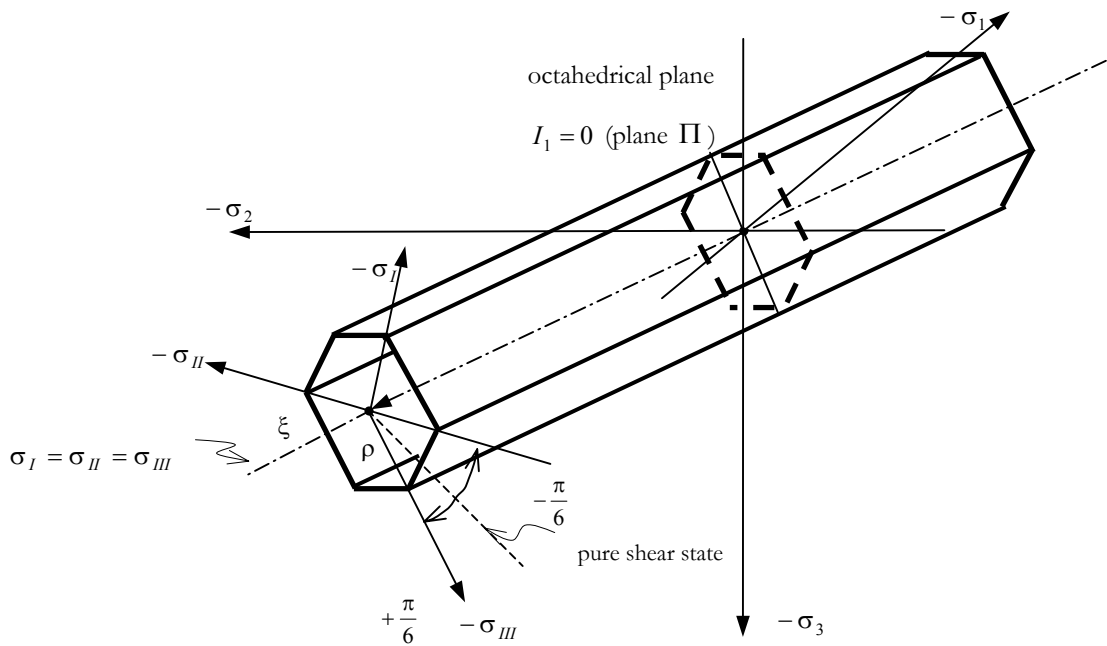
Figure 3.12: Tresca yield surface.

3.6.2 Two-parameter models

3.6.2.1 Mohr-Coulomb criterion

The simplest form of Mohr envelope is the straight line (see Figure 3.13). The equation of this line is:

$$|\tau| = c - \sigma \tan \phi \tag{3.84}$$

where c is the *cohesion* and ϕ is the *angle of internal friction*, and both are material constants determined by experiments.
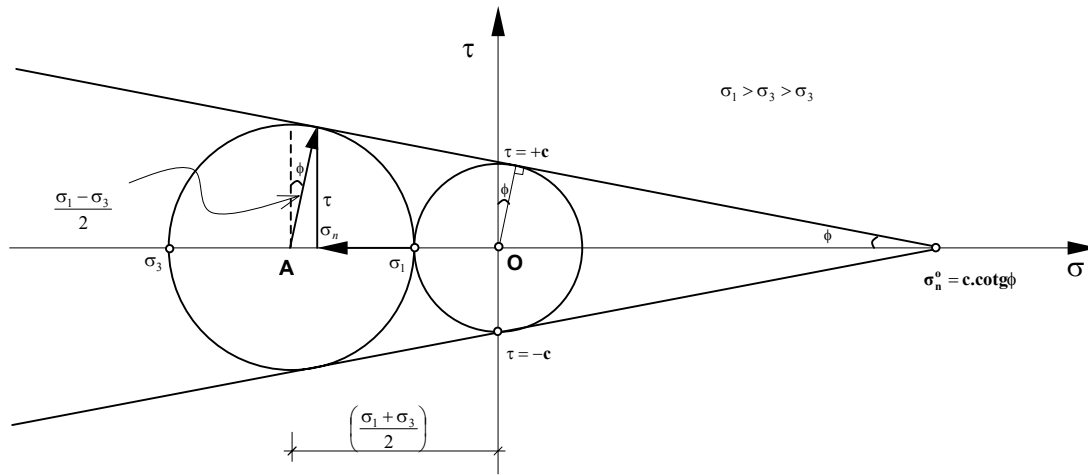
Figure 3.13: Relationship between principal stresses for the Mohr-Coulomb criterion.

Considering Figure 3.13 and equation (3.84), and taking into account that $\sigma_1 \geq \sigma_2 \geq \sigma_3$, we can write the Mohr-Coulomb criterion as:

Mohr-Coulomb criterion

Solid Mechanics

$$\frac{(\sigma_1 - \sigma_3)}{2} \cos \phi = c - \left[\frac{1}{2}(\sigma_1 + \sigma_3) + \frac{(\sigma_1 - \sigma_3)}{2} \sin \phi \right] \tan \phi$$

$$\Rightarrow \sigma_1 - \sigma_3 - \sin \phi \left(\frac{2c}{\tan \phi} - \sigma_1 - \sigma_3 \right) = 0 \tag{3.85}$$

Next, in order to deduce the critical values we will consider the sign convention adopted by soil mechanics: compression (positive) and traction (negative) $\sigma_1 \equiv -\sigma_3 ; \sigma_3 \equiv -\sigma_1$. In this case, the Mohr-Coulomb surface equation is described as:

Mohr-Coulomb Criterion

Soil Mechanics

$$\mathcal{F}(\sigma_1, \sigma_3) = \sigma_1 - \sigma_3 - \sin \phi \left(\sigma_1 + \sigma_3 + \frac{2c}{\tan \phi} \right) \tag{3.86}$$

Considering that:

$$
\mathbf{n} = \begin{bmatrix} N_1' & 0 & 0 \\ 0 & 0 & 0 \\ 0 & 0 & -N_3' \end{bmatrix} \quad ; \quad \mathbf{m} = \begin{bmatrix} M_1' & 0 & 0 \\ 0 & 0 & 0 \\ 0 & 0 & -M_3' \end{bmatrix} \tag{3.87}
$$

where N_1' and N_3' are functions of ϕ (angle of internal friction) and M_1' and M_3' are function of ψ (dilatancy angle) with:

$$
N_1' = \frac{1 - \sin\phi}{\sqrt{2\left(1 + \sin^2\phi\right)}} \;;\; N_3' = \frac{1 + \sin\phi}{\sqrt{2\left(1 + \sin^2\phi\right)}}\;;\; M_1' = \frac{1 - \sin\psi}{\sqrt{2\left(1 + \sin^2\psi\right)}}\;;\; M_3' = \frac{1 + \sin\psi}{\sqrt{2\left(1 + \sin^2\psi\right)}}
$$

The critical values θ_{crit} and $\mathcal{H}_{crit}^p$ are respectively given by:

$$
\tan^2\theta_{crit} = \frac{2N_3'M_3' + N_1'M_3' + M_1'N_3'}{2N_1'M_1' + N_1'M_3' + M_1'N_3'} \tag{3.88}
$$

$$
\mathcal{H}_{crit}^p = \frac{E}{4(1 - \nu^2)} \left[\frac{\left(2N_1'M_1' + N_1'M_3' + M_1'N_3'\right)^2}{\left(M_1' + M_3'\right)\left(N_1' + N_3'\right)} - 4N_1'M_1' \right] \tag{3.89}
$$

Substituting the values of N' and M' we can obtain that:

$$
\tan^2\theta_{crit} = -\frac{2\sin\psi\sin\phi + \sin\phi + \sin\psi}{2\sin\psi\sin\phi - \sin\phi - \sin\psi} \tag{3.90}
$$

$$
\mathcal{H}_{crit}^p = \frac{\mu(\lambda + \mu)}{(\lambda + 2\mu)} \left[\frac{\left(\sin\psi - \sin\phi\right)^2}{2\sqrt{\left(1 + \sin^2\psi\right)\left(1 + \sin^2\phi\right)}} \right] = \frac{E}{8(1 - \nu^2)} \left[\frac{\left(\sin\psi - \sin\phi\right)^2}{\sqrt{\left(1 + \sin^2\psi\right)\left(1 + \sin^2\phi\right)}} \right] \tag{3.91}
$$

Thus we can summarize:

CRITICAL VALUES FOR THE MOHR-COULOMB CRITERION	
critical angle	$\tan^2\theta_{crit} = -\dfrac{2\sin\psi\sin\phi + \sin\phi + \sin\psi}{2\sin\psi\sin\phi - \sin\phi - \sin\psi}$
critical hardening modulus	$\mathcal{H}_{crit}^p = \dfrac{E}{8(1 - \nu^2)} \left[\dfrac{\left(\sin\psi - \sin\phi\right)^2}{\sqrt{\left(1 + \sin^2\psi\right)\left(1 + \sin^2\phi\right)}} \right]$

(3.92)

3.6.2.1.1 Non-associated Mohr criterion – Particular case

In this particular case we have:

$$\mathbf{n} = \begin{bmatrix} 1 & 0 & 0 \\ 0 & 0 & 0 \\ 0 & 0 & -N' \end{bmatrix} \quad \text{and} \quad \mathbf{m} = \begin{bmatrix} 1 & 0 & 0 \\ 0 & 0 & 0 \\ 0 & 0 & -M' \end{bmatrix} \tag{3.93}$$

where

$$N' = \frac{1 - \sin\phi}{1 + \sin\phi} \quad ; \quad M' = \frac{1 - \sin\psi}{1 + \sin\psi} \qquad \text{with} \begin{cases} N' \geq 0 \\ M' \geq 0 \end{cases} \tag{3.94}$$

Substituting the values of $\mathbf{n}$ and $\mathbf{m}$, given by the expressions (3.93), into equation (3.48) for non-associated problems, we can obtain the critical angle:

$$\begin{cases} \tan^2\theta_{crit} = \dfrac{\left[(m_3 - m_1)n_2 + (n_3 - n_1)m_2\right]\nu + (2n_3 - n_1)m_3 - m_1 n_3}{\left[(m_1 - m_3)n_2 + (n_1 - n_3)m_2\right]\nu + (2n_1 - n_3)m_1 - n_1 m_3} \\[4mm] \Rightarrow \tan^2\theta_{crit} = \dfrac{2N'M' + N' + M'}{(2 + M' + N')} \end{cases} \tag{3.95}$$

and the critical value of the hardening modulus:

$$\mathcal{H}^p_{crit} = \frac{\mu(\lambda + \mu)}{(\lambda + 2\mu)} \frac{(N' - M')^2}{(1 + M')(1 + N')} = \frac{E}{4(1 - \nu^2)} \frac{(N' - M')^2}{(1 + M')(1 + N')} \tag{3.96}$$

Thus, we can summarize:

CRITICAL VALUES FOR THE MOHR CRITERION (ASSOCIATED CASE)	
critical angle	$\tan^2\theta_{crit} = \dfrac{2 - \sin\phi - \sin\psi}{2 + \sin\phi + \sin\psi}$
critical hardening modulus	$\mathcal{H}^p_{crit} = \dfrac{E}{4(1 - \nu^2)} \dfrac{(N' - M')^2}{(1 + M')(1 + N')}$

$$\tag{3.97}$$

The results (3.97) are consistent with the results presented by Ottosen & Runesson (1991b).

The above values, (3.95) and (3.96), can be directly obtained from equations (3.88) and (3.89) just by setting $N'_1 = 1$, $N'_3 = N_3$, $M'_1 = 1$ and $M'_3 = M_3$.

3.6.2.2 Drucker-Prager criterion – Two-Invariant plasticity formulation

In this special case, we can express **n** and **m**, which are coaxials, as:

$$\mathbf{n} = \frac{\partial \mathcal{F}}{\partial \boldsymbol{\sigma}} = \alpha_1 \mathbf{s} + \alpha_3 \mathbf{1}$$

$$\mathbf{m} = \frac{\partial \mathcal{G}}{\partial \boldsymbol{\sigma}} = \alpha_2 \mathbf{s} + \alpha_4 \mathbf{1}$$
(3.98)

The parameters α_1 and α_3 describe the pressure sensitive, and α_2 and α_4 are frictional material parameters.

Using equation (3.48) with **n** and **m** given by equation (3.98), we can obtain the critical angle:

- In terms of the principal deviatoric stress:

$$\tan^2 \theta_{crit} = \frac{-(1+\nu)(\alpha_1\alpha_4 + \alpha_2\alpha_3) - 2(\mathbf{s}_3 + \nu\mathbf{s}_2)\alpha_1\alpha_2}{(1+\nu)(\alpha_1\alpha_4 + \alpha_2\alpha_3) + 2(\mathbf{s}_1 + \nu\mathbf{s}_2)\alpha_1\alpha_2}$$
(3.99)

- In terms of the principal stress:

$$\tan^2 \theta_{crit} = \frac{(-6\mu - 9\lambda)(\alpha_3\alpha_2 + \alpha_1\alpha_4) + \alpha_1\alpha_2[4\mu(-2\sigma_3 + \sigma_2 + \sigma_1) + 6\lambda(\sigma_1 - \sigma_3)]}{(6\mu + 9\lambda)(\alpha_3\alpha_2 + \alpha_1\alpha_4) + \alpha_1\alpha_2[4\mu(2\sigma_1 - \sigma_3 - \sigma_2) + 6\lambda(\sigma_1 - \sigma_3)]}$$
(3.100)

The above equation can be rewritten in terms of ν and E as:

$$\tan^2 \theta_{crit} = \frac{-3(\nu+1)(\alpha_1\alpha_4 + \alpha_2\alpha_3) + [2\nu(\sigma_1 - 2\sigma_2 + \sigma_3) + 2\sigma_1 + 2\sigma_2 - 4\sigma_3]\alpha_1\alpha_2}{3(\nu+1)(\alpha_1\alpha_4 + \alpha_2\alpha_3) + [2\nu(2\sigma_2 - \sigma_3 - \sigma_1) - 2\sigma_2 - 2\sigma_3 + 4\sigma_1]\alpha_1\alpha_2}$$
(3.101)

The critical hardening parameter $\mathcal{H}_{crit}^p$ is given by the following table:

CRITICAL VALUES FOR THE DRUCKER-PRAGER CRITERION (ASSOCIATED CASE)	
critical angle	$\tan^2 \theta_{crit} = \dfrac{-(1+\nu)(\alpha_1\alpha_4 + \alpha_2\alpha_3) - 2(\mathbf{s}_3 + \nu\mathbf{s}_2)\alpha_1\alpha_2}{(1+\nu)(\alpha_1\alpha_4 + \alpha_2\alpha_3) + 2(\mathbf{s}_1 + \nu\mathbf{s}_2)\alpha_1\alpha_2}$
critical hardening modulus	$\mathcal{H}_{crit}^p = \dfrac{E}{(1-\nu^2)}\left[A_1 + A_2 + A_2\right]$
(3.102)

where

$$A_1 = \frac{\left[(1-2\nu)\mathbf{s}_3\alpha_2 + (1+\nu)\alpha_4\right]\left[(1-2\nu)\mathbf{s}_3\alpha_1 + (1+\nu)\alpha_3\right]}{(1-2\nu)}$$

$$A_3 = \frac{\left[2(\nu\mathbf{s}_2 + \mathbf{s}_1)\alpha_1\alpha_2 + (1+\nu)(\alpha_1\alpha_4 + \alpha_2\alpha_3)\right]^2}{4\alpha_1\alpha_2} \;;\; A_3 = -3(1-\nu)\frac{(1-2\nu)\tau_{oct}^2\alpha_1\alpha_2 + (1+\nu)(\alpha_3\alpha_4)}{(1-2\nu)}$$

with $\tau_{oct}^2 = \frac{1}{9}\left[(\sigma_1 - \sigma_2)^2 + (\sigma_2 - \sigma_3)^2 + (\sigma_3 - \sigma_1)^2\right]$

(a) Two-invariants

(b) Particular case
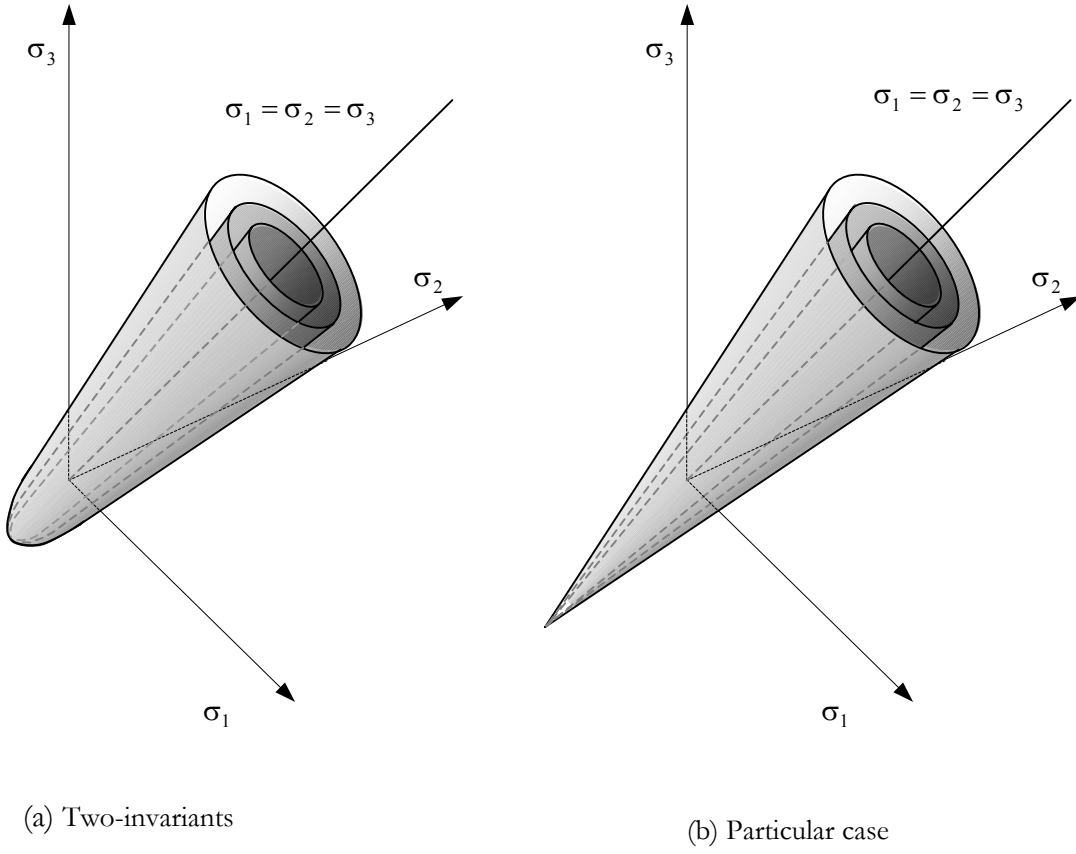
Figure 3.14: Drucker-Prager yield surface.

Localization ellipse

Using equations (3.30) and (3.31) we can obtain the localization ellipse:

$$\boxed{\frac{\left(\sigma_N - \sigma_0\right)^2}{\hat{A}^2} + \frac{\tau^2}{\hat{B}^2} = 1} \tag{3.103}$$

with

$$\sigma_0 = p - \frac{(1+\nu)}{2(1-2\nu)}\frac{(\alpha_1\alpha_4 + \alpha_2\alpha_3)}{\alpha_1\alpha_2}; \quad \sigma_N = \mathbf{N}\cdot\boldsymbol{\sigma}\cdot\mathbf{N} \tag{a}$$

$$\hat{A}^2 = \frac{(\lambda + 2\mu)\xi}{4\mu^2\mathcal{K}} = \frac{2(1-\nu)}{(1-2\nu)}\hat{B}^2 \tag{b} \quad (3.104)$$

$$\hat{B}^2 = \frac{\xi}{4\mu\mathcal{K}} = \frac{\mathcal{H}^p}{4\mu\alpha_1\alpha_2} + J_2 + \frac{3(1+\nu)}{2(1-2\nu)}\frac{\alpha_3\alpha_4}{\alpha_1\alpha_2} + \frac{(1+\nu)^2}{8(1-2\nu)(1-\nu)}\frac{(\alpha_2\alpha_3 - \alpha_1\alpha_4)^2}{\alpha_1^2\alpha_2^2} \tag{c}$$

where ξ and $\mathcal{K}$ are given by equation (3.21) in the plasticity case and $p = \dfrac{I_1}{3}$, where I_1 is the first invariant ($I_1 = \sigma_1 + \sigma_2 + \sigma_3$) and J_2 the second invariant for the deviatoric stress (see appendix A.7).

3.6.2.2.1 Particular case $\alpha_1 = \alpha_2 = 1$

In the case of the Drucker-Prager model with two invariants, the normal to the yield surface $\mathbf{n}$ and the normal to the plastic potential $\mathbf{m}$ are given by equations (3.98), with the following values $\alpha_1 = \alpha_2 = 1$. In this case the model only depends on the friction parameter of the Drucker-Prager parabolic model.

$$\begin{cases} \mathbf{n} = \mathbf{s} + \alpha_3 \mathbf{1} \\ \mathbf{m} = \mathbf{s} + \alpha_4 \mathbf{1} \end{cases} \tag{3.105}$$

The value for the critical angle can be obtained directly from equation (3.101), resulting in:

$$\tan^2 \theta_{crit} = \frac{-3(v+1)(\alpha_4 + \alpha_3) + [2v(\sigma_1 - 2\sigma_2 + \sigma_3) + 2\sigma_1 + 2\sigma_2 - 4\sigma_3]}{3(v+1)(\alpha_4 + \alpha_3) + [2v(2\sigma_2 - \sigma_3 - \sigma_1) - 2\sigma_2 - 2\sigma_3 + 4\sigma_1]} \tag{3.106}$$

The above equation can be written as:

$$\tan^2 \theta_{crit} = \frac{r - (1-2v)\left(\sigma_c - \dfrac{I_1}{3}\right) - (1+v)\left(\dfrac{\alpha_4 + \alpha_3}{2}\right)}{r + (1-2v)\left(\sigma_c - \dfrac{I_1}{3}\right) + (1+v)\left(\dfrac{\alpha_4 + \alpha_3}{2}\right)} \tag{3.107}$$

where: $\sigma_c = \dfrac{\sigma_1 + \sigma_3}{2}$; $r = \dfrac{\sigma_1 - \sigma_3}{2}$

Expression (3.107) is the same as the one obtained by Willam (2000).

The explicit expression for $\mathcal{H}^p_{crit}$ is given by:

$$\mathcal{H}^p_{crit} = \frac{E}{(1-v^2)}[A_1 + A_2 + A_3] \tag{3.108}$$

where

$$A_1 = \frac{[(1-2v)\mathbf{s}_3 + (1+v)\alpha_4][(1-2v)\mathbf{s}_3 + (1+v)\alpha_3]}{(1-2v)}$$

$$A_2 = \frac{[2(v\mathbf{s}_2 + \mathbf{s}_1) + (1+v)(\alpha_4 + \alpha_3)]^2}{4}$$

$$A_3 = -3(1-\nu)\frac{(1-2\nu)\tau_{oct}^2 + (1+\nu)\alpha_3\alpha_4}{(1-2\nu)}$$

with $\tau_{oct}^2 = \dfrac{1}{9}\left[(\sigma_1-\sigma_2)^2 + (\sigma_2-\sigma_3)^2 + (\sigma_3-\sigma_1)^2\right]$

Summarizing:

CRITICAL VALUES FOR THE **DRUCKER-PRAGER** CRITERION (ASSOCIATED CASE) PARTICULAR CASE ($\alpha_1=\alpha_2=1$)	
critical angle	$\tan^2\theta_{crit} = \dfrac{r - (1-2\nu)\left(\sigma_c - \dfrac{I_1}{3}\right) - (1+\nu)\left(\dfrac{\alpha_4+\alpha_3}{2}\right)}{r + (1-2\nu)\left(\sigma_c - \dfrac{I_1}{3}\right) + (1+\nu)\left(\dfrac{\alpha_4+\alpha_3}{2}\right)}$
critical hardening modulus	$\mathcal{H}_{crit}^p = \dfrac{E}{(1-\nu^2)}\left[A_1 + A_2 + A_3\right]$

(3.109)

3.6.3 Three-parameter models

3.6.3.1 Three-invariants plasticity formulation

Consider that in this plasticity formulation we include the effects of the three invariants in the yield function and in the plastic potential. The three invariants $(\xi, \rho, \tilde{\theta})$ are schematically sketched in Figure 3.15. For further details on this model see Willam (2000).

As a result the gradients **n** and **m** depend on the three invariants, which can be written as:

$$\mathbf{n} = \frac{\partial \mathcal{F}}{\partial \boldsymbol{\sigma}} = \alpha_1 \mathbf{s} + \alpha_3 \mathbf{1} + \alpha_5 \mathbf{s}\cdot\mathbf{s}$$
$$\mathbf{m} = \frac{\partial Q}{\partial \boldsymbol{\sigma}} = \alpha_2 \mathbf{s} + \alpha_4 \mathbf{1} + \alpha_6 \mathbf{s}\cdot\mathbf{s}$$

(3.110)

Using equation (3.48), with the values given in (3.110), one can obtain the critical angle:

$$\tan^2\theta_{crit} = -\frac{(1+\nu)(\alpha_1\alpha_4 + \alpha_2\alpha_3) + 2\alpha_1\alpha_2(\nu s_2 + s_3) + \left[(\vartheta\alpha_5 + \psi\alpha_1 + \gamma\alpha_3)\alpha_6\right] + \left[(\psi\alpha_2 + \gamma\alpha_4)\alpha_5\right]}{(1+\nu)(\alpha_1\alpha_4 + \alpha_2\alpha_3) + 2\alpha_1\alpha_2(\nu s_2 + s_1) + \left[(\varpi\alpha_5 + \chi\alpha_1 - \gamma\alpha_3)\alpha_6\right] + \left[(\chi\alpha_2 - \gamma\alpha_4)\alpha_5\right]}$$

(3.111)

and the critical hardening modulus:

$$\boxed{\mathcal{H}_{crit}^{p} = \frac{E}{(1-\nu^2)}\left[A_1 + A_2 + A_3\right]}$$
(3.112)

where

$$A_1 = \frac{\left[(1-2\nu)\mathbf{s}_3\alpha_2 + (1+\nu)\alpha_4 + B_1\right]\left[(1-2\nu)\mathbf{s}_3\alpha_1 + (1+\nu)\alpha_3 + B_2\right]}{(1-2\nu)}$$

$$A_2 = \frac{\left[(\gamma\alpha_3 + \varpi\alpha_5 + \zeta\alpha_1)\alpha_6 + (\gamma\alpha_4 + \zeta\alpha_2)\alpha_5 + 2\alpha_1\alpha_2(\mathbf{s}_1 + \nu\mathbf{s}_2) + (1+\nu)(\alpha_2\alpha_3 + \alpha_1\alpha_4)\right]^2}{4\left[\alpha_6(\mathbf{s}_3 + \mathbf{s}_1) + \alpha_2\right]\left[\alpha_5(\mathbf{s}_3 + \mathbf{s}_1) + \alpha_1\right]}$$

$$A_3 = -(1-\nu)\frac{B_3 + 2(1-2\nu)J_2\alpha_1\alpha_2 + 3(1+\nu)\alpha_3\alpha_4}{(1-2\nu)}$$

$$B_1 = \left[\left(\mathbf{s}_1^2 + \mathbf{s}_2^2 - \mathbf{s}_3^2\right)\nu + \mathbf{s}_3^2\right]\alpha_6; \quad B_2 = \left[\left(\mathbf{s}_1^2 + \mathbf{s}_2^2 - \mathbf{s}_3^2\right)\nu + \mathbf{s}_3^2\right]\alpha_5$$

$$B_3 = \left[3J_3(1-2\nu)(\alpha_1\alpha_6 + \alpha_2\alpha_5) + 2J_2(1+\nu)(\alpha_3\alpha_6 + \alpha_4\alpha_5) + \frac{9}{2}\tau_{oct}^4\alpha_5\alpha_6\right]$$

$$\zeta = 2\mathbf{s}_1^2 + \mathbf{s}_3\mathbf{s}_1 + \nu\left(\mathbf{s}_1\mathbf{s}_2 + \mathbf{s}_2\mathbf{s}_3 + \mathbf{s}_2^2\right)$$

$$J_2 = \frac{\mathbf{s}_1^2 + \mathbf{s}_2^2 + \mathbf{s}_3^2}{2}; \quad J_3 = \frac{\mathbf{s}_1^3 + \mathbf{s}_2^3 + \mathbf{s}_3^3}{3}; \quad \vartheta = 2(\mathbf{s}_1 + \mathbf{s}_3)\left(\nu s_2^2 + \mathbf{s}_3^2\right)$$

$$\varpi = 2(\mathbf{s}_1 + \mathbf{s}_3)\left(\nu s_2^2 + \mathbf{s}_1^2\right); \quad \psi = \mathbf{s}_3(\mathbf{s}_1 + 2\mathbf{s}_3); \quad \chi = \mathbf{s}_1(\mathbf{s}_3 + 2\mathbf{s}_1); \quad \gamma = (1+\nu)(\mathbf{s}_1 + \mathbf{s}_3)$$
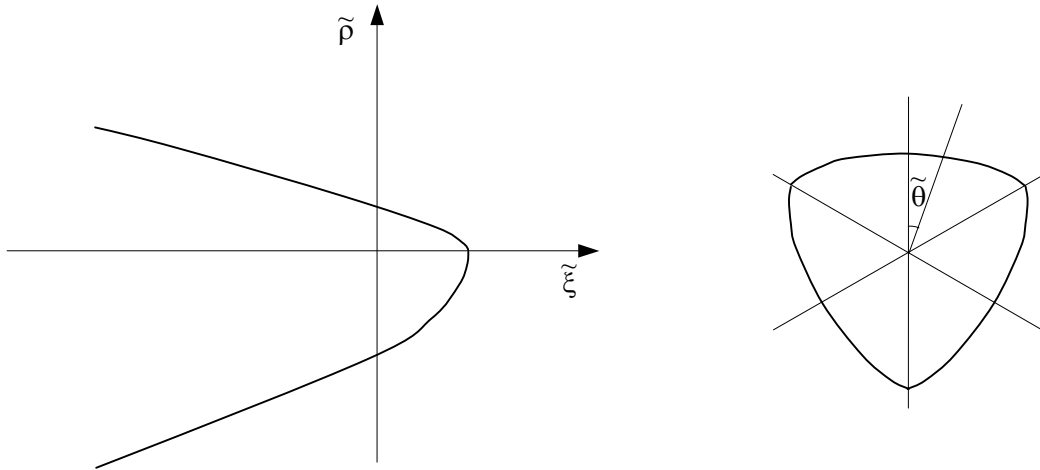
Figure 3.15: Gradients of generic three-invariants yield surface, Willam(2000).

3.6.4 Damage models

In this section we will obtain the explicit critical values for the Isotropic Damage Model described in chapter 2.

3.6.4.1 Isotropic damage model

This associated model has the following flow rule:

$$\mathbf{n} = \mathbf{m} = \boldsymbol{\varepsilon} = \begin{bmatrix} \varepsilon_1 & 0 & 0 \\ 0 & \varepsilon_2 & 0 \\ 0 & 0 & \varepsilon_3 \end{bmatrix} \tag{3.113}$$

with $\varepsilon_1 \geq \varepsilon_2 \geq \varepsilon_3$

Using equation (3.65) we can obtain the critical angle:

$$\tan^2 \theta_{crit} = -\frac{\varepsilon_3 + \nu\varepsilon_2}{\varepsilon_1 + \nu\varepsilon_2} \tag{3.114}$$

Equation (3.114) is the same as obtained by Rizzi *et al.*(1995) and through equation (3.66) we obtain the value of $\boldsymbol{\mathcal{H}}^d_{crit}$:

$$\boldsymbol{\mathcal{H}}^d_{crit} = (1-d)\left[1 - \frac{(\lambda+\mu)r^2}{\left\{ \lambda^2(\mathsf{Tr}(\boldsymbol{\varepsilon}))^2 + \left[(\varepsilon_1 - \varepsilon_3)^2 + 2\mathsf{Tr}(\boldsymbol{\varepsilon})(\varepsilon_1 + \varepsilon_3)\right]\lambda\mu + 2\mu^2(\varepsilon_1^2 + \varepsilon_3^2) \right\}} \right] \tag{3.115}$$

Localization ellipse

We can then obtain the localization ellipse (see Figure 3.16) in the Mohr circle space, according to equation (3.60):

$$\boxed{\frac{(\varepsilon_N + \varepsilon_0)^2}{\hat{A}^2} + \frac{\varepsilon_S^2}{\hat{B}^2} = 1} \tag{3.116}$$

where

$$\varepsilon_0 = \frac{\lambda(\varepsilon_1 + \varepsilon_2 + \varepsilon_3)}{2\mu} = \frac{\nu}{(1-2\nu)}(\varepsilon_1 + \varepsilon_2 + \varepsilon_3); \quad \hat{A}^2 = \frac{2(1-\nu)}{(1-2\nu)}\hat{B}^2; \quad \hat{B}^2 = \frac{\xi}{4\mu\mathcal{K}}$$
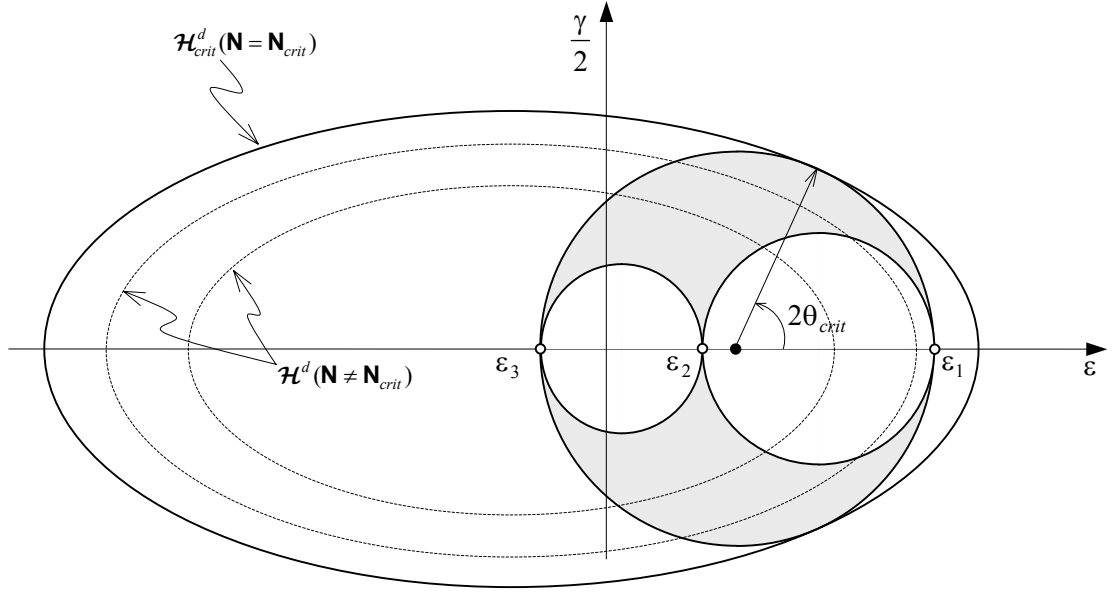
Figure 3.16: Localization ellipse.

3.7 Two dimensional case

In the two dimensional (2D) settings, we have the Plane strain case and the Plane stress case, (see Appendix A.5).

For the Plane Strain case the solution is a particular case of the 3D solutions that were previously derived.

3.7.1 Plane stress

3.7.1.1 Critical angle

3.7.1.1.1 Non-associated case ($\mathbf{n} \neq \mathbf{m}$)

$$\tan^2 \theta_{crit} = \frac{(2n_2 - n_1)m_2 - m_1 n_2}{(2n_1 - n_2)m_1 - n_1 m_2} \tag{3.117}$$

3.7.1.1.2 Associated case ($\mathbf{n} = \mathbf{m}$)

$$\tan^2 \theta_{crit} = -\frac{m_2}{m_1} \tag{3.118}$$

The angle can also be expressed as:

$$N_1 = \cos(\theta) = \sqrt{\frac{-\varepsilon_1}{(\varepsilon_2 - \varepsilon_1)}} \tag{3.119}$$

Using the property $\cos(2A) = 2\cos^2 A - 1$, we obtain:

$$\cos(2\theta) = \frac{-(\varepsilon_1 + \varepsilon_2)}{(\varepsilon_2 - \varepsilon_1)} \tag{3.120}$$

Notice that 2θ is the angle where the Mohr's circle intercept the axis of the shear deformation (see Figure 3.17). Figure 3.18 shows how to obtain the critical angles schematically.
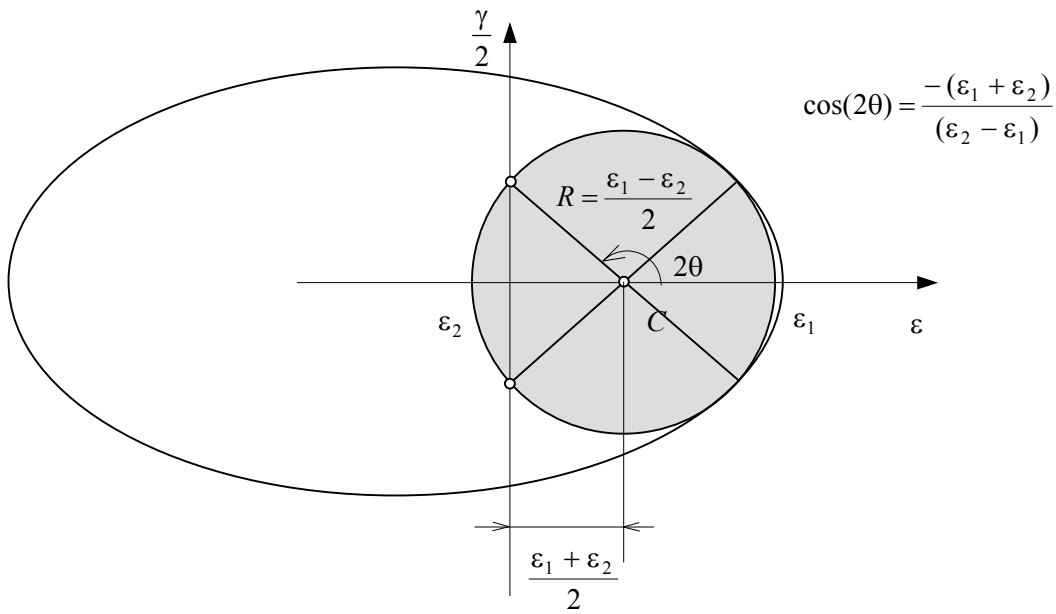
Figure 3.17: Mohr's circle – 2D isotropic damage model (associated case).
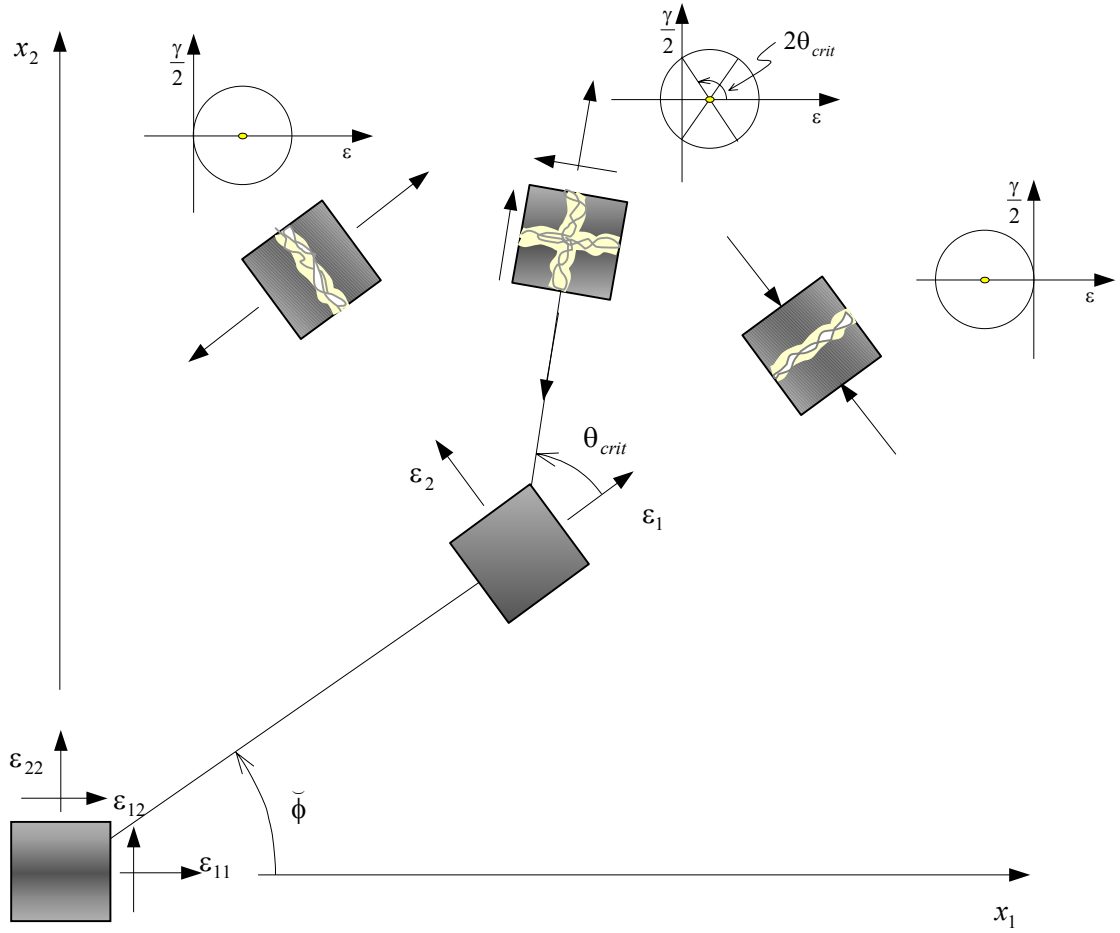
Figure 3.18: Critical angle – 2D Damage case.

3.7.1.2 Critical hardening modulus - $\mathcal{H}_{crit}$

3.7.1.2.1 Non-associated case ($\mathbf{n} \neq \mathbf{m}$)

Damage

$$\mathcal{H}_{crit}^d = \xi \left(1 - \frac{r^2}{Z_{\max}(\mathbf{N})} \right) \tag{3.121}$$

with

$$Z_{\max}(\mathbf{N}) = \frac{1}{(\bar{\lambda} + 2\mu)} \left\{ \frac{\mu(\bar{\lambda} + \mu)[(m_1 - m_2)n_1 + (n_1 - n_2)m_1]^2}{(m_1 - m_2)(n_1 - n_2)} - [\bar{\lambda}(m_1 + m_2) + 2\mu m_2][\bar{\lambda}(n_1 + n_2) + 2\mu n_2] \right\}$$

Plasticity

$$\mathcal{H}_{crit}^{p} = \frac{\mu(\bar{\lambda} + \mu)}{(\bar{\lambda} + 2\mu)} \frac{(n_1 m_2 - n_2 m_1)}{(m_1 - m_2)(n_1 - n_2)}$$ (3.122)

3.7.1.2.2   Associated case ($\mathbf{n} = \mathbf{m}$)

Damage

$$\mathcal{H}_{crit}^{d} = (1-d)\left[1 - \frac{(\bar{\lambda} + \mu)r^2}{\left\{ \bar{\lambda}^2 (m_1 + m_2)^2 + \bar{\lambda}\mu[3m_2^2 + 2m_1 m_2] + 2\mu^2 m_2^2 \right\}} \right]$$ (3.123)

Plasticity

$$\mathcal{H}_{crit}^{p} = -\frac{(3\bar{\lambda} + 2\mu)\mu}{(\bar{\lambda} + \mu)} m_2^2$$ (3.124)

Annex $3A$

Specific Material Bifurcation Analysis

In this section, we present some examples of the critical angle computation as well as the critical hardening modulus. Visualizations of functions $Z(\mathbf{N})$ and $\mathbf{Q(N)}$ are presented too.

A.1.1 Simple traction

Consider one finite element, as shown in Figure A.1, constituted by a material whose behavior obeys the isotropic damage model described in chapter 2 and has the following material properties: $\lambda = 0.0$, $\mu = 10000.00$. Displacement control is applied until a certain pseudo-time at which the strain state is the one described in Figure A.1.

$$\begin{cases} \varepsilon_1 = 4.64646464 \times 10^{-5} \\ \varepsilon_2 = 0.0 \\ \varepsilon_3 = 0.0 \end{cases}$$

Mohr's circle in strain
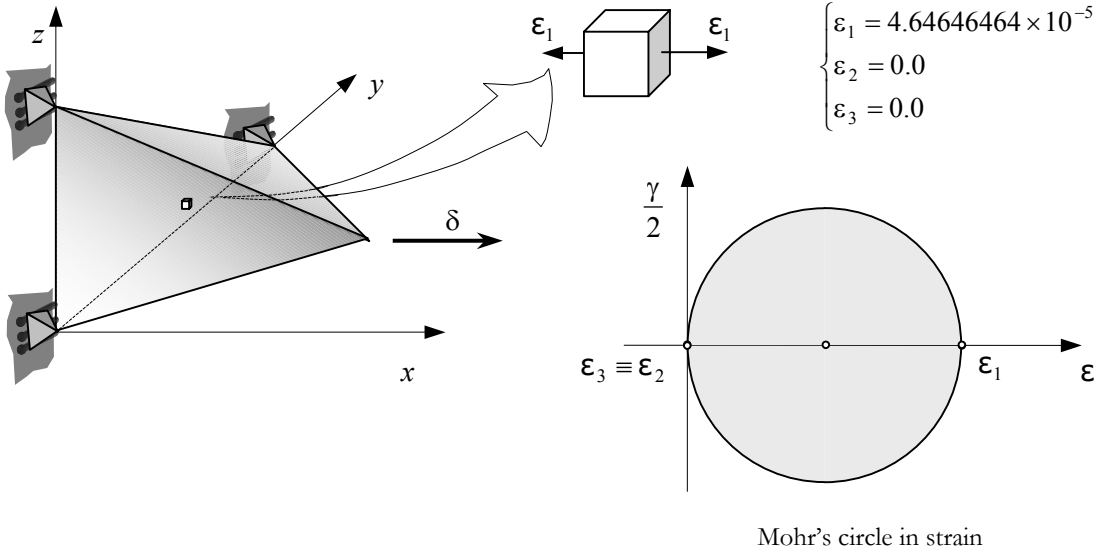
Figure A.1: Simple traction-strain state.

In this particular case, which can be regarded as a 2D case, the critical angle is $\theta_{crit} = 0°$, which was obtained by using equation (3.118). For the stress state considered, we have the following values for the variables involved in the damage model: $d = 0.0$, $q = 0.0$, $r = 7.07106781186 \times 10^{-3}$ and $\mathcal{H}^d = -0.0138889$.

Sweeping the range of variations $0 \le \alpha \le 180°$ and $0 \le \hat{\phi} \le 180°$, as defined in Figure 3.3, we can plot the function $\dfrac{|Q(N)|}{|Q^e|}$, see Figure A.2. One can verify that $Q(N)$ reaches a minimum for $\theta_{crit} = 0°$ or $\theta_{crit} = 180°$.
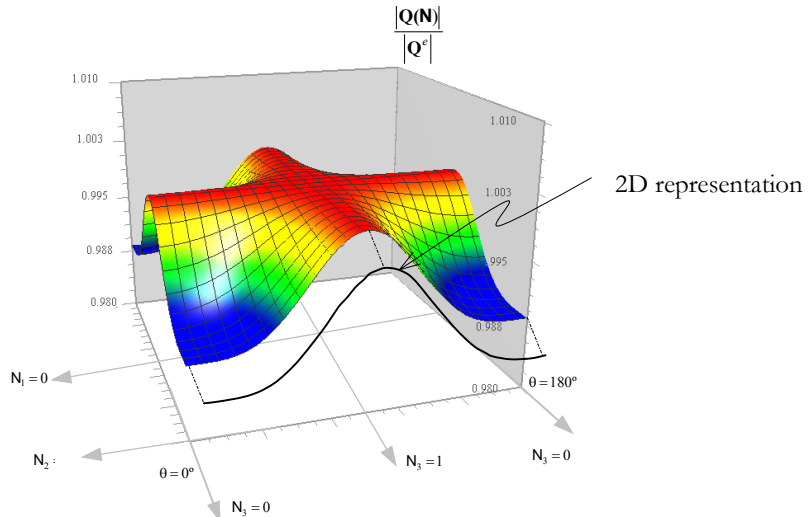
Figure A.2: Simple traction – surface $\dfrac{|Q(N)|}{|Q^e|}$

A.1.2 Triaxial case

Consider the finite element used in the preceding example with the following material properties: $E = 20000$ and $\nu = 0.2$. In this case, the load is applied in two stages in order to simulate a triaxial state, see Figure A.3.
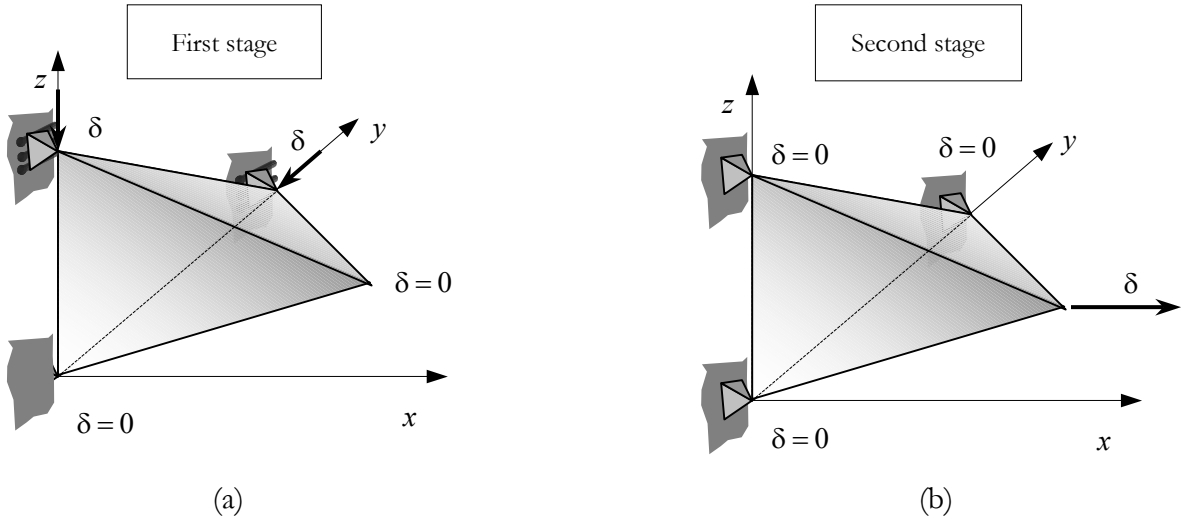
Figure A.3: Triaxial Case.

The strain state as well as the corresponding Mohr's circle in strain space is shown in Figure A.4 for a given pseudo-time in the second loading stage (see Figure A.3). The values of the damage variables for this strain state are $d = 0.0$, $r = 7.07106781186 \times 10^{-3}$, $q = 0.0$, and $\mathcal{H}^d = -0.125$. Figure A.5 illustrates surface $Z(\mathbf{N})$ and $|\mathbf{Q(N)}|/|\mathbf{Q}^e|$.

$$\varepsilon_1 = 4.746890046 \times 10^{-5}$$
$$\varepsilon_2 = 2.4985698615 \times 10^{-5}$$
$$\varepsilon_3 = -2.21515687743 \times 10^{-5}$$

Mohr's circle in strain
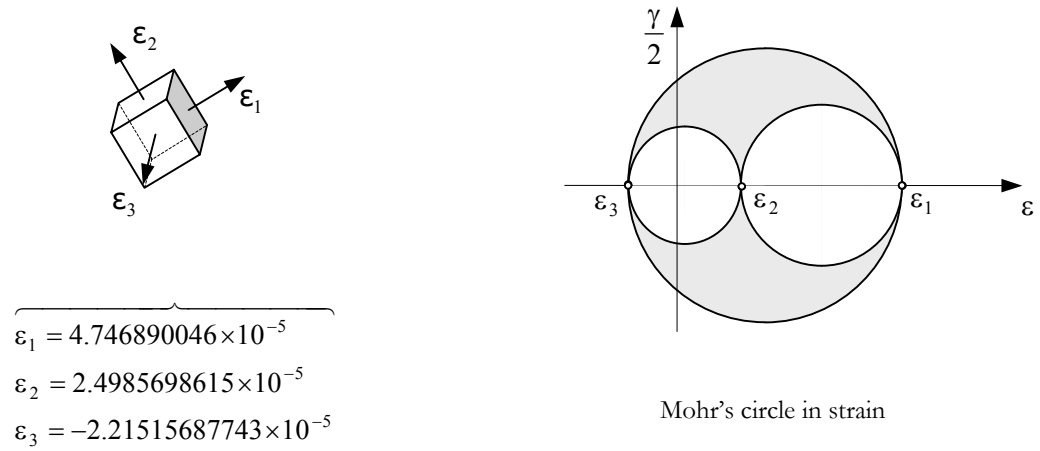
Figure A.4: Triaxial Case – strain states and Mohr's circle.

Surface $Z(\mathbf{N})$ Surface $|\mathbf{Q(N)}|/|\mathbf{Q}^e|$
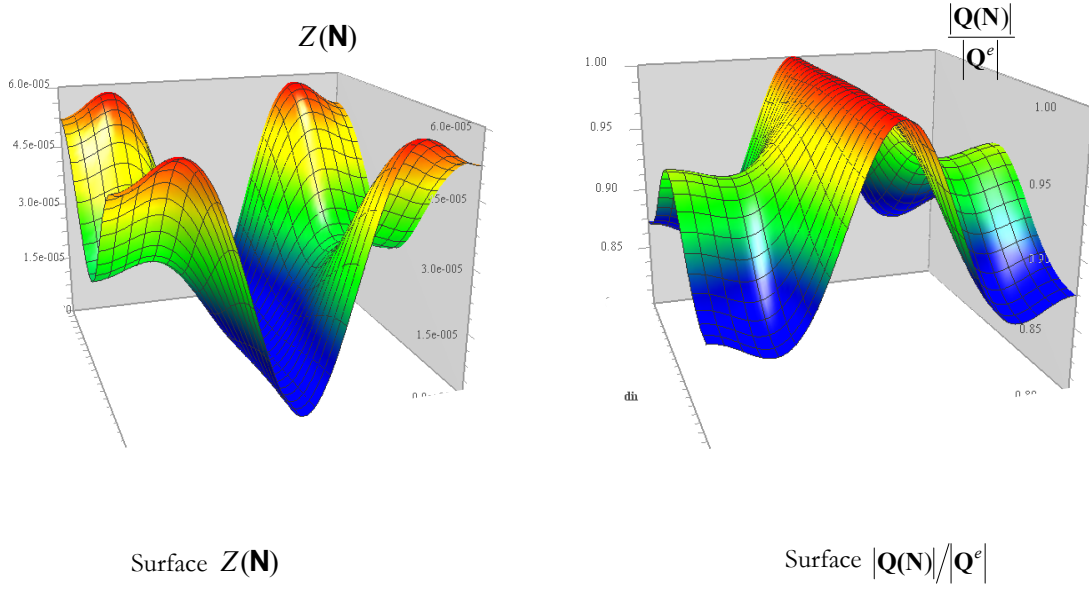
Figure A.5: Surfaces $Z(\mathbf{N})$ and $|\mathbf{Q(N)}|/|\mathbf{Q}^e|$ - Triaxial Case.

In Figure A.6 we can observe that the solutions correspondent to the planes $1-3$ and $2-3$, see Table 3.2, that intercept the Mohr's circles defined by $\varepsilon_1 - \varepsilon_3$ and $\varepsilon_2 - \varepsilon_3$ respectively. On the other hand the solution correspondent to the plane $1-2$ is not feasible.
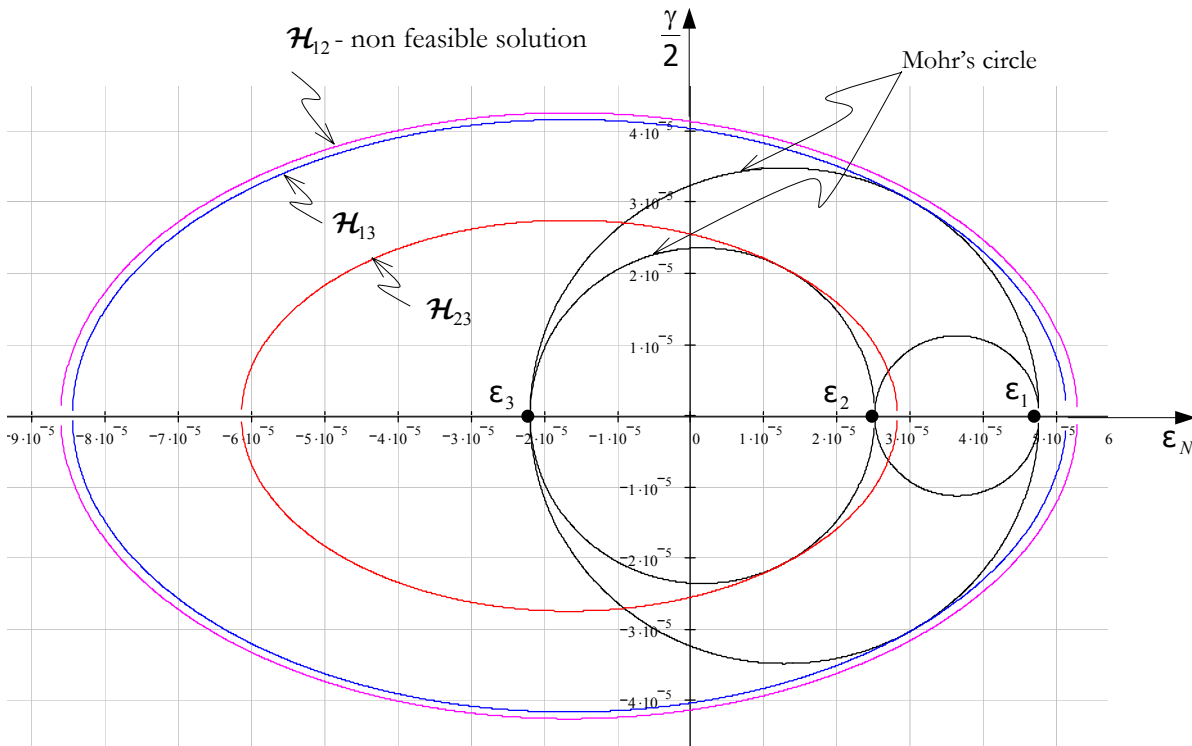
Figure A.6: Mohr's circle and localization ellipse - Triaxial Case.

A.1.3 Drucker-Prager – Non-associated case

This is a example intended to simulate a Drucker-Prager model as described in section 3.6.2.2.1. The following data are assumed:

- Material properties: $E = 10000$, $\nu = 0.2$;

- Stress state: $\begin{cases} \sigma_1 = 1.4 \times 10^{-4} \\ \sigma_2 = -1.2 \times 10^{-4} \\ \sigma_3 = -2.4 \times 10^{-4} \end{cases}$;

- Parameters of the model: $\begin{cases} \alpha_1 = 1 \\ \alpha_2 = 2 \\ \alpha_3 = 0.00005 \\ \alpha_1 = 0.00001 \end{cases}$

Figure A.7 shows the shape of surface $Z(\mathbf{N})$ and of $\det[\mathbf{Q(N)}]$ standardize and Figure A.8 the localization ellipses corresponding to the solutions $1-3$, $2-3$ and $1-2$ which intercept the Mohr's circles defined by $\sigma_1 - \sigma_3$, $\sigma_2 - \sigma_3$ and $\sigma_1 - \sigma_2$, respectively.
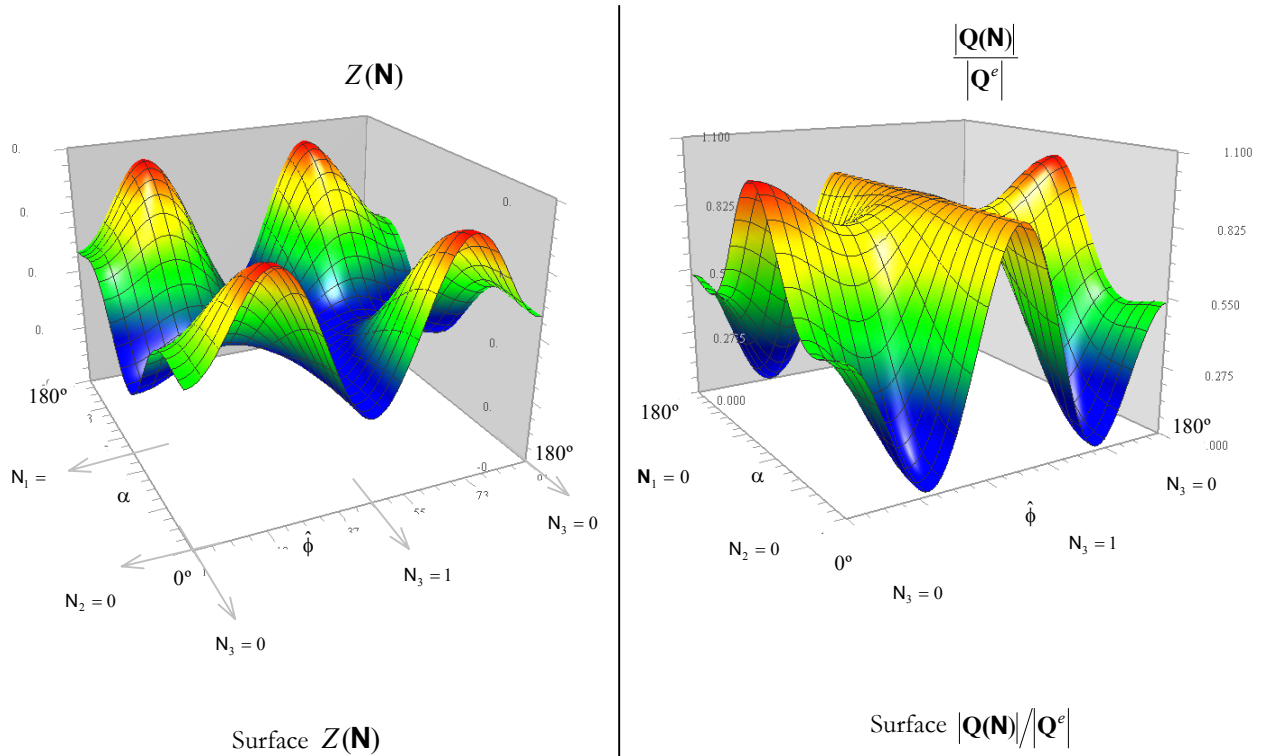
Figure A.7: Surfaces $Z(\mathbf{N})$ and $|\mathbf{Q(N)}|/|\mathbf{Q}^e|$ - Drucker-Prager Case.
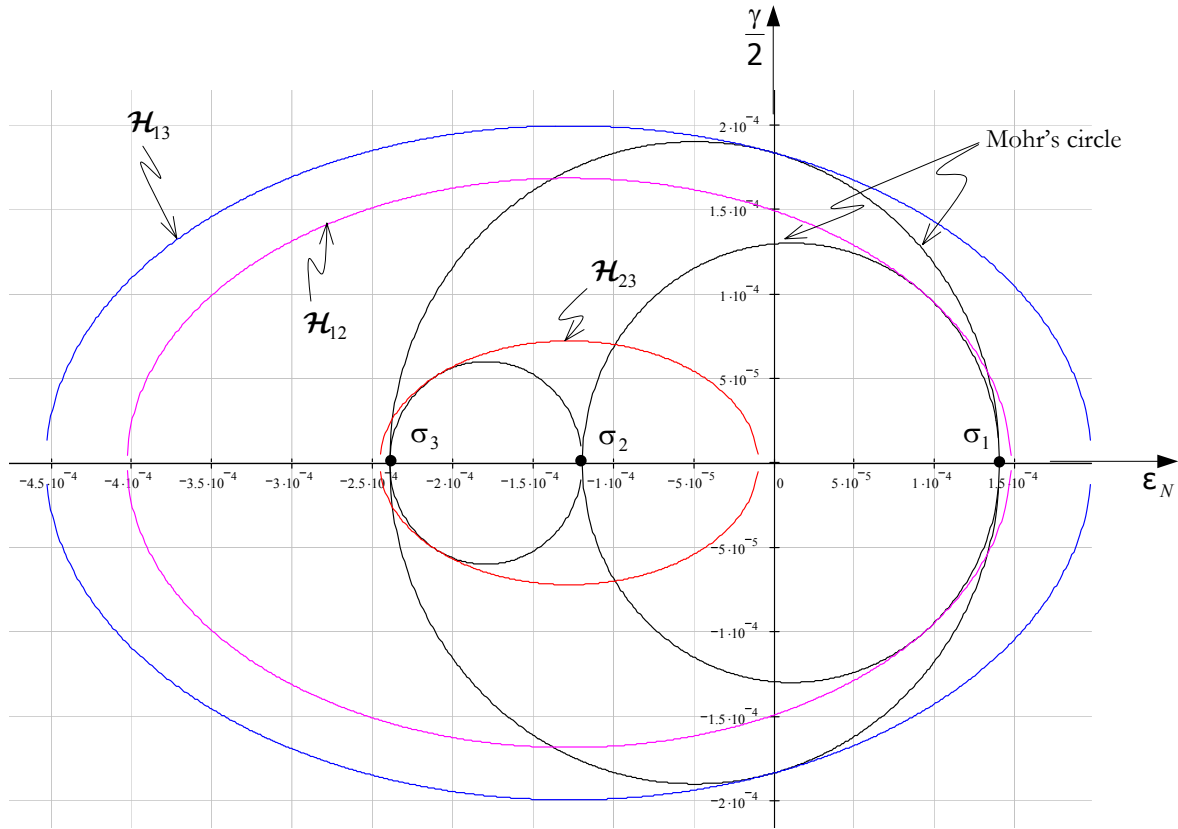
Figure A.8: Mohr's circle and localization ellipse – Drucker-Prager Case.

4

BVP Discretization and Implementation

Courant, R. (1943)

4.1 Introduction

In this chapter we present a 3D Finite Element formulation devised to solve BVP's of continua undergoing discontinuities. Such problems involve localization phenomena. To use the FEM for solving localization problems, some techniques of enriching the standard finite element formulation are required. When discontinuities are embedded into a standard finite element, this can be done in the strain or in the displacement field. Jirásek(1998) presented a table summarizing the use of these techniques (see Table 4.1).

Table 4.1: Selected approaches dealing with embedded discontinuities (Jirásek,1998).

Ortiz, Leroy and Needleman	1987	finite element for localization failure
Belytschko, Fish and Engelmann	1988	embedded localization zone
Dvorkin, Cuitiño and Gioia	1990	embedded localization line

Klisinki, Runesson and Sture	1991	inner softening band
Lotfi and Shing	1992	embedded crack
Simo, Oliver and Armero	1993	element with strong discontinuity
Simo and Oliver	1994	element with strong discontinuity
Armero and Garikipati	1995	element with strong discontinuity
Oliver	1996	element with strong discontinuity
Larsson and Runesson	1993	discontinuous displacement approximation
Larsson, Runesson and Åkesson	1995	embedded cohesive crack
Larsson and Runesson	1996	embedded localization band
Berends	1996	EAS element for fracture
Berends, Sluys and de Borst	1997	discontinuous modeling of mode-I failure
Sluys	1997	discontinuous modeling of shear banding
Sluys and Berends	1998	embedded discontinuity element

4.2 Governing equations

Consider a nonlinear solid (see Figure 4.1) that occupies a domain $\mathcal{B}$ in $\mathbb{R}^3$ with boundary $\partial\mathcal{B}$. In this body $\mathcal{B}$ with volume V the following forces are acting: $\mathbf{b}$ - body forces; $\mathbf{t}^*$ - traction forces.

We can summarize the governing equations of a BVP for the quasi-static problem with a discontinuity as (see Chapter 2):

BOUNDARY VALUE PROBLEM - BVP - With discontinuity			
Equilibrium equation	$\nabla \cdot \boldsymbol{\sigma}(\mathbf{x}) + \mathbf{b}(\mathbf{x}) = \mathbf{0}$	$\forall\, \mathbf{x} \in \mathcal{B} \setminus \mathcal{S}$	(4.1)
Constitutive equation	$\boldsymbol{\sigma} = \Sigma(\boldsymbol{\varepsilon}(\mathbf{x}))$	$\forall\, \mathbf{x} \in \mathcal{B}$	(4.2)
Kinematic equation	$\boldsymbol{\varepsilon} = \nabla^{sym}\mathbf{u} = \dfrac{1}{2}\left(\nabla \otimes \mathbf{u} + \mathbf{u} \otimes \nabla\right)$	$\forall\, \mathbf{x} \in \mathcal{B}$	(4.3)
Outer traction continuity	$\boldsymbol{\mathcal{T}}^- = \boldsymbol{\mathcal{T}}^+ \Leftrightarrow \mathbf{N}\cdot\boldsymbol{\sigma}^- = \mathbf{N}\cdot\boldsymbol{\sigma}^+$	$\forall\, \mathbf{x} \in \mathcal{S}$	(4.4)
Essential boundary conditions	$\mathbf{u} = \mathbf{u}^*(\mathbf{x})$	$\forall\, \mathbf{x} \in \partial_{\mathbf{u}}\mathcal{B}$	(4.5)
Natural boundary conditions	$\mathbf{t} = \mathbf{t}^*(\mathbf{x}) = \boldsymbol{\upsilon}\cdot\boldsymbol{\sigma}$	$\forall\, \mathbf{x} \in \partial_{\boldsymbol{\sigma}}\mathcal{B}$	(4.6)
Inner traction continuity	$\boldsymbol{\mathcal{T}}^+ = \boldsymbol{\mathcal{T}}_{\mathcal{S}} \Leftrightarrow \mathbf{N}\cdot\boldsymbol{\sigma}^+ = \mathbf{N}\cdot\boldsymbol{\sigma}_{\mathcal{S}}$	$\forall\, \mathbf{x} \in \mathcal{S}$	(4.7)
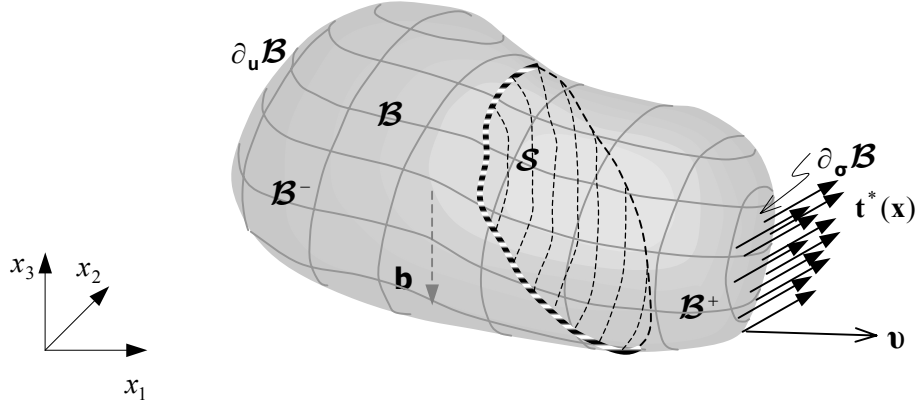
Figure 4.1: Domain of the body $\mathcal{B}$.

4.2.1 Redefinition of the kinematics

In order to devise a convenient format for the fields that are going to be discretized, a redefinition of the kinematics presented in Chapter 3 will be performed.

- The new expression of the discontinuous displacement field reads:

$$\dot{\mathbf{u}}(\mathbf{x},t) = \dot{\bar{\mathbf{u}}}(\mathbf{x},t) + \mathcal{M}_{\mathcal{S}}(\mathbf{x})[\![\dot{\mathbf{u}}]\!](\mathbf{x},t) \tag{4.8}$$

Function $\mathcal{M}_{\mathcal{S}}$ satisfies the following conditions (see Figure 4.2):

i.   The jump across $\mathcal{S}$ is $[\![\mathcal{M}_{\mathcal{S}}]\!] = 1$;

ii.   The support of $\mathcal{M}_{\mathcal{S}}$ is $\mathcal{B}_h$.

The function $\mathcal{M}_{\mathcal{S}}$ is defined as:

$$\mathcal{M}_{\mathcal{S}}(\mathbf{x}) = H_{\mathcal{S}}(\mathbf{x}) - \varphi(\mathbf{x}) \tag{4.9}$$

where $H_{\mathcal{S}}$ is the Heaviside function and φ is a continuous function which is completely arbitrary except for the following two conditions:

$$\varphi(\mathbf{x}) = \begin{cases} 0 & \forall \mathbf{x} \in \mathcal{B}^- \\ 1 & \forall \mathbf{x} \in \mathcal{B}^+ \end{cases} \tag{4.10}$$

- The corresponding enhanced strain field reads:

$$\dot{\boldsymbol{\varepsilon}}(\mathbf{x},t) = \nabla^{sym}\dot{\mathbf{u}} = \underbrace{\nabla^{sym}\dot{\bar{\mathbf{u}}}}_{\dot{\bar{\boldsymbol{\varepsilon}}}} + \underbrace{\left[[\![\dot{\mathbf{u}}]\!] \otimes \left(\delta_{\mathcal{S}}^h(\mathbf{x})\mathbf{N} - \nabla\varphi(\mathbf{x}) \right) \right]^{sym}}_{\dot{\tilde{\boldsymbol{\varepsilon}}}} \tag{4.11}$$

$$\dot{\boldsymbol{\varepsilon}}(\mathbf{x},t) = \dot{\bar{\boldsymbol{\varepsilon}}} + \dot{\tilde{\boldsymbol{\varepsilon}}}$$

where $\delta_{\mathcal{S}}^{h}$ is defined as:

$$\delta_{\mathcal{S}}^{h}(\mathbf{x}) = \begin{cases} \dfrac{1}{h}\chi_{\mathcal{S}}(\mathbf{x}) & \rightarrow \quad \textit{Weak discontinutiy} \\[2mm] & \downarrow\ h \rightarrow k \\[2mm] \dfrac{1}{k}\chi_{\mathcal{S}}(\mathbf{x}) & \rightarrow \quad \textit{Strong discontinutiy} \end{cases} \tag{4.12}$$

and $\chi_{\mathcal{S}}(\mathbf{x})$ stands for the collocation function defined as:

$$\chi_{\mathcal{S}}(\mathbf{x}) = \begin{cases} 1 & \forall \mathbf{x} \in \mathcal{B}_{h} \\ 0 & \forall \mathbf{x} \in \mathcal{B} \setminus \mathcal{B}_{h} \end{cases} \tag{4.13}$$
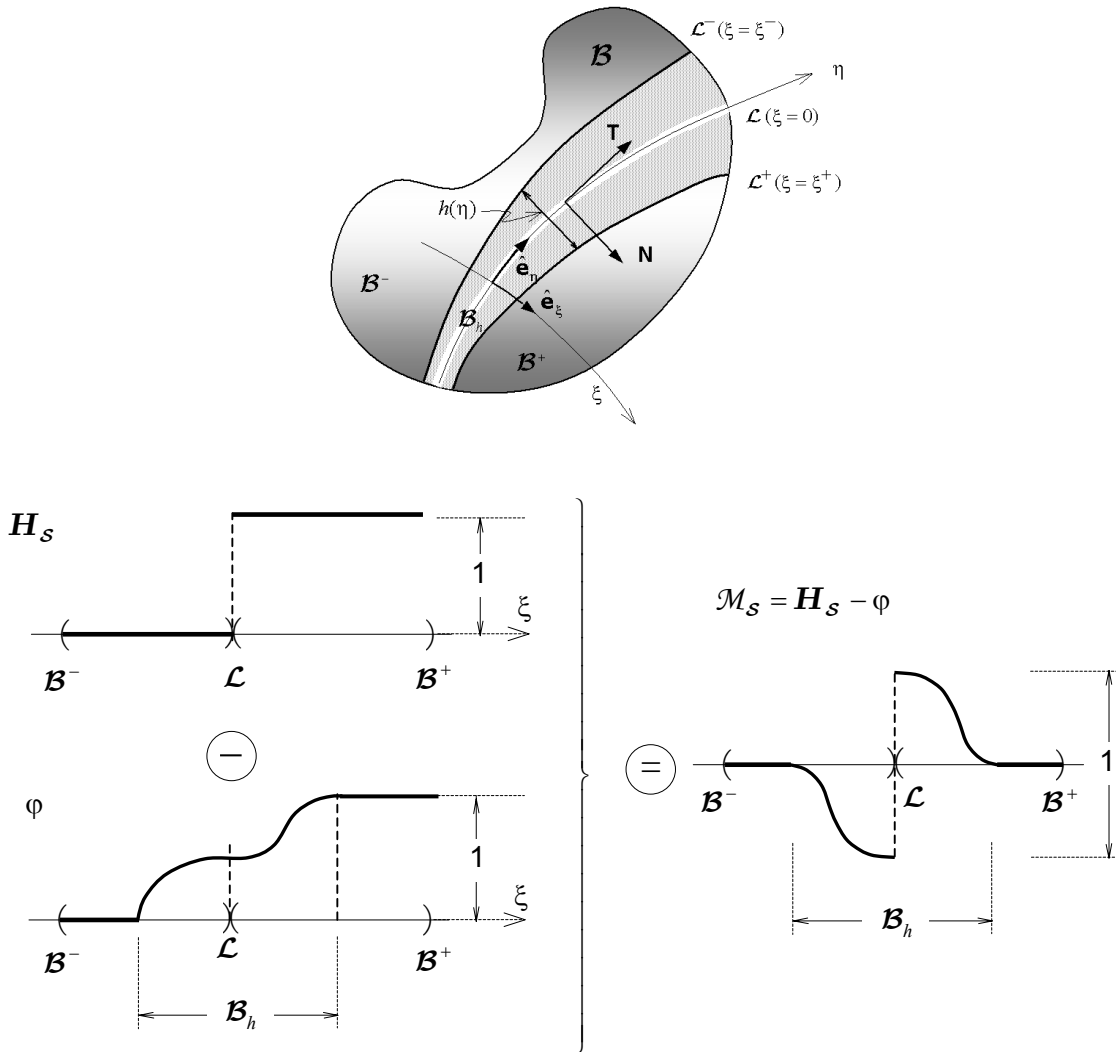
Figure 4.2: Construction of the function $\mathcal{M}_{\mathcal{S}}$.

4.3 Variational formulation

In light of the governing equations above, we consider the following variational problem:

Given:

$$\mathcal{V}_{\boldsymbol{\eta}} := \left\{ \boldsymbol{\eta} = \overline{\boldsymbol{\eta}} + \mathcal{M}_{\mathcal{S}} \widetilde{\boldsymbol{\eta}} \quad ; \quad \overline{\boldsymbol{\eta}} \in \left[H^1(V) \right]^{n_{\dim}} \quad \widetilde{\boldsymbol{\eta}} \in \left[L_2(\mathcal{S}) \right] \quad \overline{\boldsymbol{\eta}} \big|_{\partial_u \mathcal{B}} = \mathbf{u}^* \right\}$$

(4.14)

$$\mathcal{V}_{\boldsymbol{\eta}}^0 := \left\{ \overline{\boldsymbol{\eta}} \in \left[H^1(V) \right]^{n_{\dim}} \quad \overline{\boldsymbol{\eta}} \big|_{\partial_u \mathcal{B}} = \mathbf{0} \right\}$$

Find:

$$\mathbf{u} \in \mathcal{V}_{\boldsymbol{\eta}} \qquad\qquad \mathbf{u} = \overline{\mathbf{u}} + \mathcal{M}_{\mathcal{S}} [\![\mathbf{u}]\!]$$

(4.15)

Such that:

$$\int_{\mathcal{B}} \boldsymbol{\sigma}(\boldsymbol{\varepsilon}) : \nabla^{sym} \overline{\boldsymbol{\eta}} \, \mathrm{d}V - \int_{\mathcal{B}} \overline{\boldsymbol{\eta}} \cdot \mathbf{b} \, \mathrm{d}V - \int_{\partial_\sigma \mathcal{B}} \overline{\boldsymbol{\eta}} \cdot \mathbf{t}^* \, \mathrm{d}A = 0 \qquad \forall \overline{\boldsymbol{\eta}} \in \mathcal{V}_{\boldsymbol{\eta}}^0$$

(4.16)

By using standard arguments it can be shown that the strong form of Equation (4.16) are the equations (4.1), (4.4), and (4.6). Equations (4.2) and (4.3) are assumed to be imposed in strong form.

On the other hand, the inner traction continuity (4.7) has to be imposed independently of the variational statement (4.16). This can be done in weak form through:

$$\int \boldsymbol{\eta} \cdot \left(\boldsymbol{\sigma}_{\mathcal{S}} - \boldsymbol{\sigma}_{\mathcal{B} \setminus \mathcal{S}} \right) \cdot \mathbf{N} \, \mathrm{d}V = 0 \qquad \forall \boldsymbol{\eta} \in L_2(\mathcal{S})$$

(4.17)

4.4 Spatial discretization and solution

We begin by discretizing the domain $\mathcal{B}$ into elemental subdomains $\overline{\mathcal{B}}_e$ (see Figure 4.3) such that:

$$\mathcal{B} \approx \bigcup_{e=1}^{n_{el}} \overline{\mathcal{B}}_e \qquad (4.18)$$

where $\overline{\mathcal{B}}_e$ is the closure of an individual element.
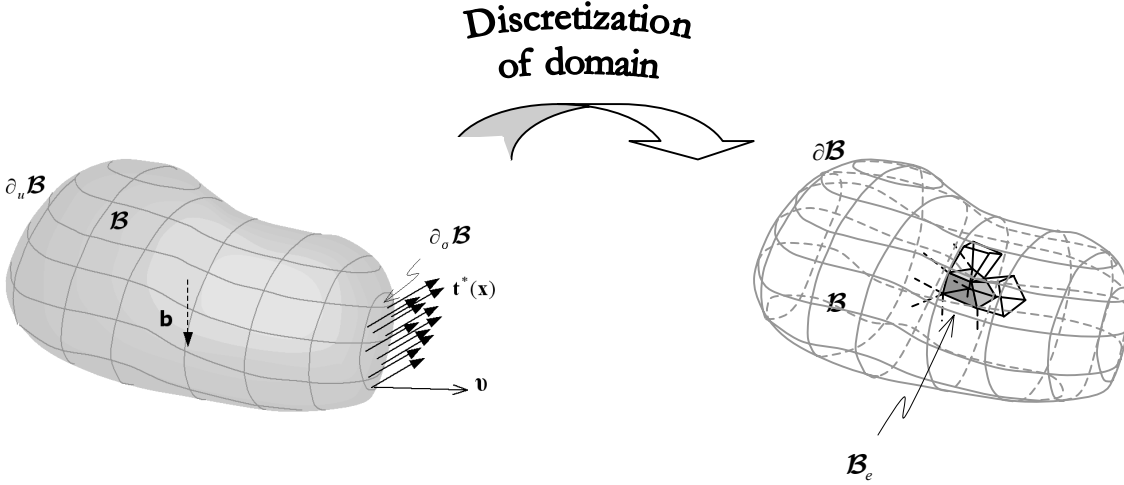
Figure 4.3: Discretization of the domain $\mathcal{B}$ by a finite element mesh.

After discretization, the independent variable **u** (displacement) is interpolated by functions of compatible order within each element, in terms of values to be determined at a set of nodal points. With the objective of developing the equations for these nodal point unknowns, an individual element may be separated from the assembled system. Inside each finite element, a scalar or a vector function is approximated by a linear combination of shape functions associated with its nodes. Within an element $\overline{\mathcal{B}}_e$ with n_{node} nodes, we define the reference geometry $\mathbf{x}^e$ and displacement field $\mathbf{u}^e$ over a typical element as:

$$\mathbf{x}^e = \sum_{i=1}^{n_{node}} \overline{\mathbb{N}}_i \hat{\mathbf{x}}_i \qquad ; \qquad \mathbf{u}^e = \sum_{i=1}^{n_{node}} \mathbb{N}_i \mathbf{a}_i \qquad (4.19)$$

where $\mathbb{N}_i$ is the matrix containing the shape functions and $\mathbf{a}_i$ is the nodal displacement. In general $\overline{\mathbb{N}}_i = \mathbb{N}_i$. The strain field[1] is given by:

$$\{\boldsymbol{\varepsilon}\} = \nabla^{sym}\mathbf{u} = \mathbb{L}_e\mathbf{u}_e = \nabla\mathbb{N}_e\mathbf{a}_e = \mathbf{B}_e\mathbf{a}_e \qquad (4.20)$$

---

[1] Here we are using the Voigt notation, see Appendix A.

where the operator $\mathbb{L}$ and the strain interpolation matrix $\mathbf{B}$ are given by:

$$\mathbb{L} = \begin{bmatrix} \dfrac{\partial}{\partial x_1} & 0 & 0 \\[2mm] 0 & \dfrac{\partial}{\partial x_2} & 0 \\[2mm] 0 & 0 & \dfrac{\partial}{\partial x_3} \\[2mm] \dfrac{\partial}{\partial x_2} & \dfrac{\partial}{\partial x_1} & 0 \\[2mm] \dfrac{\partial}{\partial x_3} & 0 & \dfrac{\partial}{\partial x_1} \\[2mm] 0 & \dfrac{\partial}{\partial x_3} & \dfrac{\partial}{\partial x_2} \end{bmatrix} \quad ; \quad \mathbf{B}_i = \begin{bmatrix} \dfrac{\partial \mathbb{N}_i}{\partial x_1} & 0 & 0 \\[2mm] 0 & \dfrac{\partial \mathbb{N}_i}{\partial x_2} & 0 \\[2mm] 0 & 0 & \dfrac{\partial \mathbb{N}_i}{\partial x_3} \\[2mm] \dfrac{\partial \mathbb{N}_i}{\partial x_2} & \dfrac{\partial \mathbb{N}_i}{\partial x_1} & 0 \\[2mm] \dfrac{\partial \mathbb{N}_i}{\partial x_3} & 0 & \dfrac{\partial \mathbb{N}_i}{\partial x_1} \\[2mm] 0 & \dfrac{\partial \mathbb{N}_i}{\partial x_3} & \dfrac{\partial \mathbb{N}_i}{\partial x_2} \end{bmatrix} \tag{4.21}$$

being i the node number.

4.4.1 Approximation of the regular part of the displacement field

In this section we deal with two types of finite elements: the tetrahedron (4 nodes element with linear interpolation of the displacement field) and the hexahedron (8 nodes element).

4.4.1.1 Tetrahedral finite element

The first-order tetrahedral finite element in the global (x_1, x_2, x_3) and local (ξ, η, ζ) coordinate systems are shown in Figure 4.4.
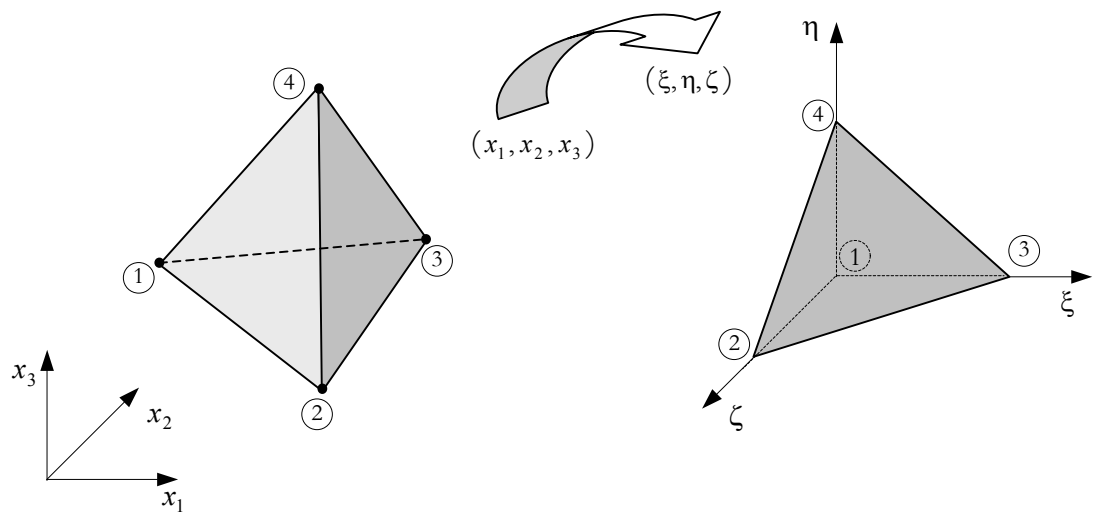
Figure 4.4: First-order tetrahedral finite element in global and local coordinates.

The displacement field in the finite element can be expressed by its nodal displacements:

$$\mathbf{u} = \begin{Bmatrix} u \\ v \\ w \end{Bmatrix} = \begin{Bmatrix} \mathbb{N}_1 u_1 + \mathbb{N}_2 u_2 + \mathbb{N}_3 u_3 + \mathbb{N}_4 u_4 \\ \mathbb{N}_1 v_1 + \mathbb{N}_2 v_2 + \mathbb{N}_3 v_3 + \mathbb{N}_4 v_4 \\ \mathbb{N}_1 w_1 + \mathbb{N}_2 w_2 + \mathbb{N}_3 w_3 + \mathbb{N}_4 w_4 \end{Bmatrix} = \mathbb{N}\mathbf{a} \tag{4.22}$$

Hence, the shape function of node i of the tetrahedron e is defined as follows:

$$\mathbb{N} = \{\mathbb{N}_1 , \ \mathbb{N}_2 , \ \mathbb{N}_3 , \ \mathbb{N}_4\} \quad ; \quad \mathbb{N}_i = \begin{bmatrix} \mathbb{N}_i & 0 & 0 \\ 0 & \mathbb{N}_i & 0 \\ 0 & 0 & \mathbb{N}_i \end{bmatrix} \tag{4.23}$$

and

$$\mathbf{a} = \begin{Bmatrix} \mathbf{a}_1 \\ \mathbf{a}_2 \\ \mathbf{a}_3 \\ \mathbf{a}_4 \end{Bmatrix} \quad ; \quad \mathbf{a}_i = \begin{Bmatrix} u_i \\ v_i \\ w_i \end{Bmatrix} \tag{4.24}$$

4.4.1.2 Hexahedral finite element

The generalization of a 3D quadrilateral is a hexahedron, commonly known in finite element literature as "brick", Felippa (2002) (see Figure 4.5).
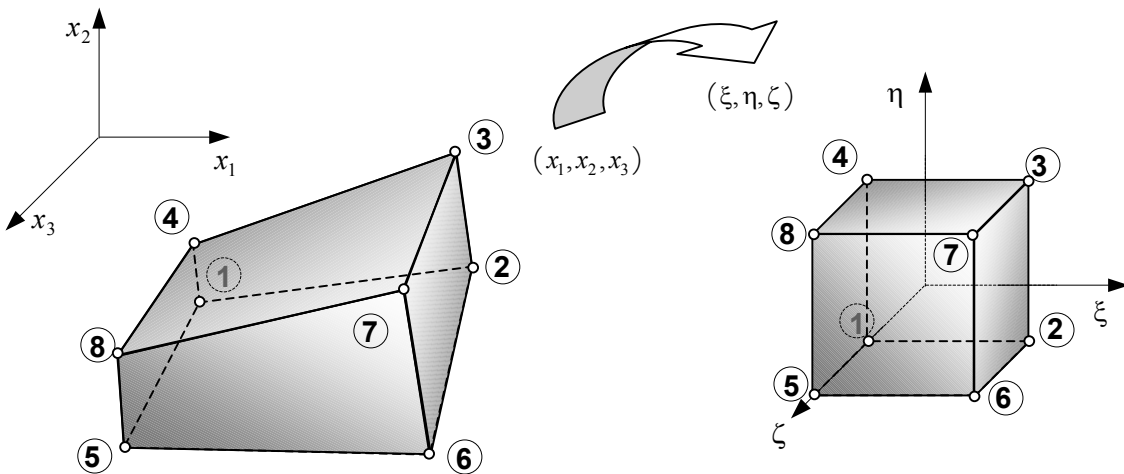
Figure 4.5: First-order hexahedral nodal finite element in global and local coordinates.

The displacement field is given by:

$$\mathbf{u} = \sum_{i=1}^{8} \mathbb{N}_i \mathbf{u}_i \quad ; \quad \mathbf{v} = \sum_{i=1}^{8} \mathbb{N}_i \mathbf{v}_i \quad ; \quad \mathbf{w} = \sum_{i=1}^{8} \mathbb{N}_i \mathbf{w}_i \tag{4.25}$$

The nodal shape function in local coordinates (ξ, η, ζ) for the hexahedral element in Figure 4.5 can be written as:

$$\mathbb{N}_i = \frac{1}{8}(1 + \xi\xi_i)(1 + \eta\eta_i)(1 + \zeta\zeta_i) \tag{4.26}$$

where (ξ_i, η_i, ζ_i) are the local coordinates of node i.

4.4.2 Approximating displacement field in an enhanced element

To capture the displacement jump $[\![\mathbf{u}]\!]$ an additional node to the standard finite element is necessary (see Figure 4.6 and Figure 4.7).
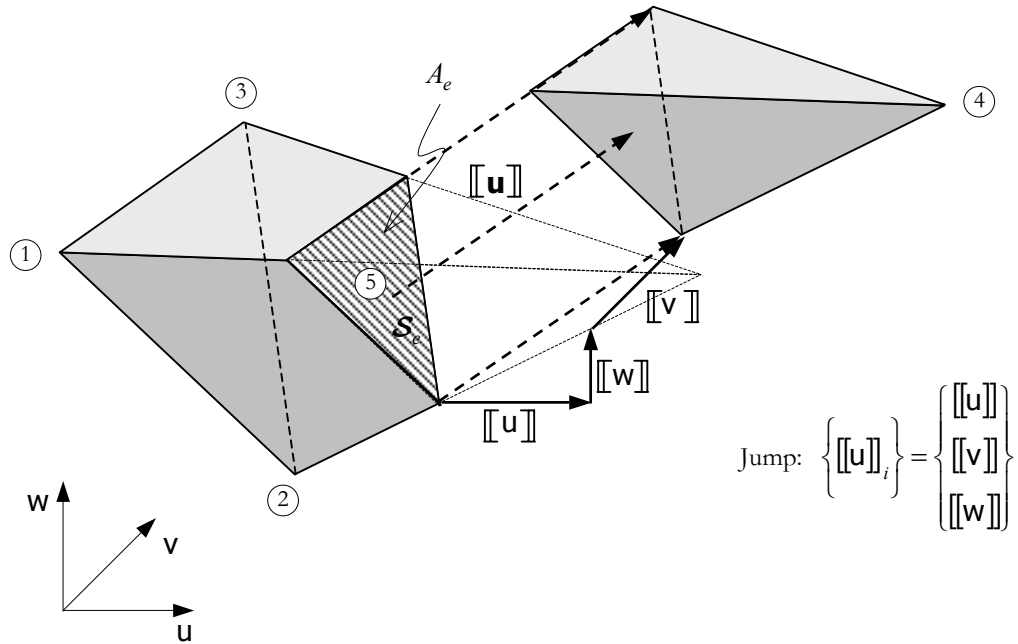
Figure 4.6: Discontinuity in displacement - Jump.
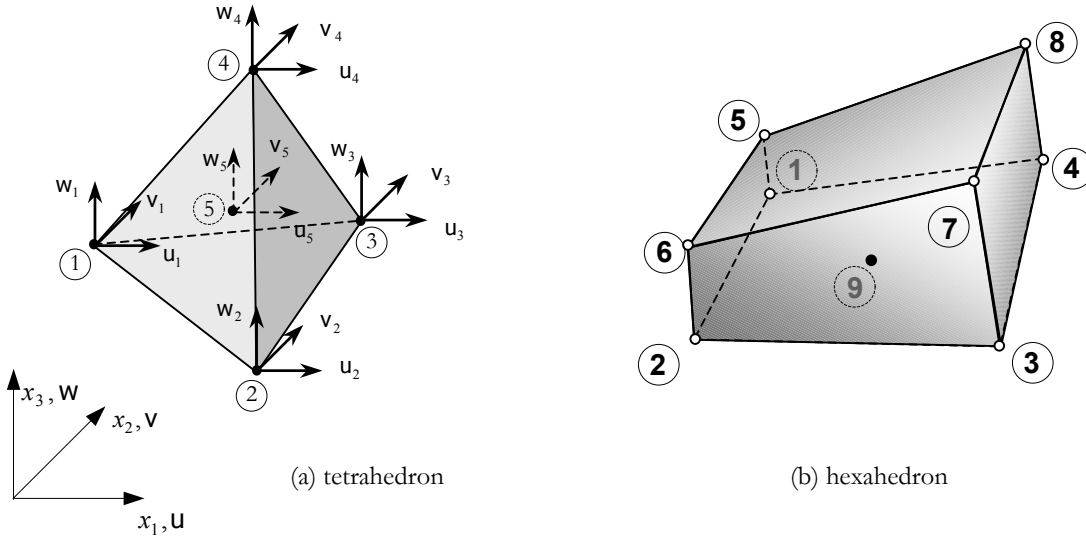
Figure 4.7: Enhanced element - Nodal displacement with additional node.

Motivated by the kinematics of equation (4.11) the following discrete displacement field is proposed:

$$\mathbf{u}(\mathbf{x},t) = \mathbb{N}(\mathbf{x})\,\mathbf{a}_e + \mathcal{M}_{\mathcal{S}}(\mathbf{x})\boldsymbol{\alpha}_e$$

$$\Rightarrow \mathbf{u}(\mathbf{x},t) = \mathbb{N}(\mathbf{x})\,\mathbf{a}_e + \left[\boldsymbol{H}_{\mathcal{S}}(\mathbf{x}) - \varphi_e(\mathbf{x})\right]\boldsymbol{\alpha}_e$$

(4.27)

where $\mathbb{N}$ contains the shape functions corresponding to the regular underlying element and $\left(\mathcal{M}_{\mathcal{S}}(\mathbf{x}) = \boldsymbol{H}_{\mathcal{S}}(\mathbf{x}) - \varphi_e(\mathbf{x})\right)$ is the unit jump function (Heaviside function) shown in Figure 4.8 for the two-dimensional (2D) case and $\boldsymbol{\alpha}_e$ represents the elemental displacement jump in global coordinates. In Figure 4.8 the discontinuity line $\mathcal{L}_e$ divides the element into two subdomains: $\mathcal{B}^-$ and $\mathcal{B}^+$. Observe that the normal $\mathbf{N}$ always points towards $\mathcal{B}^+$.

In equation (4.27), φ_e is given by the combination of the shape function of the nodes which lie down in domain $\mathcal{B}^+$:

$$\varphi_e = \sum \mathbb{N}_i \quad \forall\ i \,\Big|\ \mathbf{x}_i\ \in \overline{\mathcal{B}}_e^{\,+}$$

(4.28)

For example, in Figure 4.9(a), where we are using a Constant Strain Triangle (CST) finite element, we have the case where $\varphi_e = \mathbb{N}_4$ and in Figure 4.9(b), where we are using the tetrahedron, $\varphi_e = \mathbb{N}_2 + \mathbb{N}_4$.
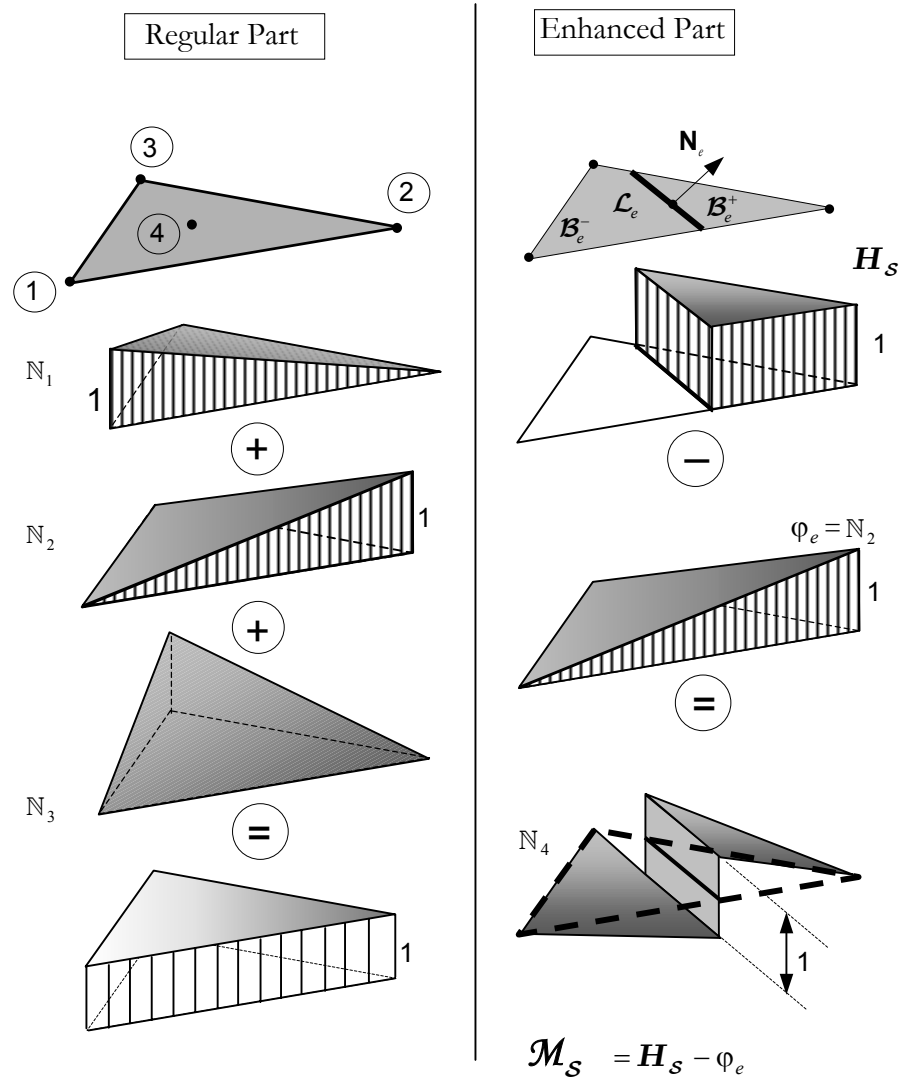
Figure 4.8: The discontinuous shape function (CST element).

(a) (b)
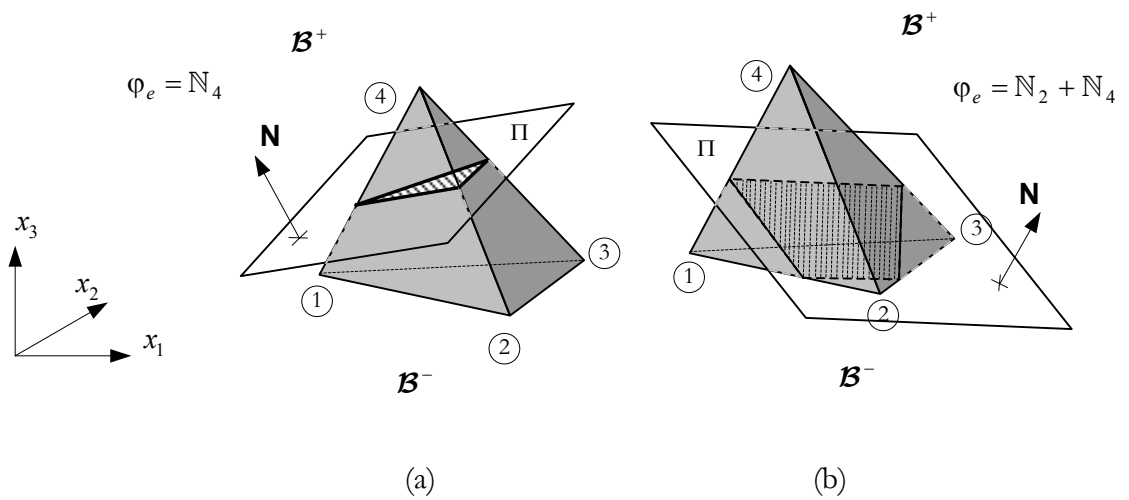
Figure 4.9: Discontinuity surface and tetrahedron intersection.

4.4.3 Approximation of the enhanced strain field

From the displacement field in equation (4.27) the corresponding (rate of) strain field reads:

$$\{\dot{\boldsymbol{\varepsilon}}\}(\mathbf{x},t) = \{\dot{\overline{\boldsymbol{\varepsilon}}}\}(\mathbf{x},t) + \{\dot{\widetilde{\boldsymbol{\varepsilon}}}\}(\mathbf{x},t) = \underbrace{\mathbf{B}(\mathbf{x},t)\dot{\mathbf{a}}_e}_{Regular} + \underbrace{\mathbf{G}_e}_{Enhanced}\dot{\boldsymbol{\alpha}}_e \tag{4.29}$$

where the first term corresponds to the strains provided by the regular underlying element with nodal degrees of freedom $\mathbf{a}_e$ and deformation matrix $\mathbf{B}$. The second term corresponds to a strain enhancement in terms of the elemental displacement jump $\boldsymbol{\alpha}_e$ and the deformation matrix $\mathbf{G}_e$ that contains the unbounded (regularized) Dirac delta distribution $\delta^h_{\mathcal{S}}$, see equation (4.12), emerging from the spatial derivation of the step function $\boldsymbol{H}_{\mathcal{B}_h}$ in equation (4.27) namely,

$$\mathbf{G}_e(\mathbf{x}) = \delta^h_{\mathcal{S}}(\mathbf{x})\boldsymbol{\mathcal{N}}(\mathbf{x}) - \nabla\varphi_e(\mathbf{x}) \tag{4.30}$$

where

$$\boldsymbol{\mathcal{N}} = \begin{bmatrix} N_1 & 0 & 0 \\ 0 & N_2 & 0 \\ 0 & 0 & N_3 \\ N_2 & N_1 & 0 \\ N_3 & 0 & N_1 \\ 0 & N_3 & N_2 \end{bmatrix} \tag{4.31}$$

thus

$$\mathbf{G}_e(\mathbf{x}) = \begin{bmatrix} \delta^h_{\mathcal{S}} N_1 - \dfrac{\partial\varphi_e}{\partial x_1} & 0 & 0 \\[2ex] 0 & \delta^h_{\mathcal{S}} N_2 - \dfrac{\partial\varphi_e}{\partial x_2} & 0 \\[2ex] 0 & 0 & \delta^h_{\mathcal{S}} N_3 - \dfrac{\partial\varphi_e}{\partial x_3} \\[2ex] \delta^h_{\mathcal{S}} N_2 - \dfrac{\partial\varphi_e}{\partial x_2} & \delta^h_{\mathcal{S}} N_1 - \dfrac{\partial\varphi_e}{\partial x_1} & 0 \\[2ex] \delta^h_{\mathcal{S}} N_3 - \dfrac{\partial\varphi_e}{\partial x_3} & 0 & \delta^h_{\mathcal{S}} N_1 - \dfrac{\partial\varphi_e}{\partial x_1} \\[2ex] 0 & \delta^h_{\mathcal{S}} N_3 - \dfrac{\partial\varphi_e}{\partial x_3} & \delta^h_{\mathcal{S}} N_2 - \dfrac{\partial\varphi_e}{\partial x_2} \end{bmatrix} \tag{4.32}$$

Now, attention must be paid to the inner traction continuity condition stated in equation (4.7). The traction vector $\boldsymbol{\mathcal{T}}$ in Voigt notation is defined as follows:

$$\mathcal{T} = \mathbf{N} \cdot \boldsymbol{\sigma} \xrightarrow{\text{Voigt}} \mathcal{T} = \mathcal{N}^T \{\boldsymbol{\sigma}\}$$

$$\begin{Bmatrix} \mathcal{T}_1^{(\hat{\mathbf{N}})} \\ \mathcal{T}_2^{(\hat{\mathbf{N}})} \\ \mathcal{T}_3^{(\hat{\mathbf{N}})} \end{Bmatrix} = \begin{bmatrix} N_1 & 0 & 0 & N_2 & N_3 & 0 \\ 0 & N_2 & 0 & N_1 & 0 & N_3 \\ 0 & 0 & N_3 & 0 & N_1 & N_2 \end{bmatrix} \begin{Bmatrix} \sigma_{11} \\ \sigma_{22} \\ \sigma_{33} \\ \sigma_{12} \\ \sigma_{13} \\ \sigma_{23} \end{Bmatrix} \tag{4.33}$$

thus

$$\mathcal{T} = \mathcal{N}^T \{\boldsymbol{\sigma}\} = \mathcal{N}^T \{\boldsymbol{\sigma}\}^+ = \mathcal{N}^T \{\boldsymbol{\sigma}\}^- = \mathcal{N}^T \{\boldsymbol{\sigma}\}_{\mathcal{B}_e \setminus \mathcal{S}_e} \tag{4.34}$$

where $\{\boldsymbol{\sigma}\}_{\mathcal{B}_e \setminus \mathcal{S}_e}$ stands for stress at $\mathcal{B}_e \setminus \mathcal{S}_e$.
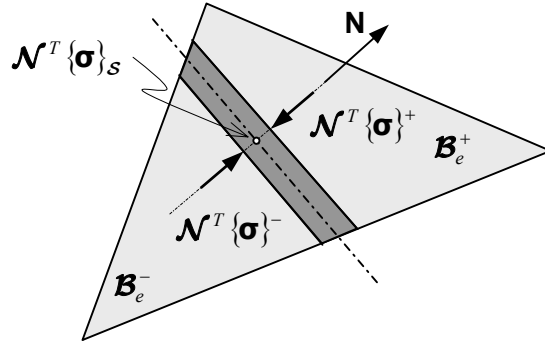
Figure 4.10: Traction vector continuity – CST finite element.

On an element by element basis the inner traction continuity equation (4.34) is imposed in weak form from equation (4.17) resulting in the additional set of equations:

$$\int_{\mathcal{B}_e} \mathbf{G}_e^{*T} \{\boldsymbol{\sigma}\} \, dV_e = \mathbf{0} \quad \forall e = 1, \dots n_e \tag{4.35}$$

with

$$\mathbf{G}_e^* = \begin{cases} \left(\delta_{\mathcal{S}}^h - \dfrac{A_e}{V_e} \right) \mathcal{N} & \mathbf{x} \in \mathcal{B}_e \\ \\ \mathbf{0} & otherwise \end{cases} \tag{4.36}$$

and A_e being the area of $\mathcal{S}_e$ (see Figure 4.6). Substitution of equation (4.36) into equation (4.35), leads to:

$$\int_{\mathcal{S}_e} \mathcal{N}^T \{\boldsymbol{\sigma}\}^h \, dA - \frac{A_e}{V_e} \int_{\mathcal{B}_e \setminus \mathcal{S}_e} \mathcal{N}^T \{\boldsymbol{\sigma}\}^h \, dV = \mathbf{0} \tag{4.37}$$

which can be rewritten as:

$$\underbrace{\frac{1}{A_e} \int_{\mathcal{S}_e} \boldsymbol{\mathcal{N}}^T \{\boldsymbol{\sigma}\}^h \; \mathrm{d}A}_{\text{average on } \mathcal{S}_e} = \underbrace{\frac{1}{V_e} \int_{\mathcal{B}_e \backslash \mathcal{S}_e} \boldsymbol{\mathcal{N}}^T \{\boldsymbol{\sigma}\}^h \; \mathrm{d}V}_{\text{average on } \mathcal{B}_e \backslash \mathcal{S}_e} \tag{4.38}$$

In 2D cases the area A_e becomes the length ℓ_e of $\mathcal{L}_e$ and the volume becomes the area of the finite element (see Figure 4.11).

Observe that the matrix $\mathbf{G}_e^*$ appearing in equation (4.36) fulfills the following condition:

$$\int_{\mathcal{B}_e} \mathbf{G}_e^* \; \mathrm{d}V = \mathbf{0} \tag{4.39}$$

It is possible to check that the spaces generated by the regular strain $\bar{\boldsymbol{\varepsilon}}$ and the enhanced strains $\widetilde{\boldsymbol{\varepsilon}}$, denoted by $\hat{\mathcal{V}}^h$ and $\widetilde{\mathcal{V}}^h$ respectively, are such that:

$$\hat{\mathcal{V}}^h \cap \widetilde{\mathcal{V}}^h = \{\mathbf{0}\} \tag{4.40}$$

Conditions (4.39) and (4.40) are sufficient to guarantee the consistency and stability requirements for the proposed assumed strain approximation, Simo&Rifai(1990).
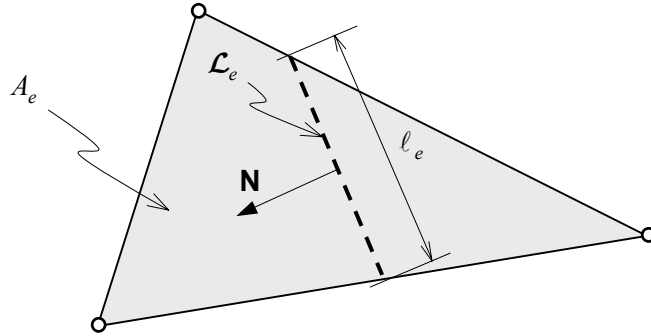
Figure 4.11: Discontinuity CST finite element.

4.4.4 System of algebraic equations

The problem to be discretized has as enhanced weak form, equations (4.16) and (4.17):

$$\begin{cases} \displaystyle\int_{\mathcal{B}} \nabla^{sym}\boldsymbol{\eta} : \boldsymbol{\sigma}(\boldsymbol{\varepsilon}) \; \mathrm{d}V = \int_{\mathcal{B}} \boldsymbol{\eta} \cdot \mathbf{b} \; \mathrm{d}V - \int_{\partial_\sigma \mathcal{B}} \boldsymbol{\eta} \cdot \mathbf{t}^* \; \mathrm{d}A \\[2em] \displaystyle\int_{\mathcal{B}_e} \boldsymbol{\eta} \cdot \left(\boldsymbol{\sigma}_{\mathcal{S}} - \boldsymbol{\sigma}_{\mathcal{B}\backslash\mathcal{S}}\right) \cdot \mathbf{N} \; \mathrm{d}V = 0 \end{cases} \tag{4.41}$$

Introducing the finite element interpolation in the weak equation (4.41) yields:

$$\mathbf{R}(\mathbf{a},\boldsymbol{\alpha}) := \mathbf{F}_{ext} - \overset{n_{el}}{\underset{e=1}{\mathbf{A}}} \left(\int_{\mathcal{B}_e \backslash \mathcal{S}_e} \mathbf{B}^T \{\boldsymbol{\sigma}\} dV_e \right) = \mathbf{0} \tag{4.42}$$

$$\mathbf{r}(\mathbf{a},\boldsymbol{\alpha}^{(e)}) := \int_{\mathcal{B}_e} \mathbf{G}_e^{*T} \{\boldsymbol{\sigma}\} dV_e = \mathbf{0} \quad \forall e = 1,...n_E \tag{4.43}$$

where $\mathbf{A}$ is the standard finite-element assembly operator and n_{el} the number of elements and n_E the number of elements which contain the discontinuity path and $\mathbf{F}_{ext}$ stands for the external forces. Thus, we can say (in rate form):

$$\begin{cases} \overset{n_{el}}{\underset{e=1}{\mathbf{A}}} \int_{\mathcal{B}} [\mathbf{B}^T \mathcal{C} \, \mathbf{B}] dV \, \dot{\mathbf{a}}_e + \int_{\mathcal{B}} [\mathbf{B}^T \mathcal{C} \, \mathbf{G}_e] dV \, \dot{\boldsymbol{\alpha}}_e = \dot{\mathbf{F}}_{ext} \\[2em] \int_{\mathcal{B}} \left[\mathbf{G}_e^{*T} \mathcal{C} \, \mathbf{B} \right] dV \, \dot{\mathbf{a}}_e + \int_{\mathcal{B}} \left[\mathbf{G}_e^{*T} \mathcal{C} \, \mathbf{G}_e \right] dV \, \dot{\boldsymbol{\alpha}}_e = \mathbf{0} \end{cases} \tag{4.44}$$

We can express the above equation as:

$$\begin{bmatrix} \mathbf{K}_{e(aa)} & \mathbf{K}_{e(a\alpha)} \\ \mathbf{K}_{e(\alpha a)} & \mathbf{K}_{e(\alpha\alpha)} \end{bmatrix} \begin{Bmatrix} \dot{\mathbf{a}}_e \\ \dot{\boldsymbol{\alpha}}_e \end{Bmatrix} - \begin{Bmatrix} \dot{\mathbf{F}}_{ext} \\ \mathbf{0} \end{Bmatrix} = \begin{Bmatrix} \dot{\mathbf{R}}_e \\ \dot{\mathbf{r}}_e \end{Bmatrix} \tag{4.45}$$

with

$$\mathbf{K}_{aa}^e = \int_{\mathcal{B}_e} [\mathbf{B}^T \mathcal{C} \, \mathbf{B}] dV$$

$$\mathbf{K}_{a\alpha}^e = \int_{\mathcal{B}_e} [\mathbf{B}^T \mathcal{C} \, \mathbf{G}_e] dV$$

$$\mathbf{K}_{\alpha a}^e = \int_{\mathcal{B}_e} [\mathbf{G}_e^{*T} \mathcal{C} \, \mathbf{B}] dV \tag{4.46}$$

$$\mathbf{K}_{\alpha\alpha}^e = \int_{\mathcal{B}_e} [\mathbf{G}_e^{*T} \mathcal{C} \, \mathbf{G}_e] dV$$

the elemental tangent stiffness matrix $\mathbf{K}_e$, which is clearly non-symmetric due to the fact that $\mathbf{G}_e \neq \mathbf{G}_e^*$.:

$$\mathbf{K}_e = \begin{bmatrix} \mathbf{K}_{aa}^e & \mathbf{K}_{a\alpha}^e \\ \mathbf{K}_{\alpha a}^e & \mathbf{K}_{\alpha\alpha}^e \end{bmatrix} \tag{4.47}$$

We can also express (4.44) in local coordinates $(\mathsf{N},\mathsf{S},\mathsf{T})$, *i.e.:*

$$\int_{\mathcal{B}} \begin{bmatrix} \begin{bmatrix} \mathbf{B}^T \mathcal{C} \, \mathbf{B} \end{bmatrix} & \begin{bmatrix} \mathbf{B}^T \mathcal{C} \, \overline{\mathbf{G}}_e \end{bmatrix} \\ \begin{bmatrix} \mathbf{G}^{*T}_e \mathcal{C} \, \mathbf{B} \end{bmatrix} & \begin{bmatrix} \mathbf{G}^{*T}_e \mathcal{C} \, \overline{\mathbf{G}}_e \end{bmatrix} \end{bmatrix} dV \begin{Bmatrix} \mathbf{a}_e \\ [[\mathbf{u}]] \end{Bmatrix} = \begin{Bmatrix} \boldsymbol{f}_{e,\text{int}} \\ \mathbf{0} \end{Bmatrix} \tag{4.48}$$

where $[[\mathbf{u}]]_i^T = \Big\{ [[\mathbf{u}]]; \quad [[\mathbf{v}]]; \quad [[\mathbf{w}]] \Big\}$ is the jump in the local coordinates (see Figure 4.12).
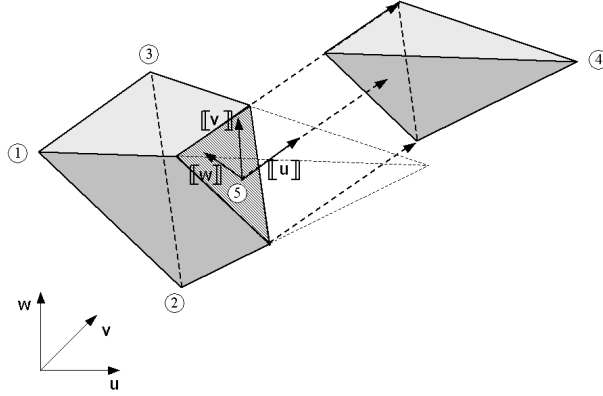
Figure 4.12: Displacement jump in local coordinates.

where :

$$\overline{\mathbf{G}}_e = \begin{bmatrix} \delta^h_{\mathcal{S}} N_1 - \dfrac{\partial \varphi_e}{\partial x_1} & 0 & 0 \\ 0 & \delta^h_{\mathcal{S}} N_2 - \dfrac{\partial \varphi_e}{\partial x_2} & 0 \\ 0 & 0 & \delta^h_{\mathcal{S}} N_3 - \dfrac{\partial \varphi_e}{\partial x_3} \\ \delta^h_{\mathcal{S}} N_2 - \dfrac{\partial \varphi_e}{\partial x_2} & \delta^h_{\mathcal{S}} N_1 - \dfrac{\partial \varphi_e}{\partial x_1} & 0 \\ \delta^h_{\mathcal{S}} N_3 - \dfrac{\partial \varphi_e}{\partial x_3} & 0 & \delta^h_{\mathcal{S}} N_1 - \dfrac{\partial \varphi_e}{\partial x_1} \\ 0 & \delta^h_{\mathcal{S}} N_3 - \dfrac{\partial \varphi_e}{\partial x_3} & \delta^h_{\mathcal{S}} N_2 - \dfrac{\partial \varphi_e}{\partial x_2} \end{bmatrix} \begin{bmatrix} N_1 & S_1 & T_1 \\ N_2 & S_2 & T_2 \\ N_3 & S_3 & T_3 \end{bmatrix} \tag{4.49}$$

with $\begin{bmatrix} N_1 & S_1 & T_1 \\ N_2 & S_2 & T_2 \\ N_3 & S_3 & T_3 \end{bmatrix}$ being the transformation matrix from global to local coordinates, see Appendix A.4.

Thus we can rewrite equation (4.49) as:

$$
\overline{\mathbf{G}}_e =
\begin{bmatrix}
\left(\delta_{\mathcal{S}}^h N_1 - \dfrac{\partial \varphi_e}{\partial x_1}\right) N_1 & \left(\delta_{\mathcal{S}}^h N_1 - \dfrac{\partial \varphi_e}{\partial x_1}\right) S_1 & \left(\delta_{\mathcal{S}}^h N_1 - \dfrac{\partial \varphi_e}{\partial x_1}\right) T_1 \\[2ex]
\left(\delta_{\mathcal{S}}^h N_2 - \dfrac{\partial \varphi_e}{\partial x_2}\right) N_2 & \left(\delta_{\mathcal{S}}^h N_2 - \dfrac{\partial \varphi_e}{\partial x_2}\right) S_2 & \left(\delta_{\mathcal{S}}^h N_2 - \dfrac{\partial \varphi_e}{\partial x_2}\right) T_2 \\[2ex]
\left(\delta_{\mathcal{S}}^h N_3 - \dfrac{\partial \varphi_e}{\partial x_3}\right) N_3 & \left(\delta_{\mathcal{S}}^h N_3 - \dfrac{\partial \varphi_e}{\partial x_3}\right) S_3 & \left(\delta_{\mathcal{S}}^h N_3 - \dfrac{\partial \varphi_e}{\partial x_3}\right) T_3 \\[2ex]
\left[\left(\delta_{\mathcal{S}}^h N_2 - \dfrac{\partial \varphi_e}{\partial x_2}\right) N_1 + \left(\delta_{\mathcal{S}}^h N_1 - \dfrac{\partial \varphi_e}{\partial x_1}\right) N_2\right] & \left[\left(\delta_{\mathcal{S}}^h N_2 - \dfrac{\partial \varphi_e}{\partial x_2}\right) S_1 + \left(\delta_{\mathcal{S}}^h N_1 - \dfrac{\partial \varphi_e}{\partial x_1}\right) S_2\right] & \left(\delta_{\mathcal{S}}^h N_2 - \dfrac{\partial \varphi_e}{\partial x_2}\right) T_1 + \left(\delta_{\mathcal{S}}^h N_1 - \dfrac{\partial \varphi_e}{\partial x_1}\right) T_2 \\[2ex]
\left[\left(\delta_{\mathcal{S}}^h N_3 \dfrac{\partial \varphi_e}{\partial x_3}\right) N_1 + \left(\delta_{\mathcal{S}}^h N_1 - \dfrac{\partial \varphi_e}{\partial x_1}\right) N_3\right] & \left[\left(\delta_{\mathcal{S}}^h N_3 - \dfrac{\partial \varphi_e}{\partial x_3}\right) S_1 + \left(\delta_{\mathcal{S}}^h N_1 - \dfrac{\partial \varphi_e}{\partial x_1}\right) S_3\right] & \left[\left(\delta_{\mathcal{S}}^h N_3 - \dfrac{\partial \varphi_e}{\partial x_3}\right) T_1 + \left(\delta_{\mathcal{S}}^h N_x - \dfrac{\partial \varphi_e}{\partial x_1}\right) T_3\right] \\[2ex]
\left[\left(\delta_{\mathcal{S}}^h N_3 - \dfrac{\partial \varphi_e}{\partial x_3}\right) N_2 \left(\delta_{\mathcal{S}}^h N_2 - \dfrac{\partial \varphi_e}{\partial x_2}\right) N_3\right] & \left[\left(\delta_{\mathcal{S}}^h N_3 - \dfrac{\partial \varphi_e}{\partial x_3}\right) S_2 \left(\delta_{\mathcal{S}}^h N_2 - \dfrac{\partial \varphi_e}{\partial x_2}\right) S_3\right] & \left[\left(\delta_{\mathcal{S}}^h N_3 - \dfrac{\partial \varphi_e}{\partial x_3}\right) T_2 \left(\delta_{\mathcal{S}}^h N_2 - \dfrac{\partial \varphi_e}{\partial x_2}\right) T_3\right]
\end{bmatrix}
\tag{4.50}
$$

with φ_e as defined in the expression (4.28) and

$$
\overline{\mathbf{G}}^*_e = \left(\delta_{\mathcal{S}}^h - \dfrac{A_e}{V_e}\right)
\begin{bmatrix}
N_1 & 0 & 0 \\
0 & N_2 & 0 \\
0 & 0 & N_3 \\
N_2 & N_1 & 0 \\
N_3 & 0 & N_1 \\
0 & N_3 & N_2
\end{bmatrix}
\begin{bmatrix}
N_1 & S_1 & T_1 \\
N_2 & S_2 & T_2 \\
N_3 & S_3 & T_3
\end{bmatrix}
\tag{4.51}
$$

or

$$
\overline{\mathbf{G}}^*_e = \left(\delta_{\mathcal{S}}^h - \dfrac{A_e}{V_e}\right)
\begin{bmatrix}
\left(N_1^2\right) & \left(N_1 S_1\right) & \left(N_1 T_1\right) \\
\left(N_2^2\right) & \left(N_2 S_2\right) & \left(N_2 T_2\right) \\
\left(N_3^2\right) & \left(N_3 S_3\right) & \left(N_3 T_3\right) \\
\left(2 N_2 N_1\right) & \left(N_2 S_1 + N_1 S_2\right) & \left(N_2 T_1 + N_1 T_2\right) \\
\left(2 N_3 N_1\right) & \left(N_3 S_1 + N_1 S_3\right) & \left(N_3 T_1 + N_1 T_3\right) \\
\left(2 N_3 N_2\right) & \left(N_3 S_2 + N_2 S_3\right) & \left(N_3 T_2 + N_2 T_3\right)
\end{bmatrix}
\tag{4.52}
$$

4.4.5 Numerical integration

The numerical integral is carried out by the use of a numerical quadrature procedure. Expressing a generalized definite integral by

$$I = \int_{-1}^{1} \int_{-1}^{1} \int_{-1}^{1} g(\xi, \eta, \zeta) \, d\xi \, d\eta \, d\zeta \tag{4.53}$$

the numerical quadrature formula is given by,

$$I = \int_{-1}^{1} \int_{-1}^{1} \int_{-1}^{1} g(\xi, \eta, \zeta) \, d\xi \, d\eta \, d\zeta = \sum_{r=1}^{nr} \sum_{q=1}^{nq} \sum_{p=1}^{np} \hat{W}_p \hat{W}_q \hat{W}_r g(\xi_p, \eta_q, \zeta_r) \tag{4.54}$$

where the weighting coefficients $\hat{W}_p, \hat{W}_q, \hat{W}_r$ and the abscissas (ξ_p, η_q, ζ_r) depend on the particular quadrature used. For more details about numerical integration see Zienkiewics&Taylor (1996a and 1996b).

Consideration of the regularized elemental discontinuity band $\mathcal{B}_e^k$ suggests a specific numerical integration rule for the described elements. Inspection of the resulting formulation in sections 4.4.3 and 4.4.4, and in view of regularization parameter k, equation (4.12) and regularized softening parameter $\mathcal{H}$, we have that strain is piecewise constant in both the domain $\mathcal{B}_e^k$ and domain $\mathcal{B}_e \setminus \mathcal{B}_e^k$ (see Figure 4.13). Thus, after examining the set of equations to solve, we conclude that only one integration point is needed in each of those domains, whose weights are equal to the corresponding area according to the following table:

Point	Domain	Weight
1	$\mathcal{B}_e \setminus \mathcal{B}_e^k$	measure$\left[\mathcal{B}_e\right] - k\ell_e$
2	$\mathcal{B}_e^k$	$k\ell_e$

where measure $\left[\mathcal{B}_e\right]$ stands for the area of $\mathcal{B}_e$. No specific location for the integration points, at the corresponding domain, needs to be specified.
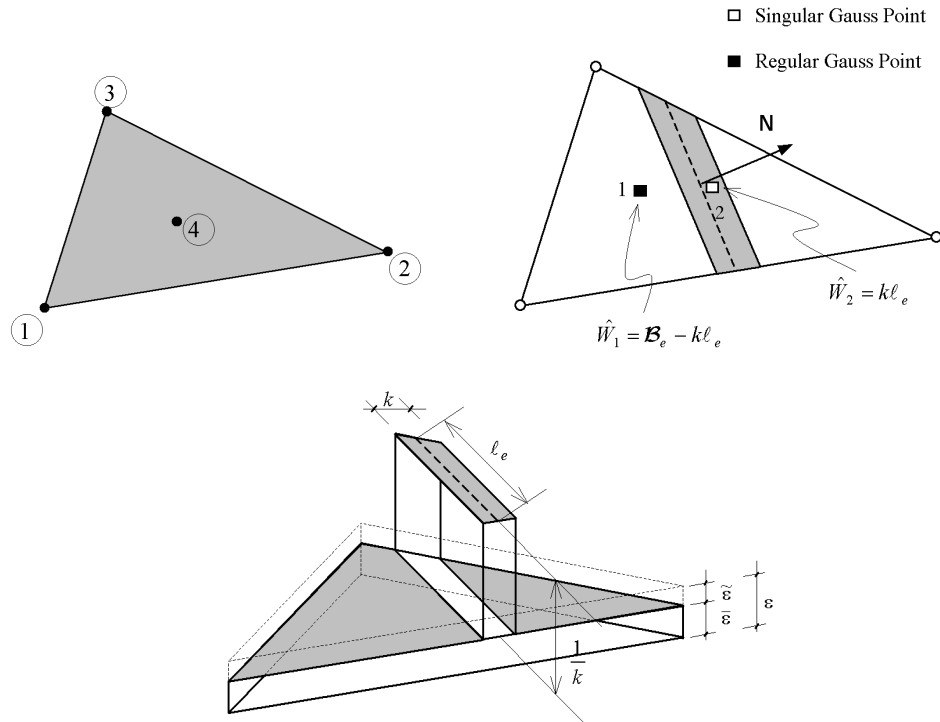
Figure 4.13: Discontinuity surface and tetrahedron intersection.
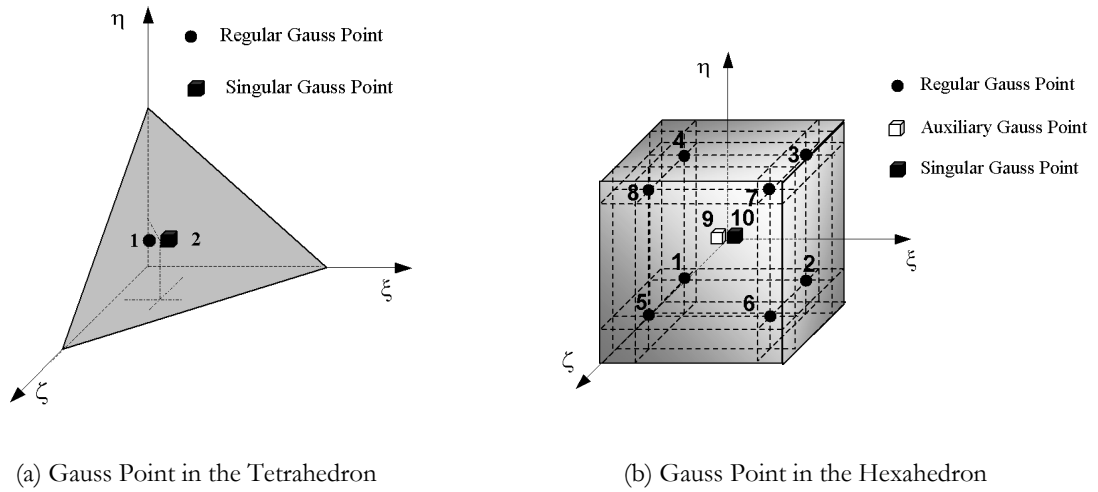
(a) Gauss Point in the Tetrahedron   (b) Gauss Point in the Hexahedron

Figure 4.14: Additional Gauss Point-3D.

4.5 Stability of the global solution

In order to circumvent the possibility of a loss of uniqueness due to arrest and activation of a discontinuity at some elements, the following modification to equation (4.44) is proposed (Samaniego 2003)

$$\dot{\mathbf{r}}_{e\,\overline{\eta}}(\mathbf{a}, \boldsymbol{\alpha}_{\mathrm{e}}, \dot{\boldsymbol{\alpha}}_{\mathrm{e}}) = \int_{\mathcal{S}_e} \overline{\eta}\, \dot{\boldsymbol{\alpha}}_{\mathrm{e}}\, \mathrm{d}A + \int_{\mathcal{B}_e} \mathbf{G}^{*T}_{e} \boldsymbol{\sigma}\, \mathrm{d}V \tag{4.55}$$

where $\overline{\eta}$ is the damping-like parameter.

Equation (4.55) can be interpreted as the residual forces vector of (4.43) plus a damping-like term intended to regularize the discrete BVP.

Applying a backward-Euler scheme for integration in time, equation (4.55) can be approximated by:

$$\dot{\mathbf{r}}_{\overline{\eta}}^{t+\Delta t} = \int_{\mathcal{S}} \overline{\eta}\, \frac{\boldsymbol{\alpha}_e^{t+\Delta t} - \boldsymbol{\alpha}_e^{t}}{\Delta t}\, \mathrm{d}A + \int_{\mathcal{B}_e} \mathbf{G}^{*T}_{e} \boldsymbol{\sigma}\, \mathrm{d}V \tag{4.56}$$

The corresponding tangent stiffness matrix can be shown to have the following form:

$$\hat{\mathbf{K}}^{e}_{\alpha\alpha} = \mathbf{K}^{e}_{\alpha\alpha} + \int_{\mathcal{S}_e} \frac{\overline{\eta}}{\Delta t} \mathbf{1}\, \mathrm{d}A \tag{4.57}$$

Thus, only sub matrix $\mathbf{K}^{e}_{\alpha\alpha}$ has to be modified by the damping term.

Remark 4.1: The additional damping acts exclusively within the elements which contain the discontinuity surface. □

4.6 Static condensation

The static condensation is employed to reduce the number of degrees of freedom per element and perform part of the solution of the total finite element system equilibrium equations prior to assembling the elemental matrices.

Consider a finite element with 4 nodes (see Figure 4.15) where $\boldsymbol{f}_{ep}$ are the forces in the nodes 1, 2, 3; $\boldsymbol{f}_{ei}$ are the forces in the internal node 4; $\boldsymbol{\delta}_{ep}$ are the displacements in the nodes 1, 2, 3 and $\boldsymbol{\delta}_{ei}$ are the displacements in the internal node 4.
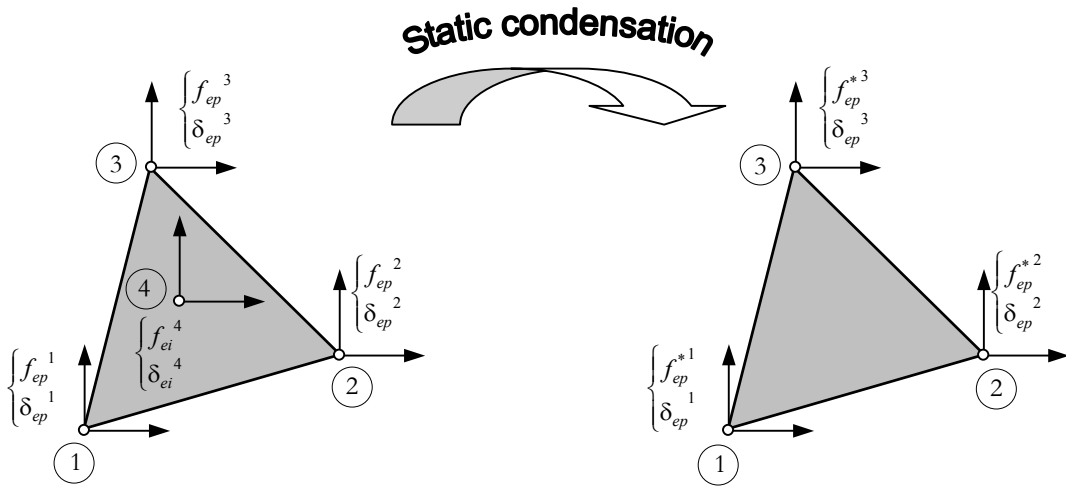
Figure 4.15: Static condensation.

At element level we can write:

$$\{\boldsymbol{f}_e\} = [\mathbf{K}_e]\{\boldsymbol{\delta}_e\} \tag{4.58}$$

We can split (4.58) in the form:

$$\left\{\begin{matrix} \boldsymbol{f}_{ep} \\ \hline \boldsymbol{f}_{ei} \end{matrix}\right\} = \left[\begin{matrix} \mathbf{K}_{epp} & \mathbf{K}_{epi} \\ \hline \mathbf{K}_{eip} & \mathbf{K}_{eii} \end{matrix}\right] \left\{\begin{matrix} \boldsymbol{\delta}_{ep} \\ \hline \boldsymbol{\delta}_{ei} \end{matrix}\right\} \tag{4.59}$$

The system above can be rewritten as:

$$\begin{cases} \boldsymbol{f}_{ep} = \mathbf{K}_{epp}\boldsymbol{\delta}_{ep} + \mathbf{K}_{epi}\boldsymbol{\delta}_{ei} \\ \boldsymbol{f}_{ei} = \mathbf{K}_{eip}\boldsymbol{\delta}_{ep} + \mathbf{K}_{eii}\boldsymbol{\delta}_{ei} \Rightarrow \boldsymbol{\delta}_{ei} = \mathbf{K}_{eii}^{-1}\left(\boldsymbol{f}_{ei} - \mathbf{K}_{eip}\boldsymbol{\delta}_{ep}\right) \end{cases} \tag{4.60}$$

Substituting the second equation from (4.60) into the first equation we can obtain the following system of equations:

$$\underbrace{\left\{ f_{e\,p} - \mathbf{K}_{e\,pi}\mathbf{K}_{e\,ii}^{\;-1} f_{e\,i} \right\}}_{f_e^*} = \underbrace{\left\{ \mathbf{K}_{e\,pp} - \mathbf{K}_{e\,pi}\mathbf{K}_{e\,ii}^{\;-1}\mathbf{K}_{e\,ip} \right\}}_{\mathbf{K}_e^*}\boldsymbol{\delta}_{e\,p}$$

(4.61)

$$f_e^* = \mathbf{K}_e^* \boldsymbol{\delta}_{e\,p}$$

4.6.1 Newton-Raphson scheme for the statically condensed version

In this section we describe the Newton-Raphson method with static condensation, Armero(1999b). Within the framework of the finite element method, equations (4.42), (4.43) can be transformed into a (global) force equilibrium equation that has to be fulfilled at every time step, $[t, t + \Delta t]$ (see Figure 4.16), of the discretized time domain. To attain this objective we have to define a residual forces vector, which has to be cancelled by means of an iterative procedure at each time step:

$$^{t+\Delta t}\mathbf{F}_{ext} - {}^{t+\Delta t}\mathcal{F}_{int}^{*\,(it-1)} = \mathbf{0}$$

(4.62)

where the vector $^{t+\Delta t}\mathbf{F}_{ext}$ stores the externally applied nodal loads and $^{t+\Delta t}\mathcal{F}_{int}^{*\,(it-1)}$ is the vector of nodal point forces that are equivalent to the element stresses in the iteration $(it-1)$. Knowing the following database:

Global database: $\boldsymbol{\delta}_{e\,p}^{\;(it)} = \boldsymbol{\delta}_{e\,p}^{\;(it-1)} + \Delta\boldsymbol{\delta}_{e\,p}^{\;(it)}$

Element database: $\boldsymbol{\delta}_{e\,i}^{\;(it-1)}$; $f_{e_i}^{\;(it-1)}$; $\left[\mathbf{K}_e^{(it-1)}{}_{ii}\right]^{-1}$; $\mathbf{K}_e^{(it-1)}{}_{ip}$

we can obtain $\mathcal{F}_{int}^{*\,(it)}$ through the following steps:

1. From the displacement in the node of the element, $\Delta\boldsymbol{\delta}_{e\,p}^{\;(it)}$ (element level) we can obtain the displacement in the internal node, $\boldsymbol{\delta}_{e\,i}^{\;(it)}$:

$$\boldsymbol{\delta}_{e\,i}^{\;(it)} = \boldsymbol{\delta}_{e\,i}^{\;(it-1)} - \left[\mathbf{K}_e^{(it-1)}{}_{ii}\right]^{-1}\left(f_{e_i}^{\;(it-1)} + \mathbf{K}_e^{(it-1)}{}_{ip}\Delta\boldsymbol{\delta}_{e\;p}^{(it)}\right)$$

(4.63)

2. From the vector of nodal point displacement we can obtain the vector of nodal internal forces:

$$\left\{\frac{\boldsymbol{\delta}_{e\,p}}{\boldsymbol{\delta}_{e\,i}}\right\}^{(it)} \xrightarrow{\;\mathbf{B},\mathbf{G},\mathbf{G}^*\;} \boldsymbol{\varepsilon}^{(it)} \xrightarrow{\;\mathcal{C}\;} \boldsymbol{\sigma}^{(it)} \xrightarrow{\;\int_{\mathcal{B}}\mathrm{d}V\;} \left\{\frac{f_{e\,p}}{f_{e\,i}}\right\}^{(it)}$$

(4.64)

where $\mathbf{B},\mathbf{G},\mathbf{G}^*$ are the matrices defined in the previous section and $\mathcal{C}$ is the matrix with elastic properties.

3. Once we have obtained the vector of nodal internal forces $\boldsymbol{f}$ in the current iteration it, we can obtain the vector of condensed forces $\boldsymbol{f}_e^{*(it)}$ as:

$$\boldsymbol{f}_e^{*(it)} = \boldsymbol{f}_{e\,p}^{(it)} - \mathbf{K}_{e\,pi}^{(it)} \mathbf{K}_{e\,ii}^{(it)\,-1} \boldsymbol{f}_{e\,i}^{(it)} \tag{4.65}$$

thus,

$$\mathcal{F}_{int}^{*\,(it)} = \mathop{\mathbf{A}}_{e=1}^{n_{el}} {}^{t+\Delta t}\boldsymbol{f}_e^{*(it)} \tag{4.66}$$

Then, we calculate the residue $\Delta \mathbf{R}^{*(it)}$ as:

$$\Delta \mathbf{R}^{*(it)} = {}^{t+\Delta t}\mathbf{F}_{ext} - \mathop{\mathbf{A}}_{e=1}^{n_{el}} {}^{t+\Delta t}\boldsymbol{f}_e^{*(it)} = \underbrace{{}^{t+\Delta t}\mathbf{F}_{ext} - {}^{t+\Delta t}\mathcal{F}_{int}^{*\,(it)}}_{\Delta R^{*(it)}} \tag{4.67}$$

where $\mathbf{A}$ is the standard finite-element assembly operator and n_{el} is the number of finite elements and $\boldsymbol{f}_e$ are the external forces.

4. Solve for the nodal displacement increment:

$$^{t+\Delta t}\mathbf{K}^{*(it)} \Delta \boldsymbol{\delta}_{e\,p}^{(it+1)} = \Delta \mathbf{R}^{*(it)} \tag{4.68}$$

thus, we can update the nodal displacement :

$$\boldsymbol{\delta}_{e\,p}^{(it+1)} = \boldsymbol{\delta}_{e\,p}^{(it)} + \Delta \boldsymbol{\delta}_{e\,p}^{(it+1)}$$

5. if $\left\| \Delta \mathbf{R}^{*(it)} \right\| < Tolerance \longrightarrow$ Convergence is reached

6. if $\left\| \Delta \mathbf{R}^{*(it)} \right\| > Tolerance$, $it \leftarrow it + 1$ go to step 1.
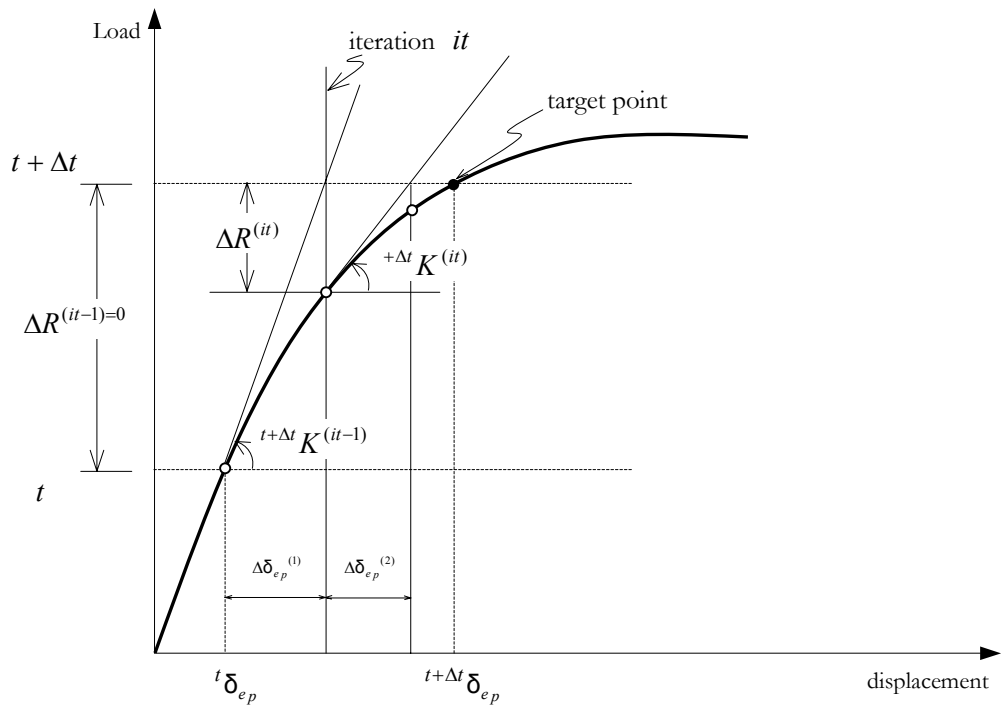
Figure 4.16: Illustration of Newton-Raphson iteration.

4.7 Algorithm for tracking the discontinuity path

In Chapter 3, we saw how to determine the direction of the critical direction which can be regarded as the discontinuity path (failure surface) at a local level (Gauss point). However, it is necessary to determine the discontinuity path for the whole body based on the information of the Gauss points. In the following sections we describe two algorithms to obtain the discontinuity line $\mathcal{L}$ (failure line) for the 2D case and the discontinuity surface $\mathcal{S}$ (failure surface) for the 3D case.

It is necessary to determine the discontinuity path because we need to know *a priori* the domains $\mathcal{B}^{+}$ and $\mathcal{B}^{-}$ (see Figure 4.17) to guarantee an appropriate kinematics, since the numerical counterpart of the SDA requires a special function to approximate the displacement field, as we outlined in section 4.4.2.

2D   **3D**

$$\mathcal{B} = \mathcal{B}^{-} \cup \mathcal{B}^{+^{(1)}} \cup \mathcal{B}^{+^{(2)}} \qquad\qquad \mathcal{B} = \mathcal{B}^{-} \cup \mathcal{B}^{+}$$
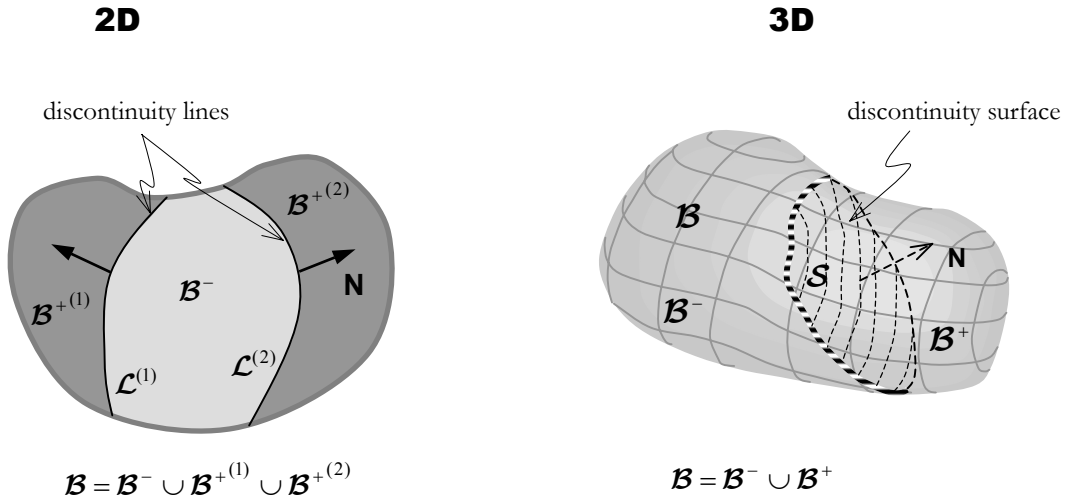
Figure 4.17: Discontinuity lines $\mathcal{L}^{(1)}$ and $\mathcal{L}^{(2)}$ in 2D case and discontinuity surface $\mathcal{S}$ in a 3D case.

In the following sections we present two techniques used in this work to track the discontinuity evolution:

- Element-by-Element Tracking;

- Overall Tracking.

4.7.1 Element-by-element tracking

2D Case

In this case the discontinuity line $\mathcal{L}$ (which must be continuous) is composed of segments $\mathcal{L}_e$ defined in each finite element by the bifurcation analysis, thus we can define $\mathcal{L}$ as:

$$\mathcal{L} = \bigcup_{e=1}^{N_{\mathcal{J}}} \mathcal{L}_e \tag{4.69}$$

where $N_{\mathcal{J}}$ is the number of elements which are intersected by the discontinuity line $\mathcal{L}$ at time t. Thus we can define a sub set $\mathcal{J}$ as:

$$\mathcal{J} := \left\{ e \in 1,2,3,...N_{\mathcal{J}} \;\middle|\; \mathcal{B}_e \subset \mathcal{B}_h \right\} \tag{4.70}$$

By "*continuous failure line*" we mean a discontinuity path which is continuous across element boundaries (see Figure 4.18(a)) and by "*discontinuous failure line*" we are referring to the case illustrated in Figure 4.18(b), the same nomenclature will be used for the discontinuity surface in the 3D case.

(a) Continuous failure line   (b) Discontinuous failure line
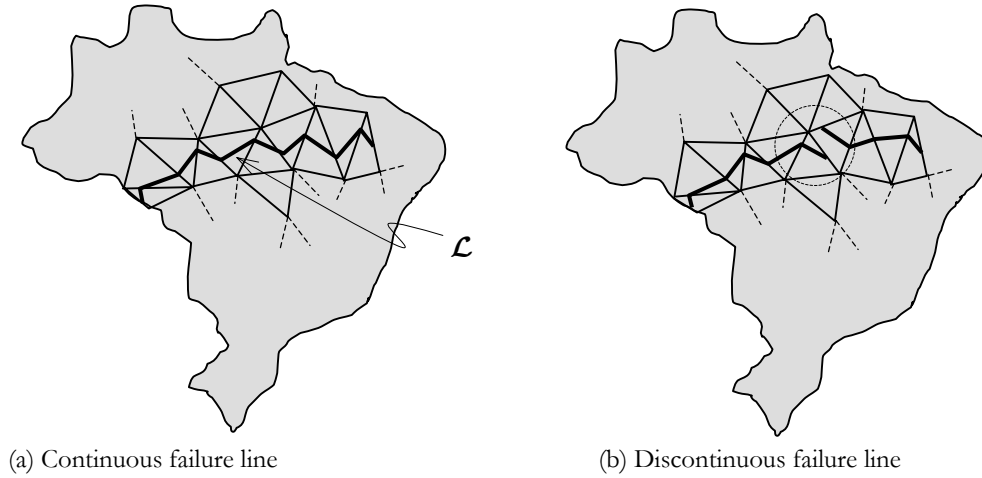
Figure 4.18: Continuous/discontinuous failure line.

Algorithm for determining the discontinuity line $\mathcal{L}$

Before we apply this technique we need to know *a priori* the following data (see Figure 4.19):

- ✓ $\mathbf{N}_{crit}$ for all the finite elements of the domain;

- ✓ An element must be chosen as a seed. This element (E^S) can be chosen to be the first one that bifurcates. Starting from this element the discontinuity line, $\mathcal{L}_1$, will spread in one of the critical directions $\mathbf{N}_{crit}^S$;

- ✓ $\vec{d}_S$ - one of critical directions in the seed element E^S;

- ✓ P_S^I - point of departure of the track on a side of the seed element E^S;

- ✓ elements which have already bifurcated.
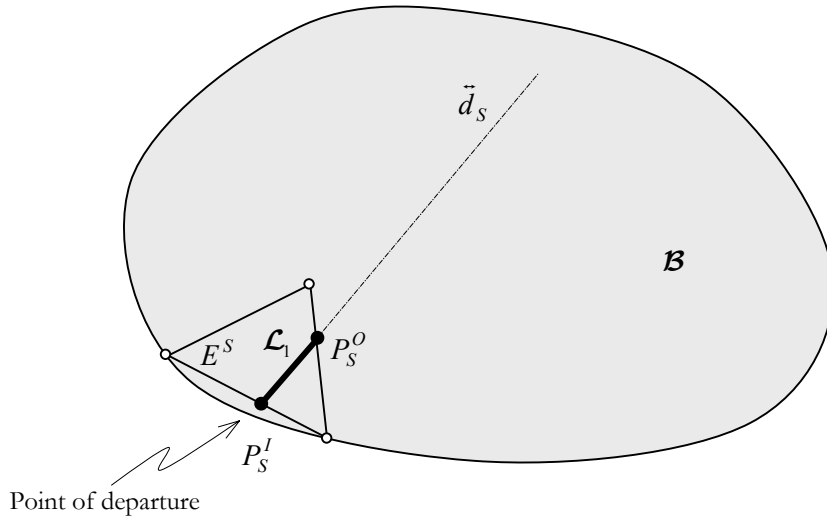
Figure 4.19: Element-by-element tracking – Initial data.

The algorithm is as follows:

1. Compute the point P_e^O for element e and identify the adjacent element on the side where the point P_e^O is placed. In Figure 4.19 we have an example where $P_e^O = P_S^O$ for the seed element E^S;

2. Choose, based on some criterion, which direction will be taken for the next element e, $\vec{d}_1^{(e)}$ or $\vec{d}_2^{(e)}$. This criterion, for instance, could be the smaller angle between $\vec{d}^{(e-1)}$ with $\vec{d}_1^{(e)}$ and $\vec{d}_2^{(e)}$. For example in Figure 4.20, $\vec{d}^{(e=E^2)} = \vec{d}_2^{(2)}$;

3. Repeat the same process for the next element $(e+1)$ until no more adjacent elements are found, *i.e.* when the boundary of the domain is reached (Figure 4.21).

Figure 4.20: Element-by-element tracking – propagating.

Figure 4.21: Element-by-element tracking.

At each time step we must calculate a new discontinuity line which can change or not, depending on the satisfaction of the bifurcation criterion in some elements. Once

bifurcation is reached for some element then the direction will not change anymore for that element.

The tracking can start from any element inside of the body. It is not necessary for it to be on the boundary as shown in the example above.

3D Case

The same strategy described above was implemented for the 3D case where a seed element E^S serves as point of departure. Thus, we can define a plane $\mathcal{S}_i$ and find the intersections in the faces of the finite element. Figure 4.22 shows the possible intersections between a plane and a regular hexahedron, these intersections serve as points to propagate the track for the adjacent elements. Thus, the discontinuity surface $\mathcal{S}$ is compounded of discontinuity segments $\mathcal{S}_e$, *i.e.:*

$$\mathcal{S} = \bigcup_{e=1}^{N_{\mathcal{J}}} \mathcal{S}_e \tag{4.71}$$

Plane-Hexahedron
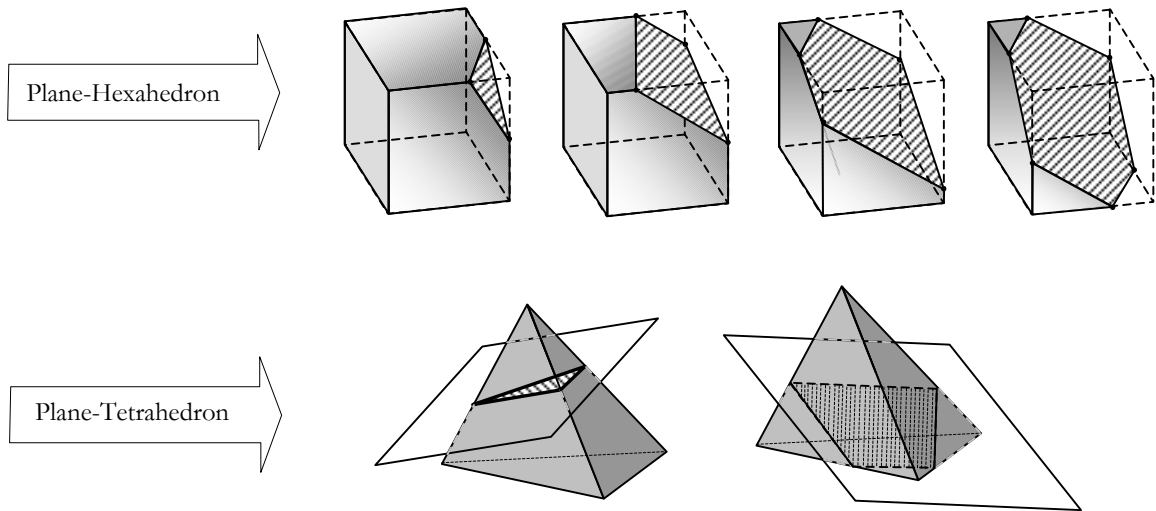
Plane-Tetrahedron

Figure 4.22: Possibilities of intersection between planes and regular hexahedron and tetrahedrons.

In the 3D propagation of the discontinuity surface we have a front of planes which are spreading in the domain. Starting from a parent element (seed element) we will form a ramification of elements which contains the segments of the discontinuity surface $\mathcal{S}_e$. A scheme of the methodology employed to define the discontinuity surface is shown in Figure 4.23.
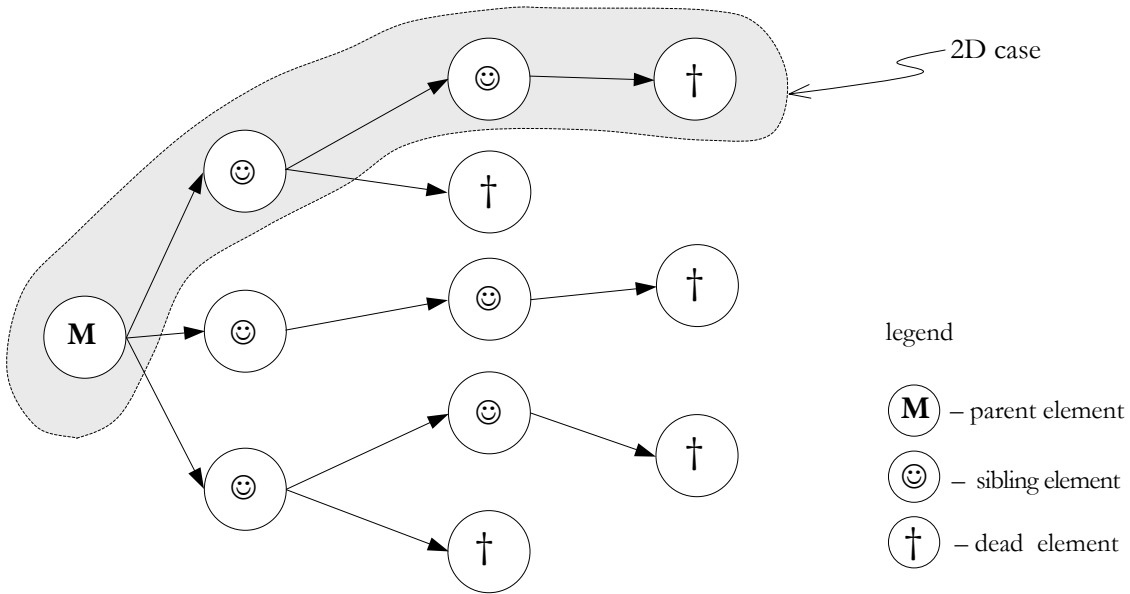
Figure 4.23: 3D propagation algorithm of the element-by-element tracking.

To define a plane we need a point and a normal to this plane or two lines in this plane. But we have as input a line which was previously defined from the adjacent element and the normal (from bifurcation analysis), thus we have a lot of choices to establish a new plane. If we adopt the line ℓ_1 (see Figure 4.24) we cannot use the normal obtained by bifurcation analysis, we are limited to a set of normals as shown in Figure 4.24.
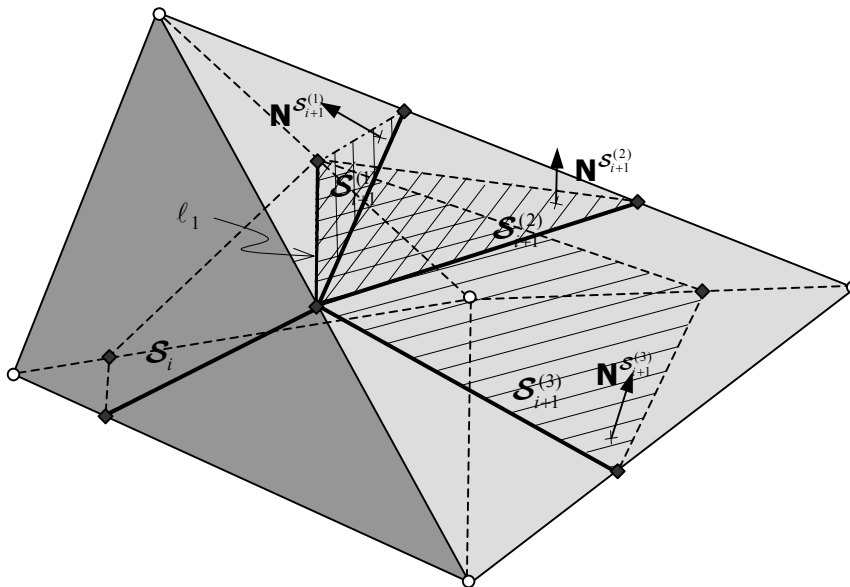
Figure 4.24: Propagating of the discontinuity surface.

Another criterion could be to choose the normal obtained by bifurcation analysis and a point in the line ℓ_1 to define a new plane. In this case in Figure 4.25 it is illustrated how

difficult is to obtain a continuous failure surface using as an example two finite elements, where the finite element $e = 1$ has connectivities 1-2-4-5 and the finite element $e = 2$ has connectivities 2-3-4-5. Once the plane $\mathcal{S}_1$ and the intersections in the faces of the finite element $e = 1$ are defined, we can build up a new plane in the adjacent element $e = 2$ having as input the normal $\mathbf{N}^{\mathcal{S}_2}$ (from bifurcation analysis) to the plane $\mathcal{S}_2$ and the point C (Figure 4.25), then we could arrive to the following situation:

$$e = 1 \rightarrow \begin{cases} \text{Nodes} \ \{1,5\} \in \mathcal{B}^+ \\ \text{Nodes} \ \{2,4\} \in \mathcal{B}^- \end{cases} \qquad e = 2 \rightarrow \begin{cases} \text{Nodes} \ \{5,2,3\} \in \mathcal{B}^+ \\ \text{Nodes} \ \{4\} \in \mathcal{B}^- \end{cases} \qquad (4.72)$$

We see that there exists an incompatibility with node number 2 which for element $e = 1$ belongs to $\mathcal{B}^-$ and for element $e = 2$ belongs to $\mathcal{B}^+$.
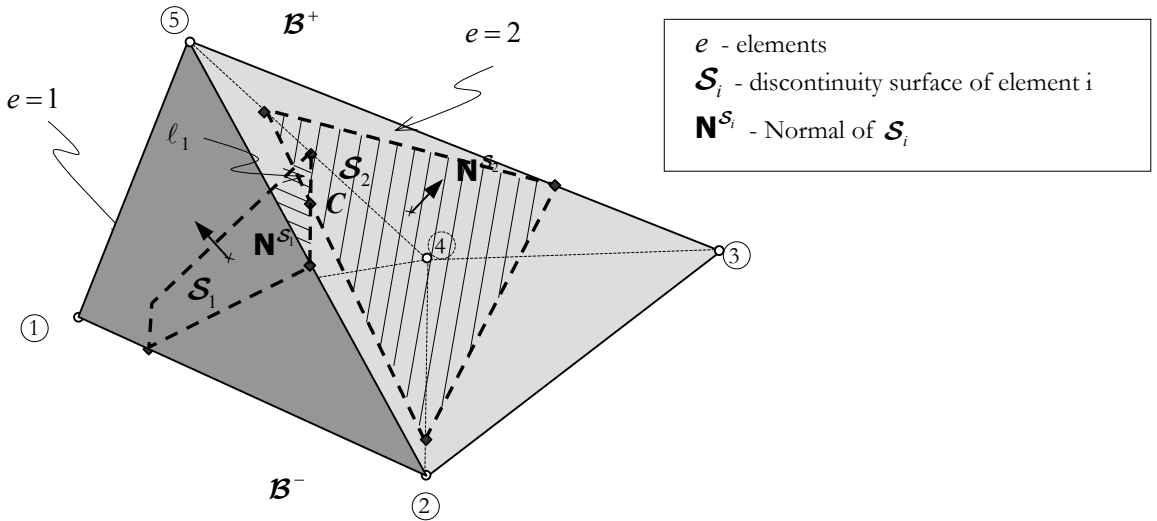
Figure 4.25: Propagating of the discontinuity surface.

Remark 4.2: The element-by-element tracking strategy is quite simple, robust and reliable when dealing with 2D problems with a single discontinuity line and it has been successfully used in the past by Manzoli(1998), Oliver(1995a,b). Unfortunately, for the three dimensional case, this methodology is not efficient. Using the Element-by-Element Tracking the continuity of the discontinuity surface $\mathcal{S}$ (3D case) is too difficult to achieve. $\square$

4.7.2 Overall tracking

A continuous failure surface is needed to establish a well conditioned problem. For this purpose a new method has been proposed by Oliver *et al.* (2002) to obtain a continuous failure surface. This idea starts from the principle that from the normal (**N**) obtained from the bifurcation analysis a family of curves (Level curves) in the 2D case or a family of surfaces (Level Surfaces) in 3D enveloping the propagation direction case can be constructed. The following analogy with the heat conduction problem (*heat conduction-like problems*) to obtain that family of surfaces Φ was presented in Oliver *et al.* (2002). This methodology consists of the following steps:

- Trace at once all the possible discontinuity paths in the time t. Since, by construction, at every point **x** of the discontinuity paths $\mathcal{S}_j$, such path has the property that there exits a family of critical direction $\mathbf{N}_{crit}$. Therefore, the construction of the envelops implicitly supplies all the possible discontinuity surfaces at time t. In 2D case we can illustrate as shown in Figure 4.26 where three discontinuities lines, $\mathcal{L}_1$, $\mathcal{L}_2$ and $\mathcal{L}_3$ ($j \in \{1,2,3\}$) can be seen. These envelops can be described by a function $\Phi(\mathbf{x})$ whose *level contours* ($\Phi(\mathbf{x})$ =constant) define all the possible discontinuity surfaces as :

$$\mathcal{S}_j := \left\{ \mathbf{x} \in \mathcal{B} \quad ; \quad \Phi(\mathbf{x}) = \Phi_j^{ref} \right\} \tag{4.73}$$

for all the meaningful values of Φ_j^{ref} and for all the material points, **x** , fulfilling the propagation condition. In the following section a methodology for the construction of such a family is provided were $\Phi(\mathbf{x})$ stands for the temperature field that is the solution of the stationary heat conduction problem and therefore, $\mathcal{S}_j$ are segments of the isothermal surfaces. In the context of a finite element analysis, this algorithm returns the nodal temperature values Φ^i.

- Identify the active discontinuity surfaces and their corresponding temperature level. For every seed element it is considered a reference discontinuity path in a seed point which belongs to the seed element. Consequently, the corresponding temperature level is the temperature for this seed point:

$$\Phi_j^{ref} = \sum_{i=1}^{n_{nodes}} \mathbb{N}_i \Phi_i \tag{4.74}$$

where n_{nodes} stands for all the number of nodes of the element (*i.e.:* in 3D case $n = 4$ for linear tetrahedrons and $n = 8$ for hexahedrons. Then, temperatures Φ_j^{ref} $j = 1,..n_d$ identify the corresponding discontinuity surface through equations (4.73).

$$(\Phi^{(3)} - \Phi_j^{ref}) < 0$$

$$\Phi^{(4)} - \Phi_j^{ref}) > 0$$

$$(\Phi^{(1)} - \Phi_j^{ref}) < 0$$
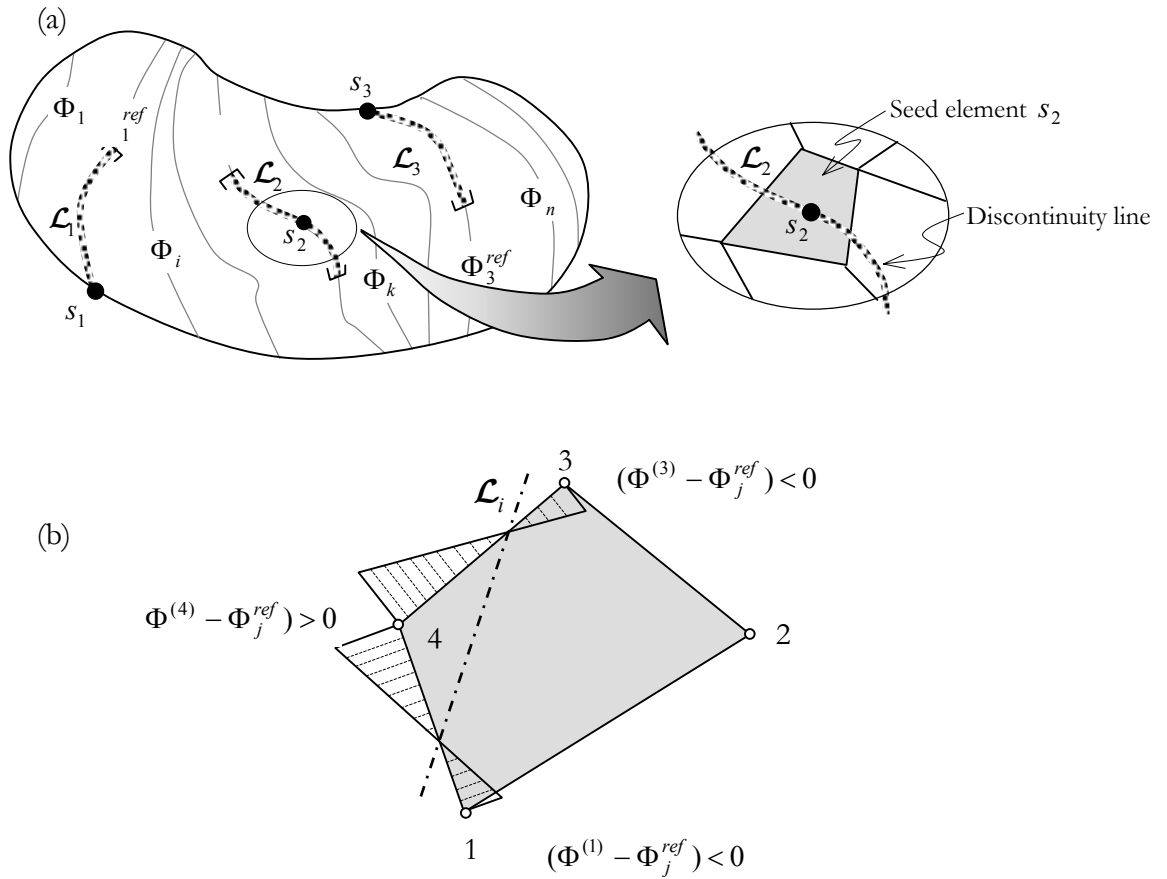
Figure 4.26: Overall tracking of discontinuities.

▪ Determine the position of the discontinuity surface inside a given element. Once the nodal temperatures Φ^i and the discontinuity surface temperatures Φ_j^{ref} are known, the position of $\boldsymbol{\mathcal{S}}_j$, inside a given element e can be immediately determined through the following algorithm (for 2D case see Figure 4.26b)

Data:

$$\begin{cases} \text{Nodal temperature of the element} : \Phi^i \\ \text{Discontinuity surface temperature} : \Phi_j^{ref} \end{cases}$$

Actions: (4.75)

Determine the sides involving a change of sign of $(\Phi^i - \Phi_j^{ref})$ at their vertices (sides crossed by $\boldsymbol{\mathcal{S}}_j$).

For every of these sides compute the position of $\boldsymbol{\mathcal{S}}_j$ through linear interpolation.

Notice that no information from the neighbour element is required in the preceding algorithm. This fact confers to the algorithm some interesting locality character that can be exploited for implementation purposes.

4.7.2.1 Heat conduction-like problem

Let $\mathbf{N}(\mathbf{x},t)$ be a family of unit vectors, defined at every point in the domain $\mathcal{B}$ at a given time t, determining the direction normal to the plane of propagation of the discontinuity. Then let $\mathbf{S}(\mathbf{x},t)$ and $\mathbf{T}(\mathbf{x},t)$ be any couple of unit vector orthogonal to $\mathbf{N}$, so that:

$$\mathbf{S}\cdot\mathbf{N} = \mathbf{T}\cdot\mathbf{N} = 0 \tag{4.76}$$

thus defining the plane (tangent to them) of propagation of the discontinuity. The family of surfaces, enveloping both vectors, $\mathbf{S}$ and $\mathbf{T}$, can be described by a scalar (temperature like) function $\Phi(\mathbf{x})$ such that the isothermal surfaces:

$$\mathcal{S}_j := \left\{ \mathbf{x}\in\mathcal{B} \quad ; \quad \Phi(\mathbf{x}) = \Phi_j^{ref} \right\} \tag{4.77}$$

for all meaningful values of Φ_j^{ref} are tangent at each point $\mathbf{x}\in\mathcal{B}$ to vectors $\mathbf{S}$ and $\mathbf{T}$. Therefore:

$$\left. \begin{aligned} \mathbf{S}\cdot\nabla\Phi = \nabla\Phi\cdot\mathbf{S} = \frac{\partial\Phi}{\partial\mathbf{S}} = 0 \\[2mm] \mathbf{T}\cdot\nabla\Phi = \nabla\Phi\cdot\mathbf{T} = \frac{\partial\Phi}{\partial\mathbf{T}} = 0 \end{aligned} \right\} \quad in \ \mathcal{B} \tag{4.78}$$

Solutions of problem (4.78) are also solutions of the following heat conduction problem:

$$\Phi(\mathbf{x}) \quad \text{such that} \quad \begin{cases} \nabla\cdot\mathbf{q} = 0 & in \ \mathcal{B} \\[2mm] \mathbf{q} = -\mathbb{K}^C\cdot\nabla\Phi = -\mathbf{S}\dfrac{\partial\Phi}{\partial\mathbf{S}} - \mathbf{T}\dfrac{\partial\Phi}{\partial\mathbf{T}} = 0 & in \ \mathcal{B} \\[2mm] \mathbf{q}\cdot\boldsymbol{\upsilon} = (\boldsymbol{\upsilon}\cdot\mathbf{S})\dfrac{\partial\Phi}{\partial\mathbf{S}} + (\boldsymbol{\upsilon}\cdot\mathbf{T})\dfrac{\partial\Phi}{\partial\mathbf{T}} = 0 & on \ \partial_{\mathbf{q}}\mathcal{B} \\[2mm] \Phi = \Phi^* & on \ \partial_{\Phi}\mathcal{B} \end{cases} \tag{4.79}$$

where $\boldsymbol{\upsilon}$ is the outward normal to the boundary $\partial\mathcal{B}$ and $\partial_{\mathbf{q}}\mathcal{B}$ and $\partial_{\Phi}\mathcal{B}$ $(\overline{\partial_{\mathbf{q}}\mathcal{B}\cup\partial_{\Phi}\mathcal{B}}=\partial\mathcal{B})$, stand, respectively, for the parts of the boundary $\partial\mathcal{B}$ where the Neumann and Dirichlet conditions are prescribed. $\mathbb{K}^{C}$ is an anisotropic conductivity tensor and given by:

$$\mathbb{K}^{c}\big(\mathbf{S}(\mathbf{x}),\mathbf{T}(\mathbf{x})\big)=\mathbf{S}\otimes\mathbf{S}+\mathbf{T}\otimes\mathbf{T}$$

$$\mathbb{K}^{c}\big(\mathbf{S}(\mathbf{x}),\mathbf{T}(\mathbf{x})\big)=\begin{bmatrix} S_1^2+T_1^2 & S_1S_2+T_1T_2 & S_1S_3+T_1T_3 \\ S_2S_1+T_2T_1 & S_2^2+T_2^2 & S_2S_3+T_2T_3 \\ S_1S_3+T_1T_3 & S_2S_3+T_2T_3 & S_3^2+T_3^2 \end{bmatrix} \tag{4.80}$$

4.7.2.2 Finite element formulation

The finite element discretization of problem (4.79) is as follows:

Given a domain $\mathcal{B}$ discretized in n_{el} finite elements and n_{nodes} nodes for each finite element where the function $\Phi(\mathbf{x})$ can be approximated by standard shape functions $\mathbb{N}$, as:

$$\Phi_e(\mathbf{x})=\sum_{i=1}^{n_{nodes}}\mathbb{N}_i\Phi_i \tag{4.81}$$

The stiffness matrix reads

$$\mathbf{K}_e^C=\int_{\mathcal{B}_e}[\nabla\mathbb{N}]^T\,\mathbb{K}_e^c[\nabla\mathbb{N}]\,\mathrm{d}V_e \tag{4.82}$$

thus

$$\mathbf{K}^C=\mathop{\mathbf{A}}_{e=1}^{n_{el}}\mathbf{K}_e^C \tag{4.83}$$

and the solution consists in solving the problem:

$$\begin{cases} \mathbf{K}^C\,\Phi=\mathbf{0} \\ \Phi^i\big|_{\partial_{\Phi}\mathcal{B}}=\Phi^* \end{cases} \tag{4.84}$$

The temperature has to be prescribed, at least, at two points in order to obtain a meaningful solution of equations (4.84). The values of the prescribed temperatures are irrelevant for the goal of the model, Oliver *et al.*(2002).

Now the algorithm is applied to the case of a normal field $\mathbf{N}(\mathbf{x},t)$ oriented in the radial direction of a cube (see Figure 4.27) with the origin at the vertex O. That normal field is then:

$$\mathbf{N}(\mathbf{x}) = \frac{\mathbf{x}}{\|\mathbf{x}\|}$$

$$\mathbf{N}(\mathbf{x}) = \left\{ N_1, \quad N_2, \quad N_3 \right\}^T \tag{4.85}$$

from which a couple of tangent vectors, $\mathbf{S}$ and $\mathbf{T}$, can be immediately extracted as:

$$\mathbf{S}(\mathbf{x}) = \left\{ 0, \quad N_3, \quad -N_2 \right\}^T$$

$$\mathbf{T}(\mathbf{x}) = \left\{ N_3, \quad 0, \quad -N_1 \right\}^T \tag{4.86}$$

In Figure 4.27(a) the finite element mesh considered, consisting of 1489 tetrahedra, is presented. In Figure 4.27(b) the isothermal surfaces are plotted together with the prescribed temperatures. Notice that, as expected, the envelopes are spherical surfaces centered at vertex O.

a) Mesh   b) Isothermal surface
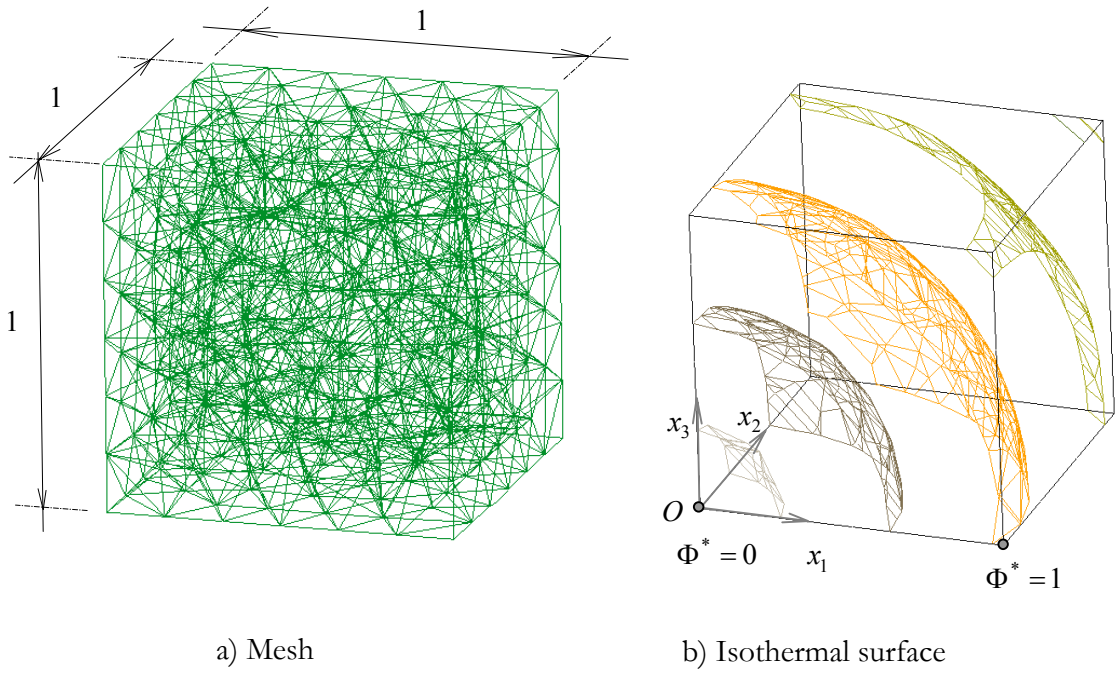
Figure 4.27: Level surfaces (3D case).

Once the value of the function Φ is obtained in the nodes and the value of the reference temperature Φ^{ref} known, we are able to determine which nodes are in domain $\mathcal{B}^-$ and which in domain $\mathcal{B}^+$. Thus the node i will be in $\mathcal{B}^+$ if:

$$\Phi^i - \Phi^{ref} > 0 \tag{4.87}$$

otherwise the node i will be in $\mathcal{B}^-$.
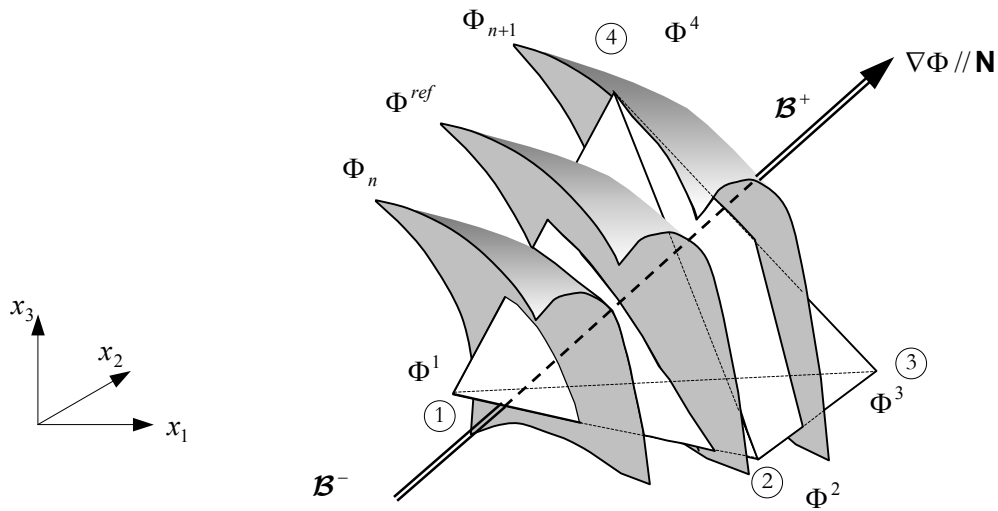
Figure 4.28: Isothermal surface in a tetrahedral finite element.

4.7.3 Flowchart of the coupled problem

Figure 4.29 shows the strategy for the entire analysis of the mechanical problem. The first phase of the process requires mechanical analysis and the second requires thermal-like analysis.
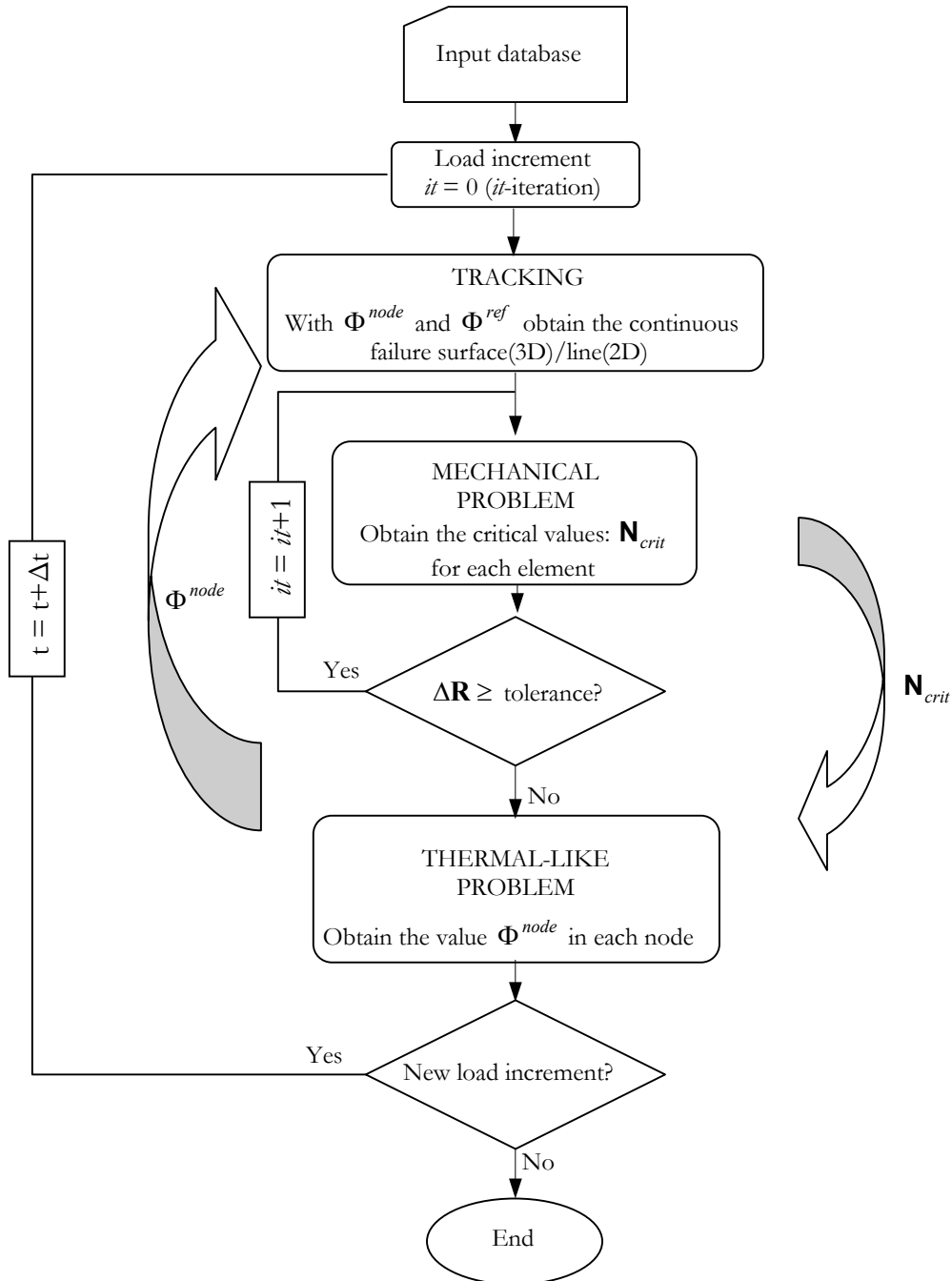
Figure 4.29: Flowchart of coupled problem.

4.7.4   Some examples of the failure surface

In this section we show some examples to describe the efficiency of the method used in this work to obtain a continuous failure surface.

4.7.4.1   Anchorage structure

This example was simulated numerically by Rots(1998) and de Borst (1986) using 2D axi-symmetric finite elements. The geometry used is shown in Figure 4.30 and Figure 4.31. The structure consists of a steel plate embedded in a massive concrete block. The plate is pulled on of the concrete by a vertical load F which is applied via a anchor bolt.

The material parameters taken were $E = 30000\, N/mm^2$, Poisson's ratio $\nu = 0.2$, tensile strength $f_{ct} = 2.5\, N/mm^2$ and fracture energy $\mathcal{G}_f = 0.1\, N/mm$. An exponential softening law was used. The 3D discretized mesh has 12029 tetrahedrons and 2980 nodes. Figure 4.32 shows the continuous failure surface which was obtained using the Overall Tracking strategy.
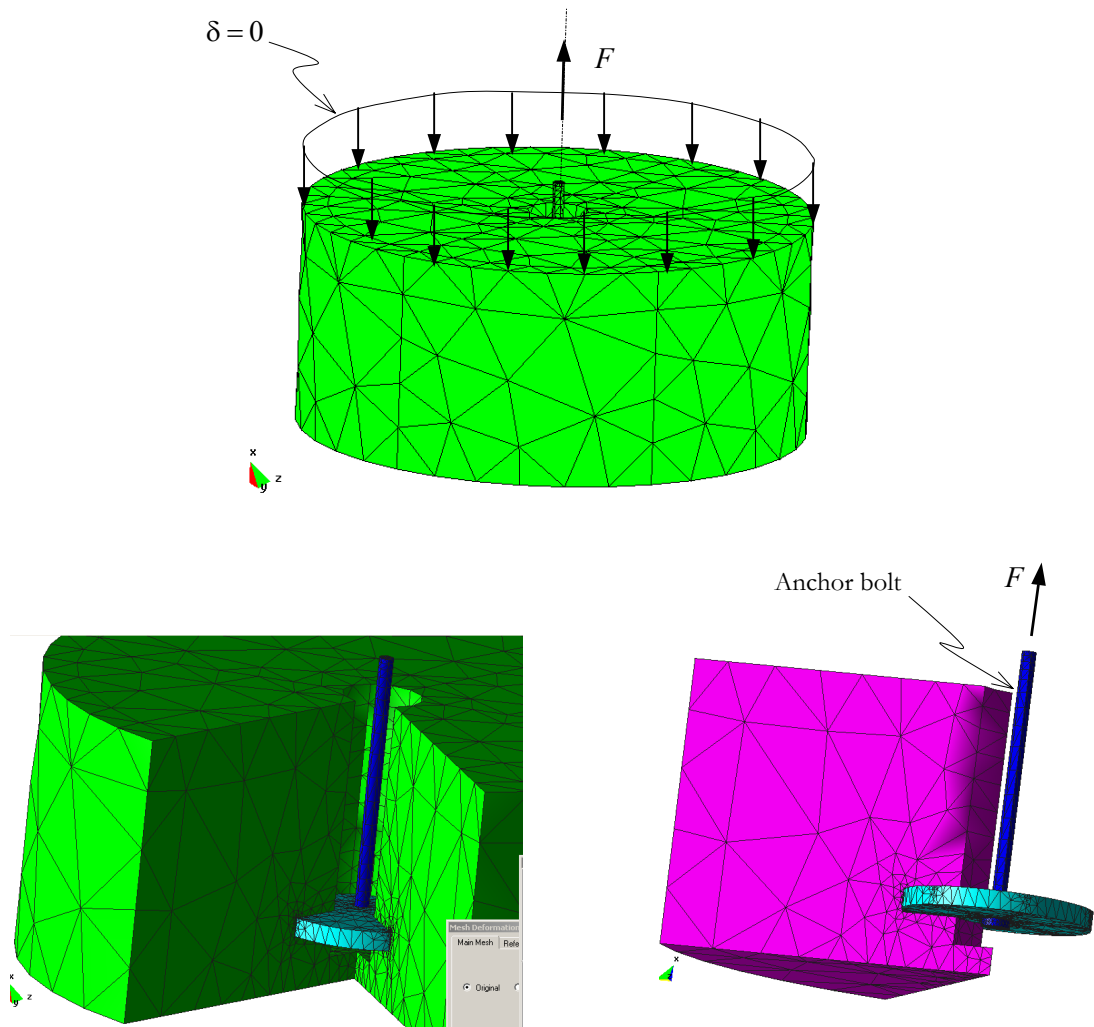
Figure 4.30: Detail of the anchorage structure.
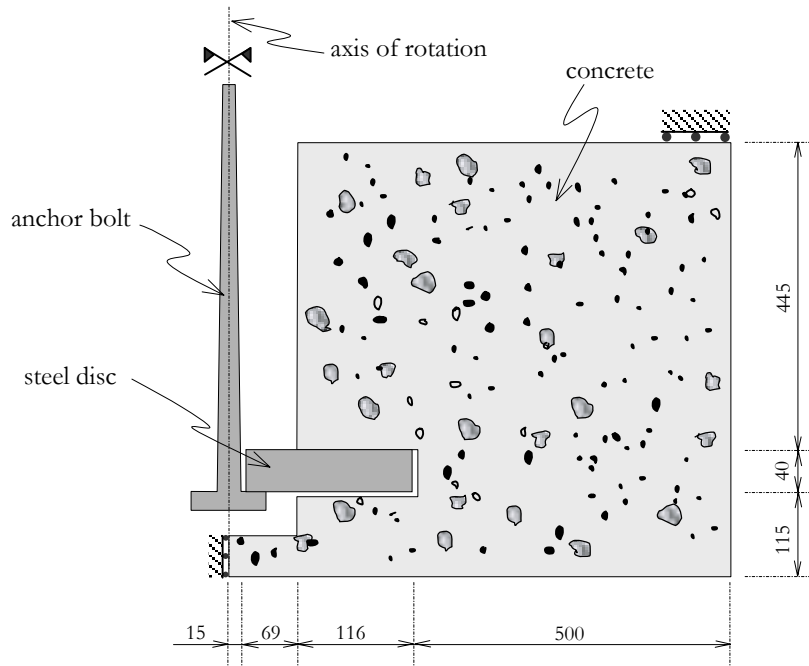
Figure 4.31: Detail of the anchorage structure – dimensions in *mm*.
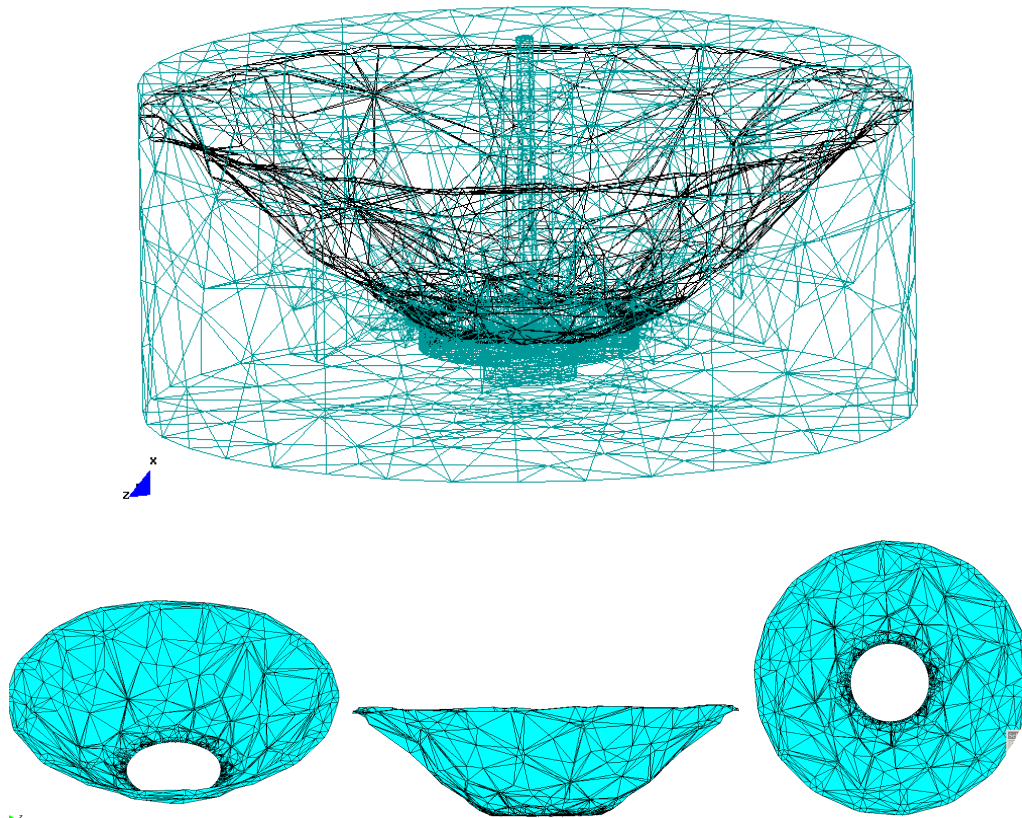
Figure 4.32: Continuous failure surface for the anchorage structure.

4.7.4.2 Double-notched shear beam

This test was performed by Bocca *et al.* (1990). The geometrical features and boundary conditions are shown in Figure 4.33. The mechanical properties are: $E = 27000 MPa$, Poisson's ratio $\nu = 0.18$, tensile strength $f_{ct} = 2.0\,N/mm^2$ and fracture energy $\mathcal{G}_f = 100\,N/m$. Figure 4.34 shows the normal vector field, and so does the Figure 4.35 but only the elements intersected by the discontinuity surfaces are considered. One must notice that for the elements intersected by the surface $\mathcal{S}^{(1)}$ the normal points toward $\mathcal{B}^{+(1)}$ and for the elements intersected by surface $\mathcal{S}^{(2)}$ the normal points toward $\mathcal{B}^{+(2)}$. In Figure 4.36(b) we show part of the beam without the elements intersected by the discontinuity surfaces so that it can compared with the crack pattern obtained by Bocca *et al.* (1990) (see Figure 4.36(a)).
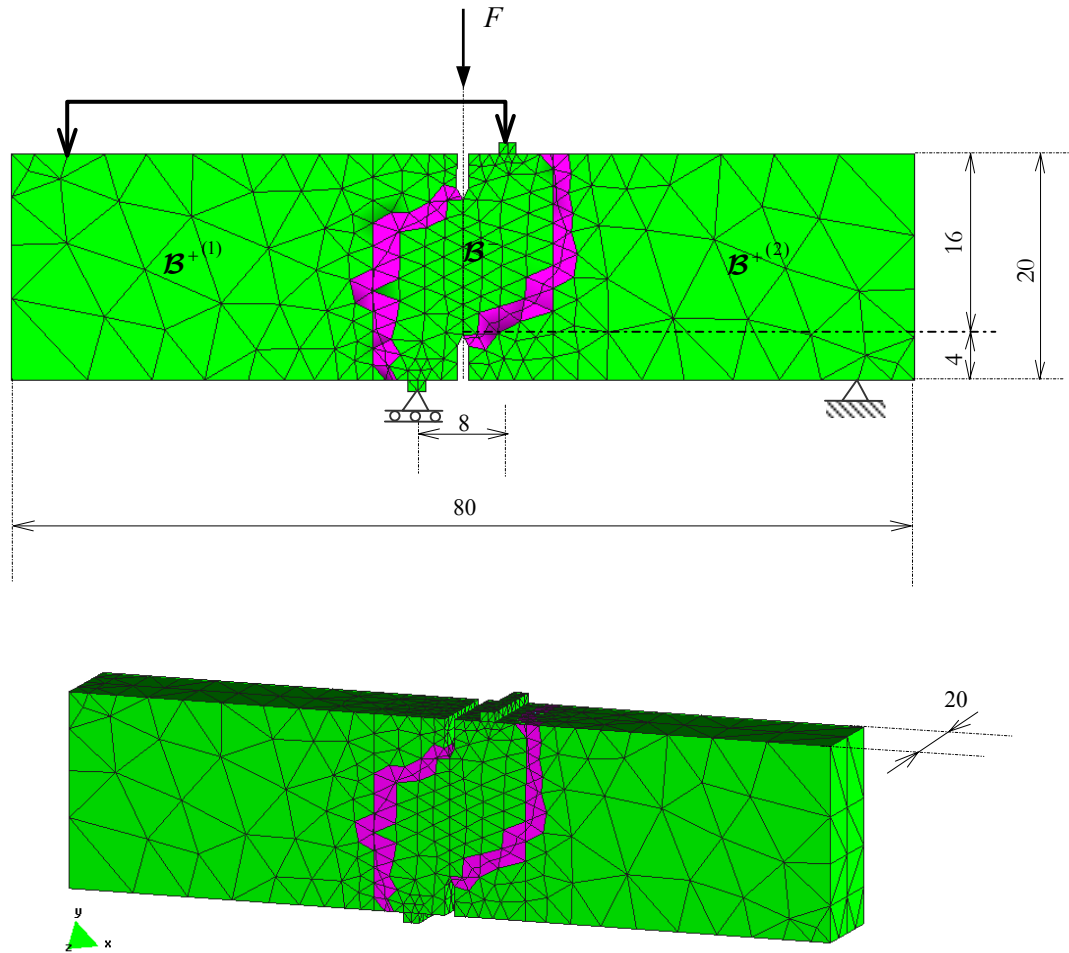
Figure 4.33: Four point shear specimen (dimensions in *cm*).
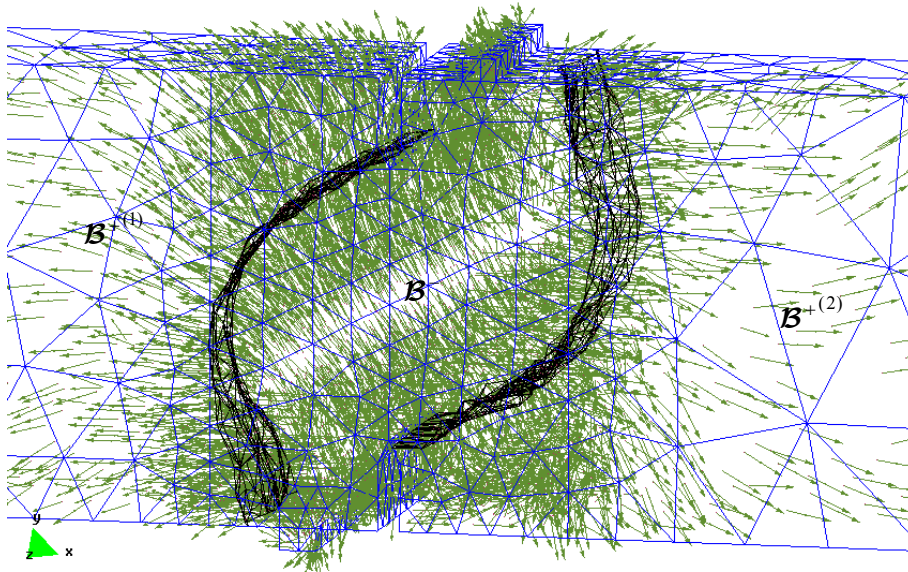
Figure 4.34: Normal vector field.
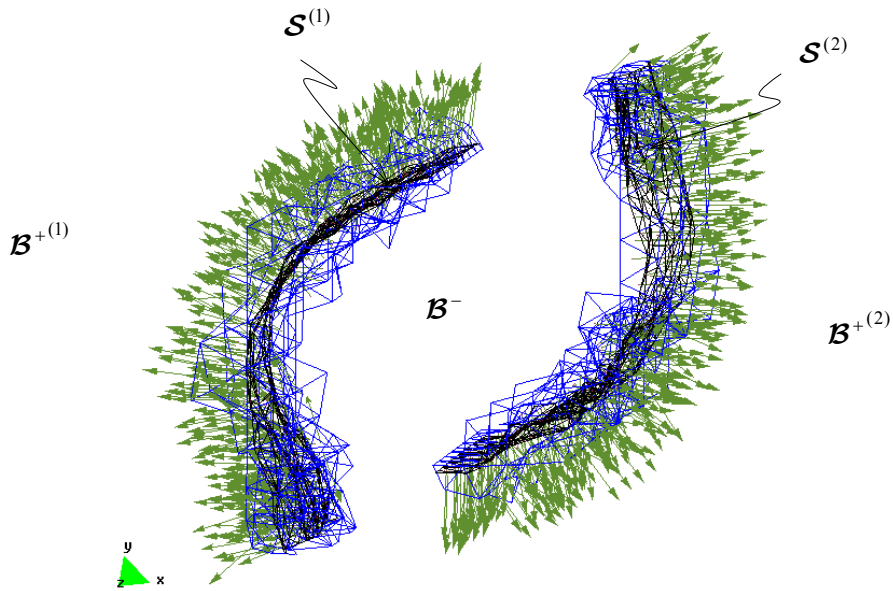
Figure 4.35: Elements intersected by failure surfaces.
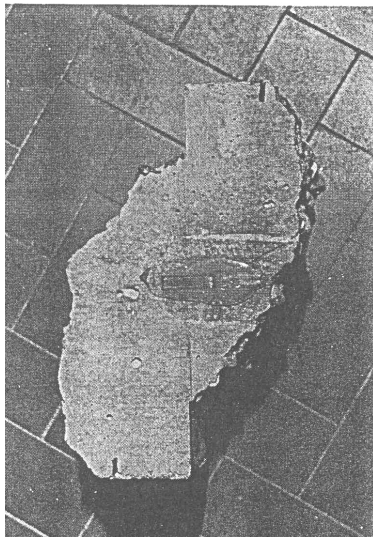
(a) Bocca *et al.* (1990)
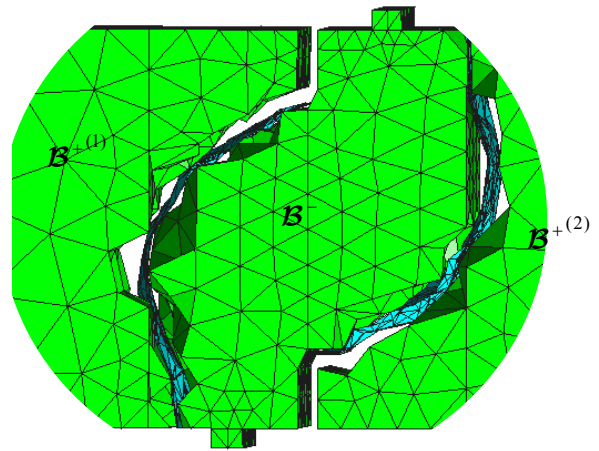
(b)
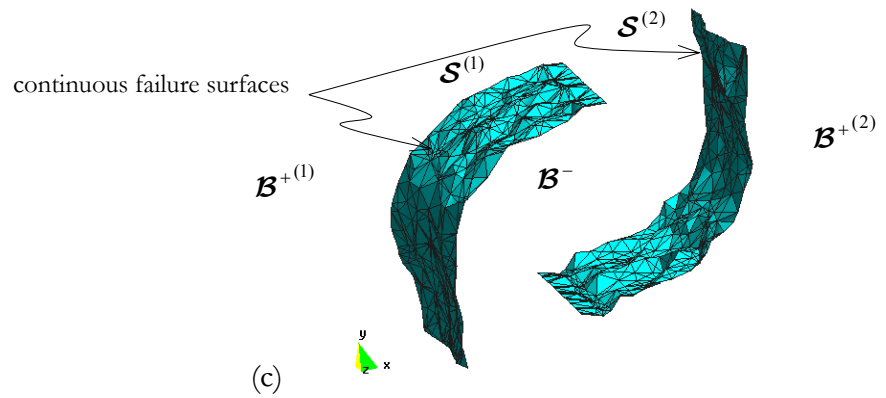
(c)

Figure 4.36: Four point shear specimen – initial failure surface.

4.7.4.3 Torsion problem

This example consist of the propagation of the crack in a hollow cylindrical pipe which is loaded by torsional moments at its ends. The pipe has a length of 63 mm and inner and outer radii of 8 and 12mm, respectively. In this example the material properties considered are: $E = 2.88 \times 10^7$, $\nu = 0.18$, $\mathcal{G}_f = 1.0$ and $f_{ct} = 2.8 \times 10^6$ and the 3D discretized mesh has 5670 tetrahedrons. Figure 4.38 shows the continuous failure surface.
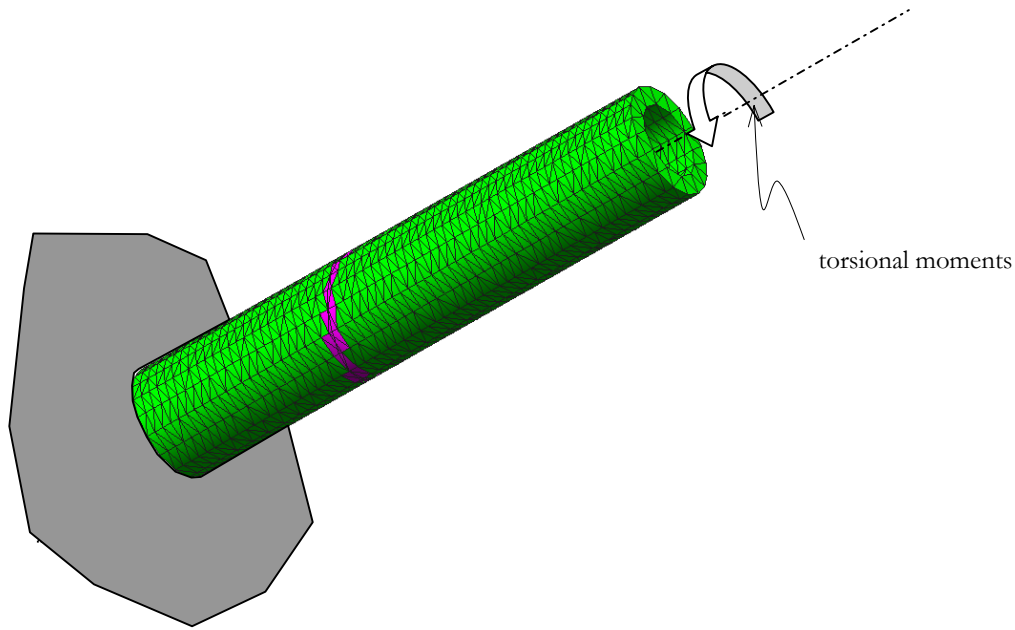
torsional moments

Figure 4.37: Crack pattern for a hollow cylindrical pipe loaded by torsional moment.
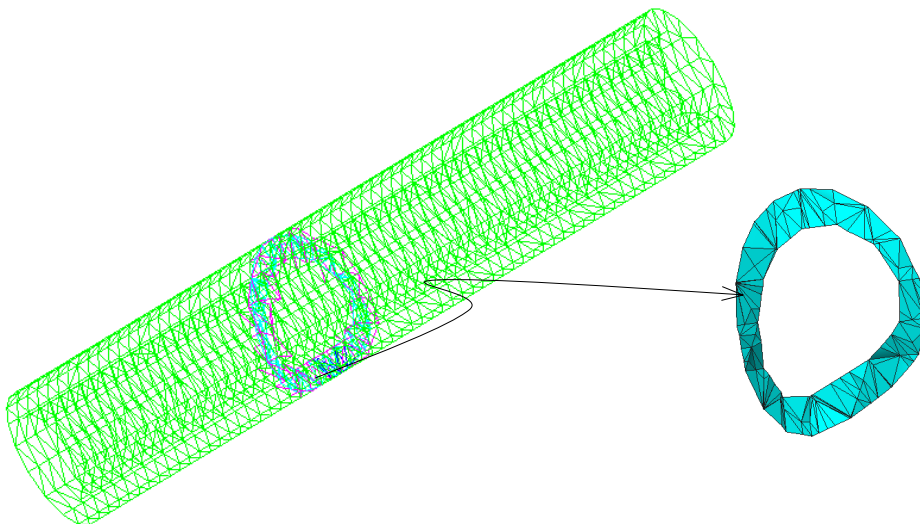
Figure 4.38: Torsion problem – failure surface.

4.7.4.4 Brazilian test

Tensile strength of a material is a measure of its ability to resist uniaxial tensile loads without yielding or fracture. A direct-pull test is difficult to apply to rocks and in many cases some type of indirect test is employed to determine tensile strength.

A concrete cylinder of length $L = 300mm$ with diameter $D = 150mm$, as shown in Figure 4.39, subjected to a line spread load. Material properties are specified as: compressive strength $f_c^{'} = 32MPa$, Young's modulus $E = 32.4GPa$, and Poisson's ratio $\nu = 0.2$, Fracture energy $\mathcal{G}_f = 115N/m$. The Brazilian Test is often used to predict the direct tensile strength of concrete as given by $f_{ct} = 2P_{ult}/\pi LD$.

Figure 4.40(a) shows the family of surfaces normal to the principal direction and Figure 4.40(a) shows the plane formed by one of the elements of this family of surfaces.
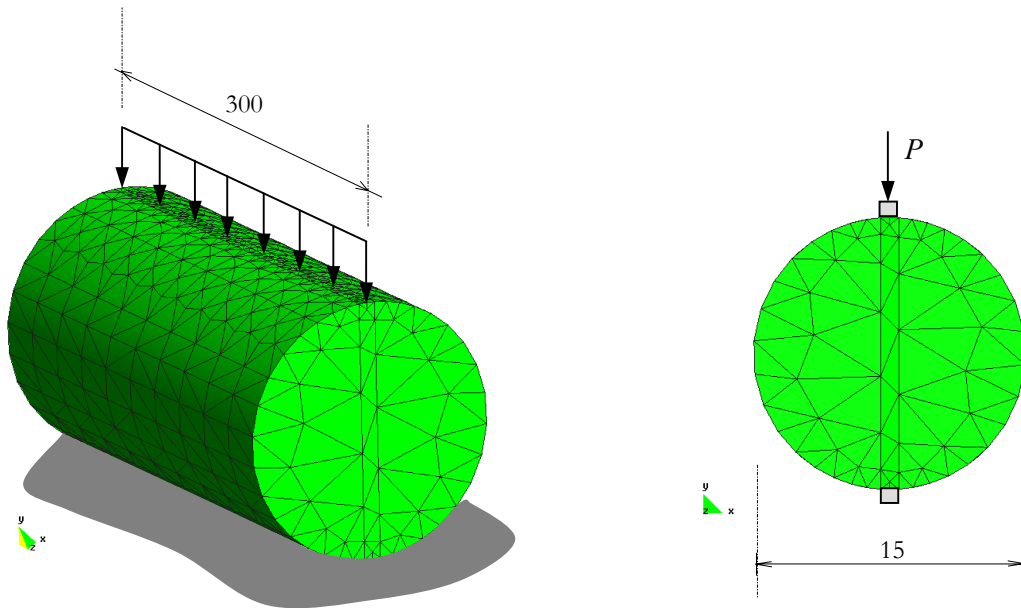
Figure 4.39: Brazilian test – Geometry (dimensions in millimeters).
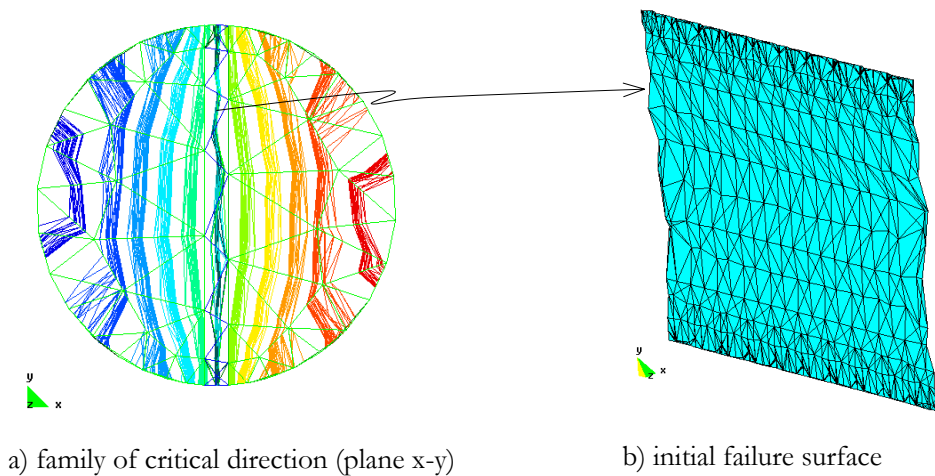
| a) family of critical direction (plane x-y) | b) initial failure surface |

Figure 4.40: Brazilian test.

5

Representative Numerical Simulations

5.1 Introduction

In this chapter some examples to illustrate the effectiveness of the method described in the previous chapters are presented. All the examples described here were simulated using the Strong Discontinuity Approach together with a damage model to represent the non-linear behavior of the material.

5.1.1 Tools

An ordinary FEM analysis tool consists of three parts (a): pre-process (*e.g.* mesh generator), main-process (*i.e.* FEM-code), and post-process (*e.g.* visualizer, etc). The pre-process and post-process were performed in the program GID, which was developed in CIMNE-UPC.

All the implementations in this work were done in COMET (Coupled Mechanical and Thermal Analysis) [Cervera *et al.*(2001)] developed in CIMNE-UPC. It is a non-linear finite element program which offers the following tools:

- Initial stiffness, full Newton-Raphson and modified Newton-Raphson methods for solving the nonlinear problem;

- Line search;

- Convergence accelerators: Secant-Newton (1 or 2 parameters), and BFGS;

- Arc-length and displacement control;

- Automatic load incrementation.

Other particular features are:

- The integration may be performed by Gauss, Lobatto or Irons rules;

- The system of linear equations can be solved by a Direct solver (using a Skyline, Banded or Sparse storage scheme), by Preconditioned conjugated gradient iterative solver, or by GMRES iterative solver.

5.2 The importance of the exact capture of the bifurcation pseudo-time

As seen in Chapter 3, for a given stress state, the critical values of the normal $\mathbf{N}_{crit}$ and of the hardening modulus $\mathcal{H}_{crit}$ can be obtained through bifurcation analysis. The bifurcation analysis, within the context of the finite element method, is performed at the gauss point level and has a local character, *i.e.*, the bifurcation analysis does not give us information about the propagation of the fissure on a global level.

With regard to propagation, the methodology employed in the numerical model considered in this work is such that, when the bifurcation condition is reached, the critical angle is frozen at the element level. Thus, the importance of an accurate determination of the critical angle is clear. A significantly biased critical angle can be computed if the steps used in the loading process are too big (see Figure 5.1).
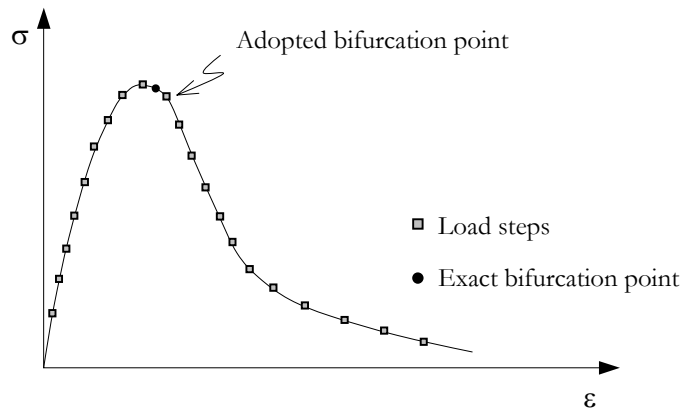
Figure 5.1: stress-strain – load steps.

To illustrate this problem, consider a two-dimensional example (a biaxial test), which has two loading stages (see Figure 5.2). In this example the isotropic damage model described in Chapter 2 was adopted, where $\mathbf{n} = \mathbf{m} = \boldsymbol{\varepsilon}$.
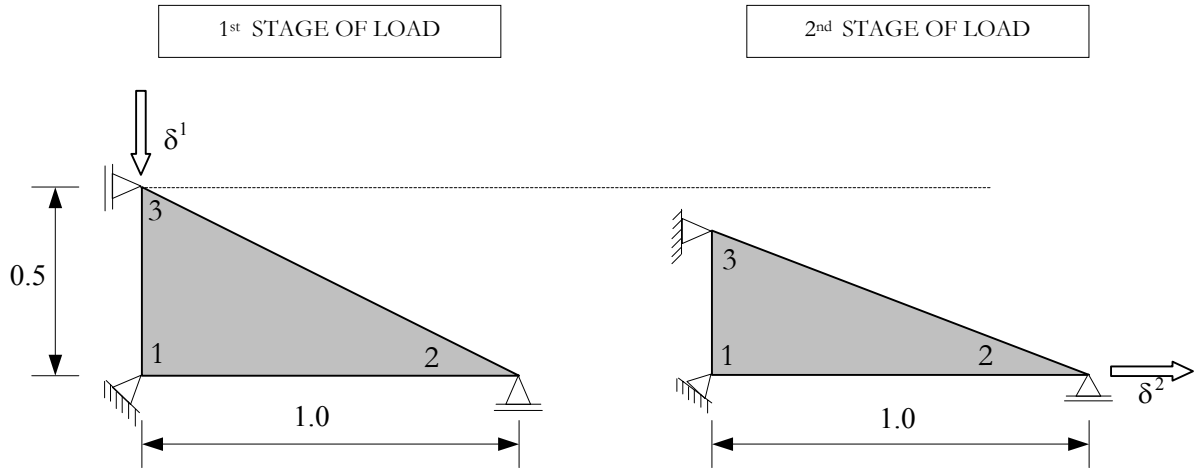
Figure 5.2: Biaxial test.

In the second loading stage, when the bifurcation condition is reached, the strain state is schematically shown in Figure 5.3 and the state of the variables of the damage model is $d = 0.0466785267$ and $r = 0.007417250882366$. Using equation (3.118), one can obtain the value of the critical angle:

$$\tan^2 \theta_{crit} = -\frac{\varepsilon_2}{\varepsilon_1} \quad \Rightarrow \quad \theta_{crit} = 31.196° \tag{5.1}$$

$$\varepsilon_1 = 5.45454545 \times 10^{-5}$$
$$\varepsilon_2 = -2.0 \times 10^{-5}$$
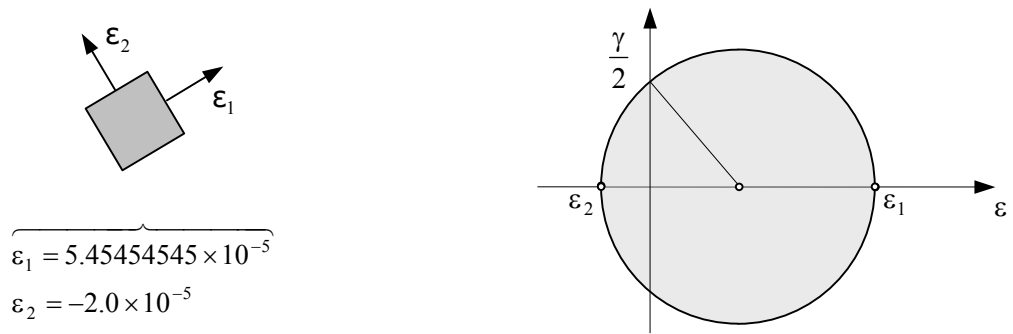
Mohr's circle in strain

Figure 5.3: Strain state of the biaxial case.

We can sketch this specific strain state in the Mohr's circle (see Figure 5.4). In the same figure we have plotted the localization ellipse for different values of $\mathbf{N}(\theta)$ to show that, for this specific strain state, $\mathcal{H}^d_{crit}$ corresponds to the most external localization ellipse.

Consider now the same example but with a different discretization of the loading process (pseudo-time discretization), which is more refined than the previous one. For this case, the first point when the bifurcation condition is reached, is characterized by the following strain state: $\varepsilon_1 = 4.583090909 \times 10^{-5}$, $\varepsilon_2 = -2.0 \times 10^{-5}$, with the damage model variables being $d = 4.44523 \times 10^{-5}$, $r = 0.0070713821220752$. At this strain state we can obtain the critical angle as:

$$\tan^2 \theta_{crit} = -\frac{\varepsilon_2}{\varepsilon_1} \quad \Rightarrow \quad \theta_{crit} = 33.4486^\circ \tag{5.2}$$

In Figure 5.5 the standardized acoustic tensor $|\mathbf{Q}|/|\mathbf{Q}^e|$ is shown in terms of the normal direction $\mathbf{N}(\theta)$. In Figure 5.6 the strain Morh's circle and its correspondent localization ellipses are constructed for the two discretizations of the loading process just considered. One can notice that there exists a difference of more than 2° for the critical angle between them.
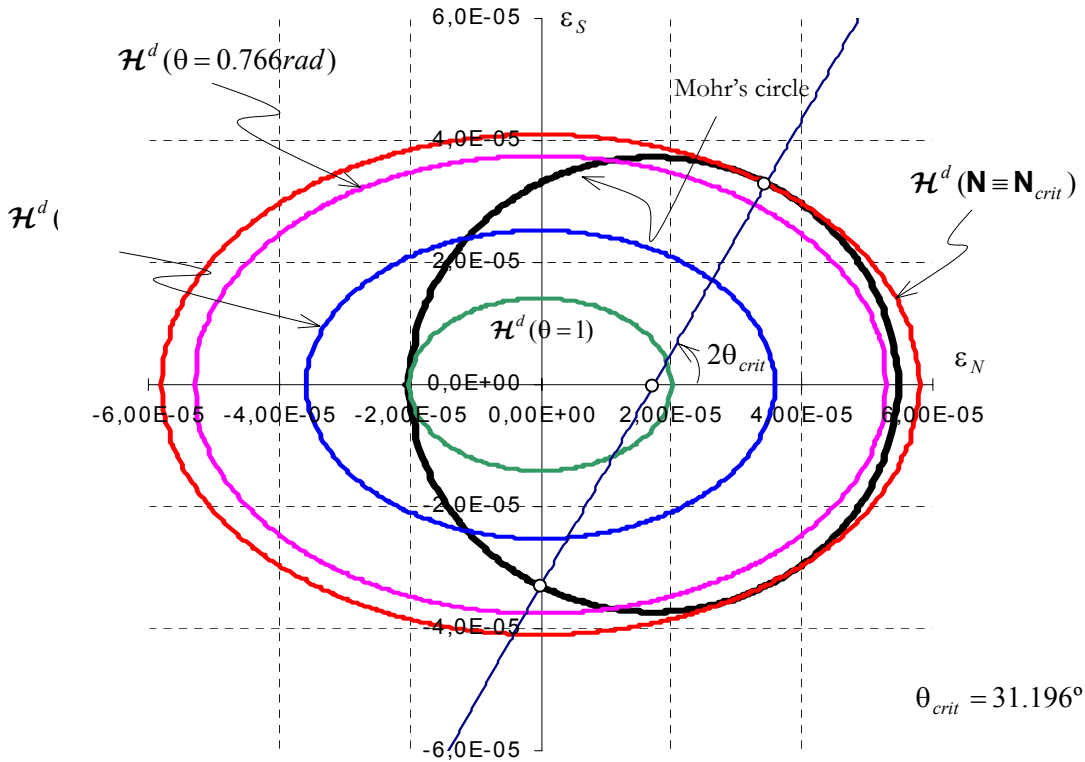
Figure 5.4: Mohr's circle and ellipse of localization.
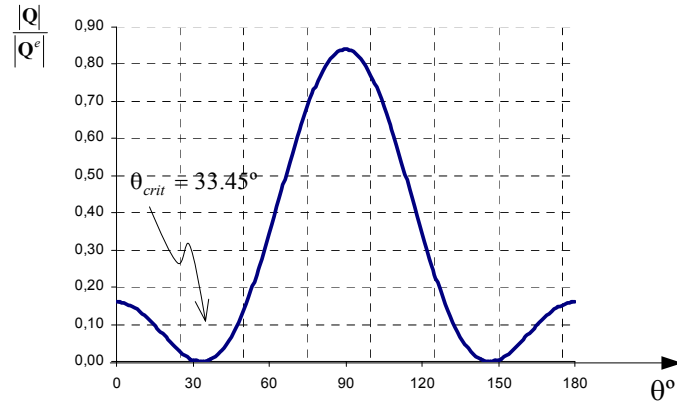
Figure 5.5: Localization properties of isotropic damage model.
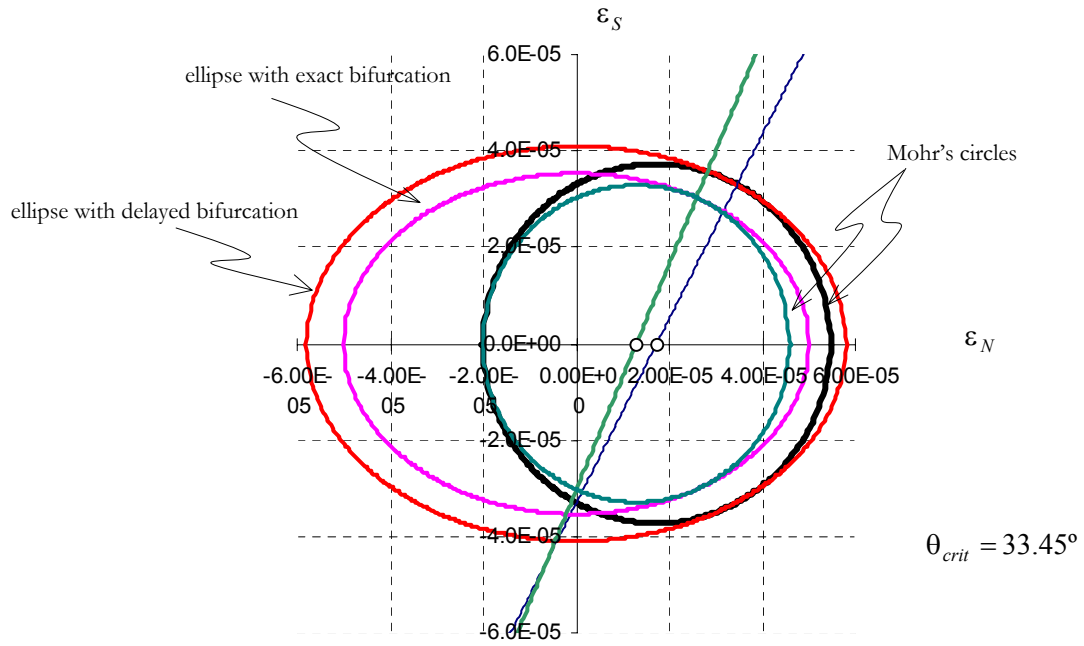
Figure 5.6: Mohr's circle and localization ellipse.

Now consider the following example whose geometry and finite element mesh are shown in Figure 5.7. Force F is applied as indicated in the same figure. We do not provide material data because this example is only illustrative. We used the same geometry and finite element mesh with different strategies for simulating the loading process. In Figure 5.7(a) and (b) we are applying displacement control.
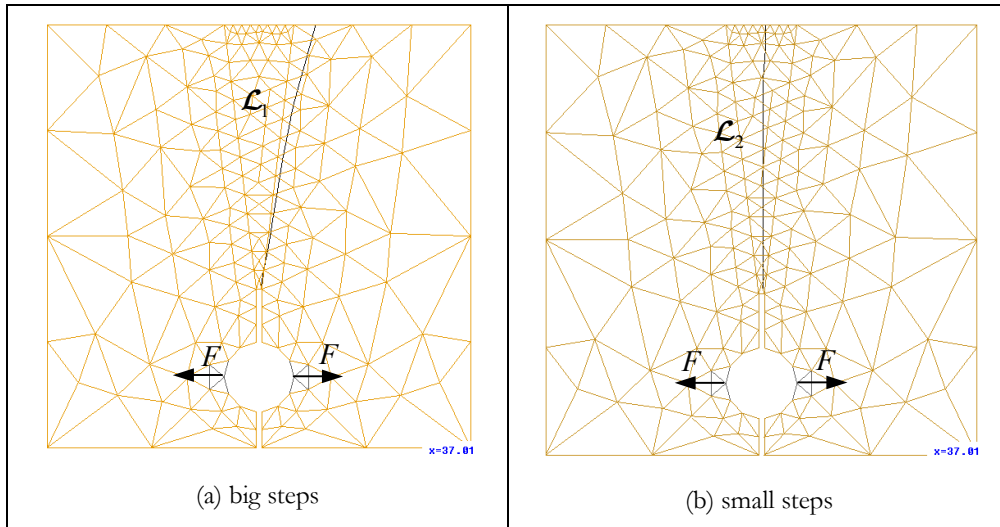
Figure 5.7: Discontinuity lines with distinct strategies.

As described in Chapter 4, on the basis of the Gauss points information we can "track" the discontinuity line $\mathcal{L}$. This "tracking" of the discontinuity line can change from step to step in the loading process. However, once the bifurcation criterion is satisfied in some element, this line does not change anymore for that element. Using the different loading strategies, described before, one can obtain distinct discontinuity lines as shown in Figure 5.7. The corresponding force *vs.* displacement curves are shown in Figure 5.8. Based on those figures, we can conclude that the resulting tracked line may be very sensitive to the discretization of the loading process adopted, due to the fact that an inaccurate capturing of the bifurcation pseudo-time can lead to non negligible errors in the global response.
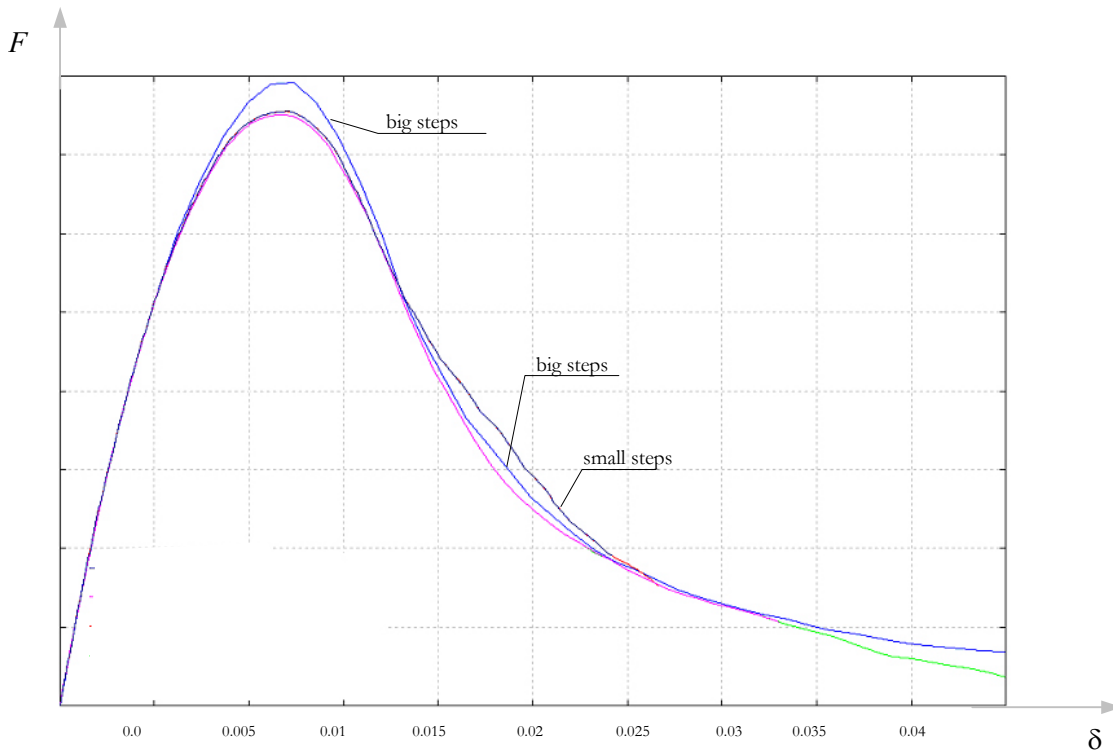
Figure 5.8: Force *vs.* displacement curve.

5.3 Tension test

5.3.1 Tension bar

In this example the bar of Figure 5.9, in a uniaxial tension process, is analyzed to assess the mesh dependence of the results. A linear softening law was used. The geometry, the boundary conditions and the material properties of the tension bar are given in Figure 5.9, where E stands for the Young's modulus, ν stands for the Poisson's ratio, f_{ct} stands for the elastic strength and $\mathcal{G}_f$ represents the fracture energy. The two meshes of tetrahedral finite elements, shown in Figure 5.10, were considered: a mesh of 267 elements (mesh 1) and a much finer mesh of 1137 elements (mesh 2). A mesh of hexahedral finite element (brick) with 132 elements (mesh 3) was also used (see Figure 5.11).

In Figure 5.12 the load-displacement curves obtained for both meshes are presented. It can be checked that the results are the same (indistinguishable in the plots), this showing the mesh size objectivity of the results.

$$E = 20000$$
$$\nu = 0.0$$
$$f_{ct} = 1.0$$
$$\mathcal{G}_f = 0.18$$
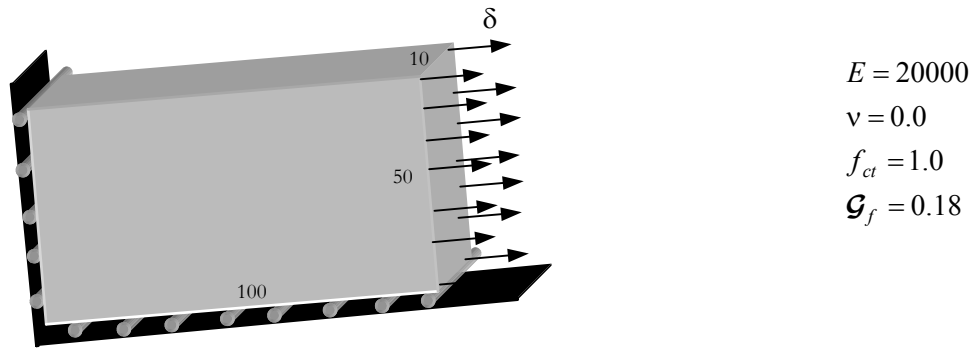
Figure 5.9: Tension bar.

Mesh 1   Mesh 2
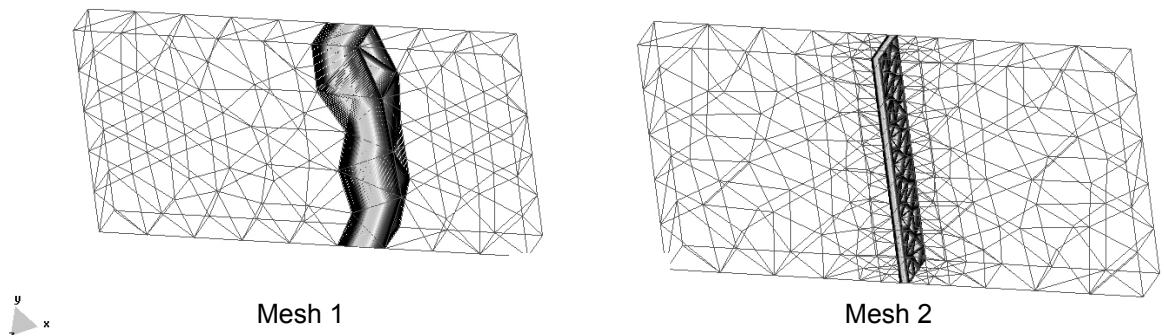
Figure 5.10: Meshes and localization bands (displacement contours) for the tension bar problem.

Mesh 3

(a) Localization band

(b) Mesh without fractured elements
with discontinuity surface $\mathcal{S}$.
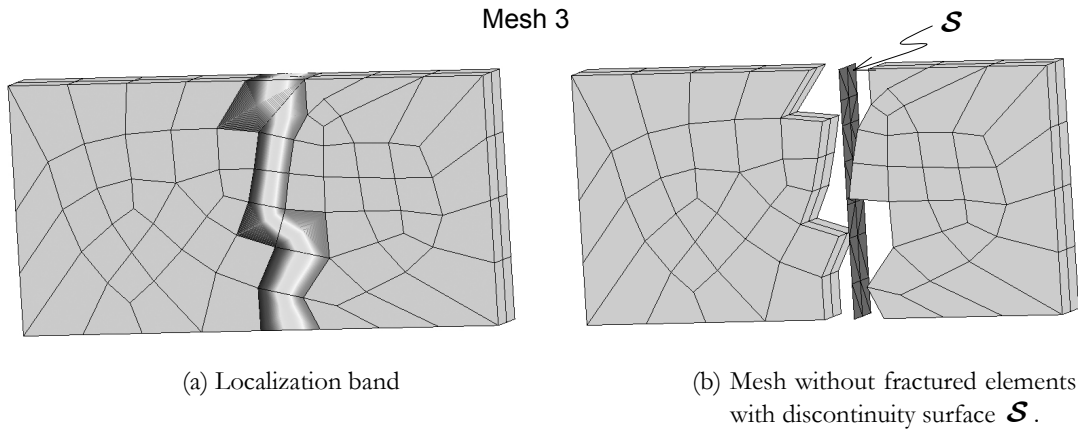
Figure 5.11: Meshes and localization bands for the tension bar problem with hexahedrons.
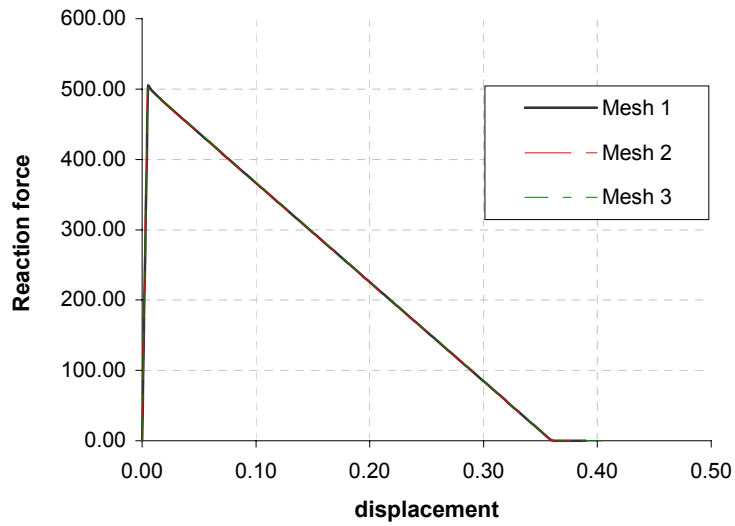
Figure 5.12: Load-displacement diagram for tension bar problem.
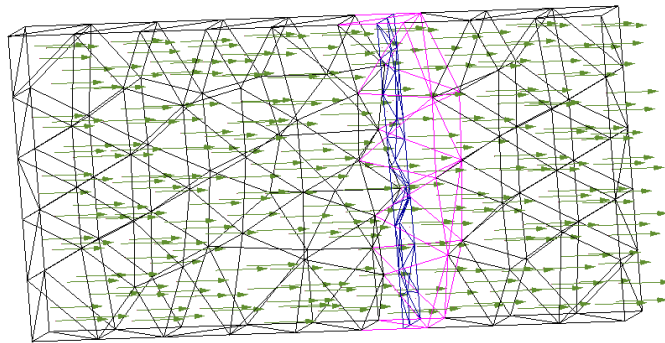
Figure 5.13: The propagation of vector fields.

5.4 Three-point bending test

The classical three-point bending test reported by Petersson (1981) is now simulated. This test was employed in 1985 to determine the fracture energy of concrete. It is now accepted as RILEM recommendation. It deals with mode I fracture of non-reinforced concrete. The size of the specimens and the testing method are described in Figure 5.14 as well as the characterization of the concrete by the following parameters: fracture energy - $\mathcal{G}_f$, tensile strength - f_{ct}, Young's modulus - E, Poisson's ratio - ν. The density of the concrete was assumed to be $\rho_{conc} = 2300\, kg/m^3$.

The experiments data were taken from Rots *et al.* (1985). The numerical solution was obtained by displacement control. Two different meshes were used to obtain the load-displacement response, details of the two meshes can be seen in Figure 5.15. Mesh 1 with 1373 elements can be seen in Figure 5.16, where its deformation is shown, and mesh 2, with 2247 elements, in Figure 5.17. Figure 5.18 shows the load-displacement curves for both meshes.

For each mesh the linear and the exponential softening law (see Figure 5.18) were used, the latter showing a better agreement with the experimental curve in the softening branch. One can note that the peak load is very sensitive to the softening law used. Thus, it seems clear that a better agreement would be obtained with an alternative type of softening law.

Data, Rots(1985):

$E = 30000 N/mm^2$

$\nu = 0.20$

$f_{ct} = 3.33 N/mm^2$

$\mathcal{G}_f = 124 N/m$

$S = 2000 mm$

$b = 50 mm$

$W = 200 mm$
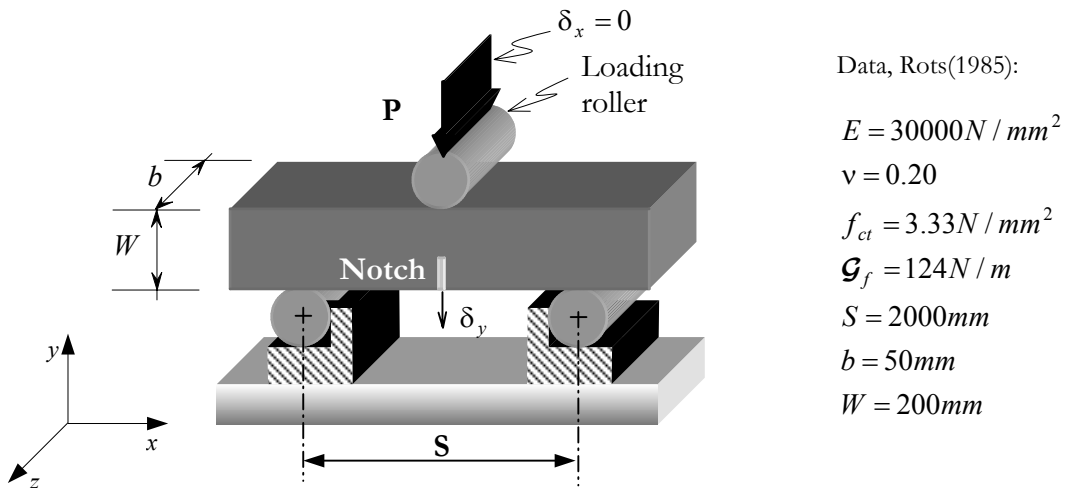
Figure 5.14: Three point notched beam.

a) mesh 1   b) mesh 2
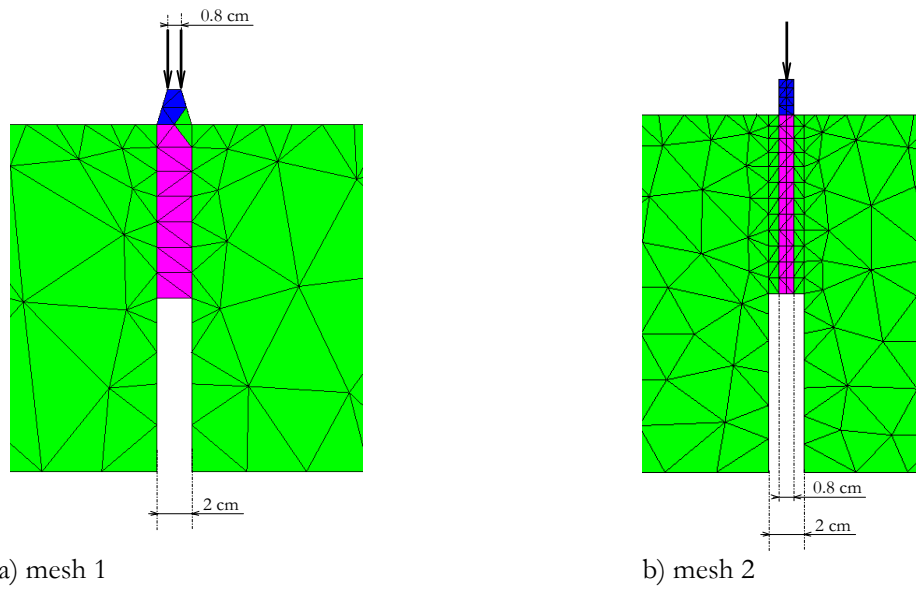
Figure 5.15: Three point notched beam - details.
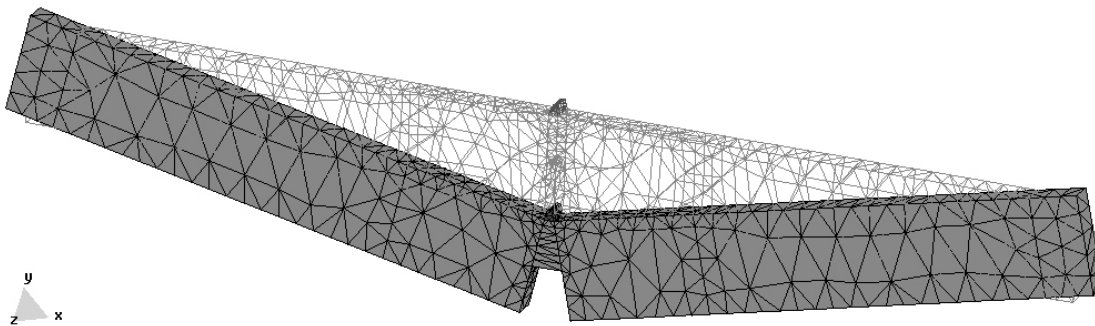
Figure 5.16: Deflection – mesh 1.
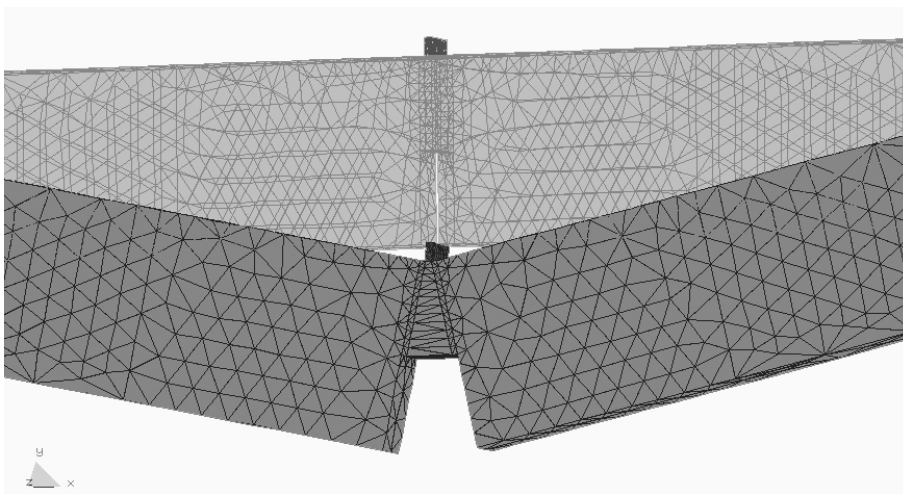
Figure 5.17: Deflection – mesh 2.
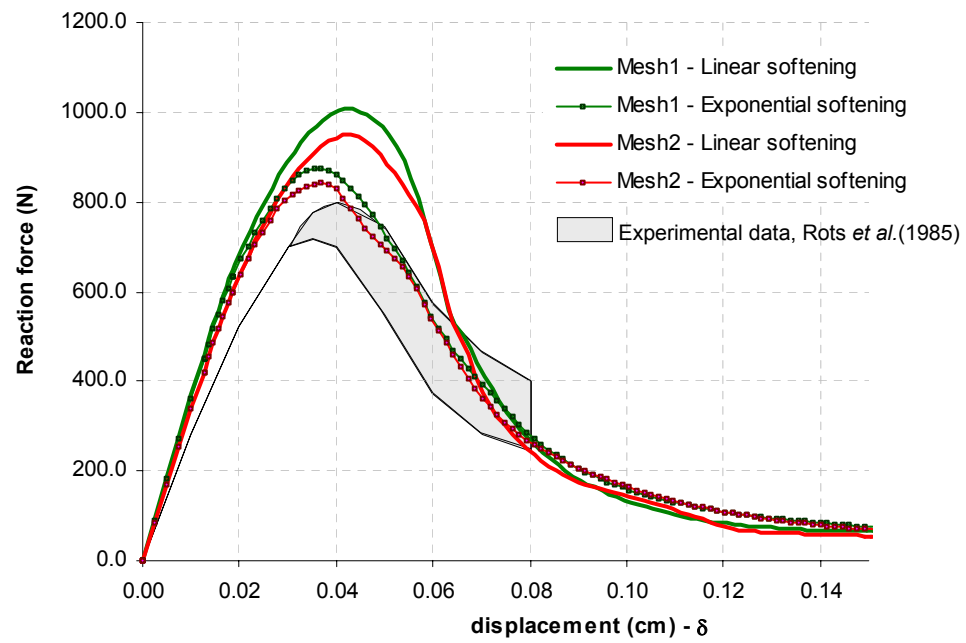
Figure 5.18: Load-displacement diagram for three point notched beam.

5.4.1   Notched bar in tension

In this test, the mode I fracture simulation of a notched specimen is undertaken by using a continuum damage model considering a tension-only damage criterion and exponential softening. Figure 5.19 shows the geometry and the considered finite element mesh. The following material parameters are adopted: fracture energy - $\mathcal{G}_f = 100.0 N / m$, tensile strength - $f_{ct} = 3.0 N / mm^2$, Young's modulus - $E = 3.0 \times 10^4 N / mm^2$, Poisson's ratio - $\nu = 0.2$. The mesh is completely unstructured, non symmetric and slightly refined in the zone where the discontinuity is expected to appear. For comparison purposes, we also used a more structured mesh, as shown in Figure 5.20. On the other hand, Figure 5.21 shows the force *vs.* displacement curve for both meshes, whereas Figure 5.22 shows the deformed mesh at the end of the analysis, where the localization of the strain field along the band of elements capturing the discontinuity can be observed.
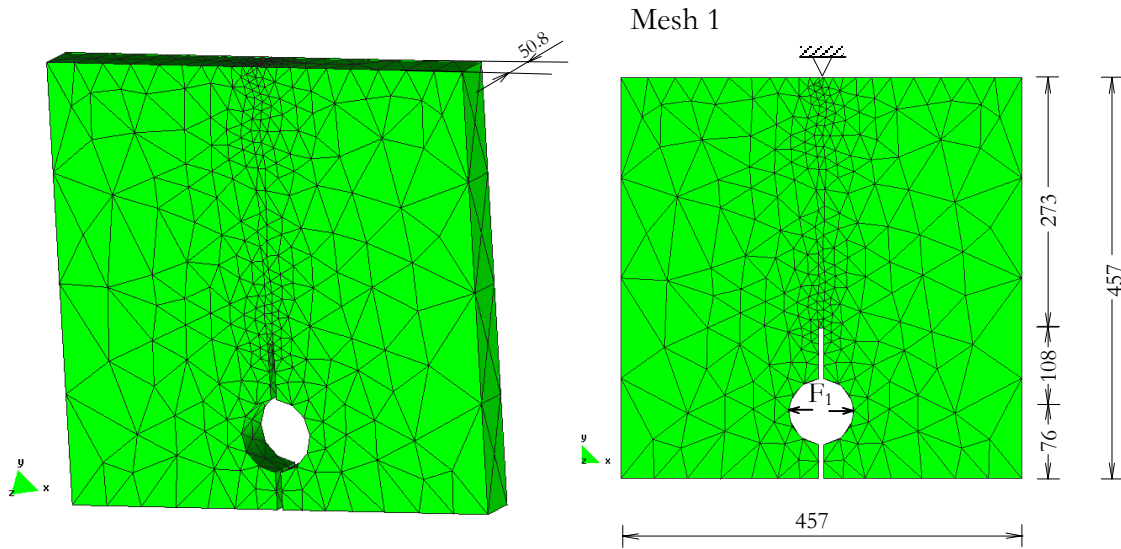
Figure 5.19: Geometry and mesh 1 (dimensions in millimeters- *mm*).
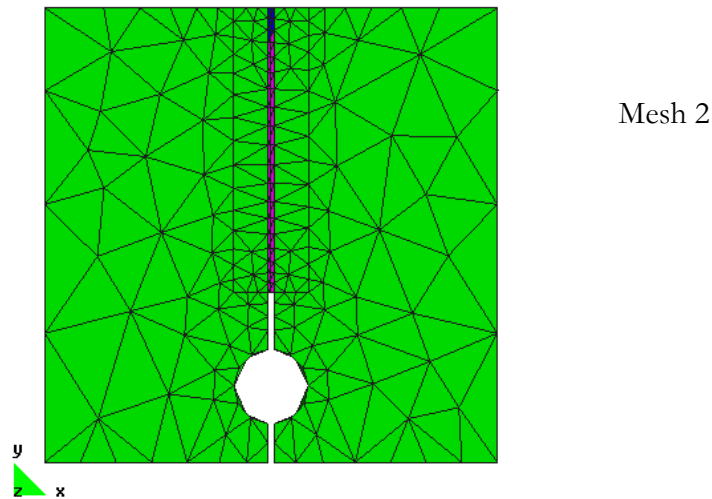
Figure 5.20: Mesh 2 and localization zone.
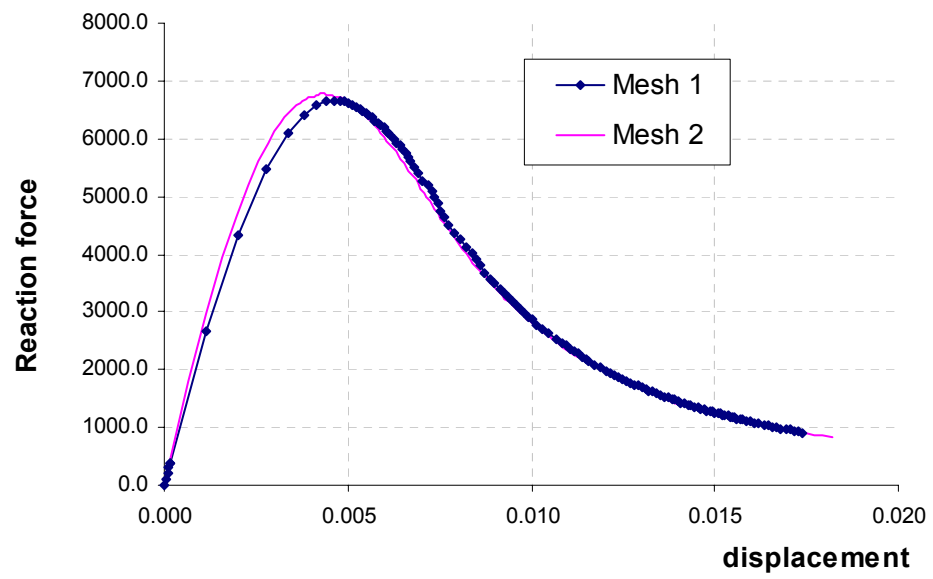
Figure 5.21: Load-displacement diagram for tension bar problem.
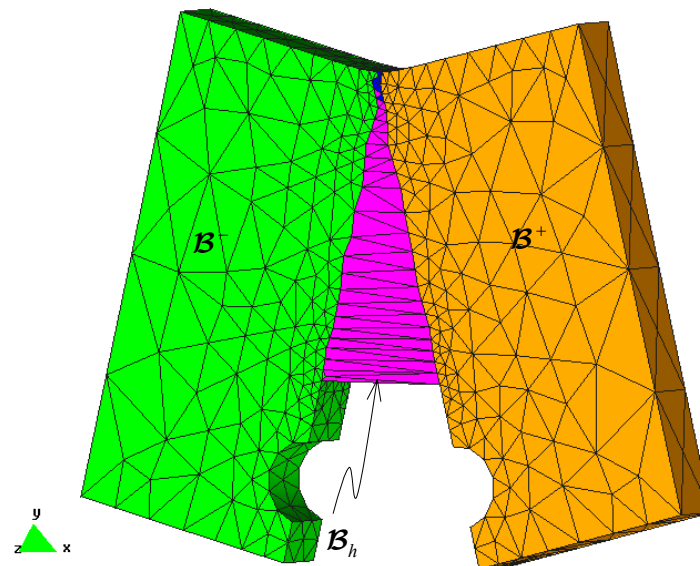
Figure 5.22: Deformation (amplified 5000 times).

5.5 Direct tension

This series of experiments, double-edge notched, were considered in Reinhardt *et al.* (1986), Hordijk *et al.* (1987) and Rots (1988). Hordijk(1991), using a different value for L, has also analyzed it for lightweight concrete.

The geometry and used mesh can be seen in Figure 5.23. The discretization consists of 8421 tetrahedral finite elements.

The material data adopted for concrete are: Young's modulus, $E = 18000\,N/mm^2$; Poisson's ratio, $\nu = 0.2$; tensile strength, $f_{ct} = 3.4\,N/mm^2$, and fracture energy $\mathcal{G}_f = 59.3\,J/m^2$. These data are in accordance with Reinhardt *et al.* (1986), Hordijk *et al.* (1987) and Rots (1988).
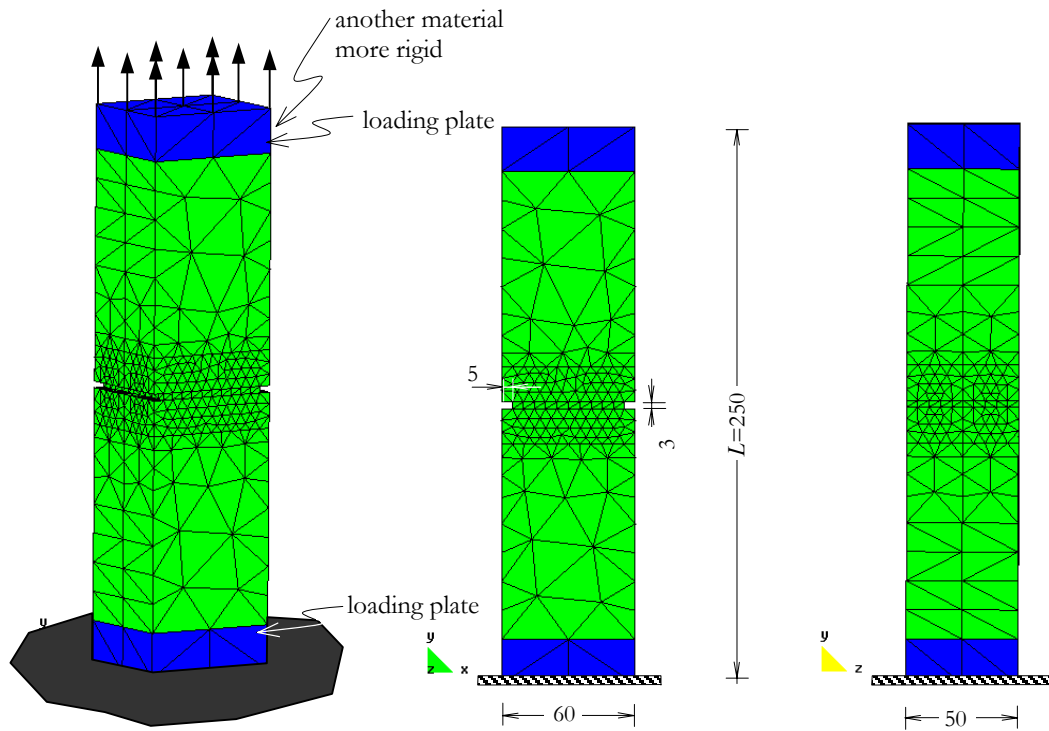
Figure 5.23: Double-notched specimen (dimensions in millimeters- mm).

This example can lead to two solutions: in one of them the crack propagations is symmetric and in the other the crack propagates from one side of the specimen to the other side.

In Figure 5.24 we can observe that anti symmetric possible crack paths are tracked based on the information obtained from the material bifurcation analysis and using an

overall tracking strategy. As loading progresses, the two crack paths tend to become one single crack path. This example is very sensitive to the boundary conditions and, thus, in practice this symmetry can be broken by material imperfections and the loading velocity. As a consequence, a global bifurcation analysis of the structure might be necessary.

For the sake of simplicity, we consider that the critical direction coincides with the stresses principal direction. Figure 5.25 shows the family of envelopes of the vector field corresponding to the normal to the first principal direction, which is used to track the crack surfaces in the remaining of this section.
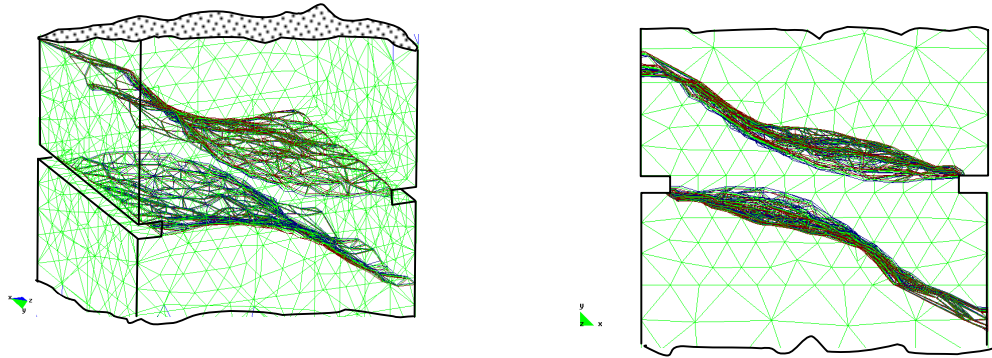
Figure 5.24: Continuous failure surfaces.
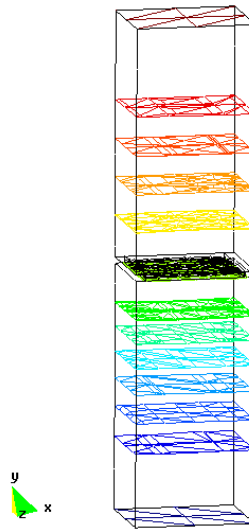
Figure 5.25: Family of envelopes of the principal direction.

In this example three different cases have been analyzed: A, B and C (see Figure 5.26). All cases were run under load control first. Then, an arc-length scheme was used to compute the response beyond the peak load. The controlled point is the center point, see Figure 5.26.

In case A we have restricted the displacement in the z direction for three points as shown in Figure 5.26. In this case the damping-like parameter considered was $\overline{\eta} = 0.005 Ns / cm^3$.
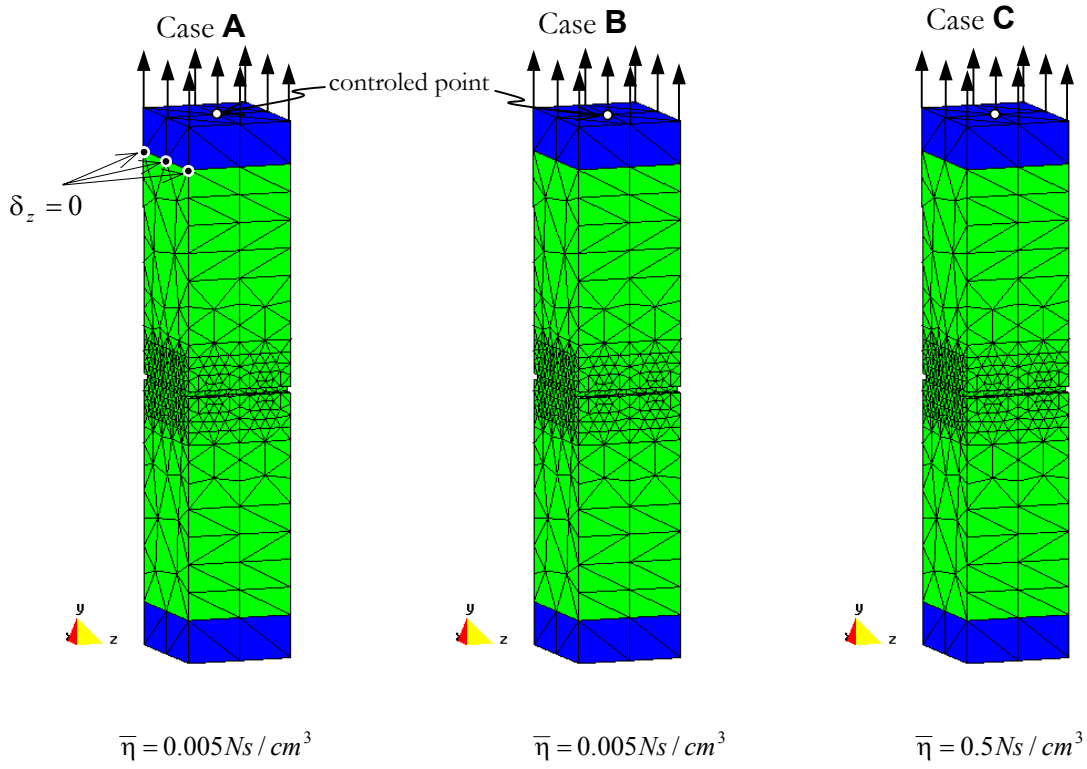
Figure 5.26: Failure material discontinuity.

5.5.1 Results for Case A

For this case the force *vs.* displacement curve is shown in Figure 5.27. In Figure 5.28 we can see the deformation corresponding to points A1, A2, A3 and A4 signaled in Figure 5.27.
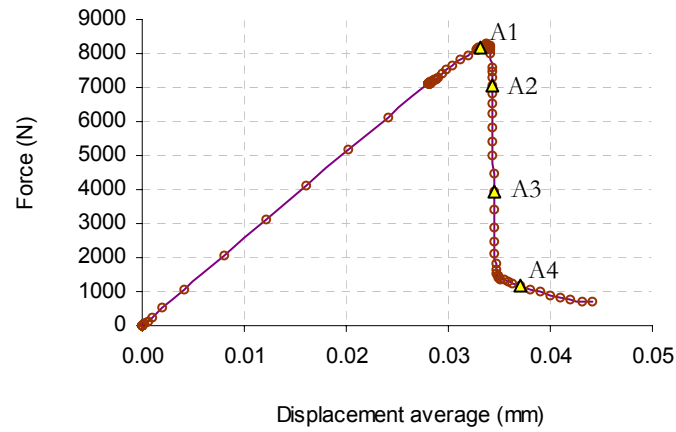
Figure 5.27: Force *vs.* displacement – Case A.
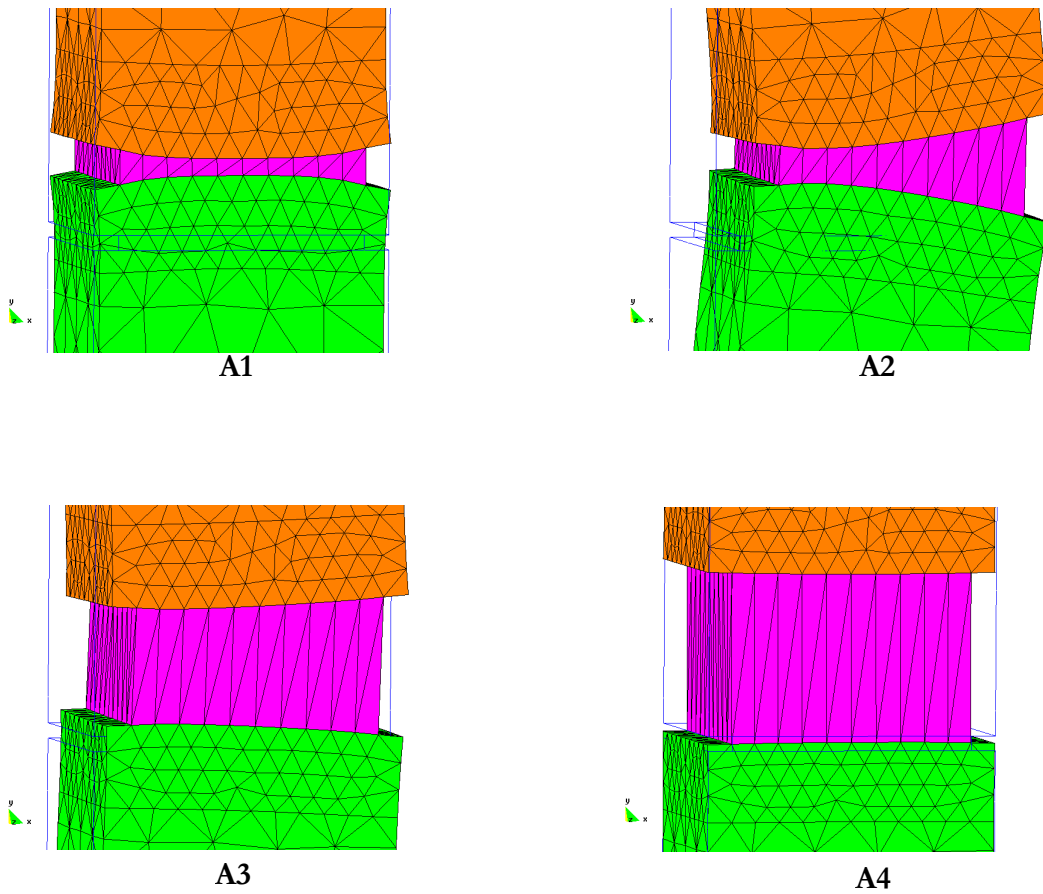
Figure 5.28: Deformation (scalar factor: 900) – Case A.

5.5.2 Results for Case B

For this case the force *vs.* displacement curve is shown in Figure 5.29. In Figure 5.30 we can see the deformations corresponding to points B1, B2, B3, B4, B5 and B6 signaled in Figure 5.29.
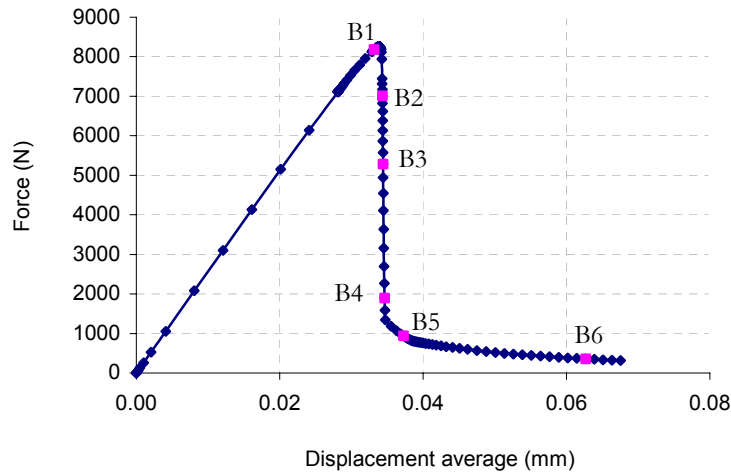
Figure 5.29: Force *vs.* displacement – Case B.
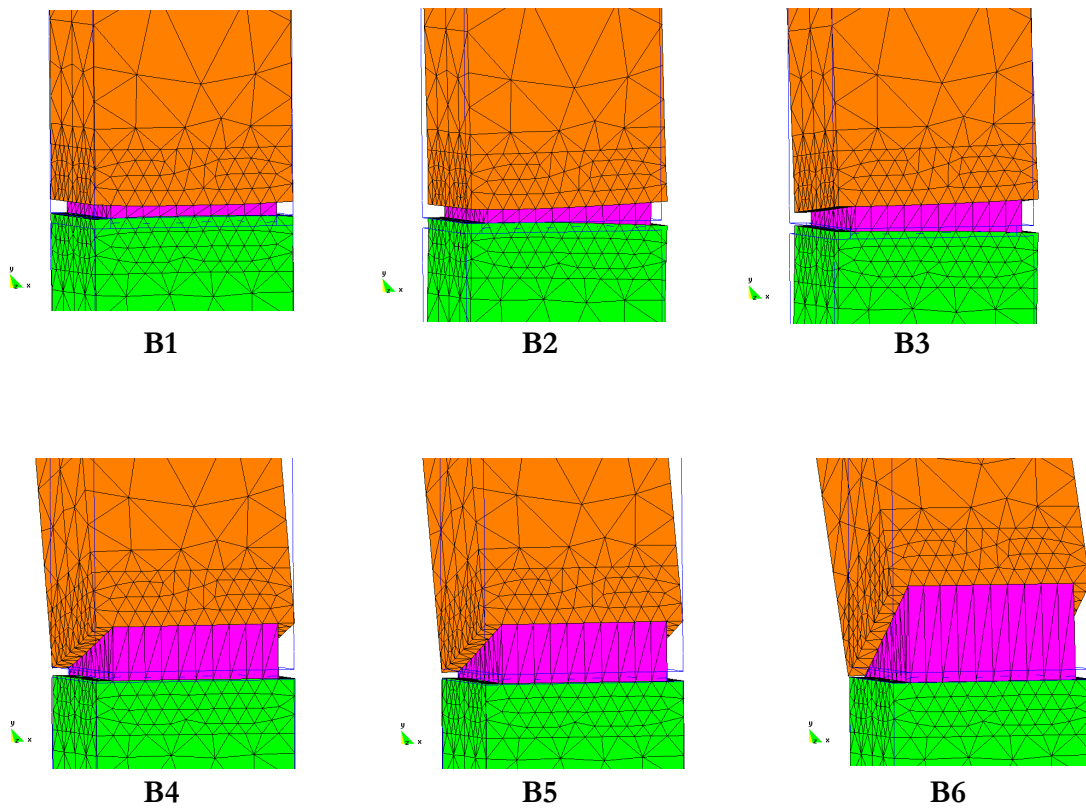
Figure 5.30: Deformation (scalar factor: 200) – Case B.

5.5.3 Results for Case C

For this case the force *vs.* displacement curve is shown in Figure 5.31. In Figure 5.32 we can see the deformations corresponding to points B1, B2, B3, B4, B5 and B6 indicated in Figure 5.31.
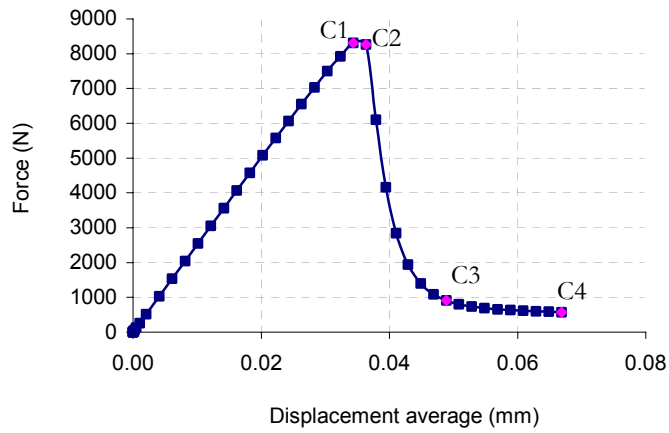
Figure 5.31: Force *vs.* displacement – Case C.
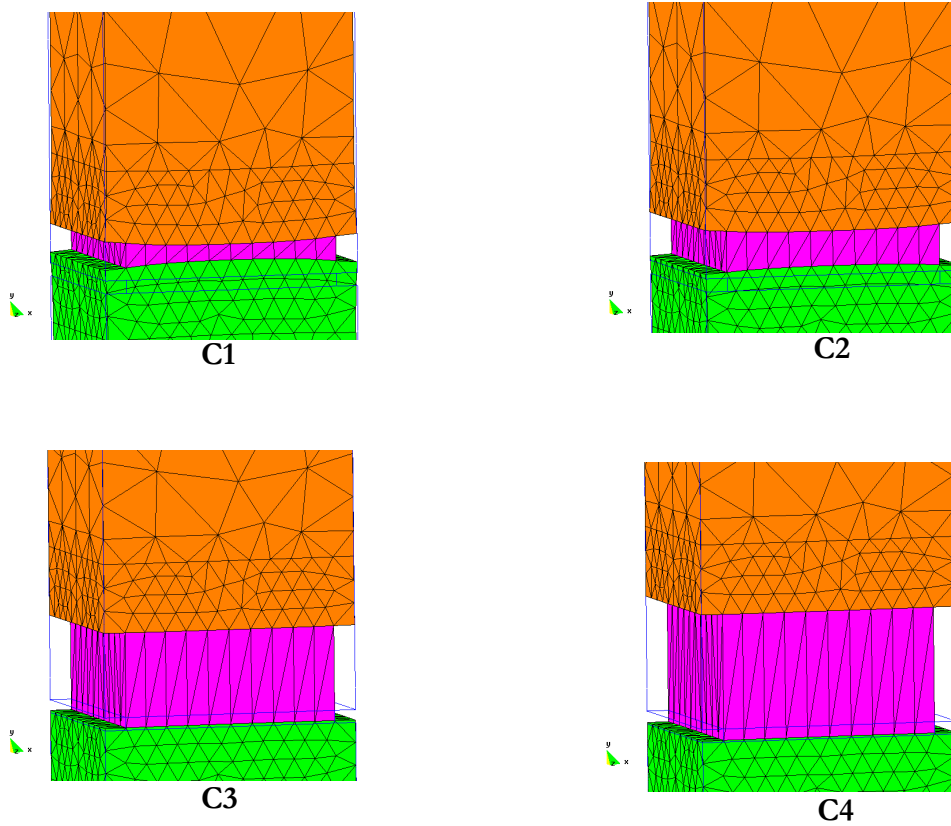
Figure 5.32: Deformation (scalar factor: 400) – Case C.

In Figure 5.33 we have the force *vs.* displacement curves for the three cases analyzed before.
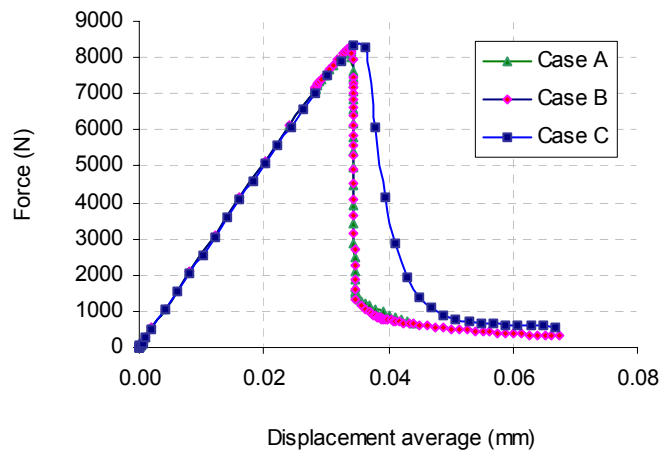
Figure 5.33: Force *vs.* displacement – Case C.

5.6 Four-point bending test

5.6.1 Single-notched shear beam

The specimen used is made of plain concrete. The testing apparatus is shown in Figure 5.34. Originally it was proposed by Arrea & Ingraffea(1982). Among the authors that have analyzed this test we can mention: Bhattacharjee&Léger (1994), Bocca *et al.* (1991), Rots *et al.*(1985), Wells(2001), Carpinteri (1993), who was trying to extend the cohesive crack model to a mixed mode propagation.

The constraints and the loading conditions are non-symmetric with respect to the notch. The experimental failure surface is shown in Figure 5.35.
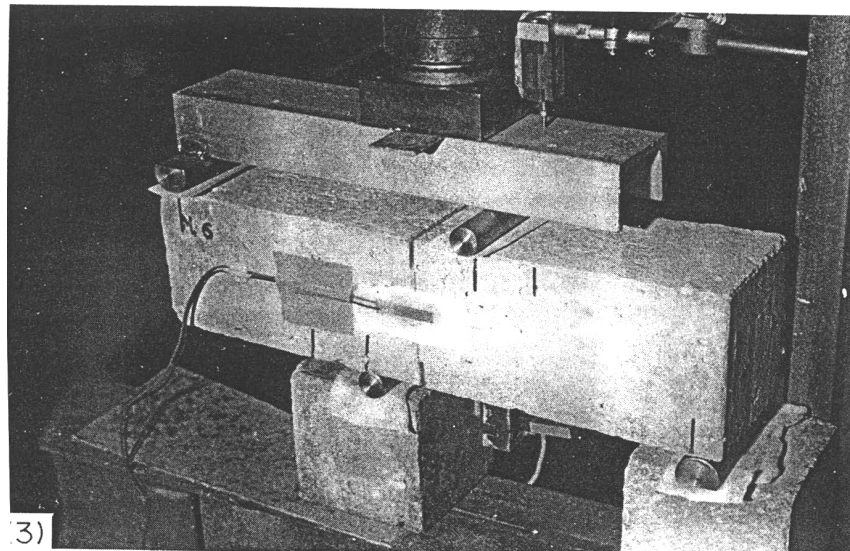
Figure 5.34: Testing apparatus, Bocca *et al.* (1990).
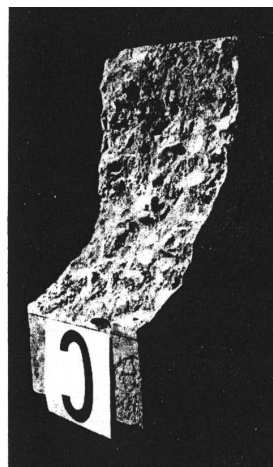
Figure 5.35: Crack pattern, Bocca *et al.* (1990).

The mesh and geometry is shown in Figure 5.36.
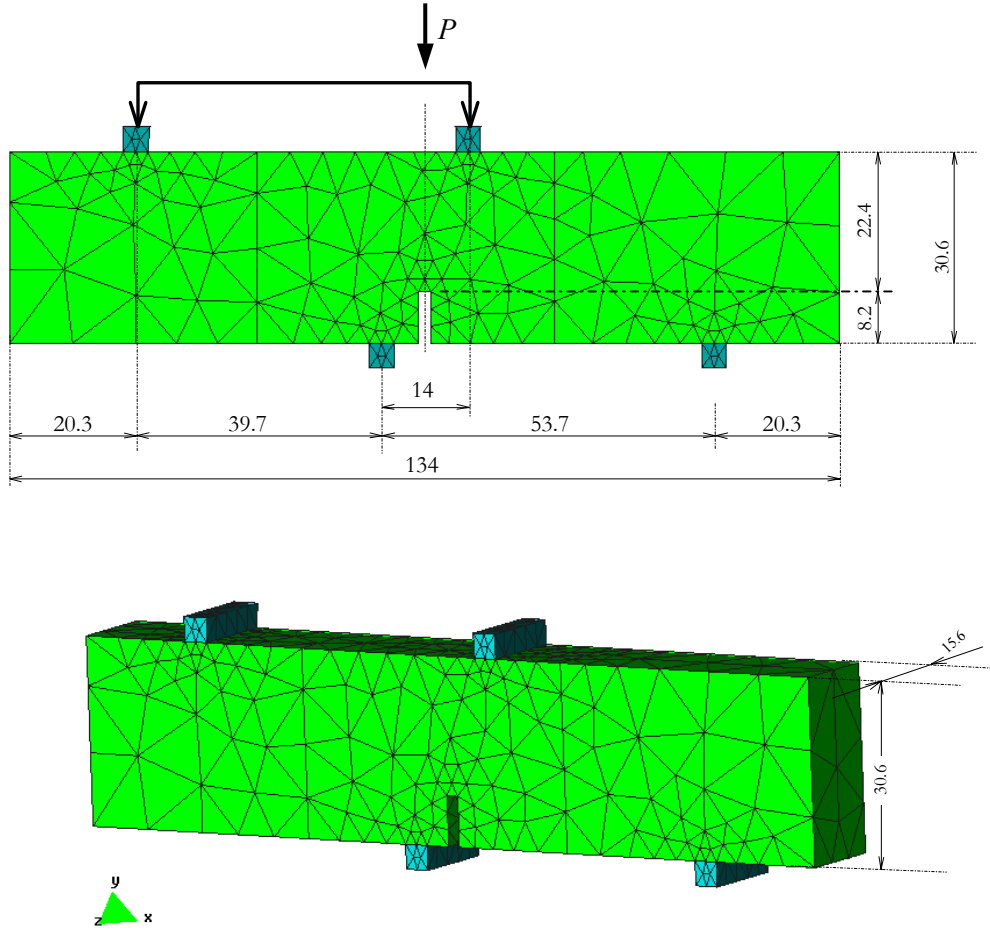
Figure 5.36: Single-notched shear beam – geometry (centimeter- cm) .

5.6.1.1 Case A

In this case the mesh is non-structured as shown in Figure 5.36. We have used $\overline{\eta} = 0.5 Ns / cm^3$ as damping-like parameter. Figure 5.37 shows the family of envelopes of the propagation directions. In Figure 5.38 we can see the part of the beam where the continuous failure surface is shown, as well as the localized finite elements and in Figure 5.39 we have detail of the mesh without fractured elements with discontinuity surface. In Figure 5.40 we can see the deformation of the beam. Figure 5.41 shows the force *vs.* displacement curve.
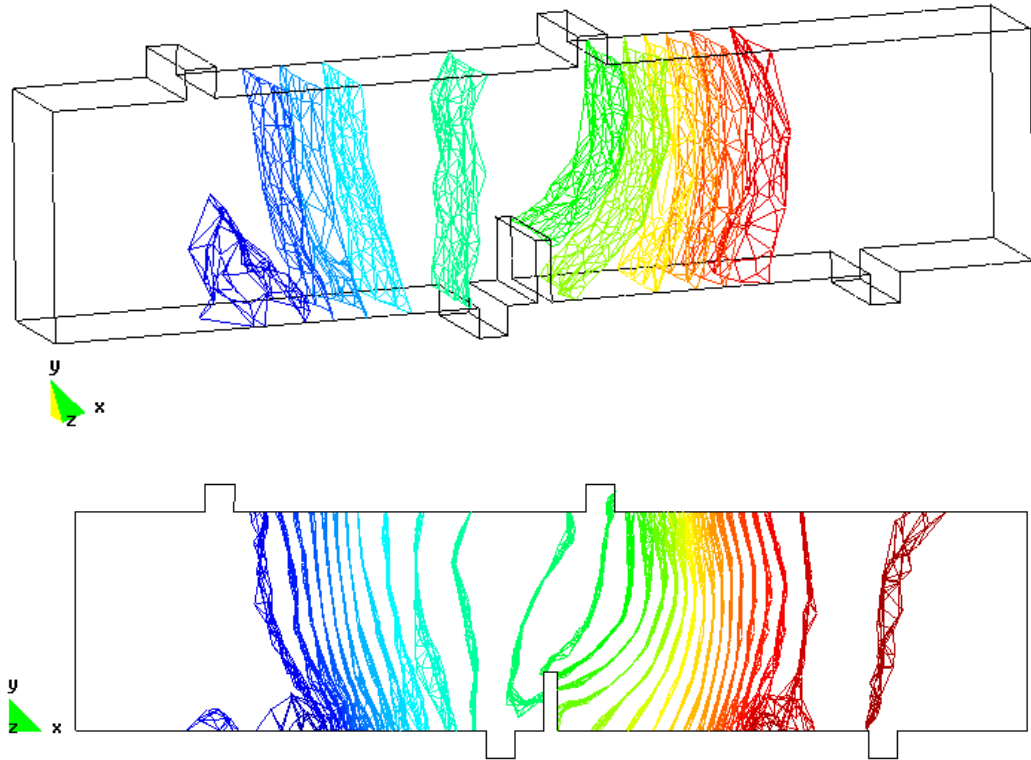
Figure 5.37: Family of envelopes of the critical direction.

a) fractured elements   a) continuous failure surface
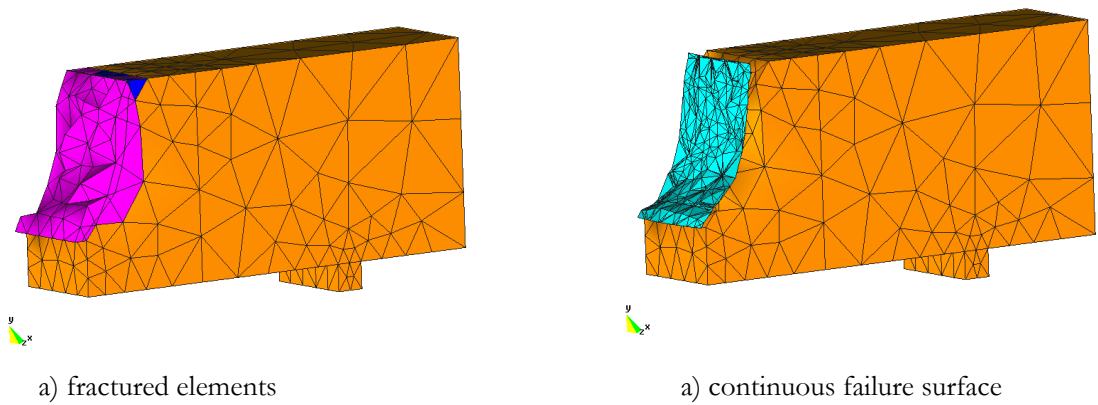
Figure 5.38: Geometry.
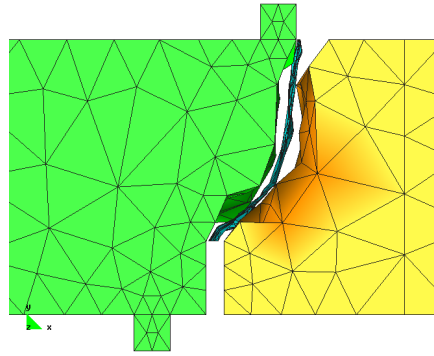
Figure 5.39: Mesh without fractured elements with discontinuity surface $\mathcal{S}$.
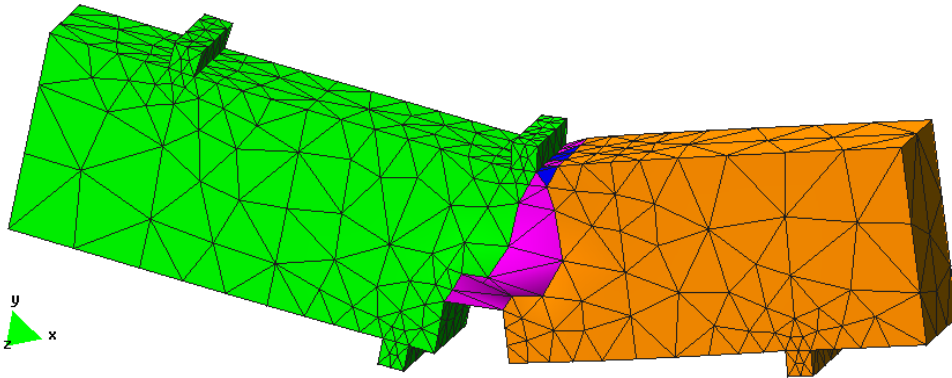
Figure 5.40: Deformation – Case A.
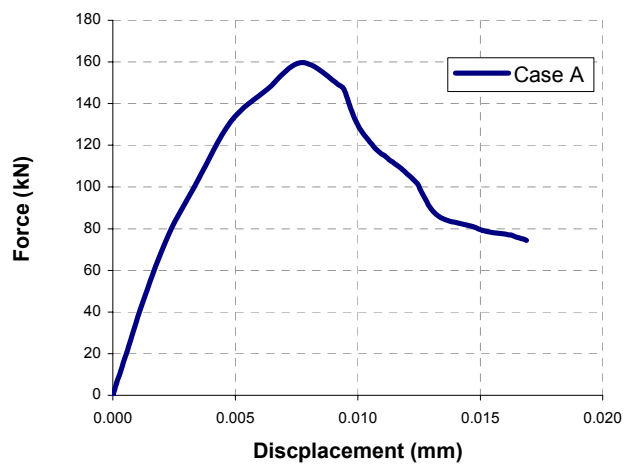
Figure 5.41: Force *vs.* displacement – Case A.

5.6.1.2 Case B

In this case, based on the a priori knowledge of the possible discontinuity surface obtained by the material bifurcation analysis plus an overall tracking algorithm, we have adopted a more structured mesh in the localization domain as show in Figure 5.42 and Figure 5.43.
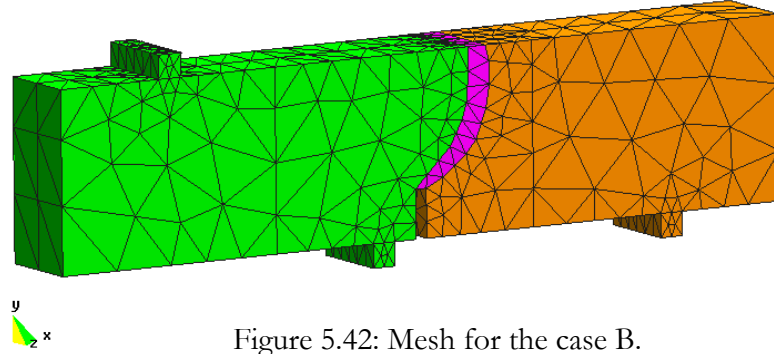
Figure 5.42: Mesh for the case B.
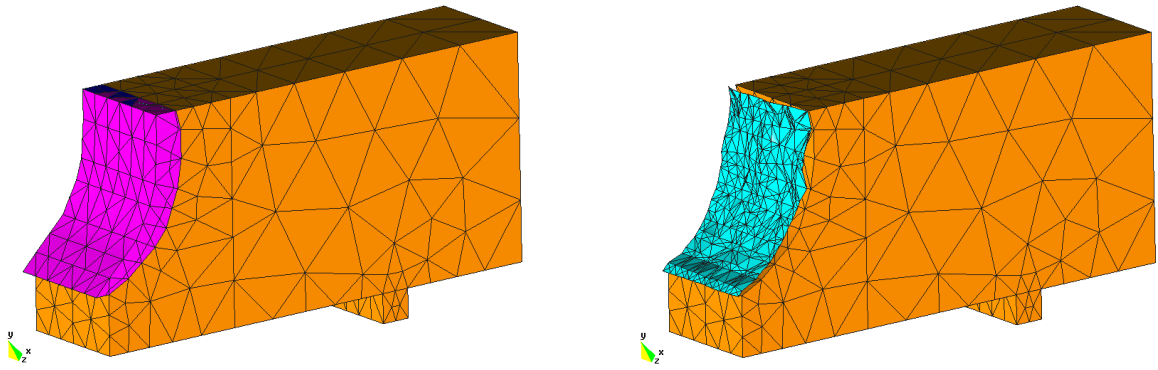
Figure 5.43: Tetrahedral finite element mesh.

This time we have used three different values for the damping-like parameter. For case B1 we have applied $\overline{\eta} = 0.5 Ns/cm^3$, for B2 we have used $\overline{\eta} = 0.2 Ns/cm^3$, and for B3 $\overline{\eta} = 0.01 Ns/cm^3$. The deformation can be visualized in Figure 5.44. We can see the force vs. displacement curves of the three cases in Figure 5.45.

Figure 5.46 plots the first case and one of the sub-cases analyzed above: case A and case B3. One must notice that some discrepancy exists due to the fact that in case A we should use a much finer discretization to obtain the same situation as in case B
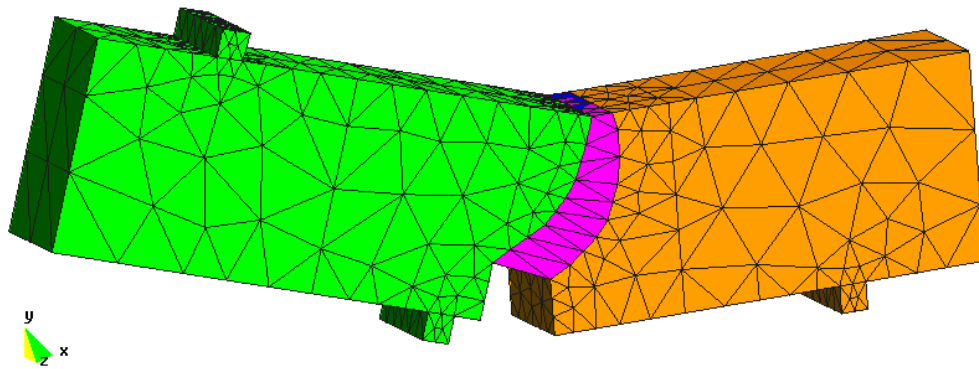
Figure 5.44: Deformation.
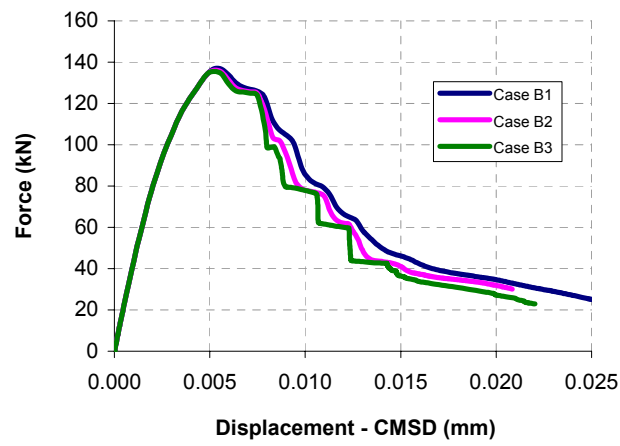
Figure 5.45: Deformation.
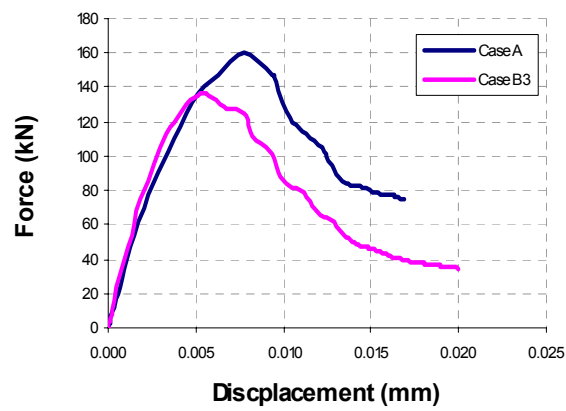
Figure 5.46: Force *vs.* displacement case A and Case B3.

Taking the case B3 as example, Figure 5.47 shows the evolution of the deformation and the evolution of the bifurcated elements (the blue color means bifurcated in failure elements). In Figure 5.48 the corresponding points in the force *vs.* displacement curve are shown.
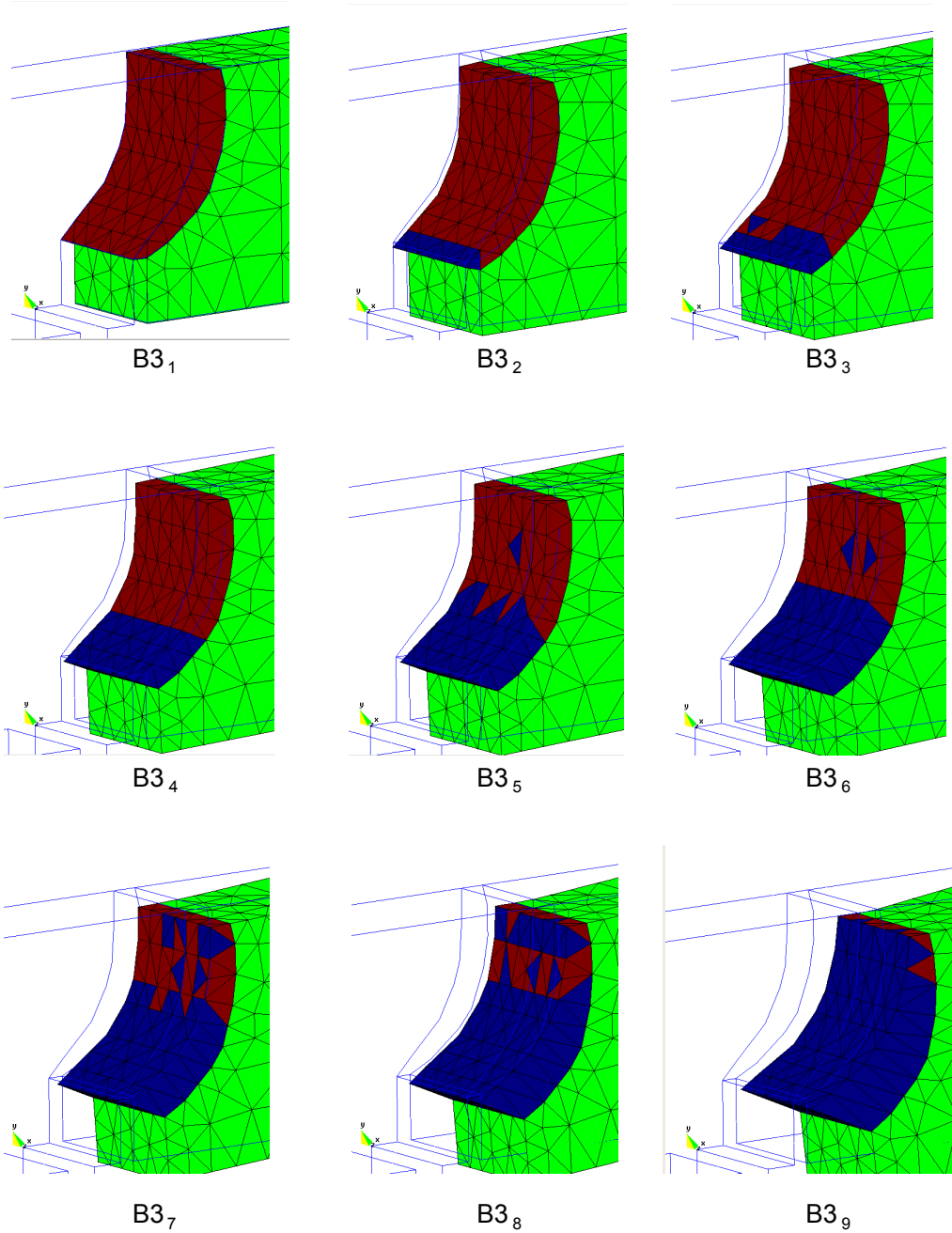

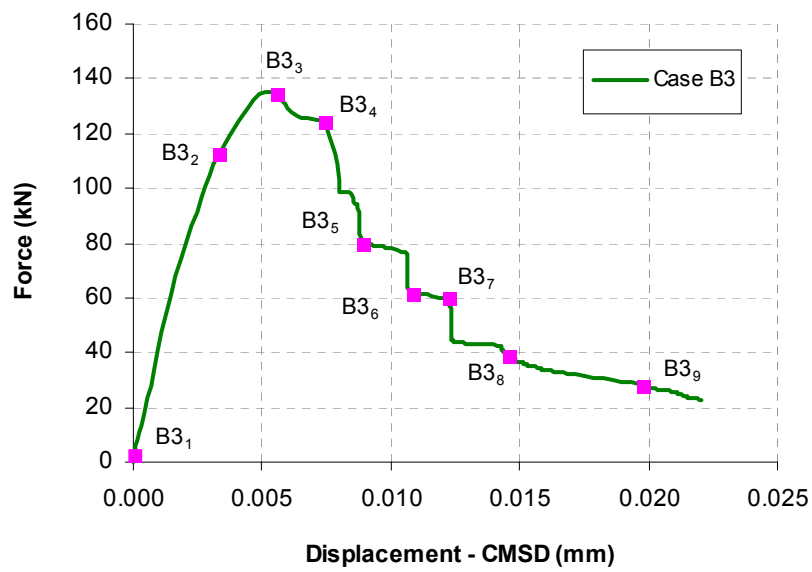Figure 5.47: Evolution of the bifurcated elements - Case B3.

Figure 5.48: Force *vs.* displacement - Case B3.

6

Conclusions and Recommendations for Further Work

6.1 Summary and conclusions of the research developed

In this work an analytical and a numerical model to simulate the phenomenon of strain localization have been developed in the ambit of Continuum Mechanics using the Strong Discontinuity Approach. This has been done in the context of an elastic-degradable medium (*viz.* Continuum Damage Model), assuming the isothermal quasi-static regime and small deformations and rotations. Furthermore, a material described as homogeneous and isotropic has been considered. We can add the following considerations:

- The behavior of the material is described throughout continuum constitutive equations in rates. Localization starts when strong ellipticity is lost, signaled by the singularity of the acoustic tensor (weak discontinuity). In this point, a variable bandwidth model begins. It is responsible for the transition from weak discontinuity to strong discontinuity.

- This theory is based on the Assumed Enhanced Strain Method (Simo&Rifai 1990) since an enriched term appears in the strain field.

- ■ A material bifurcation analysis was required to obtain the critical values, viz. the critical hardening/softening parameter and the critical angle. This information is needed for the constitutive model and for the tracking algorithms.

- ■ Two types of tracking algorithms were implemented: Element-element tracking and the Level curves/surface of the critical angle. The latter has shown to be very efficient. As mentioned above, the necessary parameters to trace the continuous discontinuity line/surface are obtained from a bifurcation analysis.

- ■ The strong discontinuity approach has proven to be very efficient to simulate brittle materials with discontinuities. This technique has the advantage of not needing the use of any remeshing technique (*viz.* it is mesh-independent) or of other artifices like introducing a material length scale to avoid stress locking.

- ■ A static condensation was implemented to reduce the number of degrees of freedom resulting in a smaller system of equilibrium equations.

6.2 Main contributions

Based on the above mentioned concepts, the main contributions made in the present work are:

- ✓ Extension of the two-dimensional Strong Discontinuity Approach to the general three-dimensional nonlinear problem using a Continuum Damage Model.

- ✓ An extensive study of material bifurcation analysis from which an explicit formula to obtain critical values is derived. By using this formula, critical values for several constitutive models are obtained too. The graphic representation of the acoustic tensor as well as of the representative critical values is presented for those models.

- ✓ Extension of the variable bandwidth model (VBM) with pre-established law to a new model named automatic VBM, for which we do not need to know the length of the transition from weak discontinuity regime to the strong discontinuity regime *a priori*.

- ✓ An extension of the 2D tracking based on a heat-conduction-like BVP developed in Samaniego (2003) to 3D settings. This technology is essential to obtain consistent numerical results in the 3D case.

6.3 Future research lines

Starting from the studies carried out in this work, we propose the following future developments aiming at the extension and deepening of some aspects that still remain open:

- Extension to finite deformation to attain a material response more realistic in cases where the infinitesimal theory is not appropriated.

- Application of the 3D formulation to reinforced concrete, because, although simplified analyses that use either beam elements or two-dimensional finite elements are quite useful, only three-dimensional analyses can fully represent all the aspects of the response of the concrete structure when a realistic constitutive model is used.

- Extension to other constitutive equations able to describe more complex material behavior and dependent of the velocity of load.

- Extension of the 3D model implemented in this work for managing several cracks simultaneously.

- Experimental and theoretical study of the instabilities appearing in certain examples.

- Introduce the study of structural bifurcation in the investigation of the material non-linearity.

A
Notation

A.1 Symbolic notation of tensors

Boldface characters are used to denote vectors and tensors. Thus, a vector expressed in a Cartesian coordinate system in the three-dimensional Euclidean space (see Figure A.1) is denoted by:

$$\mathbf{P} = P_i \hat{\mathbf{e}}_i \tag{A.1}$$

Further, the expression of a second order tensor is the following:

$$\mathbf{U} = U_{ij} \hat{\mathbf{e}}_i \otimes \hat{\mathbf{e}}_j \tag{A.2}$$

where $\otimes$ is the "open product" symbol and $i, j = 1,2,3$.

The divergence of vector $\mathbf{P}$ is denoted by $\nabla \cdot \mathbf{P}$ and reads:

$$\nabla \cdot \mathbf{P} = \frac{\partial P_i}{\partial x_i} = \frac{\partial P_1}{\partial x_1} + \frac{\partial P_2}{\partial x_2} + \frac{\partial P_3}{\partial x_3} \tag{A.3}$$

where i is a dummy index (Einstein convention is used).
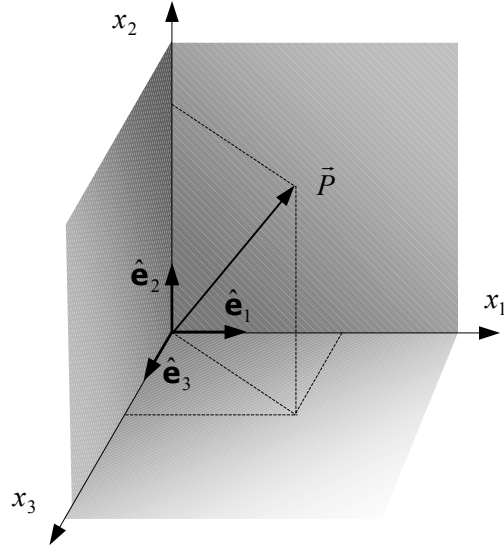
Figure A.1: Vector in Cartesian system.

A.2 Identity tensors

- 2nd order identity tensor

$$\mathbf{1} = \delta_{ij} \hat{\mathbf{e}}_i \otimes \hat{\mathbf{e}}_j \tag{A.4}$$

where δ_{ij} is the so-called Kronecker delta symbol, defined as:

$$\delta_{ij} = \begin{cases} 1 & if \quad i = j \\ \\ 0 & if \quad i \neq j \end{cases} \tag{A.5}$$

- 4th order identity tensor $\mathbb{I}$

$$\mathbb{I}_{ijk\ell} = \delta_{ik} \delta_{j\ell} \hat{\mathbf{e}}_i \otimes \hat{\mathbf{e}}_j \otimes \hat{\mathbf{e}}_k \otimes \hat{\mathbf{e}}_\ell \tag{A.6}$$

Its symmetric part is defined as

$$\mathbb{I} = \mathbb{I}^{sym} \tag{A.7}$$

The components of tensor $\mathbb{I}$ are

$$\mathbb{I}_{ijk\ell} = \frac{1}{2} \left(\delta_{ik} \delta_{j\ell} + \delta_{i\ell} \delta_{jk} \right) \tag{A.8}$$

The Kronecker Delta is often called a substitution operator for the following property:

$$\delta_{ij}V_i = V_j \tag{A.9}$$

Finally, noting that the dot product $\hat{\mathbf{e}}_i \cdot \hat{\mathbf{e}}_j$ is 1 if $i = j$ and 0 if $i \neq j$, then matching the components of δ_{ij}, we can write

$$\mathbf{e}_i \cdot \mathbf{e}_j = \delta_{ij} \tag{A.10}$$

A.3 Matrix notation

We will use the same notation for matrices as for tensors. However, for the former we will not use connective symbols to denote products, for example:

	Tensor Notation	Matrix Notation	
Dot product	$\mathbf{x} \cdot \mathbf{x}$	$\mathbf{x}^T \mathbf{x}$	(A.11)

All first order matrices will be denoted by lower case boldface letters such as $\mathbf{v}$, where:

$$\mathbf{v}^T = \{v_1, \quad v_2, \quad v_3\} \tag{A.12}$$

Usually rectangular matrices will be denoted by upper case boldface letters, such as $\mathbf{A}$ or $\mathbf{B}$, where :

$$\mathbf{A} = \begin{bmatrix} A_{11} & A_{12} \\ A_{21} & A_{22} \end{bmatrix} \qquad \mathbf{B} = \begin{bmatrix} B_{11} & B_{12} & B_{13} \\ B_{21} & B_{22} & B_{23} \end{bmatrix} \tag{A.13}$$

A.4 Coordinate transformation

The actual numerical values of the components of a tensor do depend on the coordinate system. If one changes the coordinate system, for example, rotates it, then the components of a tensor will change. Consider the coordinate system (x_1, x_2, x_3) represented by its versors $(\hat{\mathbf{e}}_1, \hat{\mathbf{e}}_2, \hat{\mathbf{e}}_3)$, see Figure A.2. In this system an arbitrary vector $\mathbf{v}$, can be represented by its components:

$$\mathbf{v} = v_1 \mathbf{e}_1 + v_2 \mathbf{e}_2 + v_3 \mathbf{e}_3 \tag{A.14}$$
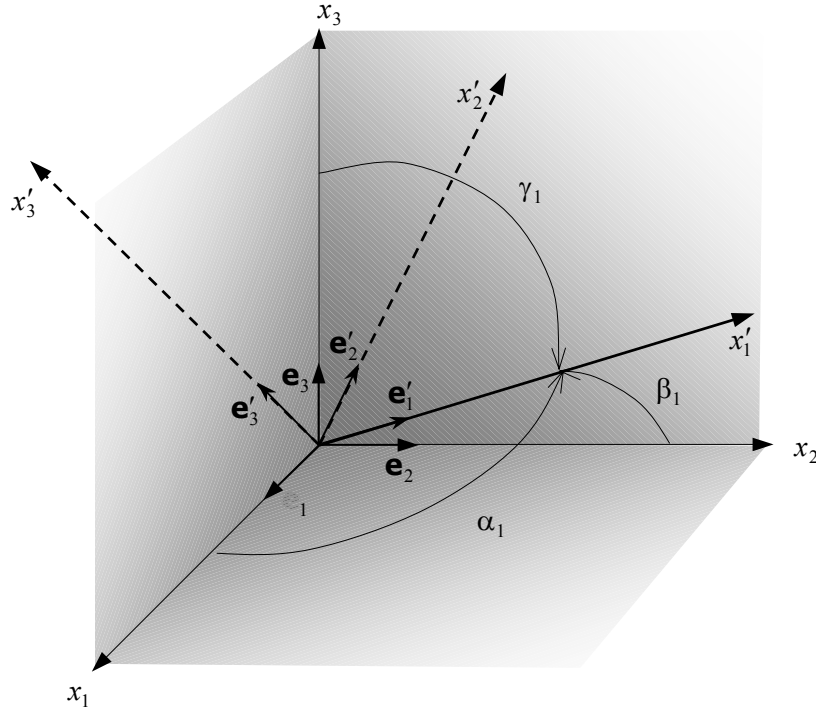
Figure A.2: Coordinate system.

It is common to express a vector by its components, *i.e.*, with the following format:

$$\mathbf{v} = \begin{Bmatrix} v_1 \\ v_2 \\ v_3 \end{Bmatrix} \tag{A.15}$$

Consider now a new orthogonal coordinate system (x_1', x_2', x_3'), represented by its versors $(\mathbf{e}_1', \mathbf{e}_2', \mathbf{e}_3')$ as shown in Figure A.2. The vectors and tensors represent physical properties that do not change with the coordinate system but its components change, thus the components of the vector $\mathbf{v}$ in this new system is given by:

$$\begin{Bmatrix} v_1' \\ v_2' \\ v_3' \end{Bmatrix} = \begin{bmatrix} \cos(x_1', x_1) & \cos(x_1', x_2) & \cos(x_1', x_3) \\ \cos(x_2', x_1) & \cos(x_2', x_2) & \cos(x_2', x_3) \\ \cos(x_3', x_1) & \cos(x_3', x_2) & \cos(x_3', x_3) \end{bmatrix} \begin{Bmatrix} v_1 \\ v_2 \\ v_3 \end{Bmatrix} \tag{A.16}$$

$$\mathbf{v}' = \mathcal{A} \cdot \mathbf{v}$$

where $\mathcal{A}$ is the coordinate transformation matrix, which is, in general, non symmetric $\mathcal{A} \neq \mathcal{A}^T$. It will be represented by its components as:

$$\mathcal{A} = \begin{bmatrix} a_{11} & a_{12} & a_{13} \\ a_{21} & a_{22} & a_{23} \\ a_{31} & a_{32} & a_{33} \end{bmatrix} \tag{A.17}$$

When we deal with an orthogonal system, we can say that: $\mathcal{A}^{-1} = \mathcal{A}^T \Rightarrow \mathcal{A}\mathcal{A}^T = \mathbf{1}$, and as a consequence:

$$\mathbf{v} = \mathcal{A}^T \cdot \mathbf{v}' \tag{A.18}$$

In a general form the coordinate transformation of the tensor components of first, second, third and fourth order are given, respectively, by:

$$\begin{aligned} S'_j &= a_{ij} S_j \\ S'_{ij} &= a_{ik} a_{jl} S_{kl} \\ S'_{ijk} &= a_{il} a_{jm} a_{kn} S_{lmn} \\ S'_{ijkl} &= a_{im} a_{jn} a_{kp} a_{lq} S_{mnpq} \end{aligned} \tag{A.19}$$

Consider now that we have a third coordinate system (x''_1, x''_2, x''_3) and that the coordinate system transformation from the system (x'_1, x'_2, x'_3) to the system (x''_1, x''_2, x''_3) is given by:

$$\mathbf{v}'' = \mathcal{B} \cdot \mathbf{v}' \tag{A.20}$$

Schematically the coordinate system transformation between this three systems is shown in Figure A.3.
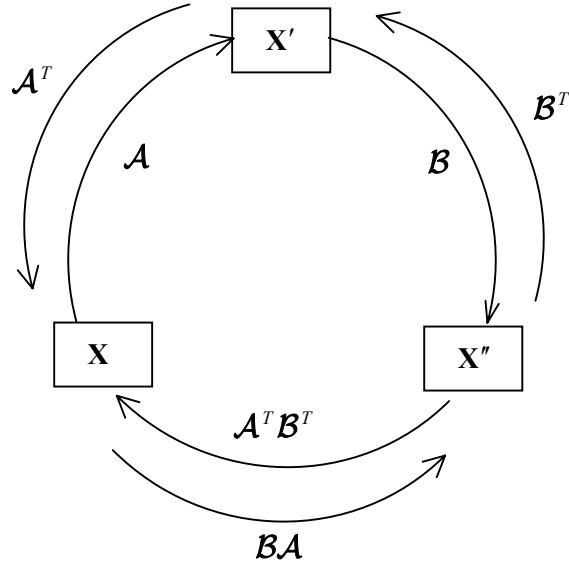
Figure A.3: Coordinate system transformation.

A.5 Elasticity

For many materials like metals, ceramics, concrete, etc., the hypotheses of isotropy and linearity are good enough for many engineering purposes. Then the classical Hooke's law of elasticity applies. A material in the elastic regime does not present dissipative mechanisms.

In the case of completely isotropic elastic responses, the constitutive tensor $\mathbb{C}^e$ depends on two parameters characteristic of each material: the Young's modulus E and the Poisson's ratio ν. $\mathbb{C}^e$ can be defined in terms of the Lamé's parameters, λ, μ, as:

$$\begin{cases} \mathbb{C}^e = 2\mu\mathbb{I} + \lambda(\mathbf{1}\otimes\mathbf{1}) \\ \mathbb{C}^e_{ijkl} = \mu(\delta_{ik}\delta_{jl} + \delta_{il}\delta_{jk}) + \lambda\delta_{ij}\delta_{kl} \qquad i,j,k,l \in \{1,2,3\} \end{cases} \tag{A.21}$$

The inverse reads:

$$\mathbb{C}^{e^{-1}} = \frac{1}{2\mu}\mathbb{I} - \frac{\lambda}{2\mu(3\lambda + 2\mu)}(\mathbf{1}\otimes\mathbf{1}) \tag{A.22}$$

or

$$\mathbb{C}^e = \kappa\mathbf{1}\otimes\mathbf{1} + 2\mu\left[\mathbb{I} - \frac{1}{3}\mathbf{1}\otimes\mathbf{1}\right] \tag{A.23}$$

where the Kronecker's delta and the unity tensor of fourth order are, respectively, given by equations (A.4) and (A.8).

Relations between the Lamé's parameters (λ, μ), the Young's modulus E, the Poisson's ratio ν are given as:

$$\lambda = \frac{\nu E}{(1+\nu)(1-2\nu)} \quad ; \quad \mu = \frac{E}{2(1+\nu)} \tag{A.24}$$

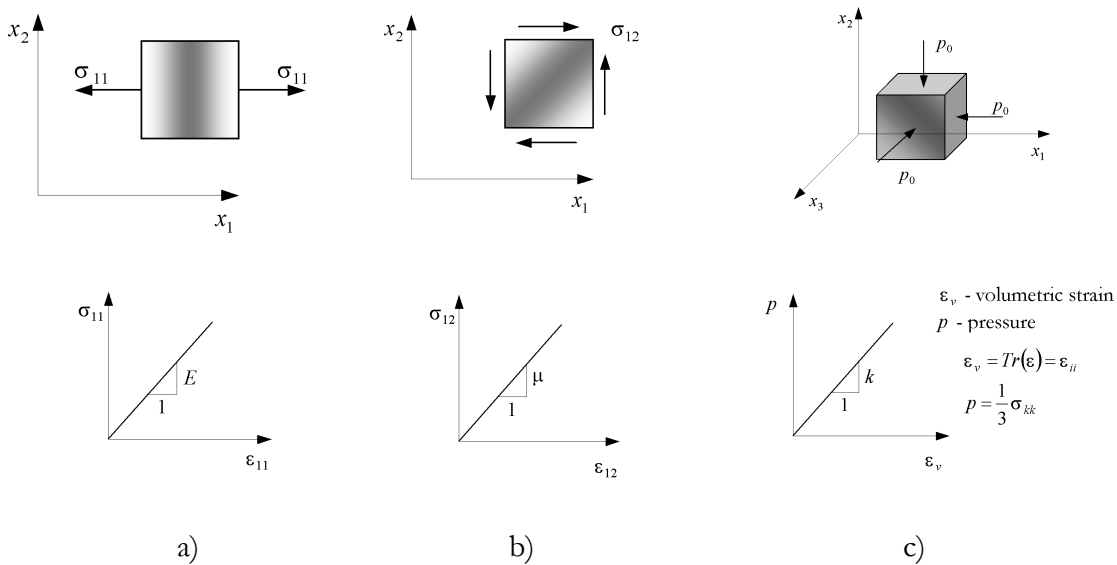and their physical interpretation is illustrated in Figure A.4.

Figure A.4: Simple test: a) Tension; b) Shear; c) Hydrostatic compression.

In the case of linear elasticity, with no initial stresses or strains, these relations are described as

$$\boldsymbol{\sigma} = \mathbb{C}^e : \boldsymbol{\varepsilon} \tag{A.25}$$

where $\mathbb{C}^e$ is the elasticity tensor characterizing the material's properties.

A.5.1 Elastic acoustic tensor

Another important tensor in elasticity is the elastic acoustic tensor $\mathbf{Q}^e(\mathbf{N})$ defined as:

$$\mathbf{Q}^e(\mathbf{N}) = \mathbf{N} \cdot \mathbb{C}^e \cdot \mathbf{N} \Rightarrow \begin{cases} Q^e_{jl}(\mathbf{N}) = N_i \mathbb{C}^e_{ijkl} N_k = (\lambda + \mu) N_j N_l + \mu \delta_{jl} \\ \mathbf{Q}^e(\mathbf{N}) = \mu \mathbf{1} + (\lambda + \mu) \mathbf{N} \otimes \mathbf{N} \end{cases} \tag{A.26}$$

And the inverse:

$$\begin{cases} Q^{e\,-1}_{jl} = \dfrac{1}{\mu} \left[\delta_{jl} - \dfrac{(\lambda + \mu)}{(\lambda + 2\mu)} N_j N_l \right] \\ \\ \mathbf{Q}^{e-1} = \dfrac{1}{\mu} \left[\mathbf{1} - \dfrac{(\lambda + \mu)}{(\lambda + 2\mu)} \mathbf{N} \otimes \mathbf{N} \right] \end{cases} \tag{A.27}$$

or in terms of E, ν

$$\mathbf{Q}^{e-1} = \frac{2(1 + \nu)}{E} \left[\mathbf{1} - \frac{1}{2(1 - \nu)} \mathbf{N} \otimes \mathbf{N} \right] \tag{A.28}$$

The determinant of the acoustic tensor $\mathbf{Q}^e$ in three dimensions is:

$$\left| \mathbf{Q}^e \right| = \mu^2 (\lambda + 2\mu) \tag{A.29}$$

and in two dimensions(2D):

$$\left| \mathbf{Q}^e \right| = \mu(\lambda + 2\mu) \tag{A.30}$$

To obtain the eigenvalues of $\mathbf{Q}^e$, it is necessary to compute the determinant:

$$\begin{vmatrix} [(\lambda + \mu) N_1 N_1 + \mu] - \varsigma & (\lambda + \mu) N_1 N_2 & (\lambda + \mu) N_1 N_3 \\ (\lambda + \mu) N_1 N_2 & [(\lambda + \mu) N_2 N_2 + \mu] - \varsigma & (\lambda + \mu) N_2 N_3 \\ (\lambda + \mu) N_1 N_3 & (\lambda + \mu) N_2 N_3 & [(\lambda + \mu) N_3 N_3 + \mu] - \varsigma \end{vmatrix} = 0 \tag{A.31}$$

This gives the characteristic equation – a third grade polynomial in ς.

Using the property $N_1^2 + N_2^2 + N_3^2 = 1$, one can obtain the following eigenvalues:

$$\begin{bmatrix} \mu \\ \mu \\ (\lambda + 2\mu) \end{bmatrix} \qquad (A.32)$$

The presence of negative or null roots represent an instability for small perturbations. The necessary and sufficient conditions for the *strong ellipticity condition* to hold is:

$$\boxed{\mu > 0 \quad , \quad \lambda + 2\mu > 0} \qquad (A.33)$$

If the condition of strong ellipticity is violated, the material will exhibit an instability associated with the formation of a non homogeneous deformation band.

The inequality (A.33) can be expressed in the following way:

$$\mu = \frac{E}{2(1+\nu)} > 0 \Rightarrow \begin{cases} \begin{cases} E > 0 \\ \nu > -1 \end{cases} \\ \begin{cases} E < 0 \\ \nu < -1 \end{cases} \end{cases} \qquad (A.34)$$

and

$$\lambda + 2\mu = 2\mu \frac{(1-\nu)}{(1-2\nu)} > 0 \Rightarrow \begin{cases} \nu < 0.5 \\ \nu > 1 \end{cases} \qquad (A.35)$$

We can summarize that, in order to satisfy the strong ellipticity conditions, it is necessary to satisfy one of the following propositions:

$$E > 0 \Rightarrow \nu \subset \left]-1 ; 0.5\right[\cup \left]1 ; \infty\right[$$
$$E < 0 \Rightarrow \nu \subset \left]-\infty ; -1\right[\qquad (A.36)$$

For physical reasons the bulk modulus (κ) (Truesdell&Noll – 1965) has to be positive. The point to point stability condition will be guaranteed by:

$$\begin{cases} \mu > 0 \\ \kappa = \lambda + \tfrac{2}{3}\mu = \dfrac{E}{3(1-2\nu)} > 0 \end{cases} \qquad (A.37)$$

For an isotropic lineal elastic material the condition for the strain energy to be positive definite is satisfied when:

$$E > 0 \quad ; \quad -1 < \nu < 0.5 \qquad (A.38)$$

Remark A.1:

- $\mathbb{C}^e$ is pointwise stable if and only if:

$$\mu > 0 \quad and \quad \frac{3\lambda + 2\mu}{3} > 0$$

- $\mathbb{C}^e$ is strongly elliptic if and only if:

$$\mu > 0 \quad , \quad \lambda + 2\mu > 0 \quad \square$$

A.5.2 Two-dimensional case

When structural calculations are performed under the approximation of plane stress or plane strain, it is convenient to write these conditions in the constitutive equation:

- Plane stress $\left(\sigma_{33} = \sigma_{13} = \sigma_{23} = 0\right)$:

- Plane strain $\left(\varepsilon_{33} = \varepsilon_{13} = \varepsilon_{23} = 0\right)$:

We can redefine some important tensors as:

- The elastic constitutive tensor:

$$\mathbb{C}^e = 2\mu\mathbb{I} + \overline{\lambda}\left(\mathbf{1} \otimes \mathbf{1}\right) \tag{A.39}$$

- The Elastic Acoustic Tensor:

$$\mathbf{Q}^e(\mathbf{N}) = \mu\mathbf{1} + (\overline{\lambda} + \mu)\,\mathbf{N} \otimes \mathbf{N} \tag{A.40}$$

where

$$\overline{\lambda} = \begin{cases} \bullet\ \lambda & \rightarrow \text{Plane Strain} \\[2mm] \bullet\ \dfrac{2\lambda\mu}{(\lambda + 2\mu)} & \rightarrow \text{Plane Stress} \end{cases} \tag{A.41}$$

A.6 Voigt-matrix representation

For implementation in a Finite element code, we usually use the Voigt notation. Voigt notation usually refers to the procedure of writing a symmetric tensor in column matrix form(vector).

Using the Voigt matrix representation for the stress tensor $\boldsymbol{\sigma}$ and the strain tensor $\boldsymbol{\varepsilon}$ the stress vector $\{\boldsymbol{\sigma}\}$ and strain vector $\{\boldsymbol{\varepsilon}\}$ obtained can be written as:

$$\sigma_{ij} = \begin{bmatrix} \sigma_{11} & \sigma_{12} & \sigma_{13} \\ \sigma_{12} & \sigma_{22} & \sigma_{23} \\ \sigma_{13} & \sigma_{23} & \sigma_{33} \end{bmatrix} \xrightarrow{Voigt} \{\boldsymbol{\sigma}\} = \begin{Bmatrix} \sigma_{11} \\ \sigma_{22} \\ \sigma_{33} \\ \sigma_{12} \\ \sigma_{13} \\ \sigma_{23} \end{Bmatrix} = \begin{Bmatrix} \sigma_x \\ \sigma_y \\ \tau_{xy} \\ \sigma_z \\ \tau_{xz} \\ \tau_{yz} \end{Bmatrix} \tag{A.42}$$

$$\varepsilon_{ij} = \begin{bmatrix} \varepsilon_{11} & \varepsilon_{12} & \varepsilon_{13} \\ \varepsilon_{12} & \varepsilon_{22} & \varepsilon_{23} \\ \varepsilon_{13} & \varepsilon_{23} & \varepsilon_{33} \end{bmatrix} \xrightarrow{Voigt} \{\varepsilon\} = \begin{Bmatrix} \varepsilon_{11} \\ \varepsilon_{22} \\ \varepsilon_{33} \\ 2\varepsilon_{12} \\ 2\varepsilon_{13} \\ 2\varepsilon_{23} \end{Bmatrix} = \begin{Bmatrix} \varepsilon_x \\ \varepsilon_y \\ \varepsilon_z \\ \gamma_{xy} \\ \gamma_{xz} \\ \gamma_{yz} \end{Bmatrix} \tag{A.43}$$

It is easy to verify that an increment in energy is given by:

$$d\boldsymbol{\varepsilon} : \boldsymbol{\sigma} \equiv \{d\boldsymbol{\varepsilon}\}^T \{\boldsymbol{\sigma}\} \tag{A.44}$$

The stiffness tensor $\mathbb{C}^e_{ijkl}$ has 81 elements which, because of the symmetries in the stiffness tensor and thermodynamic considerations, reduce to 21 independent elastic parameters. The stiffness tensor then is written as a second-order symmetric Voigt matrix:

$$\mathbb{C}^e_{ijkl} \xrightarrow{Voigt\ matrix} \boldsymbol{\mathcal{C}}^e_{mn} \equiv \boldsymbol{\mathcal{C}}^e \tag{A.45}$$

These 21 independent parameters can be further reduced. In the case of isotropy, for example, there are only two independent elastic parameters.

Thus we can represent the generalized Hook's law as:

$$\boldsymbol{\sigma} = \mathbb{C}^e : \boldsymbol{\varepsilon} \xrightarrow{Voigt\ matrix} \{\boldsymbol{\sigma}\} = \boldsymbol{\mathcal{C}}^e \{\boldsymbol{\varepsilon}\} \tag{A.46}$$

The traction vector in the Voigt notation is defined as follows:

$$\boldsymbol{\mathcal{T}} = \mathbf{N} \cdot \boldsymbol{\sigma} \xrightarrow{Voigt} \boldsymbol{\mathcal{T}} = \boldsymbol{\mathcal{N}}^T \{\boldsymbol{\sigma}\}$$

$$\begin{Bmatrix} \mathcal{T}_1^{(\hat{\mathbf{N}})} \\ \mathcal{T}_2^{(\hat{\mathbf{N}})} \\ \mathcal{T}_3^{(\hat{\mathbf{N}})} \end{Bmatrix} = \begin{bmatrix} N_1 & 0 & 0 & N_2 & N_3 & 0 \\ 0 & N_2 & 0 & N_1 & 0 & N_3 \\ 0 & 0 & N_3 & 0 & N_1 & N_2 \end{bmatrix} \begin{Bmatrix} \sigma_{11} \\ \sigma_{22} \\ \sigma_{33} \\ \sigma_{12} \\ \sigma_{13} \\ \sigma_{23} \end{Bmatrix} \tag{A.47}$$

where

$$\boldsymbol{\mathcal{N}} = \begin{bmatrix} N_1 & 0 & 0 \\ 0 & N_2 & 0 \\ 0 & 0 & N_3 \\ N_2 & N_1 & 0 \\ N_3 & 0 & N_1 \\ 0 & N_3 & N_2 \end{bmatrix} \tag{A.48}$$

Unit tensor of second order

$$\delta_{ij} \xrightarrow{\text{Voigt}} \delta_i = \{\delta\} = \begin{Bmatrix} 1 \\ 1 \\ 1 \\ 0 \\ 0 \\ 0 \end{Bmatrix} \tag{A.49}$$

Unit tensor of fourth order

$$\mathbb{I}_{ijkl} \xrightarrow{\text{Voigt}} \boldsymbol{\mathcal{I}} = \begin{bmatrix} 1 & 0 & 0 & 0 & 0 & 0 \\ 0 & 1 & 0 & 0 & 0 & 0 \\ 0 & 0 & 1 & 0 & 0 & 0 \\ 0 & 0 & 0 & \frac{1}{2} & 0 & 0 \\ 0 & 0 & 0 & 0 & \frac{1}{2} & 0 \\ 0 & 0 & 0 & 0 & 0 & \frac{1}{2} \end{bmatrix} \tag{A.50}$$

Thus we can rewritten equation (A.21) as:

$$\begin{cases} \boldsymbol{\mathcal{C}}^e = 2\mu\boldsymbol{\mathcal{I}} + \lambda\left(\overline{\mathbf{1}} \otimes \overline{\mathbf{1}}\right) \\ \boldsymbol{\mathcal{C}}^e_{ij} = 2\mu\boldsymbol{\mathcal{I}}_{ij} + \lambda\left(\delta_i \otimes \delta_j\right) \qquad i,j \in \{1,2,3,4,5,6\} \end{cases} \tag{A.51}$$

or explicitly in terms of E and ν :

$$\boldsymbol{\mathcal{C}}^e_{ij} = \frac{E(1-\nu)}{(1+\nu)(1-2\nu)} \begin{bmatrix} 1 & \dfrac{\nu}{(1-\nu)} & \dfrac{\nu}{(1-\nu)} & 0 & 0 & 0 \\ \dfrac{\nu}{(1-\nu)} & 1 & \dfrac{\nu}{(1-\nu)} & 0 & 0 & 0 \\ \dfrac{\nu}{(1-\nu)} & \dfrac{\nu}{(1-\nu)} & 1 & 0 & 0 & 0 \\ 0 & 0 & 0 & \dfrac{1-2\nu}{2(1-\nu)} & 0 & 0 \\ 0 & 0 & 0 & 0 & \dfrac{1-2\nu}{2(1-\nu)} & 0 \\ 0 & 0 & 0 & 0 & 0 & \dfrac{1-2\nu}{2(1-\nu)} \end{bmatrix} \tag{A.52}$$

A.6.1 Transformation of the stress, strain and constitutive tensors components

A.6.1.1 Stress and strain tensor

The stress and strain tensors components change of base according to the following transformation:

$$\{\boldsymbol{\sigma}\}' = \mathcal{A} \, \{\boldsymbol{\sigma}\} \, \mathcal{A}^T$$
$$\{\boldsymbol{\varepsilon}\}' = \mathcal{A} \, \{\boldsymbol{\varepsilon}\} \, \mathcal{A}^T \tag{A.53}$$

where $\mathcal{A}$ is the coordinate transformation matrix, which is, in general, non symmetric $\mathcal{A} \neq \mathcal{A}^T$. It will be represented by its components as:

$$\mathcal{A} = \begin{bmatrix} a_{11} & a_{12} & a_{13} \\ a_{21} & a_{22} & a_{23} \\ a_{31} & a_{32} & a_{33} \end{bmatrix} \tag{A.54}$$

Thus, the transformation of the components of the stress and strain tensor are, respectively:

$$\boxed{\begin{aligned} \{\boldsymbol{\sigma}\}'_{6\times 1} &= \mathcal{M}_{6\times 6} \, \{\boldsymbol{\sigma}\}_{6\times 1} \\ \{\boldsymbol{\varepsilon}\}'_{6\times 1} &= \mathcal{N}_{6\times 6} \, \{\boldsymbol{\varepsilon}\}_{6\times 1} \end{aligned}} \tag{A.55}$$

where

$$\mathcal{M} = \begin{bmatrix} a_{11}^2 & a_{12}^2 & a_{13}^2 & 2a_{11}a_{12} & 2a_{12}a_{13} & 2a_{11}a_{13} \\ a_{21}^2 & a_{22}^2 & a_{23}^2 & 2a_{21}a_{22} & 2a_{22}a_{23} & 2a_{21}a_{23} \\ a_{31}^2 & a_{32}^2 & a_{33}^2 & 2a_{31}a_{32} & 2a_{32}a_{33} & 2a_{31}a_{33} \\ a_{21}a_{11} & a_{22}a_{12} & a_{13}a_{23} & (a_{11}a_{22}+a_{12}a_{21}) & (a_{13}a_{22}+a_{12}a_{23}) & (a_{13}a_{21}+a_{11}a_{23}) \\ a_{31}a_{21} & a_{32}a_{22} & a_{33}a_{23} & (a_{31}a_{22}+a_{32}a_{21}) & (a_{33}a_{23}+a_{32}a_{23}) & (a_{33}a_{21}+a_{31}a_{23}) \\ a_{31}a_{11} & a_{32}a_{12} & a_{33}a_{13} & (a_{31}a_{12}+a_{32}a_{11}) & (a_{33}a_{12}+a_{32}a_{13}) & (a_{33}a_{11}+a_{31}a_{13}) \end{bmatrix} \tag{A.56}$$

and

$$\mathcal{N} = \begin{bmatrix} a_{11}^2 & a_{12}^2 & a_{13}^2 & a_{11}a_{12} & a_{12}a_{13} & a_{11}a_{13} \\ a_{21}^2 & a_{22}^2 & a_{23}^2 & a_{21}a_{22} & a_{22}a_{23} & a_{21}a_{23} \\ a_{31}^2 & a_{32}^2 & a_{33}^2 & a_{31}a_{32} & a_{32}a_{33} & a_{31}a_{33} \\ 2a_{21}a_{11} & 2a_{22}a_{12} & 2a_{13}a_{23} & (a_{11}a_{22}+a_{12}a_{21}) & (a_{13}a_{22}+a_{12}a_{23}) & (a_{13}a_{21}+a_{11}a_{23}) \\ 2a_{31}a_{21} & 2a_{32}a_{22} & 2a_{33}a_{23} & (a_{31}a_{22}+a_{32}a_{21}) & (a_{33}a_{23}+a_{32}a_{23}) & (a_{33}a_{21}+a_{31}a_{23}) \\ 2a_{31}a_{11} & 2a_{32}a_{12} & 2a_{33}a_{13} & (a_{31}a_{12}+a_{32}a_{11}) & (a_{33}a_{12}+a_{32}a_{13}) & (a_{33}a_{11}+a_{31}a_{13}) \end{bmatrix} \tag{A.57}$$

A.6.1.2 Constitutive tensor

In the case that $\mathbb{C}$ is not isotropic, the transformation law of a fourth order tensor is:

$$\mathbb{C}'_{ijkl} = a_{im} a_{jn} a_{kp} a_{lq} \mathbb{C}_{mnpq} \tag{A.58}$$

When $\boldsymbol{\sigma}$ and $\boldsymbol{\varepsilon}$ are expressed in Voigt notation, $\mathbb{C}$ is a second order tensor, thus:

$$\sigma_i = \mathcal{C}_{ij} \varepsilon_j$$
$$\{\boldsymbol{\sigma}\} = \mathcal{C} \, \{\boldsymbol{\varepsilon}\} \tag{A.59}$$

Using the equations (A.55) and (A.59), we can say that:

$$\{\boldsymbol{\sigma}\}' = \mathcal{M}\{\boldsymbol{\sigma}\} = \mathcal{M}\mathcal{C}\mathcal{N}^{-1}\{\boldsymbol{\varepsilon}\}'$$
$$\{\boldsymbol{\sigma}\}' = \mathcal{C}'\{\boldsymbol{\varepsilon}\}'$$

(A.60)

where: $\mathcal{C}' = \mathcal{M}\mathcal{C}\mathcal{N}^{-1}$.

It can be demonstrated that $\mathcal{M}^T = \mathcal{N}^{-1}$. Resulting that the coordinate transformation of the constitutive tensor components is given by:

$$\boxed{\mathcal{C}'_{6\times6} = \mathcal{M}_{6\times6}\mathcal{C}_{6\times6}\mathcal{M}^T_{6\times6}}$$

(A.61)

A.7 Stress deviator tensor and its invariants

Sometimes, it is convenient in material modeling to decompose the stress tensor into two parts, one called spherical or hydrostatic stress tensor and other called the stress deviatoric tensor. The hydrostatic stress tensor is that whose elements are $p\delta_{ij}$, where p is the mean stress and is given by

$$p = \frac{1}{3}\sigma_{kk} = \frac{1}{3}(\sigma_{11} + \sigma_{22} + \sigma_{33}) = \frac{1}{3}I_1$$

(A.62)

where $I_1 = \sigma_{kk}$ is the *first invariant of the stress tensor*; that is, its value would be the same regardless of rotation of the coordinate axes. Other important invariants are:

$$I_2 = (\sigma_{11}\sigma_{22} + \sigma_{22}\sigma_{33} + \sigma_{33}\sigma_{11}) - \varepsilon_{12}^2 - \varepsilon_{23}^2 - \varepsilon_{13}^2$$

(A.63)

$$I_3 = \sigma_{11}\sigma_{22}\sigma_{33}$$

From equation (A.62), it is apparent that p is the same for all possible orientations of the axes. The stress deviator tensor s_{ij} is derived by subtracting the spherical state of stress from the actual state of stress. Thus, we have

$$\sigma_{ij} = \mathsf{s}_{ij} + p\delta_{ij} \quad \Rightarrow \quad \mathsf{s}_{ij} = \sigma_{ij} - p\delta_{ij}$$

(A.64)

The components of this tensor are given by:

$$\mathsf{s}_{ij} = \begin{bmatrix} \mathsf{s}_{11} & \mathsf{s}_{12} & \mathsf{s}_{13} \\ \mathsf{s}_{21} & \mathsf{s}_{22} & \mathsf{s}_{23} \\ \mathsf{s}_{31} & \mathsf{s}_{32} & \mathsf{s}_{33} \end{bmatrix} = \begin{bmatrix} (\sigma_{11} - p) & \sigma_{12} & \sigma_{13} \\ \sigma_{21} & (\sigma_{22} - p) & \sigma_{23} \\ \sigma_{31} & \sigma_{32} & (\sigma_{33} - p) \end{bmatrix}$$

(A.65)

The invariants of the stress deviator tensor s_{ij}, are:

$$J_1 = \mathsf{s}_{ij} = 0$$

$$J_2 = \frac{1}{2}\mathsf{s}_{ij}\,\mathsf{s}_{ji} \tag{A.66}$$

$$J_3 = \frac{1}{3}\mathsf{s}_{ij}\,\mathsf{s}_{jk}\,\mathsf{s}_{ki} = \mathsf{s}_{11}\,\mathsf{s}_{22}\,\mathsf{s}_{33}$$

Bibliography

AIFANTIS, E.C. (1984). On the microstructural origin of certain inelastic models. *J. Eng. Mater. Tech.*, vol. 106, pp.326-330.

ARMERO, F. & CALLARI, C.(1999). An analysis of strong discontinuities in saturated poroplasticity solid. *Int. J. Numer. Anal. Meth. Geomech.,* 46, pp. 1673-1698.

ARMERO, F. & GARIKIPATI, K. (1995). Recent advances in the analysis and numerical simulation of strain localization in inelastic solids. In D. Owen, E. Oñate and H.E., (Eds.), *Proc. International Conference on Computational Plasticity V*, pp. 547-561, Barcelona, CIMNE.

ARMERO, F. & GARIKIPATI, K. (1996). An analysis of strong discontinuities in multiplicative finite strain plasticity and their relation with the numerical simulation of strain localization in solids. *Int. J. Solids Struct.,* 33 (20-22), 2863-2885.

ARMERO, F. (1997). Localized anisotropic damage of brittle materials. In. D. Owen, E. Oñate, and H.E., (Eds.), *Proc. International Conference on Computational Plasticity V*, Barcelona, CIMNE.

ARMERO, F. (2001). On the Characterization of Localized Solutions in Inelastic Solids: An Analysis of Wave Propagation in a Softening Bar. *Comput. Method Appl. Mech. Eng.*, 191, 181-213.

ARMERO, F. (2000). On the Locking and Stability of Finite Elements in Finite Deformation Plane Strain Problems, *Comput. & Struct.*, 75, 261-290.

ARMERO, F. & GLASER, S. (1996). Enhanced Strain Finite Element Methods for Finite Deformation Problems, *Proc. of III Congress of SEMMI,* Zaragoza, Spain.

ARREA, M. & INGRAFFEA, A.R. (1982). *Mixed-mode crack propagation in mortar and concrete.* Report N°81-13, Department of Structural Engineering, Cornell University, Ithaca, New York.

BARDET, J.P. (1991). Orientation of shear bands in frictional soils. *J. Eng. Mech.- ASCE,* Vol. 117, N°. 7, pp. 1466-1484.

BAŽANT, Z. & BELYTSCHKO, T.B. (1985). Wave propagation in a softening bar: Exact solution. *J. Eng. Mech.-ASCE*, 111:381-389.

BAŽANT, Z. & CEDOLIN, L. (1979). Blunt crack band propagation in finite element analysis. *J. Eng. Mech.-ASCE*, Vol.105, N° EM2, pp. 297-315.

BAŽANT, Z. & LIN, F.B. (1988). Non-local yield limit degradation . *Int. J. Num. Meth. Eng.,* 26:1805-1823.

BAŽANT, Z. & OH, B.H.. (1983). Crack band theory for fracture of concrete. *Matériaux et Constructions*, 93(16):155-177.

BAŽANT, Z. & PLANAS, J. (1998). *Fracture and size effect in concrete and other quasibrittle materials.* CRC Press LLC, USA.

BAŽANT, Z. (1976). Instability, ductility and size effect in strain softening concrete. *J. Eng. Mech.-ASCE*, 102:331-344.

BAŽANT, Z. (1993). Scaling laws in mechanics of failure. *J. Eng. Mech.-ASCE*, 119(9):1828-1844.

BAŽANT, Z.; BELYTSCHO, T.B. & CHANG, T.P. (1984). Continuum theory for strain softening. *J. Eng. Mech.-ASCE*, 110:1666-1692.

BAŽANT, Z.P. & OH, B.H. (1983). Crack band theory for fracture of concrete. *Mater. Struct.*, RILEM, Vol. 16, N°94, pp.155-177.

BAZELY, G.P.; CHEUNG, Y.K.; IRONS, B.M. & ZIENKIEWICZ, O.C.(1965). Triangular elements in plate bending – Conforming and noncoforming solutions, *Proc. First Conference on Matrix Methods in Structural Mechanics*, Wright-Patterson ATBFB, Ohio.

BELYTSCHKO,T.; FISH, J. & ENGELMANN, B.E. (1988). A finite element with embedded localization zones. *Comput. Method Appl. Mech. Eng.,* 70(1), pp. 59-89.

BELYTSCHKO,T.; LU, Y.Y. & GU, L. (1994). Element free Galerkin methods. *Int. J. Numer. Methods Eng.,* 37: 229-256.

BHATTACHARJEE, S.S. & LÉGER, P. (1994). Application of NLFM models to predict cracking in concrete gravity dams. *J. Struct. Eng.-ASCE*, Vol. 120. pp. 1255-1271.

BIGONI, D. & HUECKEL, T. (1991). Uniqueness and localization – I. Associative and non-associative elastoplasticity. *Int. J. Solids Struct.*, 28(2), pp. 197-213.

BIGONI, D. & ZACCARIA, D. (1993). On strain localization analysis of elastoplastic materials at finite strains. *Int. J. Plasticity*, 9 N° 1, pp. 21-33.

BIGONI, D. (2000). Bifurcation and instability of non-associative elastoplastic solids. CISM Lecture Notes. *Material Instabilities in elastic an plastic Solids*, H. Petryk (IPPT, Warsaw) Coordinator, 2000.

BLAAUWENDRAAD, J.& GROOTENBOER, H.J. (1981). Essentials for discrete crack analysis. *IABSE Colloquium on Advanced Mechanics of Reinforced Concrete*, Delft, pp. 263-272.

BOCCA, P.; CARPINTERI, A. & VALENTE, S.(1990). Size effects in the mixed mode crack propagation: Softening and snap-back analysis. *Eng. Fracture Mech.*, 35:159-170.

BOCCA, P.; CARPINTERI, A. & VALENTE, S. (1991). Mixed mode crack of concrete. *Int. J. Solids Struct.,* Vol. 27, N° 9, pp. 1139-1153.

CALLISTER (1997). *Materials Science and Engineering. An Introduction.* Third Edition Vol. 1 and 2. John Wiley and Sons Inc., New York.

CAROL, & WILLAM, K. (1997) Application of analytical solutions in elasto-plasticity to locaization analysis of damage models. In Owen,. D.R.J., Oñate, E., and Hinton, E. (Eds.), *Computational Plasticity (COMPLAS V)*, pp. 714-719, Barcelona. Pineridge Press.

CAROL, I.; RIZZI, E. & WILLAM, K. (1994) A unified theory of elastic degradation and damage based on a loading surface. *Int. J. Solids Struct.*, 31(20), 2835-2865.

CAROL, I.; RIZZI, E. & WILLAM, K. (1998) On the formulation of isotropic and anisotropic damage. *Computational Modelling of Concrete Structures*, de Borst *et al.* (Eds), 183-192.

CARPINTERI, A.; VALENTE, S.; FERRARA, G. & MELCHIORRI, G. (1993). Is mode fracture energy a real material property? *Comput. & Struct.*, 48(3):397-413.

CARPINTERI, A.; VALENTE, S.; ZHOU, F.P.; FERRARA, G. & MELCHIORRI, G. (1995). Crack propagation in concrete specimens subjected to sustained loads. In F.H. Wittmann (ed.) *Proceedings of the Second International Conference on Fracture Mechanics of Concrete Structures*, (FRA.M.CO.S. II): 1315-1328

CERVERA, M; AGELET DE SARACIBAR, C. & CHIUMENTI, M.(2001). *COMET: a multipurpose finite element code for numerical analysis in solid mechanics.* CIMNE, Technical University of Catalonia (UPC), Barcelona, Spain.

ČERVENKA, V. (1970). *Inelastic Finite Element Analysis of Reinforced Concrete Panels Under In-Plane Loads.* Ph.D. Thesis, University of Colorado, Boulder (USA).

CHABOCHE, J.L. (1979). Le concept de contrainte effective appliqué à l'élasticité et à la viscoplasticité en presence d'un endommagement anitrope. *Colloque EUROMECH* 115, Grenoble Edition du CNRS.

CHAVES, E.W.V. & OLIVER, J. (2001). On the Strong Discontinuity Approach in 3D settings. *XXII CILAMCE*, November 7th to 9th, 2001.Campinas – Brazil.

CHEN, A. & CHEN, W.F.(1975). Constitutive relations for concrete. *J. Eng. Mech.-ASCE,* 101:465-481.

CHEN, J.-S.; WU, C.-T. & BELYTSCHKO, T. (2000). Regularization of material instabilities by meshfree approximations with intrisic length scales. *Int. J. Numer. Methods Eng.,* 47:1303-1322.

CHEN, W.F. & HAN, D.J.(1988). *Plasticity for Structural Engineers.*, Springer-Verlag New Yor Inc.

CHEN, W.F.(1982). *Plasticity in reinforced concrete.*, McGraw-Hill, Inc. USA.

COPE, R.J.; RAO, P.V.; CLARK, L.A. & NORRIS, P. (1980). Modelling of reinforced concrete behaviour for finite element analysis of bridgeslabs. *Numerical Methods for Nonlinear problems 1* Taylor,C.; Hinton,E. and Oden, D.R.J. (Eds.), Pineridge Press, Swansea, 457-470.

COSSERAT, E. & COSSERAT, F.(1909). *Théorie des Corps Deformables.* Librairie Scientifique A. Hermann et Fils, Paris.

COURANT, R., (1943) Variational methods for the solution of problems of equilibrium and vibrations, *Bulletin of the American Mathematical Society* 49 (1943), 1-23.

CRISFIELD, M.A. (1981). A fast incremental iterative solution procedure that handless "snap through". *Comput. & Struct.,* 13:55-62.

CRISFIELD, M.A. (1997). *Non-Linear Finite Element Analysis of Solids and Structures*, volume 1,2. John Wiley and Sons, New York, USA.

DE BORST, R. & MÜHLHAUS, H.-B.(1992). Gradient-dependent plasticity: Formulation and algorithmic aspects. *Int. J. Numer. Methods Eng.,* 35, pp. 521-539.

DE BORST, R. & NAUTA, P. (1985). Non-Orthogonal cracks in a smeared finite element model. *Eng. Comput.*, 2, 35-46.

DE BORST, R. (1986). Non-linear analysis of frictional materials. *Dissertation*, Delft University of Technology, Delft, Netherlands.

DE BORST, R. (1991). Simulation of strain localization: A reappraisal of the Cosserat continuum, *Eng. Comput.*, 8, p. 317-332.

DE BORST, R.; SLUYS, L. MÜHLHAUS, H. & PAMIN, J. (1993). Fundamental issues in finite element analyses of localization of deformation. *Eng. Computation*, 10: 99-121.

DESAI, C.S. & SIRIWARDANE, H.J. (1984). *Constitutive laws for engineering materials with emphasis on geologic materials.* Prentice-Hall, Inc.USA.

DRUCKER, D.C. (1959). A definition of stable inelastic materials. *J. Appl. Mech.*, 26, pp. 101-106.

FARIA, R. & OLIVER, X. (1993). A rate dependent plastic-damage constitutive model for large scale computations in concrete structures. *Monograph CIMNE Nº17,* International Center for Numerical Methods in Engineering, Barcelona, Spain.

FARIA, R. (1994). Avalição do comportamento sísmico de barragens de betão através de um modello de dano conitinuo. *Dissertação(Ph.D. in Portuguese)*, Porto University, Portugal.

FEENSTRA, P.H. & DE BORST. (1995). A plasticity model and algorithm for mode –I cracking in concrete. *Int. J. Numer. Methods Eng.,* Vol. 38, pp 2509-2529.

FELIPPA,C.A. (2002). Introduction to Finite Element Methods. *Course Notes, see World Wide Web:* **http://caswww.colorado.edu/Felippa.d/FelippaHome.d/Home.html**

FUNG, Y.C. (1965). *Foundations of solids mechanics*, Prentice Hall Inc.

GURTIN, M. E. (1996). *An introduction to continuum mechanics.* NY: Academic Press, Inc.

GARIKIPATI, K. (1996). On strong discontinuities in inelastic solids and their numerical simulation. *Dissertation ,* Stanford University, California – USA.

GRIFFITH, A. A. (1921). The phenomena of rupture and flow in solids. *Philos. T. Roy. Soc.* A- 221, 163-197.

HADAMARD, J. (1903). *Lenços sur la propagation des ondes et les equations de l'hydrodynamique.* Librairie Scientifique A. Hermann et Fils, Paris.

HILL, R. (1952). On discontinuous plastic states, with special reference to localized necking in thin sheet. *J. Mech. Phys. Solids,* 1, 19.

HILL, R. (1958). A general theory of uniqueness and stability in elastic-plastic solids. *J. Mech. Phys. Solids*, 6, pp. 236-249.

HILL, R. (1962). Acceleration waves in solids. *J. Mech. Phys. Solids*, 16, 1-10.

HILLERBORG, A. (1985). Numerical methods to simulate softening and fracture of concrete. *Fracture Mechanics of Concrete. Structural Apllication and Numerical Calculation,* G. C. Sih and A. Di Tommaso, Eds., Martinus Nijhoff, Dordrecht, pp.141-169.

HILLERBORG, A.; MODEER, M. & PETERSSON, P.E. (1976). Analysis of crack formation and crack growth in concrete by means of fracture mechanics and finite elements. *Cement and Concrete Research*, 6, p.773-782.

HORDIJK, D.A.; REINHARDT, H.W. & CORNELISSEN, H.A.W. (1987). Fracture mechanics parameters of concrete from uniaxial tests as influenced by specimen length. Proc. SEM-RILEM *Int. Conf. On Fracture of Concrete and Rock*, S.P. Shah and S.E. Swartz (eds.), SEM, Bethel, 138-149.

HORDIJK, D.A.; REINHARDT, H.W. & CORNELISSEN, H.A.W. (1987). Fracture mechanics parameters of concrete from uniaxial tests as influenced by specimen length. Proc. SEM-RILEM *Int. Conf. On Fracture of Concrete and Rock*, S.P. Shah and S.E. Swartz (eds.), SEM, Bethel, 138-149.

INGLIS, C. (1913). Stress in a plate due to the presence of cracks and sharp corners. *Proc. Int. Naval Architects*, N° 60.

INGRAFEA, A. R. & SAOUMA, V. (1985). Numerical modeling of discrete crack propagation in reinforced and plain concrete. *Fracture Mechanics of Concrete. Structural Application and Numerical Calculation*, G. C. Sih and A. Di Tommaso, Eds., Martinus Nijhoff, Dordrecht, pp.171-225.

INGRAFEA, A. R. (1977). *Discrete fracture propagation in rock: laboratory tests and finite element analysis*. PhD Dissertation, University of Colorado at Boulder.

IORDACHE, M.-M. (1996). *Failure Analysis of Classical and Micropolar Elastoplastic Materials*. Ph.D. Dissertation, University of Colorado at Bolder.

IRWIN, G. (1957), Analysis of stresses and strain near the end of a crack traversing a plate. *J. Appl. Mech.- ASME*, 24, 361-364.

JIRÁSEK, M. & ZIMMERMANN, T. (1998). Analysis of rotating crack model, *J. Eng. Mech.- ASCE*, 124 , 842-851.

JIRÁSEK, M. (1998). Element-free galerkin method applied to strain-softening materials. Proc. *Computational Modelling of Concrete Structures (EURO-C)*, Badgastein, Austria. R. de Borst, N. Bićanić, H. Mang, and G. Meschke, Balkema, Rotterdam.

JIRÁSEK, M. (1998). Embendded crack models for concrete fracture. In de Borst *et al.*, editor, *Proc. EURO-C 1998 Computer Modelling of Concrete Structures*, pp. 291-300. Balkema.

JIRÁSEK, M. (1998). Finite elements with embedded cracks. *LSC Internal Report 98/01*, April.

KACHANOV, L. M. (1958). Time of rupture process under creep conditions. *Inzvestia Akademii Nauk. Otd Tech Nauk*. 8, 26-31.

KACHANOV, L. M. (1986). *Introduction to Continuum, Damage Mechanics*. Nijhoff, Dordrecht, The Netherlands.

KLISINSKI, M.; RUNESSON, K. & STURE, S. (1991). Finite element with inner softening band. *J. Eng. Mech.-ASCE*, 117(3):575-587.

KOBAYASHI, A.S.; HAWKINS, M.N.; BARKER, D.B. & LIAW, B.M. (1985). Fracture process zone of concrete. *Application of Fracture Mechanics to Cementitious Composite*. Shah S.P. (Ed.), Matinus Mijhoff Publ., Dordrecht, 25-50.

LARSSON, R.; RUNESSON, K. (1995). Cohesive crack models for semi-brittle materials derived from localization of damage coupled to plasticity. *Int. J. Fracture*, 69:899-911.

LARSSON, R.; RUNESSON, K. & ÅKESSON, M. (1995a). Embedded localization band based on regularized strong discontinuity, *Computational Plasticity – Fundamentals and Applications*, D.R.J. Owen and E. Oñate (eds.), Vol. 1, 599-610, Pineridge Pres, Swansea, U.K.

LARSSON, R.; RUNESSON, K. & ÅKESSON, M. (1995b). Embedded cohesive crack models based on regularized discontinuous displacements. In Fracture Mechanics of Concrete

Structures, Proceedings of FraMcoS-2, ed. by Wittmann, F.H., Aedificatio Publishers, Freiburg, Germany, pp.899-911.

LARSSON, R.; RUNESSON, K. & OTTOSEN, N.S. (1993). Discontinuous displacement approximation for capturing plastic localization. *Int. J. Numer. Meth. Eng.*, 36:2087-2105.

LARSSON, R.; RUNESSON, K. & STURE, S. (1996). Embedded localization band in undrained soil based on regularized strong discontinuity – theory and FE-analysis. *Int. J. Solids Struct.*, 33(20-22): 3081-3101.

LEGENDRE, D. (1984). Prévision de la ruine des structures en béton par une approche aombinée: mécanique de Fendommagent mécanique rupture. Thèse de Doctorat, Univesité Paris 6 – LMT Cachan.

LEMAITRE, J. (1996). *A course on damage mechanics.* Spring-Verlag Berlin Heidelberg., Germany.

LEMAITRE, J. & CHABOCHE, J.-L. (1990). *Mechanics of Solids materials.* Cambridge University Press, Cambridge.

LI, S. & LIU, W.K. (2000). Numerical simulations of strain localization in inelastic solids using meshfree methods. *Int. J. Numer. Meth. Eng.,* 48, pp. 1285-1309.

LOFTI, H. & SHING, P. (1995). Embedded representation of fracture in concrete with mixed finite elements. *Int. J. Numer. Meth. Eng.*, 38:1307-1325.

LOVE, A.E.H. (1944). *A treatise on the Mathematical Theory of Elasticity.* Cambridge University Press, London.

MAIER, G. & HUECKEL, T. (1979). Non-associated and coupled flow rules of elasto-plasticity for rock-like materials. *Int. J. Rock Mech. Min.*, 16, 77-92

MALVERN, L.E. (1969). *Introduction to the mechanics of a continuous medium.* Prentice-Hall, Inc. New Jersey.

MANDEL, J. (1964). Proppagation des surfaces de discontinuité dans un milieu élastoplastique, *Int. Ymp. on Stress Waves in anelastic solids*, pp.331-340, Springer, Berlin.

MANDEL, J. (1966). Conditions de stabilité et postulat de drucker. In. J. Kravtchenko and P. Sirieys, editors, *Rheology and Soil Mechanics*, pp 58-68, Berlin.

MANZOLI, O.; OLIVER, J. & CERVERA, M. (1999). *Localización de deformación: Análisis y simulación numérica de discontinuidades en la mecánica de sólidos.* Centro Int. De Métodos Num. En Ingeniería (CIMNE), Monografía N. 44, Barcelona – Spain.

MANZOLI, O.L.(1998). *Un modelo analítico y numérico para la simulación de discontinuidades fuertes en la mecánica de sólidos.* Ph.D. Thesis, Technical University of Catalonia, Barcelona España.

MARSDEN, J. E. & HUGHES, T. J.R. (1983). *Mathematical foundations of elasticity.* Dover Publications, Inc., New York.

MASE, G.E. (1977). *Mecánica del Medio Continuum.* McGraw-Hill, USA.

MAZARS, J.(1986). A Description of micro- and macroscale damage of concrete structures. *Eng. Fracture Mech.*, V.25, No. 5/6. pp.729-737.

MAZARS, J. & PIJAUDIER-CABOT, G.(1996). From damage to fracture mechanics and conversely: a combined approach. *Int. J. Solids Struct.,* Vol. 33, N° 20, pp 3327-3342.

MÜHLHAUS, H.-B. & VADOULAKIS, I. (1987). The thickness of shear bands in granular materials, *Geotechnique*, 37, p.271-283.

MÜNZ, T.; WILLAM, K. & RUNESSON, K. (1998). Viscoplastic algorithmic operators and their localization properties. In. de Borst, Bićanić, Mang & Meschke (ed.) *Computational Modelling of Concrete Structures*. Balkema, Rotterdam.

NEILSON, M.K. & SCHREYER, H.L. (1993). Bifurcations in elastic-plastic materials. *Int. J. Solids Struct.,* Vol. 3, No. 4, pp. 521-544.

NGO, D. & SCORDELIS, A.C. (1967). Finite element analysis of reinforced concrete beams. *Journal of the American Concrete Institute*, Vol. 64, N°3, pp. 152-163.

OGDEN, R.W. (1943). *Non-linear elastic deformations.* Dover Publications, Inc., New York.

OLIVER, J. & AGELET DE SARACÍBAR, C. (2000). *Mecánica de medios continuos para ingenieros.* Ediciones UPC, Barcelona, España.

OLIVER, J. (1989). A consistent characteristic length for smeared cracking models. *Int. J. Num. Meth. Eng.*, 28:461-474.

OLIVER, J. (1995a). Continuum modelling of strong discontinuities in solid mechanics using damage models. *Comput. Mech.*, 17(1/2):49-61.

OLIVER, J. (1995b). Continuum modelling of strong discontinuities in solid mechanics. In D. Owen, E. Oñate and H.E., editors, Proc. *International Conference on Computational Plasticity IV*, pp. 455-479, Barcelona, CIMNE

OLIVER, J. (1996a). Modeling strong discontinuities in solids mechanics via strain softening constitutive equations. Part 1: Fundamentals. *Int. J. Num. Meth. Eng.* , 39(21):3575-3600.

OLIVER, J. (1996b). Modeling strong discontinuities in solids mechanics via strain softening constitutive equations. Part 2: Numerical simulation. *Int. J. Num. Meth. Eng.* , 39 (21) : 3601 - 3623.

OLIVER, J. (1998). The strong discontinuity approach: an overview. In: Idelsohn,S., Oñate, E.,Dvorkin, E.N. (Eds.), Computational Mechanics. New Trends and Applications. Proceedings (CD-ROM) of the *IV World Congress on Computational Mechanics (WCCM98).* CIMNE, pp. 1-19.

OLIVER, J. (2000). On the discrete constitutive models induced by strong discontinuity kinematics and continuum constitutive equations. *Int. J. Solids Struct.*, 37:7207-7229.

OLIVER, J. (2002). Topics on Failure Mechanics. *Monograph CIMNE Nº 68*, International Center for Numerical Methods in Engineering, Barcelona, Spain.

OLIVER, J.; CERVERA, M. & MANZOLI, O. (1997). On the use of J2 plasticity models for the simulation of 2D strong discontinuities in solids. In: Owen,D., Oñate, E., Hinton, E. (Eds.*), Proc. Int. Conf. On Computational Plasticity, Barcelona*, Spain. CIMNE, pp. 38-55.

OLIVER, J.; CERVERA, M. & MANZOLI, O. (1998). On the use of strain-softening models for the simulation of strong discontinuities in solids. In R. de Borst and E. van der Giessen, editors, *Material Instabilities in Solids.* John Wiley and Sons Ltd.

OLIVER, J.; CERVERA, M.; OLLER, S. & LUBLINER, J. (1990). Isotropic damage models and smeared crack analysis of concrete. In N. Bićanić et al. (ed) Proc.. *SCI-C Computer Aided Analysis and Design of Concrete Structures*, pp. 945-957.

Oliver, J.; Cervera, M.; Oller, S. & Lubliner, J. (1990). Isotropic damage models and smeared crack analysis of concrete. In N. B. et al., Eds, *SCI-C Computer Aided Analysis and Design of Concrete Structures*, pp. 945-957, Swansea, Pineridge Press.

Oliver, J.; Cervera, M.; Pulido, M.D.G. & Chaves, E. (1999). Sobre la aproximación continua de discontinuidades en mecánica de sólidos. *Congreso Español de Método Numérico en Ingeniería*. R. Abascal, J. Dominguez y G. Bugeda (Eds.) SEMNI.

Oliver, J.; Huespe, A.E.; Pulido, M.D.G. & Chaves, E. (2000). Modelação de fissuras em estruturas de concreto mediante uma aproximação de descontinuidades fortes *VI Congresso Nacional de Mecânica Aplicada e Computacional*, Aveiro – Portugal.

Oliver, J.; Huespe, A.E.; Pulido, M.D.G. & Chaves, E.W.V. (2001). From continuum Mechanics to fracture mechanics: the strong discontinuity approach. *Eng. Fracture Mech.*, 69, 113-136.

Oliver, J.; Huespe, A.E.; Samaniego, E. & Chaves, E.W.V. (2002). Elementos finitos con discontinuidades internas. Estudio del bloqueo de tensiones y de sus posibles soluciones. *Métodos Numéricos en Ingeniería V*, Goicolea *et al.* (Eds.), SEMNI, Madrid – España.

Oliver, J.; Huespe, A.E.; Samaniego, E. & Chaves, E.W.V. (2002). On strategies for tracking strong discontinuities in computational failure mechanics. *WCCM V - Fifth World Congress on Computacional Mechanics*, July 7-12, Vienne, Austria H.A. Mang *et al.* (Eds.) .

Oliver, J. & Simo, J. (1994). A new approach to the analysis and simulation of strong discontinuities. In. Z.P. Bažant *et al.*, editors, *Fracture and Damage in Quasi-brittle Structures*, E&FN Spon, pp. 25-39.

Oller, S. (1988). *Un modelo de daño continuo para materials friccionales*, Ph.D. thesis. Universidad Politécnica de Cataluña, Barcelona, España.

Oller, S. (2001). *Fractura mecánica. Un enfoque global*. CIMNE, Barcelona, España.

Ortiz, M & Quigley, J. (1991). Adaptive mesh refinement in strain localization problems. *Comput. Method Appl. Mech. Eng.,* 90: 781-804.

Ortiz, M. (1987). An analytical study of the localized failure modes of concrete. *Mech. Mater.*, Vol. 6, pp. 159-174.

Ortiz, M.; Leroy, Y. & Needleman, A. (1987). A finite element method for localized failure analysis. *Comput. Method Appl. Mech. Eng.*, 61:189-214.

Ottosen, N.S. & Runesson, K. (1991a). Acceleration waves in elasto-plasticity. *Int. J. Solids Struct.*, 28(2): pp. 135-159.

Ottosen, N.S. & Runesson, K. (1991b). Discontinuous bifurcations in a nonassociated Mohr material. *Mech. Mater.*, 12 pag.255-265. Elsevier.

Ottosen, N.S. & Runesson, K. (1991c). Discontinuous bifurcations in elasto-plasticity, *Int. J. Solids Struct.* 27, 401-421.

Pamin, J.(1994). *Gradient-dependent plasticity in numerical simulation of localization phenomena*. PhD Thesis, Delft University of Technology, Delft, Netherlands.

Peerlings, R. H.J.(1999). *Enhanced damage modelling for fracture and failure*. PhD Thesis, Delft University of Technology, Delft, Netherlands.

PETERSSON, P. E. (1981). Crack growth and development of fracture zones in plain concrete and similar materials. Report Nº TVBM-1006, *Division of Building Materials*, University of Lund, Sweden.

PIJAUDIER-CABOT & BAŽANT, Z.P. (1987). Nonlocal damage theory. *J. Eng. Mech.-ASCE,* 113, pp.1512-1533.

PLANAS, J. & ELICES, M. (1992). Nonlinear fracture of cohesive materials. *Int. J. Fracture,* 51:139-157.

POTTS, D.M. & ZDRAVKOVIĆ, L. (1999). *Finite element analysis in geotechnical engineering.* Thomas Telford Publishing, London.

RABOTNOV, Y.N. (1969). *Creep problems in structural members.* Amsterdam, North-Holland.

RASHID, .R. (1968). Analysis of prestressed concrete pressure vessel. *Nucl. Eng. Des.,* 7(4), 334-355.

REGUEIRO, R. & BORJA, R. (1999). A finite element model of localized deformation in frictional materials taking a strong discontinuity approach. *Finite Elem. Anal. Des.* 33, 283-315.

REINHARDT, H.W.; CORNELISSEN, H.A.W. & HORDIJK, D.A. (1986). Tensile tests and failure analysis of concrete. *J. Struct. Eng.-ASCE*, 112(11), 2462-2477.

RICE, J. (1976). The localization of plastic deformation. *14th Int. Congress on Theoretical and Applied Mechanics.* W.T. Koiter, editor, 1, pag. 207-220. North-Holland Publ. Co. Delft, The Netherlands.

RICE, J.R. & RUDNICKI, J.W. (1980). A note on some feature of the theory of localization of deformation, *Int. J. Solids Struct.,* 16, pp.597-605.

RICE, J.R.(1973). Plasticity and Soil Mechanics. *Proc. of the Symposium on the Role of Plasticity in Soil Mechanics.* Palmer, A.C. (Ed.), p.263. Cambridge, England.

RIZZI, E.; CAROL, I. & WILLAM, K. (1995). Localization analysis of elastic degradation with application to scalar damage. *J. Eng. Mech.-ASCE* , Vol. 121. Nº4.

ROTS, J. & BLAAUWENDRAAD, J. (1989). Crack models for concrete: discrete or smeared? Fixed, multi-directional or rotating?, *HERON,* Delft University of Technology, The Netherlands, 34(1).

ROTS, J.; NAUTA, P.; KUSTERS, G.M.A. & BLAAUWENDRAAD, T. (1985). Smeared crack approach and fracture localization in concrete. *HERON*, 30(1): 48.

ROTS, J.G. & DE BORST, R. (1987). Analysis of mixed-mode fracture in concrete. *J. Eng. Mech.-ASCE,* Vol. 113, Nº 11, pp 1739-1758.

ROTS, J.G. (1988). *Computational modeling of concrete fracture.* Dissertation, Delft University of Technology, Delft, Netherlands.

ROTS, J.G.; NAUTA, P.; KUSTERS, G.M. & BLAAUWENDRAAD, J. (1985), Smeared crack approach and fracture localization in concrete. *HERON*, 30(1):48.

RUDNICKI, J.W. & RICE, J.R. (1975). Condition for the localization of the deformation in pressure-sensitive dilatant material. *J. Mech. Phys. Solids,* 23, 371-394.

RUNESSON, K. & MROZ, Z. (1989). A note on nonassociated plastic flow rules. *Int. J. Plasticity*, 5, 639-658.

RUNESSON, K. ; OTTOSEN, N. & PERIĆ, D. (1991). Discontinuity bifurcation of elastic-plastic solutions at plane stress and plane strain. *Int. J. Plasticity*, 7:99-121.

SAMANIEGO, E. (2002). *Contributions to the continuum modelling of Strong Discontinuities in two-dimensional solids*. PhD Thesis, Technical University of Catalonia, Barcelona, Spain.

SIMO, J. & ARMERO, F. (1992). Geometrically non-linear enhanced strain mixed methods and the method of incompatible modes. *Int. J. Num. Meth. Eng.* 33:1413-1449.

SIMO, J. & HUGHES, T.J.R. (1998). *Computational Inelasticity*. Spriner-Verlag, New York.

SIMO, J. & JU, J.W. (1997a). Strain- and stress-based continuum damage models – I. Formulation. *Int. J. Solids Struct.,* 23:281-840.

SIMO, J. & JU, J.W. (1997b). Strain- and stress-based continuum damage models – II. Formulation. *Int. J. Solids Struct.,* 23:841-869.

SIMO, J. & OLIVER, J. (1994). Modelling strong discontinuities by means of strain softening constitutive equations. In H. Mang *et al.*, editor, *Proc. EURO-C 1994 Computer Modeling of concrete structures*, pp. 363-372, Swansea. Pineridge Press.

SIMO, J. & RIFAI, S. (1990). A class of mixed assumed strain methods and the method of incompatible modes. *Int. J. Num. Meth. Eng.,* 29:1595-1638.

SIMO, J.; OLIVER, J. & ARMERO, F. (1993). An analysis of strong discontinuities induced by strain-softening in rate-independent inelastic solids. *Comput. Mech.*, 12:277-296.

SLUYS, L.J. (1992). *Wave propagation, localization and dispersion in softening solids.* Printed by: W.D. Meinema B.V. Delft.

SLUYS, L.J. & DE BROST, R. (1992). Wave propagation and localization in a rate-dependent crack medium: Model formulation and one-dimensional examples. *Int. J. Solids Struct.* 29:2945-2958.

SOKOLNIKOFF, I.S. (1987). *Mathematical Theory of Elasticity*. Robert E. Krieger Publishing Company, Florida-USA.

STEINMANN, P. & WILLAM, K. (1991). Localization within the framework of micropolar elasto-plasticity, *Advances in continuum mechanics*, Ed. V Mannl *et al.*, Springer Verlag, Berlin, p.296-313.

STEINMANN, P. & WILLAM, K. (1994). Finite-element analysis of elastoplastic discontinuities. *J. Eng. Mech.-ASCE*, 120(11):2428-2442.

STEINMANN, P. (1998). A model adaptive strategy to capture strong discontinuities at large inelastic strains. In: Idelsohn,S., Oñate, E., Dvorkin, E.N. (Eds.), Computational Mechanics. New Trends and Applications. Proceedings (CD-ROM) of the *IV World Congress on Computational Mechanics (WCCM98)*. CIMNE.

STEINMANN, P. (1999). A finite element formulation for strong discontinuities in fluid-saturated porous media. *Mech. Cohes.-Frict. Mater.*, 4, pp.133-152.

TANO, R. (1997). *Localization modelling with inner softening band finite elements*. Ph.D. Thesis, Luleå University of Technology.

THOMAS, T. (1961). *Plastic flow and fracture in solids*. Academic Press, New York, N.Y.

TRUESDELL, C.A. & NOLL, W. (1965). The non-linear field theories of mechanics, in *Handuch der Physik*, Vol. III/3, S. Flügge (Ed.), Springer-Verlag, Berlin.

TVERGAARD, V. & NEEDLEMAN, A.(1995) Effects of nonlocal damage in porous plastic solids. *Int J Solids Struct.*, 32(8/9): 1063-1077.

VARDOULAKIS, I. (1981). Bifurcation analysis of the plane rectilinear deformation on dry sand samples. *Int. J. Solids Struct.*, 17(11):1085-1101.

VARDOULAKIS, I.; GOLDSCHEIDER & GUDEHUS, G. (1978). Formation of shear bands in sand bodies as a bifurcation problem. *Int. J. Numer. Anal. Meth. Geomech.*, 2:99-128

WELLS, G.N. & SLUYS, L.J. (2000). Application of embedded discontinuities for softening solids. *Eng. Fracture Mech.,* 65, 263-281.

WELLS, G.N. (2001). *Discontinuous modeling of strain localization and fracture.* Dissertation, Delft University of Technology, Delft, Netherlands.

WILLAM, K. & SOBH, N. (1987). Bifurcation analysis of tangential material operators. In. G.N. Pande and J. Middleton, editors, Transient/Dynamic Analysis and Constitutive Laws for Engineering Materials, C4/1—13. Martinus-Nijhoff Publishers.

WILLAM, K. (2000). *Constitutive models for materials: Encyclopedia of Physical Science & Technology*, 3rd edition. Academic Press.

WILLAM, K.; BIĆANIĆ & STURE, S. (1984). Constitutive and computational aspects of strain-oftening and localization in solids. In K.A. Willam, editor, Constitutive Equations: macro and computational aspects, pp. 845-867, New York.

WILSON, E.L.; TAYLOR, R.L.; DOHERTY, W.P. & GHABOUSSI, J. (1973). Incompatible displacement models, in S.J. Fenves *et al.*(eds.*), Numerical and Computer Models in Structural Mechanics*, Academic Press New York.

ZIENKIEWICS, O.C. & TAYLOR, R.L. (1994a). *El método de los elementos finitos. Volumen 1: Formulación básica y problemas lineales.* CIMNE, Barcelona, 4ª edition.

ZIENKIEWICS, O.C. & TAYLOR, R.L. (1994b). *El método de los elementos finitos. Volumen 2: Mecánica de sólidos y fluidos. Dinámica y no linealidad.* CIMNE, Barcelona, 4ª edition.

Index

Author Index

V

W

Z